THE UNIVERSITY *of* EDINBURGH

Computational Modelling of Concrete Structures Subjected to High Impulsive Loading

by

Jiaming Xu

A thesis submitted in fulfilment of the requirements

for the degree of Doctor of Philosophy

Institute of Infrastructure and the Environment

School of Engineering

The University *of* Edinburgh

2016

Declaration

This thesis entitled, “Computational modelling of concrete structures subjected to high impulsive loading” is submitted to the University of Edinburgh for the degree of Doctor of Philosophy.

The research work described and reported in this thesis has been completed solely by Jiaming Xu under the supervision of Professor Yong Lu and Professor Asif Usmani. I confirm:

- that the thesis has been composed by the author, and
- either that the work is the author’s own, or, if the author has been a member of a research group, that the author has made a substantial contribution to the work, such contribution being clearly indicated, and
- that the work has not been submitted for any other degree or professional qualification except as specified, and
- that any included publications are the author’s own work, except where indicated throughout the thesis and summarised and clearly identified on the declarations page of the thesis.

Several publications have been produced based on this thesis project, including:

Xu, J. and Lu, Y., 2013. “A Comparative Study of Modelling RC Slab Response to Blast Loading with Two Typical Concrete Material Models.” *International Journal of Protective Structures* 4(3): 415–32.

Xu, J. and Lu, Y., 2016. “Numerical Modelling For Reinforced Concrete Response to Blast Load: Understanding The Demands On Material Models.” *ACI Special Publication* 306: 3.1-3.22.

Lu, Y., Xu, J. and Weerheijm, J., 2013. “A mesoscale modelling perspective of cracking process and fracture energy under high strain rate tension.” *FraMCoS-8: 8th International Conference on Fracture Mechanics of Concrete and Concrete Structures*. March 2013, Toledo, Spain.

Lu, Y. and Xu, J., 2013. “Simulation of reinforced concrete response to blast with sshydrocode material models.” *15th ISIEMS:15th International Symposium on Interaction of the Effects of Munitions with Structures*. September 2013, Potsdam, Germany.

Xu, J. and Lu, Y., 2015. “Evaluation of residual structural capacity of blast-damaged RC members.” *CONFAB 2015: The First International Conference on Structural Safety under Fire & Blast* . Glasgow, Scotland, UK.

Xu, J., Lu, Y. "Transient high shear and its effect on RC members subject to blast load: a numerical study". (In final preparation to be submitted to *International Journal of Impact Engineering*).

Jiaming Xu

May 2016

Abstract

The behaviour of concrete structures subjected to high impulsive loading such as blast involves complex responses at the constituent material as well as local to global structural levels. To fully describe the processes involved, detailed numerical simulation is generally required and it is in fact commonly employed nowadays in this field of investigations. However, the demands on a rigorous computational model with the capability to represent different regimes of responses throughout the entire process, namely the stress wave stage under the immediate impulsive (blast) loading, the development of local composite mechanism (such as shear), and finally the global bending / residual structural state, have not been established nor thoroughly investigated in the literature. This thesis aims to fill in this gap and develop an effective and efficient modelling framework for reinforced concrete (RC) structures under impulsive loading, with a particular focus on the analysis of complex dynamic shear mechanisms and the residual structural capacities.

This thesis uses a benchmark RC slab as a testbed to firstly examine the validity of commonly applied finite element setup and typical material models for the analysis of the structural response into the global deformation phase and the residual state. This is followed by a detailed scrutiny of the demands on the concrete material model in terms of preserving a realistic representation of the tension/shear behaviour and the significance of such features in simulating realistically the structural response in a reinforced concrete environment. Deficiencies of a widely used concrete material model, namely the Karagozian and Case concrete (KCC) model, in this respect are investigated and a modification scheme to the relevant aspects of the material model is proposed. The modification is demonstrated to result in satisfactory improvement in terms

of ensuring more robust simulation of reinforced concrete response to blast loading.

To deal with the inevitable modelling uncertainties in the part of concrete surrounding reinforcing bars in a numerical model, an equivalent transitional layer model is proposed for use in finite element modelling of RC structures subjected to impulsive loading. The main objectives of the equivalent transitional layer are to achieve a consist transfer of stress between rebar to concrete outside the transitional zone, and to maintain a realistic relative “sliding” displacement between the outer edge of the transitional layer and the rebar, while the inner edge of the transitional layer is perfectly bonded (with node-sharing) to the rebar. With appropriate descriptions of the softening and failure of the material for the transitional layer, the deformation profile and the strength can be reasonably represented in a consistent manner using the perfect-bond scheme which is commonly adopted in this field of applications. The transitional layer also incorporates features to ensure mesh-independent bond strength. Validation of proposed transitional layer model is carried out against results from RC pull-out and beam experiments.

The above modelling framework is subsequently employed to investigate the dynamic shear resistance of RC beam/slab under impulsive loading, recognising that the information on the dynamic shear strength in very scarce in the literature. The influence of loading rate on the change of shear span, which alters the shear resistance mechanism and generally results in an increase of the shear capacity, is discussed. The influence of the strain rate enhancement of the material strength on the dynamic shear capacity is also evaluated.

Keywords: Impulsive load, blast, dynamic effects, reinforced concrete, numerical modelling, shear resistance

Lay summary

Computational simulation has been widely used for building design against blast and impact. To fully describe the behaviour and failure process of reinforced concrete structures after the blast, detailed numerical simulation is generally required and commonly employed nowadays in this field of investigations. However the requirements of the simulation method to describe different regimes of responses throughout the entire process have not been established nor thoroughly investigated in the literature. This thesis aims to fill in this gap and develop an effective and efficient modelling method to investigate what happens when reinforced concrete structures are exposed to blast.

This thesis firstly identifies the demands on the modelling of concrete material in terms of preserving a realistic representation of its shear and tensile behaviour and the significance of such features in simulating realistically the structural response in a reinforced concrete environment. Modification has been proposed to existing simulation method for concrete, and the author also introduces a practical method to consider the interaction between the concrete and the steel reinforcement bars.

The above modelling method is subsequently employed to investigate the dynamic performance of RC beam and slab under blast. The influence of different blast types on the load-carrying mechanism and performance of concrete members, is discussed. A simplified analytical method has been proposed to predict the demand of blast load and the performance of reinforced concrete members.

Acknowledgements

This thesis marks the end of my journey in obtaining the PhD, as well as my 25 years' time of being a student. It can hardly be completed without the support of numerous people including my supervisor, colleagues, family and friends. At the beginning of my thesis I would like to thank everyone who have made this thesis possible and I'm so grateful for every little help and encouragement along the way.

First and foremost, I would like to express sincere gratitude to my supervisor Professor Yong Lu, whose guidance and support have been invaluable in this project. His constructive suggestions, criticisms, and the willingness to generously give time to the project and the thesis during the last four years are much appreciated and duly acknowledged. While his exceptional domain expertise was imperative in shaping me as a rigorous researcher, his logical way of thinking and a rational perspective in problem-solving have been a great value for me.

I would like to thank my co-supervisor Professor Asif Usmani for his help on my research. I have enjoyed a great deal working with both of my supervisors and a student could not have asked for more.

A very sincere thanks to my colleagues and friends in the 3rd floor of AGB building in particular Lei Mao, Yu Dong, Jiang Jian, Mohammedreza Ebrahimi, Prashant Gupta, J.P. Morrisey, Payam Khazaeinejad, Colin Brett, Rongxin Zhou, Chuanchuan Hou, Xiaobo Chen, Ofonime Harry and Zhenhuan Song for their helpful comments, suggestions and great friendship.

I take this opportunity to sincerely acknowledge the China Scholarship Council and the University of Edinburgh for providing financial assistance which buttressed me to performance my study comfortably.

Special thanks to my roommate Rui Chen and Xin Li, who treated me as family during my stay in the cosy and warm flats in the beautiful Grange area, and have been around in both sorrow and joy.

Last but not least, a special gratitude is due to my mum and dad, to whom this thesis is dedicated. Without their everlasting love, support, tolerance and encouragement I would never have embarked on my doctoral study abroad and would not have had the opportunity to write this thesis.

Contents

Declaration i

Abstract iii

Lay summary v

Acknowledgements vi

Contents viii

List of figures xvi

List of tables xxviii

List of abbreviations xxix

Chapter 1: Introduction 1

1.1 Background 1

1.2 Objective and scope 3

1.3 Organisation of the thesis 5

Chapter 2: Literature review 7

2.1 Introduction 7

2.1.1 Outline of the literature review 8

2.2 Failure mechanism of concrete and its constitutive description 9

2.2.1 Failure mechanisms of concrete under varied pressure regime 9

2.2.2 Choice of numerical methodology on modelling plasticity and damage 11

2.3 Review of typical concrete material models used in hydrocodes 13

2.3.1 Concrete damage plasticity (CDP) model 14

2.3.2 Pseudo-tensor (PT) model 16
2.3.3 Geologic cap (GC) model 18
2.3.4 Brittle damage concrete (BDC) model 19
2.3.5 Winfrith concrete (WC) model 20
2.3.6 Johnson and Holmquist concrete (JHC) model 21
2.3.7 RHT model 23
2.3.8 Summarised on features of material models and simulation recommendations 25
2.4 Brief review on numerical simulation of RC members under impulsive loading 27
2.4.1 Simulation on flexure-dominated structural response and failure 28
2.4.2 Simulation on shear-dominated structural response and failure 37
2.4.3 Concluding remarks 50
Chapter 3: Numerical modelling of RC structural response to blast loading: common practice and issues 51
3.1 Introduction 51
3.2 Overview and general discussion on the KCC and CSC models 53
3.2.1 Strength surfaces and damage definition in KCC model 54
3.2.2 Strength surfaces and damage definition in CSC model 58
3.2.3 Consideration of fracture energy and mesh convergence 61
3.2.4 Further discussion on interpretation of the damage indices 64
3.3 Numerical simulations with the two concrete models and comparison with experimental results 67
3.3.1 Simulation of RC slab response to blast load 68
3.3.2 Simulation of RC beam under quasi-static load 78

3.3.3 Discussion on the abnormal over-ductile tensile behaviour of CSC model……..84

3.4 Conclusions 88

Chapter 4: Modification to KCC model and holistic modelling of RC flexural and shear response 90

4.1 Introduction 90

4.2 Further investigation on the premature failure of interaction between concrete and rebar 91

4.2.1 Examination of the two rebar models using a pull-out test 94

4.2.2 Effect of transverse stirrups in reducing the “bond” demand in RC members..... 100

4.3 Proposed modification to the standard KCC model..... 105

4.3.1 General discussion of the modification strategy 105

4.3.2 Modifications to the softening law in KCC model..... 106

4.3.3 Parameterisation of η-λ curve and b_1 factor..... 109

4.4 Simulation of RC response using modified KCC model 112

4.4.1 Validation of the proposed modification in a pull-out setting..... 112

4.4.2 Simulation of the RC beam and slab response using the modified KCC model 113

4.5 Further validation against RC beam experiments tested at University of Edinburgh 115

4.5.1 Experimental programme and numerical modelling 116

4.5.2 Beam S0 & D12: diagonal tension failure..... 118

4.5.3 Beam D18: flexure failure 120

4.5.4 Overall comment on the performance of simulating RC shear failure….. 120

4.6 Conclusions 121

Chapter 5: An equivalent transitional layer model for modelling concrete-rebar interaction 123

5.1 Introduction 123

5.1.1 Characteristic of bond interaction between concrete and rebar ... 124

5.1.2 Modelling scales and numerical approaches 127

5.2 Basic framework and parameter generation for equivalent transitional layer 128

5.2.1 The equivalence objective of the transitional layer between concrete and rebar 128

5.2.2 Equivalent stress state in the transitional layer 130

5.2.3 Definition of failure surfaces for the equivalent transitional layer 136

5.2.4 Equivalent strain state and “slip” deformation 141

5.3 Validation studies with experiment 143

5.3.1 Validation with Baena’s test 144

5.3.2 Validation with Eligehausen’s test 146

5.4 Conclusions 149

Chapter 6: Transient high shear phenomenon and transition of response modes of RC members subjected to blast load 151

6.1 Introduction 151

6.2 Numerical analysis with beam elements 153

6.2.1 RC beam specimen and characteristic flexural period 153

6.2.2 Numerical model with beam elements and material properties ... 155

6.2.3 Blast loading 157

6.3 Shear response of simply supported RC member 158

6.3.1 Response under blast load in quasi-static regime ($t_d \approx T_f$)..... 158

6.3.2 Response under blast load in impulsive regime (e.g. t_d = 1 ms ≈ T_f/40) 160

6.3.3 Response under blast load in dynamic regime ($t_d \approx T_f/5$) 163

6.3.4 Influence of loading rate on simply supported beams 165

6.4 Shear response of fixed-supported RC member 170

6.4.1 Response under blast load in quasi-static regime ($t_d \approx T_f$) 170

6.4.2 Response under blast load in impulsive regime (t_d=1ms ≈ T_f/16) 172

6.4.3 Response under blast load in dynamic regime ($t_d \approx T_s/4$)..... 174

6.4.4 Influence of loading rate on the fixed-end beam 176

6.5 Concluding remarks..... 179

Chapter 7: Dynamic shear resistance of RC member: shear mechanisms and influence of material rate effect 182

7.1 Introduction 182

7.2 Numerical modelling 185

7.2.1 FE model set-up 185

7.2.2 Analysis of quasi-static behaviour of simply-supported RC beam 186

7.2.3 Analysis of quasi-static behaviour of fixed-supported RC beam... 190

7.2.4 Determination of effective shear span and shear resistance under distributed load 193

7.3 Dynamic shear behaviour and dynamic shear resistance for simply-supported RC beam..... 195

7.3.1 Dynamic shear behaviour in “quasi-static” regime (blast duration on order of flexural mode period) 196

7.3.2 Dynamic shear behaviour in “dynamic” regime (blast duration a fraction of flexural mode period) 198

7.3.3 Dynamic shear behaviour in “impulsive” regime 201

7.4 Dynamic shear behaviour and dynamic shear resistance for fixed-supported RC beam 204

7.4.1 Dynamic shear behaviour under blast duration in the order of flexural period ($t_d > T_f$) 204

7.4.2 Dynamic shear behaviour under blast duration close to dynamic regime ($t_d \approx 0.2T_f$) 207

7.4.3 Dynamic shear behaviour under blast duration close to impulsive regime ($t_d \approx 0.03T_f$) 209

7.5 Variation of the effective shear span in dynamic shear response 212

7.5.1 Effect of loading rate on effective dynamic shear span 212

7.5.2 Effect of loading rate on dynamic increase of shear resistance 214

7.6 Definition and implementation of strain rate effect in concrete and reinforcement steel 216

7.6.1 DIF curves 217

7.6.2 Numerical implementation of material DIF effect in the concrete model 219

7.6.3 Verification of modified DIF effect on dynamic fracture energy 220

7.7 Influence of material rate effect: simply-supported RC beam 222

7.7.1 Material rate effect on dynamic shear strength in “impulsive” regime 222

7.7.2 Material rate effect on dynamic shear strength in “dynamic” regime 225

7.7.3 Material rate effect on dynamic shear strength in “quasi-static” regime……228

7.8 Influence of material rate effect: fixed-supported RC beam 230

7.8.1 Material rate effect on dynamic shear strength in “impulsive” regime……230

7.8.2 Material rate effect on dynamic shear strength in “dynamic” regime……233

7.8.3 Material rate effect on dynamic shear strength in “quasi-static” regime……236

7.9 Influence of material rate effect on dynamic shear resistance under varied load durations 239

7.10 Concluding remarks 241

Chapter 8: Analysis of dynamic shear demands using simplified SDOF models and assessment of shear response 243

8.1 Introduction 243

8.2 Representative SDOF systems 245

8.2.1 Flexural mode 246

8.2.2 Direct shear mode 250

8.2.3 Diagonal shear mode 256

8.3 Validation and modification of the proposed SDOF parameters..... 264

8.4 Correlation between SDOF predictions and actual responses concerning transient high shear 267

8.4.1 Shear response dominated by flexural mode..... 268

8.4.2 Shear response dominated by direct shear mode 270

8.4.3 Shear response dominated by diagonal shear mode..... 272

8.5 Simplified assessment of dynamic shear response 273

8.5.1 Direct shear resistance 274
8.5.2 Diagonal shear resistance 277
8.5.3 General procedure of simplified assessment for dynamic shear response 282
8.6 Concluding remarks 284
Chapter 9: General conclusions and recommendation for further works ... 285
9.1 Summary of main conclusions 285
9.1.1 Development of a holistic FE framework for modelling RC structures under impulsive loading 285
9.1.2 Development of a transitional layer model to estimate the bond interaction between concrete and rebar 288
9.1.3 Transition of response modes, transient high shear phenomenon and dynamic shear resistance of RC structures under impulsive loading . 288
9.1.4 Proposal of a SDOF based simplified assessment for dynamic shear response of RC structures under blast loading 291
9.2 Recommendations for future works 292
Reference 294

List of figures

Fig. 2.1 Typical behaviours and local damage modes of concrete, after Mazars and Pijaudier-Cabot (1989) 10
Fig. 2.2 Unloading response of a) elastic damage, b) elasto-plastic and c) elasto-plastic damage models (adapted from Jason et al., 2006) 12
Fig. 2.3 Different shapes of κ curves defining both hardening and softening effect (Lee 1996) 16
Fig. 2.4 Two definition of failure surfaces for Pseudo-tensor model (LSTC 2012) 16
Fig. 2.5 The yield surface of the two-invariant Geologic cap model (LSTC 2012) 18
Fig. 2.6 The shear-pressure strength response of the JH model (after Polanco-Loria et al., 2008a) 22
Fig. 2.7 Failure surfaces and stress update in RHT model 24
Fig. 2.8 Elasto-plastic Drucker-Prager model based FE simulation (after Kishi et al. 2011) 30
Fig. 2.9 Crack pattern on tension side and deflection history of slab blast tests, after El-Dakhakhni et al. (2009) 32
Fig. 2.10 Post-test deformation of the RC column, after Magallanes (2008a) ... 33
Fig. 2.11 Deflection and reaction history of the impacted column Thilakarathna et al. (2010) 34
Fig. 2.12 Time histories of mid-span deflection of RC slab under blast pressure (after Wu et al. 2014) 36
Fig. 2.13 Comparison of crack patterns and deflection histories from experiments and simulations (after Wesevich et al. 2011) 37

Fig. 2.14 Numerical analysis of failure mechanisms under varied loading rates (after Adhikary et al. 2012) 39
Fig. 2.15 Numerical analysis of failure mechanisms under varied loading rates (after Adhikary et al. 2012) (continued) 40
Fig. 2.16 Numerical and experimental damage mode of RC beams under impact (Murray et al. 2007) 41
Fig. 2.17 Numerical and experimental damage mode of RC beam under vehicle collision (Murray et al. 2007) 42
Fig. 2.18 FE analysis for RC beam at varied drop height, after Jiang et al. (2015) 44
Fig. 2.19 Comparison of post-blast deflected shapes and damage patterns (after Williams 2009) 45
Fig. 2.20 Comparison of mid-span time histories and damage profiles for 132kg equivalent TNT test (after Kyei 2014) 46
Fig. 2.21 Damage pattern of FE simulation and test under different impact velocities (after Abu-odeh 2008) 48
Fig. 2.22 Simulation of RC column subjected to contact explosive (after Wu et al. 2011)..... 49
Fig. 3.1 Failure surfaces defined in KCC model..... 54
Fig. 3.2 Default η-λ curve defined in KCC model 55
Fig. 3.3 Incremental plastic strain multiplier vs. hydrostatic pressure..... 57
Fig. 3.4 Failure surfaces defined in CSC model..... 58
Fig. 3.5 Strain softening and stiffness reduction due to damage accumulation in CSC model (after Murray 2007) 60
Fig. 3.6 Tensile response of singe element with varied element sizes 62
Fig. 3.7 Compressive response of singe element with varied element sizes..... 63
Fig. 3.8 Uniaxial stress-strain curves and damage indices produced by the two models..... 65
Fig. 3.9 Relationship between SDF in KCC and D in CSC model..... 67

Fig. 3.10 Outside and inside view of the slab from the pressure tube (Thiagarajan 2013) 68
Fig. 3.11 Details of tested RC slab (after Thiagarajan 2013) 69
Fig. 3.12 Layout of the ¼ FE model for the slab and the end support beam 70
Fig. 3.13 Stress-strain curve of rebar 70
Fig. 3.14 Time history of applied pressure 70
Fig. 3.15 Time history of central deflection and reaction 71
Fig. 3.16 Damage distribution in the slab surface and over cross-section (KCC: 1.97~2.00; CSC: 0.3~1.0) 72
Fig. 3.17 Experimental crack distribution after blast (courtesy of Thiagarajan 2013) 73
Fig. 3.18 Development of axial stress distribution along longitudinal rebar 74
Fig. 3.19 Development and distribution of damage in concrete elements connected with rebar 75
Fig. 3.20 Principal (tensile) strain in concrete elements connected to rebar 77
Fig. 3.21 Experimental RC beam and its FE model 78
Fig. 3.22 Comparison of central deflection vs. mid-span moment curves 80
Fig. 3.23 Damage pattern of RC beam under quasi-static load (KCC: 1.97~2.00; CSC: 0.3~1.0) 80
Fig. 3.24 Axial stress distribution along the length of rebar 82
Fig. 3.25 Principle strain in concrete elements connected to rebar 83
Fig. 3.26 Different stress paths and correspondent stress invariant ratios 85
Fig. 3.27 Behaviour of CSC material model under confined tension 86
Fig. 4.1 Different modelling approaches for rebar in FE models 93
Fig. 4.2 Test specimen and pull-out setup (after Eligehausen et al. 1982a) 95
Fig. 4.3 Numerical model setup of the pull-out specimen 97
Fig. 4.4 Simulation of the bond-free length and inserted plastic sheet by contact surface 97
Fig. 4.5 Cross-sectional photo of specimens after failure (Eligehausen et al. 1982a) 98

Fig. 4.6 Damage contour of pull-out specimen at failure modelled by KCC model (SDF: 1.97~2.00) 98
Fig. 4.7 Comparison of global bond-slip relation 99
Fig. 4.8 Dimensions of doubly reinforced RC beam specimen 101
Fig. 4.9 Experimental and numerical crack patterns of Miyamoto's beam test 101
Fig. 4.10 Load-displacement curves of Miyamoto's beam test 102
Fig. 4.11 Distribution of rebar force and cracking development at different deflection levels (beam-rebar models) 103
Fig. 4.12 Modification to η-λ curve 106
Fig. 4.13 Modified η-λ curve 108
Fig. 4.14 Influence of η-λ law on stress-strain curves (element size = 25.4mm) 109
Fig. 4.15 Influence of b_1 value on stress-strain curves (element size = 25.4mm) 111
Fig. 4.16 Stress-strain curves under confined compression after modification (element size = 25.4mm) 111
Fig. 4.17 Bond-slip relations using modified KCC model 113
Fig. 4.18 Central deflection – mid-span moment curves of RC beam under quasi-static load using modified KCC model 114
Fig. 4.19 Re-calculated RC slab response to blast load using modified KCC model 115
Fig. 4.20 Dimensions and cross-section of the RC beam specimens 116
Fig. 4.21 Schematic view of FE model for RC beam 117
Fig. 4.22 Comparison between numerical response and test data for beam S0 118
Fig. 4.23 Comparison between numerical response and test data for beam D12 119
Fig. 4.24 Comparison between numerical response and test data for beam D18 120
Fig. 5.1 Transfer mechanism of bond interaction between concrete and rebar 125
Fig. 5.2 Analytical monotonic bond stress-slip relationship 126

Fig. 5.3 Three scales of bond simulation (after Cox and Herrmann 1998) 127
Fig. 5.4 Schematic representation of equivalent transitional layer 129
Fig. 5.5 Equivalent transitional layer between concrete and rebar 130
Fig. 5.6 Determination of confining pressure in the transitional layer (pre-cracking stage) 132
Fig. 5.7 Determination of confining pressure in the transitional layer (post-cracking stage) 134
Fig. 5.8 Failure surfaces representing gross bond-slip behaviour of the transitional layer 137
Fig. 5.9 Failure surfaces extracted from Malvar's pull-out tests (after Cox and Herrmann 1998) 138
Fig. 5.10 Modified failure surfaces for equivalent transitional layer 139
Fig. 5.11 Equivalence of "slip" deformation and modifications for "bond-slip" curves 141
Fig. 5.12 Modified η - λ curves to varied mesh sizes (s_m=1mm, s_u=5mm) 143
Fig. 5.13 Pull-out test specimen and setup (after Baena et al. 2009) 144
Fig. 5.14 FE model using transitional layer with varied mesh sizes 145
Fig. 5.15 Numerical bond-slip curves for rebar with a diameter of 16 mm 146
Fig. 5.16 Numerical bond-slip curves for rebar with a diameter of 12 mm 146
Fig. 5.17 Numerical implementation of the plastic sheets 147
Fig. 5.18 Modelling bond-slip relationship with transitional layer 148
Fig. 5.19 Modelling effect of transverse pressure on bond-slip relationship with transitional layer 149
Fig. 6.1 Considered RC beam specimen 154
Fig. 6.2 Schematic view of beam element model for RC beam 155
Fig. 6.3 Simplified triangular shaped blast load 157
Fig. 6.4 Time histories of simply-supported RC beam under blast in quasi-static regime (I_0=4 kPa·s; p_m=0.25 MPa; t_d=32 ms) 159
Fig. 6.5 Deflection and force distribution of simply-supported beam under blast in quasi-static regime (I_0=4 kPa·s; p_m=0.25 MPa; t_d=32 ms) 160

Fig. 6.6 Global response of simply-supported beam under blast in impulsive regime (I_0=4 kPa·s; p_m=8 MPa; t_d=1 ms) 161
Fig. 6.7 Deflection and force distribution of simply-supported beam under blast in impulsive regime (I_0=4 kPa·s; p_m=8 MPa; t_d=1 ms) 162
Fig. 6.8 Global response of simply-supported beam under blast in dynamic regime (I_0=4 kPa·s; p_m=1 MPa; t_d=8 ms) 164
Fig. 6.9 Deflection and force distribution of simply-supported beam under blast in dynamic regime (I_0=4 kPa·s; p_m=1 MPa; t_d=8 ms) 165
Fig. 6.10 Time histories of midspan deflection and shear force under different load durations (I_0=4 kPa·s) 167
Fig. 6.11 Maximum shear force of simply-supported beams under different load durations (I_0=4 kPa·s) 167
Fig. 6.12 Normalised SFD and BMD of simply-supported beam under different load durations (I_0=4kPa·s) 168
Fig. 6.13 Normalised SFD and BMD of simply-supported beam under different load durations (I_0=4 kPa·s) (continued) 169
Fig. 6.14 Global response of fixed-supported beam under blast in quasi-static regime (I_0=4 kPa·s; t_d=16 ms) 171
Fig. 6.15 Deflection and force distribution of fixed-supported beam under blast in quasi-static regime (i=4 kPa·s; td=16 ms) 172
Fig. 6.16 Global response of fixed-supported beam under blast in impulsive regime (I_0=4 kPa·s; p_m=8 MPa; t_d=1 ms) 173
Fig. 6.17 Deformation and force distribution of fixed-supported beam under blast in impulsive regime (I_0=4 kPa·s; p_m=8 MPa; t_d=1 ms) 174
Fig. 6.18 Global response of fixed-supported beam under blast in dynamic regime (I_0=4 kPa·s; p_m=2 MPa; t_d=4 ms) 175
Fig. 6.19 Deformation and force distribution of fixed-supported beam under blast in dynamic regime (I_0=4kPa·s; p_m=2MPa; t_d=4ms) 175
Fig. 6.20 Deformation and force distribution of fixed-supported beam under blast in dynamic regime (I_0=4kPa·s; p_m=2MPa; t_d=4ms) (continued) 176

Fig. 6.21 Time histories of deflection and shear force of fixed-supported beam under different load durations (I_0=4 kPa·s) 177
Fig. 6.22 Shear force diagram of simply-supported beam under blast with different loading rates (I_0=4kPa·s) 178
Fig. 6.23 Shear force diagram of simply-supported beam under blast with different loading rates (I_0=4kPa·s) (continued) 179
Fig. 7.1 Layout of analysed RC beam for blast load 185
Fig. 7.2 Layout of analysed RC beam under uniformly distributed load..... 187
Fig. 7.3 Quasi-static performance of analysed simply-supported RC beam under uniformly distributed load 188
Fig. 7.4 Layout of analysed RC beam under four-point load (symmetric) 189
Fig. 7.5 Failure pattern of simply-supported RC beam under varied a/d ratios 189
Fig. 7.6 Shear resistance of simply-supported RC beam under varied a/d ratios 190
Fig. 7.7 Quasi-static performance of analysed fixed-supported RC beam under uniformly distributed load 191
Fig. 7.8 Failure pattern of fixed-supported RC beam under varied a/d ratios . 192
Fig. 7.9 Shear resistance of fixed-supported RC beam under varied a/d ratios 193
Fig. 7.10 Schematic view of practical method to determine the width of effective shear span 194
Fig. 7.11 Failure pattern of simply-supported RC beam under load duration t_d=40ms 196
Fig. 7.12 Time history of deflection and shear force of simply-supported RC beam under load duration t_d=40 ms 197
Fig. 7.13 Distribution of shear force and bending moment of simply-supported RC beam under load duration t_d=40 ms..... 198
Fig. 7.14 Failure pattern of simply-supported RC beam under load duration t_d=4.0 ms 199
Fig. 7.15 Time histories of deflection and shear force of simply-supported RC beam under load duration t_d=4.0 ms 200

Fig. 7.16 Distribution of shear force and bending moment of simply-supported RC beam under load duration t_d=4.0 ms 201
Fig. 7.17 Time histories of deflection and shear force of simply-supported RC beam under load duration t_d=1.0 ms 202
Fig. 7.18 Damage pattern of simply-supported RC beam under load duration t_d=1.0 ms 203
Fig. 7.19 Distribution of shear force and bending moment of simply-supported RC beam under load duration t_d=1.0 ms 203
Fig. 7.20 Time histories of response of fixed-supported RC beam under load duration t_d=20.0 ms 205
Fig. 7.21 Damage pattern of fixed-supported RC beam under load duration t_d=20.0 ms 206
Fig. 7.22 Distribution of shear force and bending moment of fixed-supported RC beam under load duration t_d=20.0ms 206
Fig. 7.23 Failure pattern of simply-supported RC beam under load duration t_d=4.0 ms 207
Fig. 7.24 Time histories of response of fixed-supported RC beam under load duration t_d=4.0 ms 208
Fig. 7.25 Response of fixed-supported RC beam under load duration t_d=4.0 ms 209
Fig. 7.26 Time histories of response of fixed-supported RC beam under load duration t_d=0.5 ms 210
Fig. 7.27 Failure pattern of fixed-supported RC beam under load duration t_d=0.5 ms 211
Fig. 7.28 Response of fixed-supported RC beam under load duration t_d=4.0 ms 211
Fig. 7.29 Effective shear span of RC beams under varied load durations 213
Fig. 7.30 Dynamic shear resistance (maximum shear) of RC beams under varied load durations 214
Fig. 7.31 Dynamic enhancement factor under varied load durations 215

Fig. 7.32 DIF curves for yielding and ultimate strength of reinforcement steel 218
Fig. 7.33 Tensile and compressive DIF curves for concrete 219
Fig. 7.34 Measured stress-strain data reflecting the effect of strain rate (Crawford et al. 2012)..... 220
Fig. 7.35 Dynamic stress-strain relation for concrete in KCC model (element size = 7mm; “NO (m)” mean no DIF but with modified fracture energy)..... 221
Fig. 7.36 Response of simply-supported RC beam under load duration t_d=1.0 ms 223
Fig. 7.37 Final damage patterns of simply-supported RC beam under load duration t_d=1.0 ms..... 223
Fig. 7.38 Strain rate contour of simply-supported beam under load duration t_d=1.0 ms 224
Fig. 7.39 Average strain rate in the shear failure zone load duration t_d=1.0 ms 225
Fig. 7.40 Response of simply-supported RC beam under load duration t_d=4.0 ms 226
Fig. 7.41 Final damage patterns of simply-supported RC beam under load duration t_d=4.0 ms..... 226
Fig. 7.42 Strain rate contour of simply-supported beam under load duration t_d=4.0 ms 227
Fig. 7.43 Average strain rate in the shear failure zone load duration t_d=4.0 ms 227
Fig. 7.44 Response of simply-supported RC beam under load duration t_d=40 ms 228
Fig. 7.45 Final damage patterns of simply-supported RC beam under load duration t_d=40 ms..... 228
Fig. 7.46 Strain rate contour of simply-supported beam under load duration t_d=40 ms 229
Fig. 7.47 Average strain rate in the shear failure zone load duration t_d=40 ms 229

Fig. 7.48 Response of simply-supported RC beam under load duration t_d=0.5 ms 231
Fig. 7.49 Final damage patterns of simply-supported RC beam under load duration t_d=0.5 ms 231
Fig. 7.50 Strain rate contour of simply-supported beam under load duration t_d=0.5 ms 232
Fig. 7.51 Average strain rate in the shear failure zone load duration t_d=0.5 ms 233
Fig. 7.52 Response of simply-supported RC beam under load duration t_d=4.0 ms 234
Fig. 7.53 Final damage patterns of simply-supported RC beam under load duration t_d=4.0 ms 234
Fig. 7.54 Strain rate contour of simply-supported beam under load duration t_d=4.0 ms 235
Fig. 7.55 Average strain rate in the shear failure zone under load duration t_d=4.0 ms 236
Fig. 7.56 Response of simply-supported RC beam under load duration t_d=16.0 ms 237
Fig. 7.57 Final damage patterns of simply-supported RC beam under load duration t_d=20 ms 238
Fig. 7.58 Strain rate contour of simply-supported beam under load duration t_d=16.0 ms 238
Fig. 7.59 Average strain rate in the shear failure zone; load duration t_d=16.0 ms 239
Fig. 7.60 Dynamic shear resistance of RC beams with and without DIF effect 240
Fig. 8.1 Equivalent SDOF model for flexural mode 246
Fig. 8.2 Resistance function for flexural mode 248
Fig. 8.3 Coefficient for moment of inertia of cracked sections (UFC 3-340-02, 2008) 250
Fig. 8.4 Assumed deflected shape for direct shear mode 251

Fig. 8.5 Equivalent SDOF system for direct shear mode 252
Fig. 8.6 The shear stress-slip model proposed by Krauthammer et al. (1986) . 254
Fig. 8.7 Assumed deflected shape for diagonal shear mode 257
Fig. 8.8 Equivalent SDOF system for diagonal shear mode 258
Fig. 8.9 Shear force diagrams and shear deformation under diagonal shear mode 261
Fig. 8.10 Shear stiffness calculation using VATM (After Kim and Mander 2007) 262
Fig. 8.11 Dimensions and cross-section of the RC beam specimen D18..... 264
Fig. 8.12 Prediction for flexural and shear stiffness of cracked cross-section .. 266
Fig. 8.13 Validation of SDOF model for simply-supported RC beam dominated by flexural mode (I_0=4 kPa·s; t_d=40 ms) 268
Fig. 8.14 Validation of SDOF model for simply-supported RC beam dominated by flexural mode (I_0=12 kPa·s; t_d=40 ms) 269
Fig. 8.15 Validation of SDOF model for fixed-supported RC beam dominated by flexural mode (I_0=10 kPa·s; t_d=20 ms) 270
Fig. 8.16 Validation of SDOF model for simply-supported RC beam dominated by direct shear mode (I_0=7 kPa·s; t_d=1.0 ms) 271
Fig. 8.17 Validation of SDOF model for fixed-supported RC beam dominated by direct shear mode (I_0=5 kPa·s; t_d=0.5 ms) 271
Fig. 8.18 Validation of SDOF model for simply-supported RC beam dominated by diagonal shear mode (I_0=11 kPa·s; t_d=4.0 ms) 273
Fig. 8.19 Validation of SDOF model for fixed-supported RC beam dominated by diagonal shear mode (I_0=6 kPa·s; t_d=4.0 ms) 273
Fig. 8.20 Determination of factor α_1 for dynamic shear resistance 276
Fig. 8.21 Resultant forces in the investigated compressive region (after Choi and Park 2007)..... 278
Fig. 8.22 Static shear resistance V_{Rs2} for diagonal shear mode under varied a/d ratios 280

Fig. 8.23 Dynamic increase factor α_2 for structural dynamic effect under varied load durations 281
Fig. 8.24 Comparison of dynamic shear resistance prediction..... 282

List of tables

Table 2.1 Key features of concrete models in hydrocode 26
Table 4.1 Properties of concrete in the RC beam test..... 117
Table 6.1 Material properties for RC beam 154
Table 8.1 Natural period of flexure and shear modes 267

List of abbreviations

ACI	American Concrete Institute
BDC	Brittle damage concrete model
BMD	Bending moment diagram
CDP	Concrete damage plasticity model
CEB	Comité Européen du Béton - European Committee for Concrete
CSC	Continous surface cap model
DIF	Dynamic increase factor
EOS	Equation of state
FE	Finite element
GC	Geologic cap model
JHC	Johnson and Holmquist concrete model
KCC	Karagozian and Case concrete model
PT	Psedo-tensor model
RC	Reinforced concrete
SDF	Scaled damage factor
SDOF	Single-degree-of-freedom
SFD	Shear force diagram
TNT	Trinitrotoluene
UFC	Unified Facilities Criteria
UMKC	University of Missouri Kansas City
WC	Winfrith concrete model

to my parents

Chapter 1: Introduction

1.1 Background

When a reinforced concrete (RC) structure is subjected to impulsive load, particularly blast, the immediately affected RC components will undergo several stages of the dynamic responses, including firstly a shock and stress wave phase within the material, followed by structural level response characterised by shear and bending deformation due to the energy imparted by the load impulse. The structural response can be further divided into three consecutive stages according to the dominant force effects, namely intense concentrated shear near support (direct shear), intense shear over a relatively small shear span (diagonal shear), and global bending (flexure) stage.

It is generally understood that, depending on the intensity of the shear forces that may develop in the first two consecutive stages, direct shear and diagonal shear failure may occur, leading to partial or total failure of the structural member at these stages. If the member can survive from the above shear-dominated stages, global flexural response can then develop which will largely depend upon the impulse of the blast load.

So far in practice, the majority of the blast response analysis methods and the assessment criteria have been based on a global bending mode of responses. The transient high shear phenomena have not been dealt with in a systematic way.

On the one hand, there is a lack of generally accepted method for the analysis of the high transient shear forces; on the other hand, there is very little understanding about the dynamic shear resistance mechanisms and how they should be appropriately analysed.

As the behaviour of concrete structures subjected to blast type of high impulsive load involves such complex responses at both the constituent material level as well as the structural level, to fully describe the processes requires sophisticated numerical model. In fact there has been extensive research effort in recent years to employ numerical model techniques in attempt to simulate the high dynamic responses of concrete structures under blast and impact loads. However, a comprehensive computational model with the capability to represent different regimes of responses throughout the entire process, covering rigorously the stress wave effects and the different stages of the structural responses, so as to yield realistic response predictions, has not been thoroughly investigated.

It is generally understood that the dominate mechanisms in the global deformation phase can be significantly different from those in the high-intensity transient local response phase; the fact that the pressure level becomes low in this phase of response requires the material model to be able to accommodate tension, shear, as well as the relatively simple compression behaviour under low pressure but still complex multi-axial stress condition. Thus a numerical model which has shown sound performance in high-intensity stress applications may not necessarily perform as well in a reinforced concrete environment under a global deformation scenario. The demand on the material model being able to exhibit appropriate behaviour in tension and shear becomes particularly important in reinforced concrete structures to ensure that transfer of stresses between concrete and reinforcing bars in the structural response phases can take place in a realistic “reinforced concrete” composite manner.

This thesis aims to fill in this gap and develop an effective modelling framework for reinforced concrete (RC) structures under impulsive loading. One of the key issues to be addressed is to ensure the concrete material model perform robustly not only in the intensive stress wave phase of the response but also in the subsequent structural response stages, and to this end a comprehensive investigation into the concrete model behaviour under different working conditions has to be carried out. On the basis of establishment of a robust computational model for RC member for high dynamic analysis, investigation is extended into the dynamic shear phenomena including the transient shear response, the development of shear span under different rates of loading, and ultimately the dynamic shear resistance.

1.2 Objective and scope

The main objective of this research work is to develop a holistic computational model to be capable of analysing the response of RC members throughout the entire process of impulsive dynamic responses. The model is then applied to investigate the key characteristics of the dynamic response of reinforced concrete members under shock and blast loading. Specific objectives and the scope of the main tasks are listed as follows:

- Through a numerical simulation of an experimental RC slab under blast loading, issues and demands on the reinforced concrete models that would be capable of modelling both the stress wave behaviour as well as the structural behaviour are scrutinised.
- Detailed investigations into the concrete material model in terms of its ability in preserving a realistic representation of the tension/shear behaviour in a reinforced concrete environment follow. Modifications to the widely used Karagozian & Cases concrete (KCC) model are proposed

to rectify issues relating to premature failure of the interaction to reinforcing bars.

- Considering practical applications where steel reinforcement often needs to be modelled as one-dimensional bar (or beam) element, an interface layer model is proposed to represent the equivalent layer of concrete surrounding the fictitious rebar elements for use in practical finite element modelling of RC structures. The proposed model is validated against pull-out experiments available from the literature.
- A representative beam member is modelled to demonstrate the transient high shear phenomena under different rates of loading. The transient high shear force developed in the early response (prior to the global bending) in terms of the amplitude and distribution is scrutinised. The increase of the dynamic shear resistance is also observed.
- An extensive modelling investigation is then conducted on the dynamic shear resistance of RC beam/slab under impulsive loading. The contributors to the increase of the dynamic shear resistance are thoroughly examined. In particular, the change of shear span with the loading rate, which alters the shear resistance mechanism and generally results in increase of shear capacity, is discussed. The contribution of material rate effect, as well as other structural effect, in the dynamic shear capacity increase is evaluated.
- By characterising the three deformation modes, a simplified analytical approach is proposed to predict the high shear force demand of RC structures under impulsive loading using the SDOF approach. The dynamic shear resistance in the simplified analysis is established through the relation between the developed effective shear span and the structural and material rate effect in relation to the loading rate.

1.3 Organisation of the thesis

After a general introduction of the thesis in Chapter 1, Chapter 2 presents a review of the literature with an aim to identify key issues in the establishment of a holistic FE modelling framework for analysing reinforced concrete structures under impulsive load. This includes a comprehensive discussion on the concrete material models available in hydrocodes, and a review on some recent numerical modelling developments in this field. The review of more specific techniques concerning each topical area is incorporated in the respective individual chapter.

Chapter 3 uses a benchmark RC slab as a testbed to firstly examine the validity of commonly applied finite element setup and typical material models for the analysis of the RC structural response. This is followed by a detailed scrutiny of the demands on the concrete material model in terms of preserving a realistic representation of the tension/shear behaviour. The abnormal behaviour of the material model in this respect is investigated to pave a way for the development of possible remedies.

In Chapter 4, a modification scheme is proposed in order to rectify the behaviour of the KCC model towards the retention of a minimum level of residual tensile strength under large deformation. The scheme encompasses a modification to the damage accumulation law (the η -λ curve) and an adjustment to the softening control parameter in the model. The modification is demonstrated to improve the KCC model behaviour in the reinforced concrete response regime remarkably.

Chapter 5 presents the development of an equivalent transitional layer model to deal with the numerically-induced uncertainties in the part of concrete surrounding reinforcing bars in a numerical model, especially when a fictitious line-element model is employed to represent the reinforcing bars. The equivalent stress and strain states in the transitional zone are derived. Descriptions of the failure surfaces and softening rules are introduced. Validation of the proposed

transitional layer model is carried out against results from RC pull-out and beam experiments available from the literature.

In Chapter 6, a simplified beam model is utilised to look into and demonstrate the key phenomena associated with the development of high shear forces, especially when the blast pulse duration gets very short. The process of the beam response moving through the high shear stages to global bending is examined and the dominant deformation modes are characterised. The increasing demand on the shear resistance as loading rate increases is examined and discussed.

In Chapter 7, a comprehensive numerical investigation into the transient high shear phenomena is conducted. The detailed response modes and failure mechanisms, in connection with the timescales, are examined. The development of the transient high shear response is further characterised in connection with the load pulse duration. The increase of the dynamic shear resistance is analysed firstly from the perspective of shortened shear span. The influence of the strain rate enhancement of the material strength on the dynamic shear capacity is also evaluated.

Chapter 8 characterises the three dominant deformation modes, and presents a simplified SDOF-based approach to predict the high shear demand. Empirical formula to predict the dynamic direct and diagonal shear resistance is proposed. Parameters considering the structural and material rate effect are incorporated.

Chapter 9 summarizes the main conclusions and recommendations of further research.

Chapter 2: Literature review

2.1 Introduction

Understanding and subsequently modelling the mechanical/material behaviour of concrete under different loading states is an essential yet challenging task for civil engineers. Unfortunately, attention to constitutive modelling, especially for highly damaged material states, is too often left underappreciated and material models are commonly used outside their domain of applicability. Moreover, FE analysts are often faced with selecting from an array of different concrete constitutive models but may only have limited experience and background upon which to select the most appropriate model and deploy it reliably.

Recent years have witnessed increasing use of high fidelity FE simulation techniques, and developments in this area have made it possible to investigate the structural failure mechanisms localised in a smaller scale of observation. However at this scale of observation complexities often arise due to using refined mesh size, high nonlinearity from significant damage localisation, and involvement of crack propagation. Such complicities present challenges to the applicability of traditional smeared crack- based constitutive models.

On the other hand, when RC structures are subjected to a high impulsive load, the mechanisms in global deformation phase can be significantly different from those in the high-intensity transient local response phase. This would demand the material models to be able to exhibit appropriate behaviour in both low and high pressure regimes.

The intension of this chapter is not to present a systematic review of numerical study on the RC response under impulsive loading. Instead, it is aimed to provide an overarching review on a few relevant major topical areas including the constitutive models within the context of predicting concrete response covering both low and high pressure regimes, and recent FE practices in simulating the high dynamic impulsive response of RC structures. The literature review of more specific topics will be incorporated in the individual chapters.

2.1.1 Outline of the literature review

The reviews starts with a brief summary on the basic failure characterisation of concrete under the load scenarios of interest (e.g. covering both low and high pressure regimes), and the corresponding descriptions in the constitutive models. This is followed by a discussion on the choice of concrete models and a proper description for damage.

The chapter then continues with a detailed review on representative concrete constitutive models and discussion on their ability to reproduce basic concrete response. The important differences between the models in their behaviours under both low and high pressure scenarios are illustrated. Recent developments in the hydrocode FE application are reviewed, and in particular the performance of representative concrete models including Karagozian & Cases concrete (KCC) model (Malvar and Crawford 1997) and Continuous Surface Cap (CSC) models (Murray et al. 2007), under different loading conditions is assessed. A systematic examination of the performance of these material models extending into the global deformation phase is then conducted.

The review will highlight that both KCC and CSC models tend to work satisfactorily in scenarios where damage is dominated by localised material failure, such as in close-in blast and higher rate impact. However, when the

(global) structural response becomes more important, both models tend to exhibit deficiencies but in somewhat opposite directions; while KCC model tends to result in steep loss of strength in the tension/shear and rebar anchorage areas, and hence a premature global failure, CSC model tends to over-estimate the tension/shear capacities leading to over-prediction of the residual strength capacity and underestimation of the plastic deformation.

By comparing the pros and cons of these concrete models, the direction of improvements in order to make them behave more robust in catering the need in both quasi-static and impulsive load regimes is clarified.

2.2 Failure mechanism of concrete and its constitutive description

2.2.1 Failure mechanisms of concrete under varied pressure regime

The applicability of a concrete model in particular load scenarios lies in the capability of the model to capture the essential concrete behaviours in such loading conditions. This is an essential consideration on model assessment throughout this chapter. To this end, it is necessary to review the main aspects of the behaviour of concrete in the first place and this will provide a guide in examining the choices in the theoretical formulation.

Typical failure modes of concrete may be distinguished from the following aspects: i) the collapse of the micro-porous structure of the cement matrix, also known as the dilation and compaction effect; and ii) the developing, linking and propagation of micro cracks, most often located in the cement matrix. For general classification in constitutive modelling for concrete, the first mechanism is often treated as plasticity development, while the second is normally considered as damage process and described by damage variables.

Both failure types are very much related with the confining environment. Under low confining pressures, concrete behaves in a brittle manner; it cracks in tension and crushes in compression, as a result of micro cracking development. The brittle behaviour of concrete disappears when the confining pressure is sufficiently large to prevent crack propagation. In these circumstances failure is driven by the consolidation and collapse of the concrete micro-porous microstructure, leading to a macroscopic response that resembles that of a ductile material with work hardening. To sum up, as presented by Mazars and

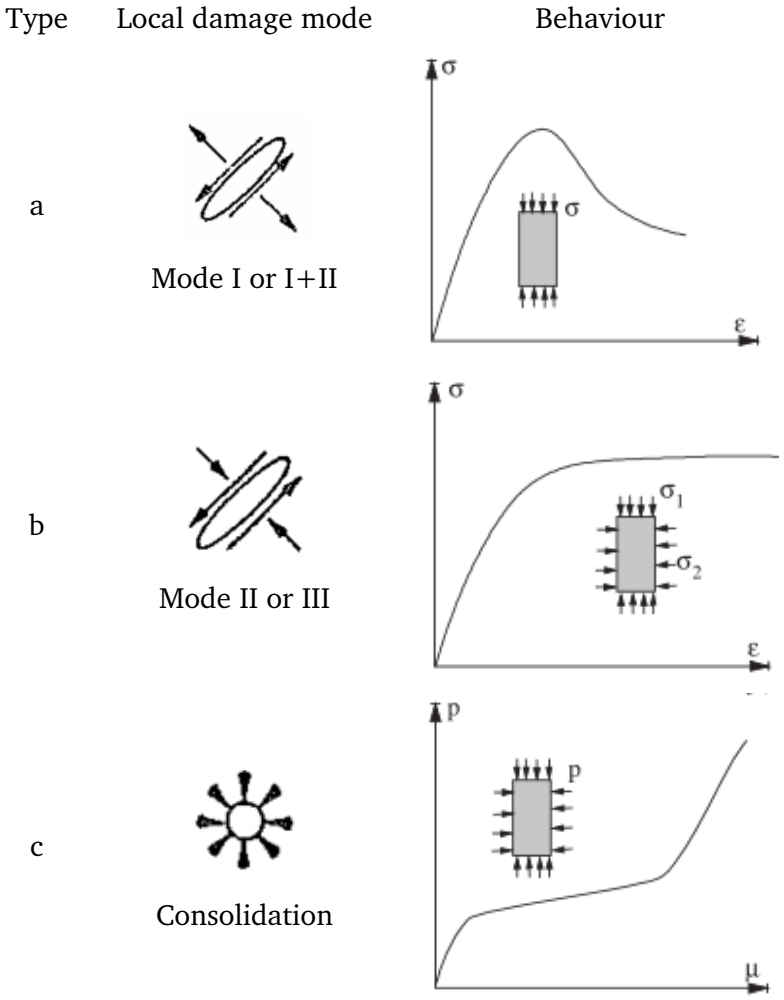

Fig. 2.1 Typical behaviours and local damage modes of concrete, after Mazars and Pijaudier-Cabot (1989)

Pijaudier-Cabot (1989), for concrete, three different failure situations arise depending upon the type of loading, see also Fig. 2.1:

a) Brittle failure dominated by cracking in mode I or I+II related to local extension, under tension and/or compression with low lateral pressure;
b) Ductile failure dominated by cracking in mode II or III without any local extensions, under compression with moderate lateral pressure (compressive crushing, dilation effect);
c) Failure related to the application of a strong hydrostatic pressure which leads to collapse of micro voids (compaction).

The first and second failure modes generally apply for low pressure scenarios (e.g. quasi-static or seismic load) and the third applies for high pressure scenarios (e.g. blast and impact). The failure process is characterized by irreversible deformations and degradation of the material stiffness. Once implemented into numerical material model, these mechanisms are often mathematically described by:

a) Damage-induced isotropic or anisotropic strength and stiffness degradation and growth of inelastic strain;
b) Plasticity-induced hardening and softening effect, plasticity flow rule and growth of plastic strain;
c) Pressure sensitive yield surface and volumetric moduli, with the latter often described as equation of state in hydrocodes.

2.2.2 Choice of numerical methodology on modelling plasticity and damage

Plasticity theories have been used successfully in modelling the behaviour of metals where the dominant mode of internal rearrangement is the slip process. Although the mathematical theory of plasticity is thoroughly established, its potential usefulness for representing a wide variety of material behaviour has

not been yet fully explored. There are many researchers who have used plasticity alone to characterise the concrete behaviour (e.g. Bažant 1978; Schreyer 1983; Voyiadjis and Abu-Lebdeh 1994; Grassl et al., 2002, to name a few). The main characteristic of these models is a plasticity yield surface that includes pressure sensitivity, path sensitivity, non-associative flow rule, and work or strain hardening; however they are unable to address the degradation of the material stiffness due to micro-cracking.

On the other hand, many others have used the continuum damage theory alone to model the material nonlinear behaviour. In such models the mechanical effects of the progressive micro-cracking and strain softening are represented by a set of internal state variables which act on the elastic behaviour (i.e. decrease of the stiffness) at the macroscopic level. Examples of these models include Ortiz and Popov, 1982; Krajcinovic, 1983, 1985; Simo and Ju, 1987a,b; Mazars and Pijaudier-Cabot, 1989; Lubarda et al., 1994. However, there are several facets of concrete behaviour, such as irreversible deformations and inelastic volumetric expansion in compression particularly at high-confining pressures, which cannot be represented by this method. Just as plasticity, the continuum damage model by itself is insufficient to describe the full behaviour of concrete.

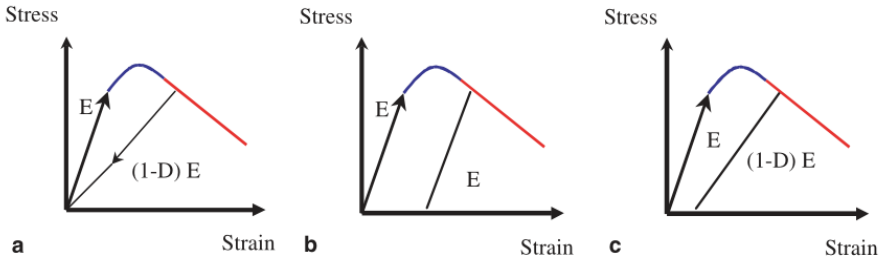

Fig. 2.2 Unloading response of a) elastic damage, b) elasto-plastic and c) elasto-plastic damage models (adapted from Jason et al., 2006)

As shown in Fig. 2.2, even a damage or plasticity model is capable of capturing the same material response under monotonic loading, neither approach alone can capture the evolution of unloading stiffness accurately. At a given point on

the stress-strain relation, neglecting plastic strain in a pure damage approach would artificially increase the damage (secant unloading slope). Neglecting damage effects in a pure plastic model, on the other hand, would ignore the stiffness reduction, and more importantly, result in a residual state that cannot be described objectively as a function of the applied strains (Chatzigeorgiou et al., 2005). Because even for the same strain state, different levels of damage are to be expected according to different loading process.

Since both micro-cracking and irreversible deformations are contributing to the nonlinear response of concrete, a constitutive model should address equally the two physically distinct modes of irreversible changes. For this reason, coupled damage-plasticity models are a necessity in numerical problems dealing with concrete structures (Jason et al., 2006).

2.3 Review of typical concrete material models used in hydrocodes

Many material models for concrete-like materials have been developed and made available in commercial hydrocodes. These models generally share in common some basic features of brittle materials such as pressure hardening, strain hardening and strain rate dependency. However, for simplicity some models adopt highly restrictive assumptions, consequently their applicability is limited to a certain class of problems. In cases where the loading environment of the material is very complex and cannot be pre-defined, more robust material models that are capable of describing the varying concrete material behaviours under different loading conditions are desired.

In this section, typical material models that are developed specifically for concrete under high dynamic loading are reviewed and commented, with a summary and recommendation comments given in the end of this section. Many

of these material models are available in the hydrocode LS-DYNA (LSTC 2012), ABAQUS EXPLICT (Dassault Systèmes 2007) and AUTODYN (ANSYS 2009). Among these models, the Karagozian and Case concrete (KCC) model and the Continuous Surface Cap (CSC) model, which are the major concrete material models employed and discussed in this thesis, are introduced and reviewed in a detailed way in Section 3.3.

2.3.1 Concrete damage plasticity (CDP) model

The concrete damaged plasticity model in ABAQUS was originally developed by Lubliner et al. (1989) and later modified by Lee (1996) and Lee and Fenves (1998). The model aims to capture the effects of irreversible damage associated with the failure mechanisms that occur in concrete under fairly low confining pressures, it is primarily intended to predict RC structures under cyclic and/or dynamic (seismic) loading.

The model follows the additive decomposition of elastic and plastic strain tensor, and uses a single scalar variable κ to describe both hardening and softening behaviour. The stress state is implemented as

$$\boldsymbol{\sigma} = \left(1 - d\left(\kappa\right)\right) \cdot \mathbf{E}_0 : \left(\boldsymbol{\varepsilon} - \boldsymbol{\varepsilon}^{\mathrm{p}}\right) \tag{2.1}$$

where d is a scalar plastic-damage index that is a function of internal variable κ. The yield surface is defined in the actual (damaged) stress space as

$$F\left(\boldsymbol{\sigma}, \kappa\right) = \frac{1}{1-\alpha}\left(\alpha I_1 + \sqrt{3J_2} + \beta \hat{\sigma}_{\max}\right) - c\left(\kappa\right) \leq 0 \tag{2.2}$$

where α , β and c are constants defining the shape and size. $\hat{\sigma}_{\max}$ denotes the maximum principle stress. The model uses a non-associative flow rule to

generate the spherical and deviatoric part of the plastic strain and thus the dilatancy is controlled.

The damage index d is considered separately in the tensile and compressive regime and overall damage is defined as a combination of the two:

$$d(\kappa) = 1 - (1 - d_c(\kappa)) \cdot (1 - s \cdot d_t(\kappa)) \tag{2.3}$$

where d_t and d_c are the damage variables under tensile and compressive states respectively, determined by the corresponding value of damage variable κ. The factor s ranges from 0 to 1, and defines the compressive/tensile state.

The variable κ can be determined via the principle plastic strain $\dot{\varepsilon}^p_{\max}$ and $\dot{\varepsilon}^p_{\min}$, as defined in:

$$\dot{\kappa} = \frac{f_c}{g_c} \cdot a_c(\hat{\boldsymbol{\sigma}}, \kappa) \dot{\varepsilon}^p_{\max} + \frac{f_t}{g_t} \cdot a_t(\hat{\boldsymbol{\sigma}}, \kappa) \dot{\varepsilon}^p_{\min} \tag{2.4}$$

where f_t and f_c are the initial concrete strength, g_t and g_c are dissipated energy density which is known to depend on the size of localisation zone (crack band), and are determined in a way such that a prescribed fracture energy G_{ft} or G_{fc} of concrete is achieved. a_t and a_c are parameters that control the shape of the κ function, which in turn controls plasticity and damage simultaneously, as depicted in Fig. 2.3.

The basic framework of this model is capable of dealing with confinement effect, and it has also been calibrated under intermediate pressure regime (Rodríguez et al. 2013). However, the porous compaction effect, which is important for concrete under extreme loading, is not considered.

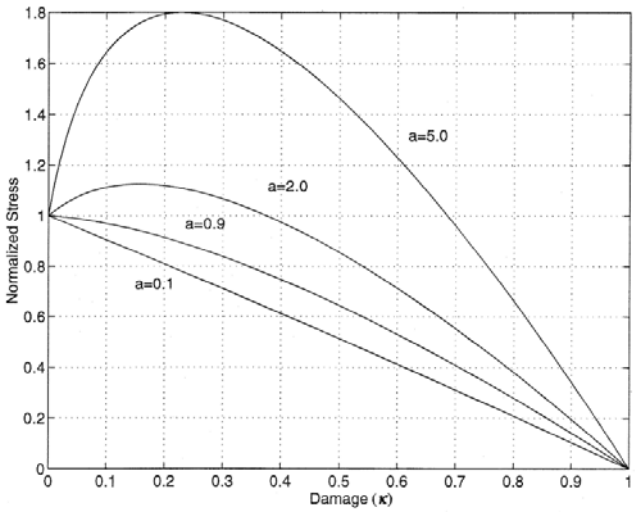

Fig. 2.3 Different shapes of κ curves defining both hardening and softening effect (Lee 1996)

2.3.2 Pseudo-tensor (PT) model

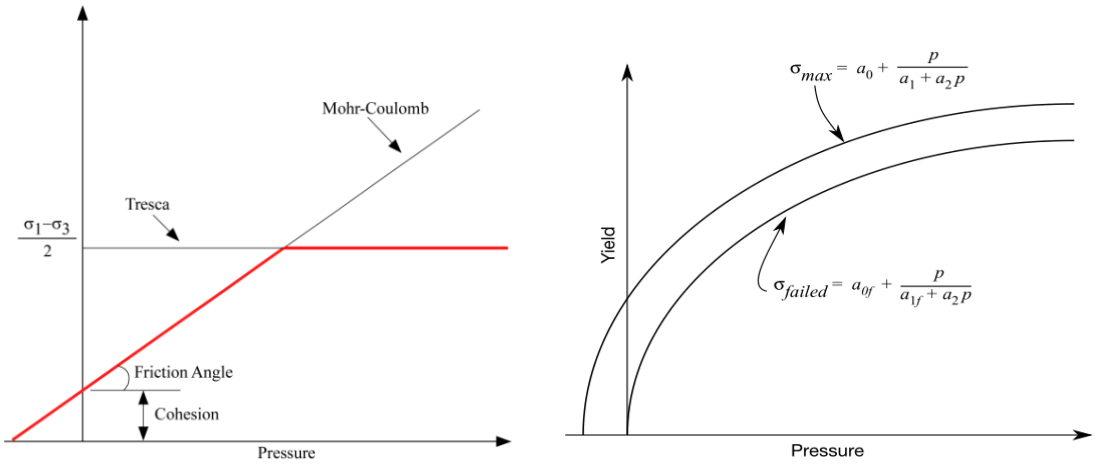

a) Mohr-Coulomb with Tresca limit b) Two surfaces with damage and failure

Fig. 2.4 Two definition of failure surfaces for Pseudo-tensor model (LSTC 2012)

The pseudo-tensor model is a geological model available in LS-DYNA as MAT 16. It offers two major modes: a simple bi-linear pressure-dependent Mohr-Coulomb yield surface with a Tresca limit, as shown in Fig. 2.4a, and two user-defined "yield stress versus pressure" functions with the capability to transit from the

yield surface to the maximum surface, as shown in Fig. 2.4b. The latter mode has a general form for the curves as

$$\sigma = \sigma_y + \eta\left(\sigma_m - \sigma_y\right) \tag{2.5}$$

in which the maximum and yield functions are

$$\begin{aligned} \sigma_y &= a_{0y} + \frac{p}{a_{1y} + a_{2y} p} \\ \sigma_m &= a_{0m} + \frac{p}{a_{1m} + a_{2m} p} \end{aligned} \tag{2.6}$$

where a_{0y}, a_{1y}, a_{2y}, a_{0m}, a_{1m} and a_{2m} are user-defined parameters. The change in stress is a function of plastic strain, and is affected by the hydrostatic pressure when the cracking occurs, which gives rise to the "confinement" effect on concrete behaviour. To account for this phenomenon, a "damage" function was defined and incorporated in the given form via plastic strain:

$$\lambda = \int_0^{\varepsilon^p} \left(1 + \frac{p}{f_t}\right)^{-b_1} d\varepsilon^p \tag{2.7}$$

in which ε^p is the plastic strain, f_t is the tensile strength, and b_1 a damage scaling parameter. The η-λ relation is a user put value as suggested by the LS-DYNA user manual (LSTC 2012).

The equation of state (EOS) is used to describe the volumetric response and compaction behaviour of the material. The model uses a single scalar damage to describe the post-yield behaviour of the material. As such, the model is unable to distinguish the different softening behaviours of concrete under compression and tension. Detailed assessment and introduction of this model can be find in Burton et al. (1982) and Yonten et al. (2005).

2.3.3 Geologic cap (GC) model

Geologic cap model (MAT 25 in LS-DYNA) is a kinematic hardening cap model, initially proposed by Sandler and Rubin (1979) and further implemented by Simo et al. (1988). It adopts a non-softening convex yield surface defined by a shear failure envelope f_1 and a hardening cap f_2, and a tensile cut-off surface f_3, as depicted in Fig. 2.5.

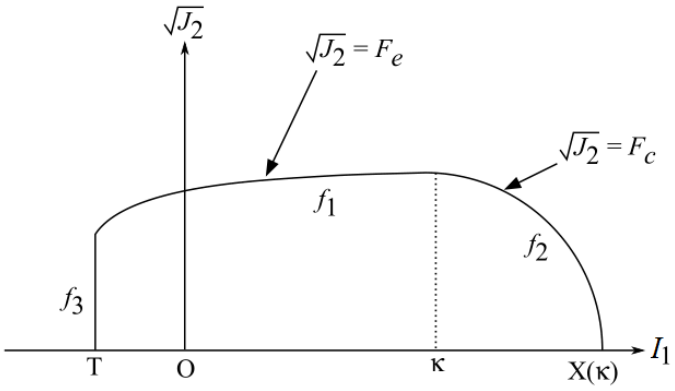

Fig. 2.5 The yield surface of the two-invariant Geologic cap model (LSTC 2012)

The shear failure envelope surface f_1 is defined as:

$$f_1 = \sqrt{J_2} - F_e(I_1) = \sqrt{J_2} - \alpha + \gamma \cdot \exp(-\beta \cdot I_1) - \theta \cdot I_1 \tag{2.8}$$

where α , β , γ and θ are parameters defining the shape of the function, I_1 and J_2 are invariants of stress tensor. The cap surface f_2 is given in an ellipse function:

$$f_2 = \sqrt{J_2} - F_c(I_1, \kappa) = \sqrt{J_2} - \frac{1}{R}\sqrt{[X(\kappa) - L(\kappa)]^2 - [I_1 - L(\kappa)]^2} \tag{2.9}$$

in which R is the radius, κ and $X(\kappa)$ are the intersection points of the cap function f_2 with surface f_1 and I_1 axis, and $L(\kappa)$ is defined by

$$L(\kappa) = \begin{cases} \kappa & \kappa > 0 \\ 0 & \kappa \le 0 \end{cases} \tag{2.10}$$

The hardening parameter κ is further related to the plastic volumetric strain change ε_v^p and defined as

$$\varepsilon_v^p = W\{1-\exp[-D(X(\kappa)-X_0)]\} \tag{2.11}$$

where W denotes the maximum volumetric strain, D and X_0 are parameters define the hardening law. Linking Eq. 2.9 and 2.11, the cap expands ($X(\kappa)$ and κ increase) and contracts to simulation volumetric compaction. The tensile cut-off surface f_3 is defined by

$$f_3 = T - I_1 \tag{2.12}$$

With the above defined surfaces, the model uses associated flow rule proposed by Koiter (1953) to describe the material plastic flow. Such flow rule is capable of controlling the dilatancy produced by shear loading.

A major limitation of the model is that the failure surface definition lacks the involvement of third invariant of stress tensor, without which it leads a circular deviatoric plane that can cause unrealistic behaviour especially in the low pressure regime. Additionally, without any damage definition the softening behaviour, and the confining effect under triaxial stress state, are not satisfactorily predicted.

2.3.4 Brittle damage concrete (BDC) model

The brittle damage model is a smeared-crack based anisotropic model based on the work of Govindjee, Kay, and Simo (1995), and is available as MAT 96 in LS-DYNA. It provides a basic tensile softening behaviour for characterising concrete behaviour. Once cracking occurs, a smeared crack is initiated and damage is handled by treating a 4-rank elastic stiffness tensor as an internal variable for

the material. For the failure surface, it adopts a one-invariant function, as follows:

$$\phi_t = (\mathbf{n} \otimes \mathbf{n}) : \sigma - f_n + f_n \cdot (1 - \varepsilon) \cdot [1 - \exp(-H\alpha)] \tag{2.13}$$

where $\mathbf{n}$ is the normal vector of the smeared crack direction, f_n is the initial principal tensile strength, H is an internally determined parameter that governs the rate of softening and maintains a prescribed fracture energy following a characteristic length method (Oliver 1989). α is an internal variable that is determined by equivalent plastic strain.

As for compressive behaviour, the failure is governed by a simple J_2 flow correction, which is unable to capture the various behaviours of concrete under extreme loadings, namely pressure hardening, compaction and dilation, rate dependency, third stress invariant-dependence. Therefore, its applicability is relatively limited (Magallanes 2008).

2.3.5 Winfrith concrete (WC) model

The Winfrith concrete model is a smeared crack model, implemented in LS-DYNA as MAT 84, and was developed by Broadhouse and Neilson (1987) and Broadhouse (1995). The shear failure surface proposed by Ottosen (1977) is adopted as

$$F(I_1, J_2, \cos 3\theta) = a\frac{J_2}{\left(f_c^{'}\right)^2} + \lambda\frac{\sqrt{J_2}}{f_c^{'}} + b\frac{I_1}{f_c^{'}} - 1 \tag{2.14}$$

where a and b are parameters defining the shape of the function, $f_c^{'}$ is the unconfined compressive strength. λ is the term determined by the third invariant of stress tensor, and θ is the Lode angle, which are defined as

$$\lambda = \begin{cases} k_1 \cos\left[\frac{1}{3}\arccos\left(k_2 \cos 3\theta\right)\right] & \cos 3\theta \geq 0 \\ k_1 \cos\left[\frac{\pi}{3} - \frac{1}{3}\arccos\left(-k_2 \cos 3\theta\right)\right] & \cos 3\theta < 0 \end{cases} \qquad (2.15)$$

$$\cos 3\theta = \frac{3\sqrt{3}}{2}\frac{J_3}{J_2^{1.5}}$$

The model has been mainly tailored for cases where tensile cracking is the primary failure mode. For tensile cracking, the strain softening response is simplified to bi-linear or linear straight lines, and the area under this curve is determined in a way by the fracture energy or crack width specified by input. Such treatment, however, ignores the post-peak softening and assumes a perfect-plastic response for compressive behaviour. A detailed introduction on this model can be found at Schwer (2010, 2011), and it is further verified by Magallanes (2008), Wu et al. (2012) and Algaard et al. (2005).

2.3.6 Johnson and Holmquist concrete (JHC) model

The Johnson and Holmquist concrete model, originally proposed by Holqmuist and Johnson (1993) for penetration/perforation physics and available in LS-DYNA, assumes the material as linear elastic before any failure criterion is reached. The failure surface, as presented in Fig. 2.6, is defined by a two-invariant pressure-dependent function, and the post-yield surface is calculated by reducing the cohesion strength value of the initial failure surface.

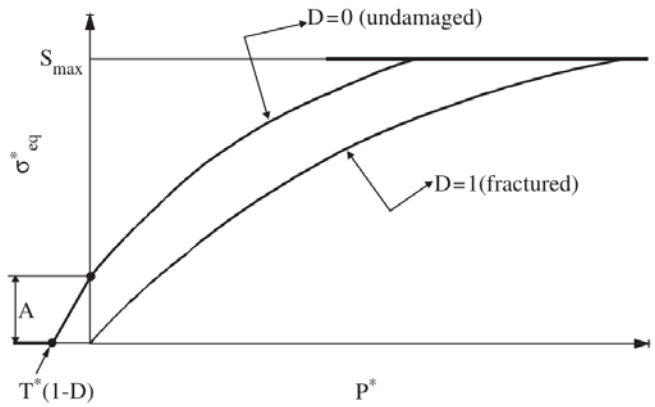

Fig. 2.6 The shear-pressure strength response of the JH model (after Polanco-Loria et al., 2008a)

$$\sqrt{3J_2} = \begin{cases} \left[A \cdot (1-D) + B \cdot \left(\frac{I_1}{f_c^{'}} \right)^N \right] \cdot \left[1 + C \cdot \ln \varepsilon^* \right] \cdot f_c^{'} \le 0 & \sqrt{3J_2} \le S_{\max} \\ S_{\max} & \sqrt{3J_2} > S_{\max} \end{cases} \tag{2.16}$$

In Eq. 2.16, ε^* is a normalised deviatoric strain rate. *A*, *B*, *C* and *N* are parameters calibrated by experiments. *D* is a scalar damage index, which is accumulated from both equivalent deviatoric strain ε_{eq}^p caused by plastic shear deformation and equivalent volumetric strain μ_{eq}^p caused by compaction of concrete void. The evolution of *D* is defined incrementally by

$$\Delta D = \frac{\Delta \varepsilon_{eq}^p + \Delta \mu_{eq}^p}{\varepsilon_p^f + \mu_p^f} \tag{2.17}$$

In Eq. 2.17, $\varepsilon_p^f + \mu_p^f$ is the ultimate plastic strain at fracture. Beyond the fracture point, the material remains a residual stress state, in which $D = 1$ in Eq. 2.16.

Material models like the HJC model, which adopts a relatively simple failure surface and only considers a circular deviatoric plane, will not be able to capture the actual shear variations in the deviatoric plane and the post-peak softening behaviour (Magallanes, 2008). Other important aspects, including stiffness

degradation, third stress invariant dependence, and different tensile and compressive DIFs (dynamic increase factor) are not included. A modified version of JH model can be found in Polanco-Loria et al. (2008).

2.3.7 RHT model

The RHT model (Riedel et al. 1999; Riedel 2009) was developed as an enhancement to the JH concrete model by the introduction of several new features, including strain hardening and the third invariant dependence. Aiming at bringing together shock physics and macroscopic concrete properties, the RHT model provides adequate description in compression from low impact to extremely high dynamic shock waves, which is a key aspect to capture penetration resistance. It is pointed out by Borrvall and Riedel (2011) that deficiencies for a wider applicability of RHT model lie in the details of low pressure strength, and proper prediction of spalling, scabbing and crack propagation. Modifications to some aspects of the problems have been proposed by Tu and Lu, (2009, 2010). Further details on this model can be found in relevant paper on the theoretical frameworks (Borrvall and Riedel, 2011; Riedel, 2009; Riedel et al., 2010, 1999).

The shear and pressure parts of the failure surfaces in RHT model are coupled, in which the pressure is described by the Mie-Gruneisen form with a polynomial Hugoniot curve and a pre-defined pressure-porosity compaction relation. As the shear part, three independent strength surfaces, namely failure surface Y_f, elastic surface Y_e, and residual surface Y_r were incorporated to allow for a more appropriate modelling of the material softening response, as presented in Fig. 2.7a. The failure surface Y_f is given by

$$Y_f\left(p^*,F_r\right)=f_c\cdot\begin{cases}A\left(p^*-\dfrac{F_r}{3}+\left(\dfrac{A}{F_r}\right)^{-1/n}\right)^n & 3p^*\geq F_r\\ \dfrac{F_r f_s^*}{Q_1}+3p^*\left(1-\dfrac{f_s^*}{Q_1}\right) & 0\leq 3p^*<F_r\\ \dfrac{F_r f_s^*}{Q_1}-3p^*\left(\dfrac{1}{Q_2}-\dfrac{f_s^*}{Q_1 f_t^*}\right) & 3p_t^*\leq 3p^*<0\\ 0 & 3p^*<3p_t^*\end{cases} \tag{2.18}$$

where $p^*=p/f_c$ is the normalised hydrostatic pressure, Q_1 and Q_2 are factors determined by the Lode angle θ, $F_r(\dot{\varepsilon})$ represents the rate effect as a function of the strain rate $\dot{\varepsilon}$. $Y_y^*\left(p^*,F_r\right)$ defines the basic shape of the pressure and rate dependant surface function. In these expressions, f_s^* and f_s^* are the tensile and shear strength relative to compressive strength f_c. A and n are constants and p_t^* is the normalised tensile cut-off strength.

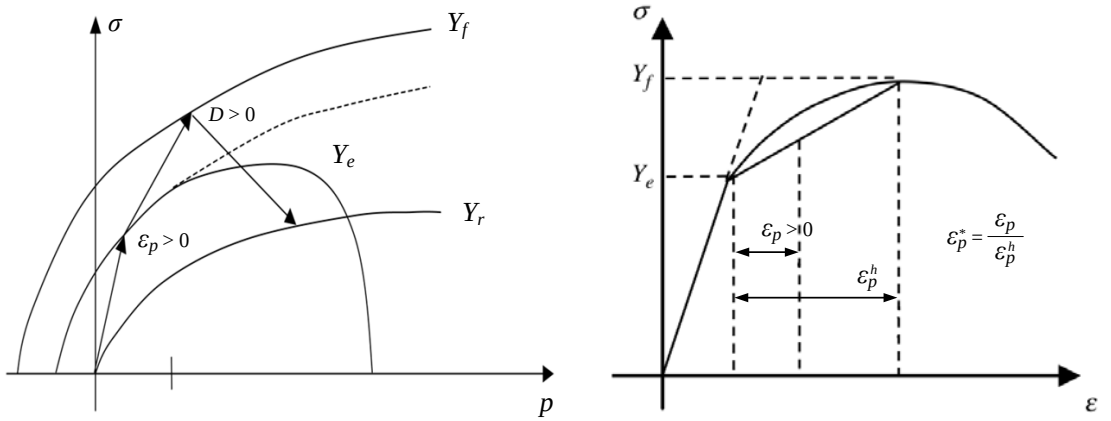

a) Stress surfaces b) Illustration of strain hardening

Fig. 2.7 Failure surfaces and stress update in RHT model

Before the failure surface Y_f is reached, an elastic strength surface Y_e is introduced to account for strain hardening behaviour, and is obtained through scaling the failure surface Y_f in the radial direction by a factor γ, as given in Fig. 2.7b and in the form of:

$$Y_e = Y_f\left(\frac{p^*}{\gamma}\right)\cdot\gamma\cdot R_3(\theta)$$
$$\gamma = \varepsilon_p^* + (1-\varepsilon_p^*)\cdot F_e\cdot F_c \tag{2.19}$$

where $\varepsilon_p^* = \varepsilon_p / \varepsilon_p^h$ is the normalised strain, $F_e(p^*)$ is an elastic strength parameter and $F_c(p^*)$ is a cap function. The residual surface is defined as

$$Y_r(p^*)A = A_f(p^*)^{n_f} \tag{2.20}$$

where A_f and n_f are constants defining the shape of the curve. The resulting damaged surface is then expressed in Eq. 2.21 as interpolation between the failure and residual surfaces in terms of a damage index D.

$$Y_d = (1-D)\cdot Y_f + D\cdot Y_r \tag{2.21}$$

The damage parameter is accumulated with plastic strain according to

$$D = \int\frac{d\varepsilon_p}{\varepsilon_p^f} \tag{2.22}$$

where ε_p^f is the plastic strain at failure.

Meanwhile, the plastic flow is defined to occur in the direction of deviatoric stress, and a von Mises potential is adopted, neglecting associativity and low-pressure shear dilation, with an option to partially incorporate the influence of volumetric strain.

2.3.8 Summarised on features of material models and simulation recommendations

As an outcome of above discussion on concrete models in hydrocodes, their key features with respect to simulating reinforced concrete structures under

impulsive loading are summarised in Table 2.1. It is generally understood that, simple models including CDP, pseudo-tensor, geologic cap and BDC model, which originally were designed for cases where tensile cracking is the primary failure mode in concrete, had reasons not to consider features that may be important for concrete under extreme loading.

On the other hand, for concrete models that were developed with specific aims for applications in shock physics and penetration or contact detonation type of problems, the detailed post-peak stress-strain states and residual shear resistance are secondary considerations, and hence it is understandable that these models may be weak in these aspects.

Table 2.1 Key features of concrete models in hydrocode

Material model	*Third invariant (Lode angle)*	*Shear dilation (non-associative flow rule)*	*Porous compaction (EOS)*	*Confinement effect (pressure-dependent)*	*Anisotropic damage*	*Fracture energy control*	*Rate enhancement (DIF effect)*
CDP	Y	Y	N	Y	Y	Y	Y
PT	N	N	Y	Y	N	N	Y
GC	N	Y	Y	N	N	N	N
BDC	N	N	N	N	Y	Y	N
WC	Y	N	Y	Y	N	Y	Y
JHC	N	N	Y	N	N	N	Y
RHT	Y	Y	Y	Y	N	N	Y
KCC	Y	Y	Y	Y	Y	Y	Y
CSC	Y	Y	Y	Y	Y	Y	Y

This leaves a few more versatile models, such as KCC and CSC model which will

be reviewed and discussed in greater detail in Sections 3.2, that one may find suitable for modelling of problems that involve both high and low pressure response stages.

2.4 Brief review on numerical simulation of RC members under impulsive loading

At the backdrop of all the simulation developments it is worth pointing out that the response of a concrete structure or structural component subjected to a high impulsive load would invariably experience distinctive response phases from the initial contact with the incoming shock load to the later global deformation response. Some typical concrete models including RHT, Winfrith, JH and KCC models as introduced in Section 2.3, are found to generally perform satisfactorily in the analyses involving high pressure and localised material response, for example projectile perforation of concrete targets (Abdel-Kader and Fouda, 2014; Ågårdh and Laine, 1999; Hansson and Skoglund, 2002; Jiang and Chorzepa, 2014; Liu et al., 2009; Lu et al., 2012; Polanco-Loria et al., 2008b; Ranjan et al., 2014; Swaddiwudhipong et al., 2010; Tai, 2009), and concrete members subjected to high-velocity impact (Booker et al., 2009; Farnam et al., 2010; Teng et al., 2008; Trivedi and Singh, 2013) and close-in blast (Li and Hao, 2014; Tabatabaei et al., 2013; Tai et al., 2011; Wang et al., 2008; Xu and Lu, 2006; Yun and Park, 2013; Zhou et al., 2008).

It should be borne in mind that the performance of a particular material model could vary in significantly different structural and loading conditions. If a structural member survives from the initial shock and stress wave effects, it enters into a structural response phase with effects closely related to the global deflection in much the same way as in a quasi-static loading situation. The fact that the high pressure largely diminishes and becomes low in the structural phase of response requires the material model to be able to accommodate

tension, shear, as well as the relatively simple compression behaviour under low pressure. The demand on the material model being able to exhibit appropriate behaviour in tension and shear becomes particularly important in reinforced concrete structures to ensure that transfer of stresses between concrete and reinforcing bars can take place in a realistic “reinforced concrete” composite manner. In high shear force region, the shear stress (or “bond” stress on the actual physical interface) between rebar and concrete will tend to play an important role in determining the residual state of the overall structural member.

Numerous studies have been carried out recently to examine and verify numerical models developed in hydrocodes for impulsive loading analysis in the global deformation regime (e.g. ARUP, 2009; Magallanes, 2008; Wu et al., 2012, to name a few). However, systematic examination of the performance of such material models extending into the global deformation phase is relatively limited. The following sections of this review summarises recently numerical practices in simulating reinforced concrete structures under global-dominated blast loading, mostly using KCC and CSC models, with a special focus on the tensile/shear behaviour in the low pressure regime.

2.4.1 Simulation on flexure-dominated structural response and failure

A few recent papers from the same research group (Bhatti et al. 2012; Kishi and Bhatti 2010; Kishi et al. 2011) employed elasto-plastic Drucker-Prager model to simulate the response of RC beams to impact loading. These studies tend to demonstrate that simple concrete model and coarse mesh could be suitable for RC beam analysis involving local as well as limited distributed damage. The authors assumed elasto-plastic compressive and elasto-brittle tensile responses for concrete, as shown in Fig. 2.8a. Constant failure strain was defined and a fictitious tensile strength was introduced by scaling the actual tensile strength

with mesh size to keep a same area under the softening stress-strain curve, in order to ensure mesh objectivity.

The test RC beam that was modelled was originally subjected to a series of impacts from drop weight with increasing drop height. The beam had a rectangular cross section of 250 mm×200 mm and a clear span of 3 m. The authors reported a good comparison of the maximum and residual deflection between the numerical simulation and the physical test, while the maximum reaction forces are nearly 50% larger than the experimental results, as plotted in Fig. 2.8b and c. The maximum impact velocity was 6 m/s and the maximum deflection following the final impact test (on an already heavily damage state) was just around 70mm or 2.3% of the span length.

Fig. 2.8d and e shows comparisons between the experimental crack patterns and the numerical zero-stress contours. Note that because the material was assumed perfectly brittle, elements in a tension failure state would have developed into a zero tensile stress state and so by identifying elements with virtually zero stress (in the analysis this was set at 0∼0.001 MPa) the crack pattern can be illustrated. It can be observed that punching (shear) cracks emerged and intensified after each impact test with increasing impact velocity, this led to the formation of a plastic zone in the middle of the beam which appeared to be the main source of the plastic deformation. The FE crack patterns as represented by “zero stress” traces appear to match the test results nicely.

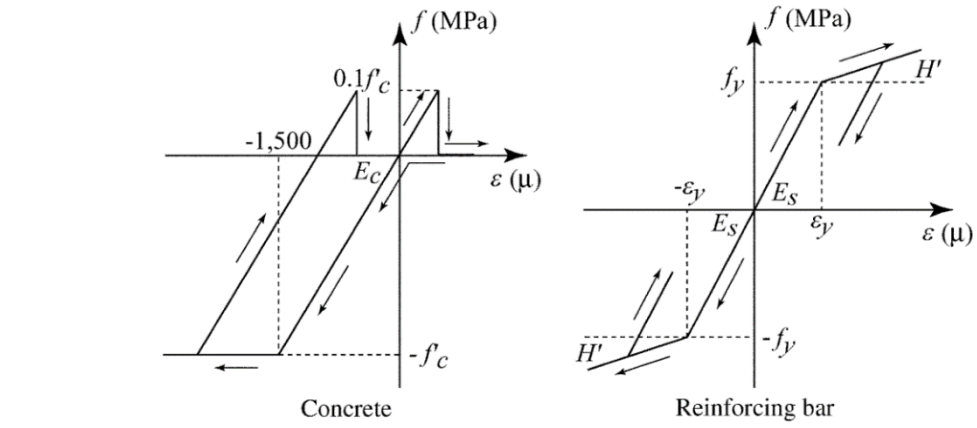

a) Stress-strain relationship for concrete and reinforcing bar

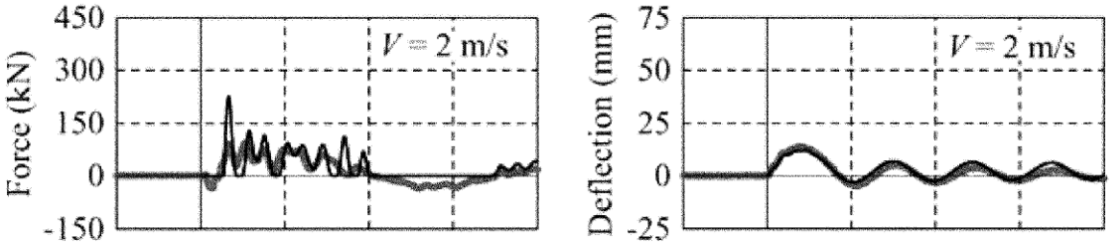

b) Time histories of reaction force and central deflection (V=2m/s)

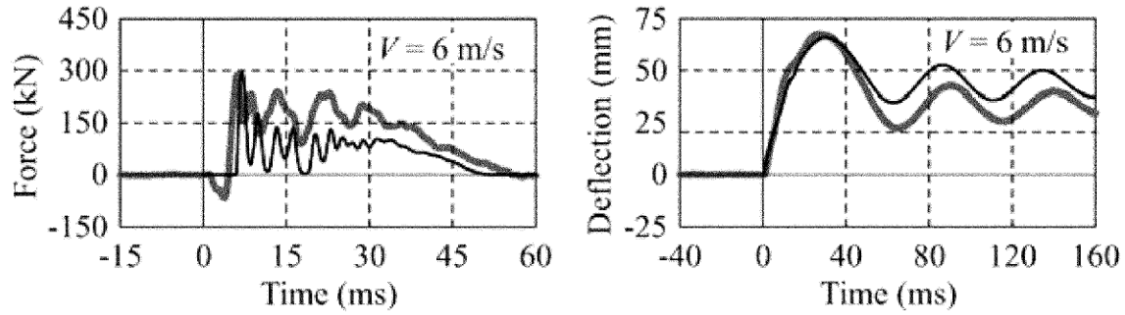

c) Time histories of reaction force and central deflection (V=6m/s)

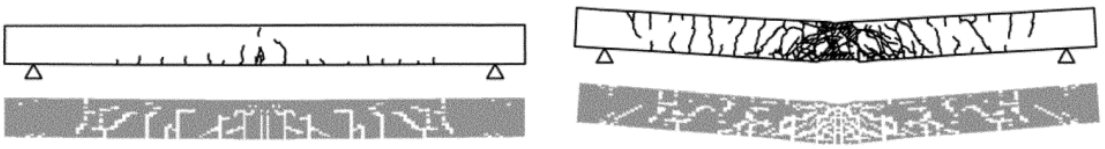

d) Damage pattern (V=2m/s) e) Damage pattern (V=6m/s)

Fig. 2.8 Elasto-plastic Drucker-Prager model based FE simulation (after Kishi et al. 2011)

El-Dakhakhni et al. (2009) modelled the RC slab tested by Razaqpur et al. (2007) under blast loading using the KCC model. The dimension of the RC slab

was 1000 mm×1000 mm×70 mm, and it was doubly reinforced with welded steel mesh of rebar of 5.74 mm in diameter, and spacing of 152 mm in each direction. The slab was clamped on all four sides and subjected to a detonation that recorded a peak pressure of 5712 kPa and an impulse of 2412 kPa·ms. The maximum deflection of the slab from the test was 12.1 mm or 1.2% of the span length, and the slab fractured badly but did not dis-integrate.

The main simulation results are summarised in Fig. 2.9. The simulated maximum deflection was 13.1 mm, which agreed fairly well with the test result. It is interesting to note that the tensile cracks at the bottom (tensile) surface exhibited an orthogonal pattern, while diagonal cracks were also visible. Comparing to the experiment, the numerical crack pattern appeared to be much denser and followed closely the pattern of the reinforcement mesh. The comparison tends to suggest that the steel-concrete interaction was damaged more severely in the numerical model than in the actual slab, although this was not discussed in the paper.

The above mentioned relative weakness in the concrete-rebar connection in the numerical simulation using KCC model echoes well the observations and discussion presented in Chapter 3 about the numerical premature failure of concrete-rebar interaction using the same concrete material model but under larger deflections. This work is part of a blind simulation contest for slab blast (University of Missouri-Kansas City 2013). More about that study will be discussed later in Chapter 3.

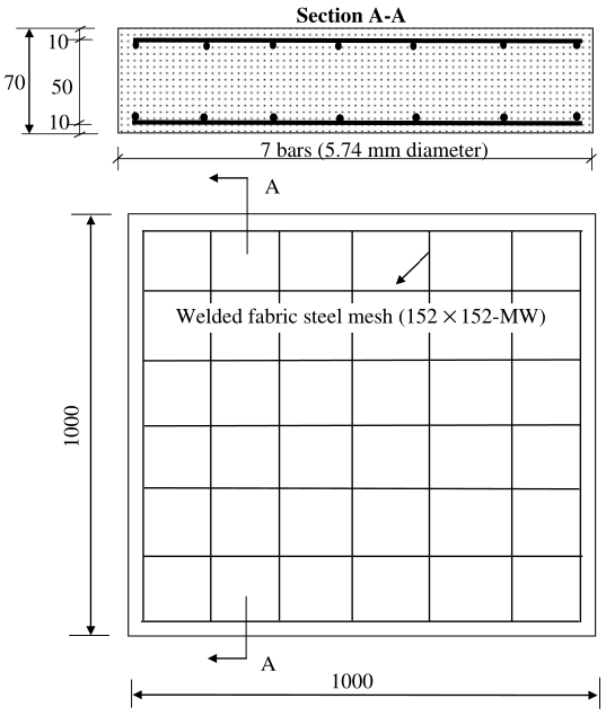

a) Test specimen layout

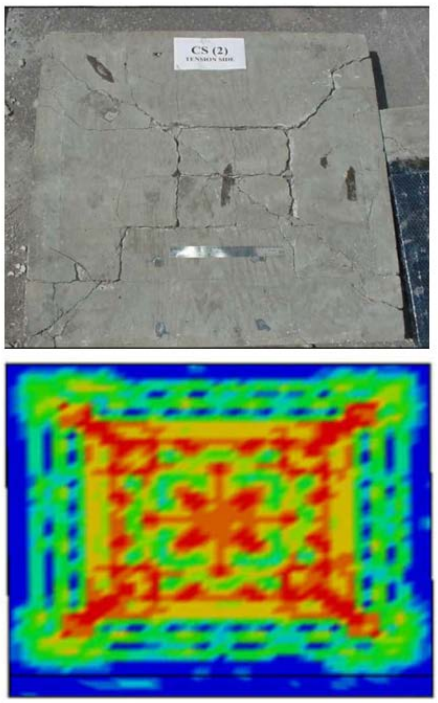

b) Specimen damage pattern

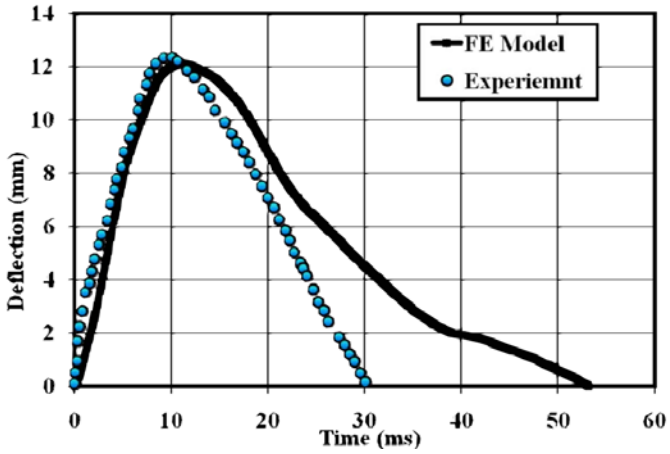

c) Time history of central deflection

Fig. 2.9 Crack pattern on tension side and deflection history of slab blast tests, after El-Dakhakhni et al. (2009)

Magallanes (2008a) compared the performance among several concrete material models, including KCC and CSC models, as presented in Fig. 2.10. The author first simulated the response of a 355 mm square RC column which was originally tested as part of a building subjected to bare explosive charge. The test column was constructed with 45 MPa concrete and Grade 60 steel rebars. During the

test, the column sustained a shear failure near the two supports in the early stage, and subsequently exhibited tensile membrane behaviour under large deformation, with a measured mid-span deflection of 280 mm.

The author was able to reproduce the damage distribution and the global deformation with KCC model. The CSC model was found to under-predict the overall displacement, with a localised diagonal shear failure zone at about one-quarter column height. It was also noted that HJC and the brittle damage model severely underestimated the overall response, and hence were regarded as inadequate for predicting structural response to impulsive loading due to the lack of proper representation of tensile fracture.

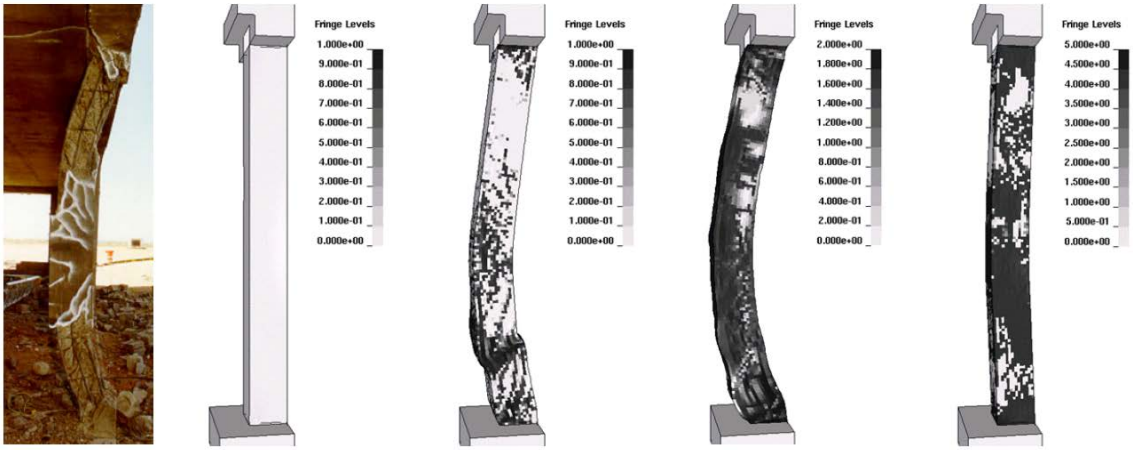

Fig. 2.10 Post-test deformation of the RC column, after Magallanes (2008a)

Thilakarathna et al. (2010) conducted a similar simulation of axially loaded columns under transverse drop-weight impact load using KCC model. The test column had a cross section of 300 mm×300 mm and a net span of 4 m. The column was pre-loaded with axial force before impact test; however it should be noted that the level of axial force was rather small, and it amounted to only about 3.7% of the axial capacity of the column. So essentially the specimen still belonged to the typical beam category. The impact load was generated by

dropping a weight of 1.14 ton from a height resulting in an impact velocity of 3 m/s.

The deflection and reaction force time histories produced from the numerical simulation agreed well with the test results. The damage pattern, represented by the effective strain, appear to resemble reasonably the crack pattern from the experiment. However, the maximum global deflection was quite small, at about 30 mm or less than 1% of the member span, and the response and the damage was primarily caused by the impact stress and stress wave effects. Therefore what we read from the comparison here could not be automatically extended to situations where large global deformation is involved, despite that the test specimen was a slender structural member.

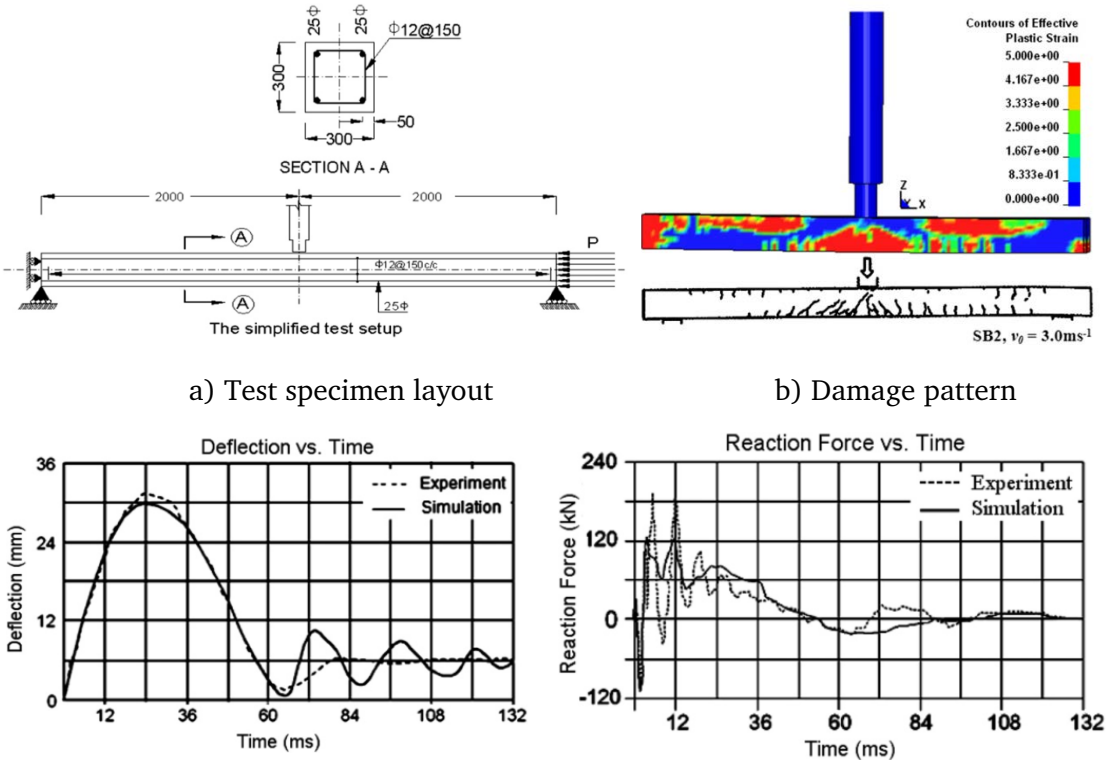

a) Test specimen layout b) Damage pattern

c) Deflection history d) Reaction history

Fig. 2.11 Deflection and reaction history of the impacted column Thilakarathna et al. (2010)

The Blind Blast Contest (Thiagarajan 2013), held in 2013 at the University of Missouri Kansas City (UMKC), provided an ideal benchmark for validation of FE modelling framework. The overall structural response in such a loading scenario was primarily of a monotonic process, and consequently the performance of these material models was expected not to differ significantly. A preliminary analysis based on this experiment is also conducted and presented in greater details in Chapter 3.

Wu et al. (2014) also conducted comparative simulation for RC slab blast using test data obtained from the above blast contest, using KCC and CSC models. It was reported by the authors that using KCC model, the deflection matched test data very well when the rate effects were modelled appropriately, and when these were ignored, a huge discrepancy existed. The CSC model showed negligible influence from the rate effects and the results agreed with test data quite well. However as also predicted by other models, the rate effect is believed to have a limited influence when the specimen has already entered global deformation stage after blast. The unexpected over-prediction of deflection by KCC model when rate effect is not considered, is consistent with the findings presented in Chapter 3. On the other hand, Winfrith and RHT models tended to underpredict the deflection, and opposite rate effect was observed from the Winfrith model.

Another simulation study using the same experimental data reported above was carried out by Thiagarajan et al. (2014) and Wesevich et al. (2011). For the RC slab, concrete was modelled by solid elements using KCC and Winfrith model, and steel rebar was modelled by beam element. The keyword “Constrained Lagrange in Solid” was applied to model the interaction between rebar and concrete, which couples the rebar beam elements with the concrete solid elements in which the one-dimensional rebar passes through. The nodes of the concrete and rebar are not necessarily in the same position but they are forced to

have same DOFs and displacements, thus a perfect bond is assumed. Mesh size of 25.4 mm and 12.7 mm were adopted.

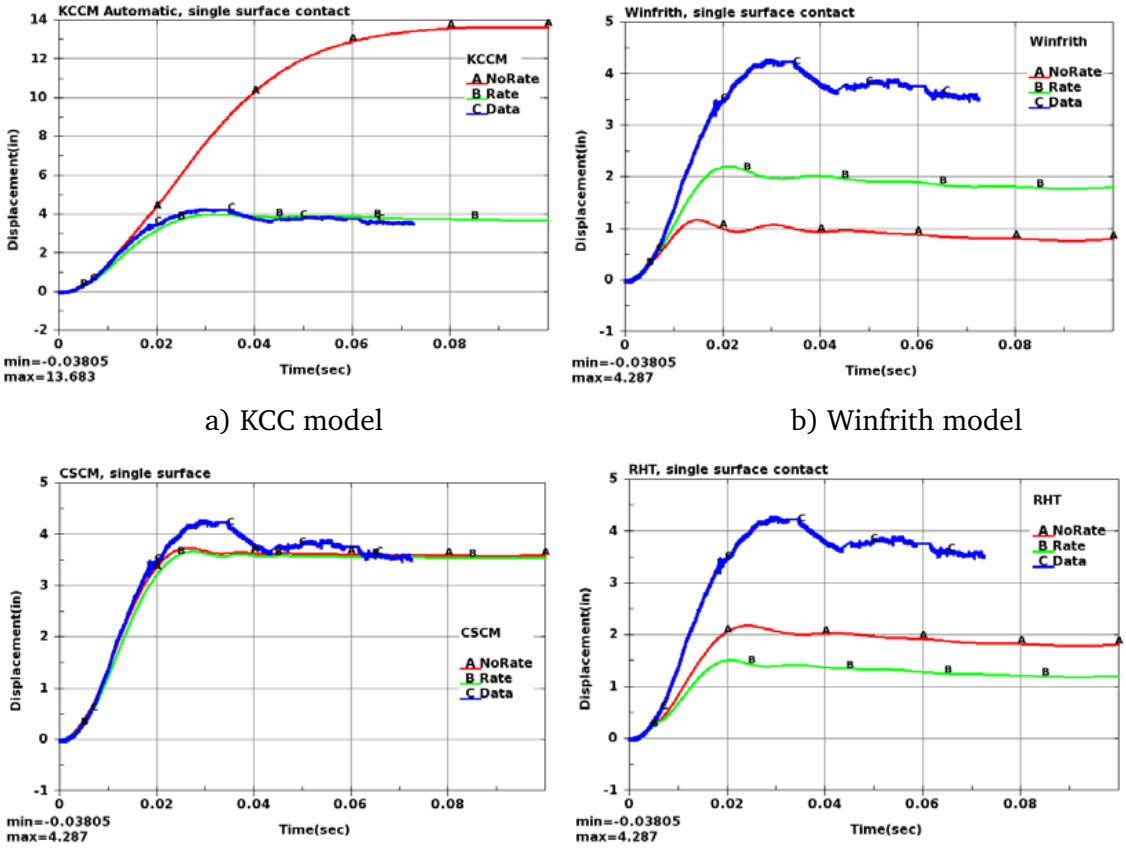

a) KCC model b) Winfrith model

c) CSC model d) RHT model

Fig. 2.12 Time histories of mid-span deflection of RC slab under blast pressure (after Wu et al. 2014)

As observed from the results, the peak deflection was generally matched by simulation with mesh size of 25.4 mm, but it increased 55% and 75% respectively when mesh size reduced from 25.4 mm to 12.7 mm. A possible cause for this was the strain-based but mesh-dependent erosion criterion. Results also revealed that initial stiffness from KCC curves didn't agree well with the experiment, which might be caused by severe damage and erosion of concrete elements near both sides of the supports, due to stress concentration brought by

the boundary restraints. This actually prevents the increasing of rebar force and reduced the possibility of concrete-rebar interaction deterioration.

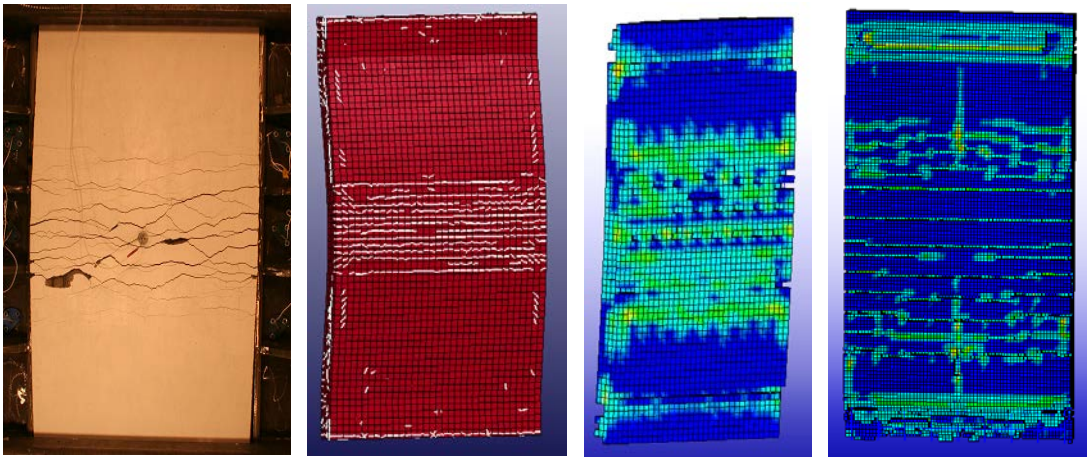

a) Test crack profile b) Winfrith (25.4 mm) c) KCC (25.4 mm) d) KCC (12.7 mm)

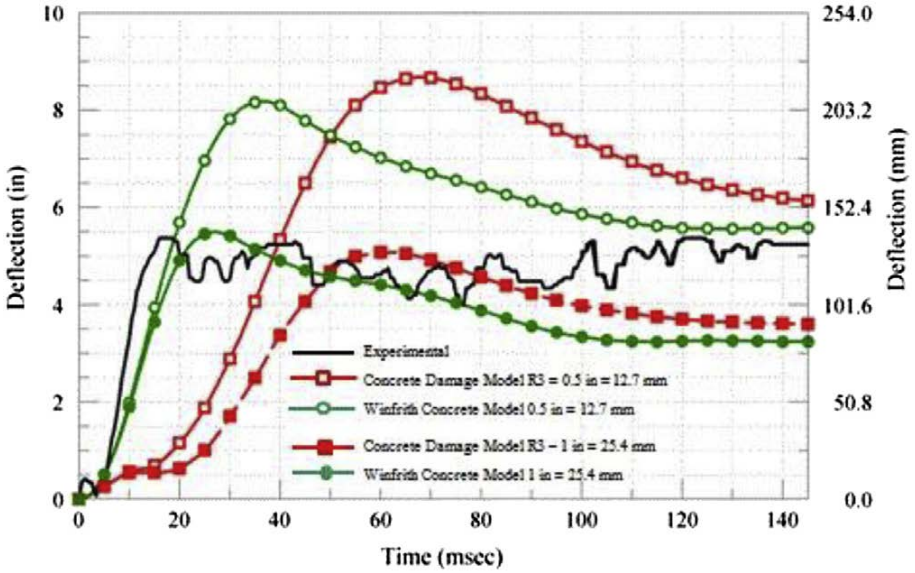

e) Time histories of mid-span deflection

Fig. 2.13 Comparison of crack patterns and deflection histories from experiments and simulations (after Wesevich et al. 2011)

2.4.2 Simulation on shear-dominated structural response and failure

Adhikary et al. (2012) modelled the response of RC beams of a relatively small span-depth ratio to drop-weight impact, using KCC model in LS-DYNA. The

beams were originally tested with drop-weight at different impact velocities up to 2m/s, and had a shear-span-to-effective-depth ratio of 3.3, a longitudinal reinforcing ratio of 2.4%. One group of specimens had no shear reinforcement (for a shear-critical response), and another group had moderate shear reinforcement with a transverse reinforcing ratio at 0.56% (for a flexure-critical response). The damage patterns from static and low to medium velocity impact tests were quite similar, and only static and high velocity impact cases are discussed here.

For the shear-critical cases, the damage from the static experiment clearly showed a shear failure. The numerical model was able to reproduce a shear failure zone; however it also indicated a large tension damage zone in the lower central area which did not seem to have occurred in the experiment. For the high velocity impact case, the failure mode from the experiment was still dominated by shear but rapid loading appeared to have enabled the development of shear failure on both sides of the beam forming an extended shear plug. The numerical model appeared to be able to generate a shear plug but it was much more concentrated around the impact zone. From the comparison of the load vs. midspan deflection curves, it can be observed that the numerical results generally under-predicted the residual strength, and this seems to echo the discussion earlier that the numerical model with KCC model tends to result in more rapid structural degradation (i.e. certain premature structural failure) than in actual physical experiment.

For the flexure-critical cases, the numerical results again tend to show more rapid post-peak degradation than in actual tests. In particular, for the high velocity impact case the numerical model exhibited a rather brittle failure process with a minimum residual strength, whereas in the physical test the response was fairly ductile. The damage distributions from the numerical simulation barely resemble the overall damage zones of the tests but the detailed patterns could hardly be identified.

It was observed that peak load was increased sharply in shear-critical beams and then fell instantly (brittle shear failure) for both static and low loading rates but the specimen had a significant amount of residual strength, while flexure-critical beams had a much milder response, except in the high rate case (v = 2m/s) where a very steep descending branch was seen in FE result indicating catastrophic failure but the experimental response suggests that it resisted the catastrophic failure and the response was relatively ductile.

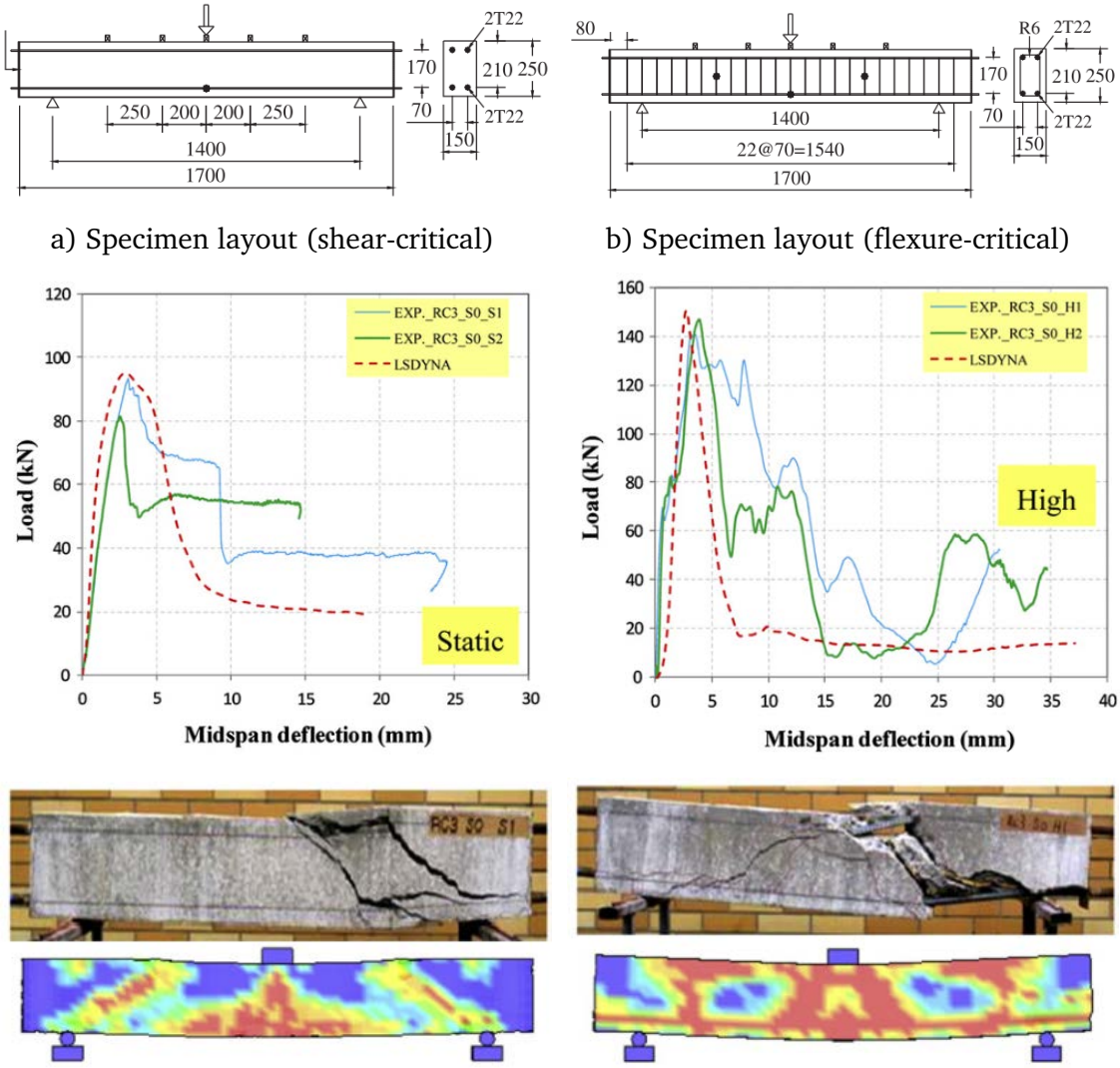

a) Specimen layout (shear-critical) b) Specimen layout (flexure-critical)

c) Load-displacement curves and damage patterns for shear-critical specimen

Fig. 2.14 Numerical analysis of failure mechanisms under varied loading rates (after Adhikary et al. 2012)

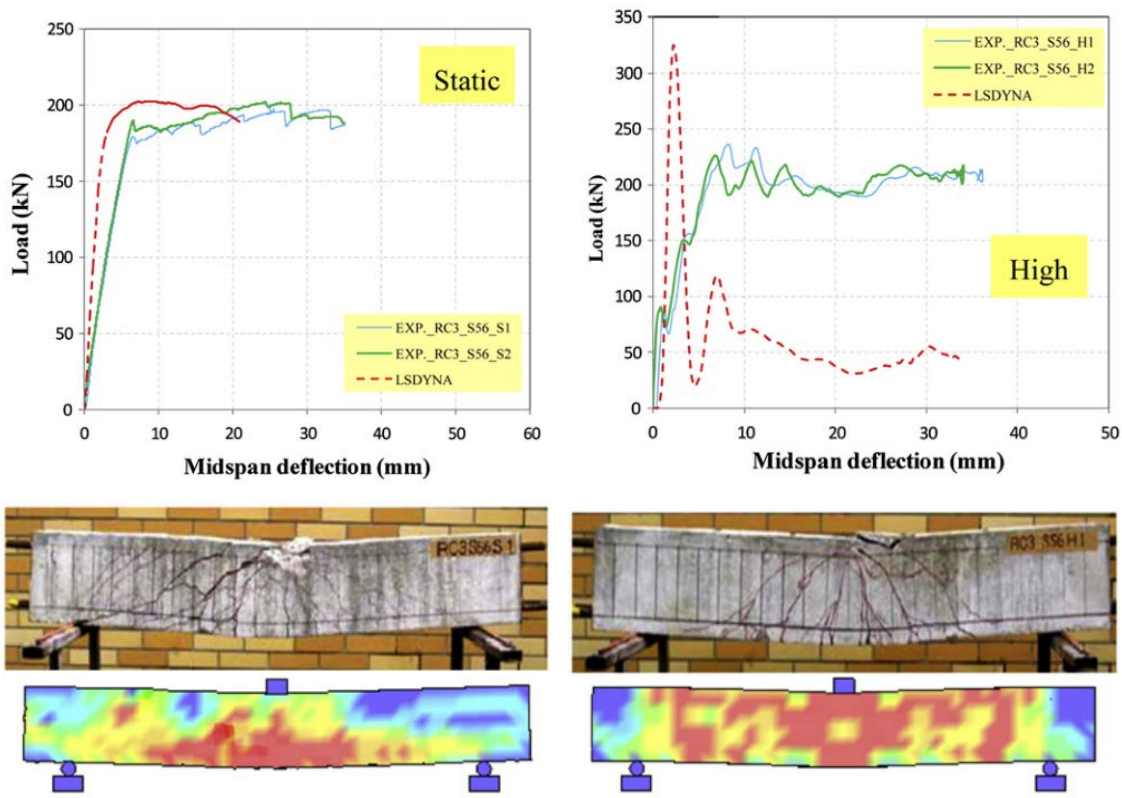

d) Load-displacement curves and damage patterns for flexure-critical specimen

Fig. 2.15 Numerical analysis of failure mechanisms under varied loading rates (after Adhikary et al. 2012) (continued)

For the over-reinforced beam, the impact loads had an impulse of 332 Ns and a impact energy of 850 J. The major crack patterns appeared to agree with the test results. For the under-reinforced beam, the impact load produced two major cracks at around the the impact loading points, which effectively broke the beam into three segments. Additional cracks appeared at around the quarter-span points. The numercial results were able to reproduce the damage regions; however the material damage appeared to be much severer in the numerical simulation than in actual test. The author also remarked that the rebar material was a controlling factor and removing the rate effect in the rebar increased the maximum deflection by 50 percent.

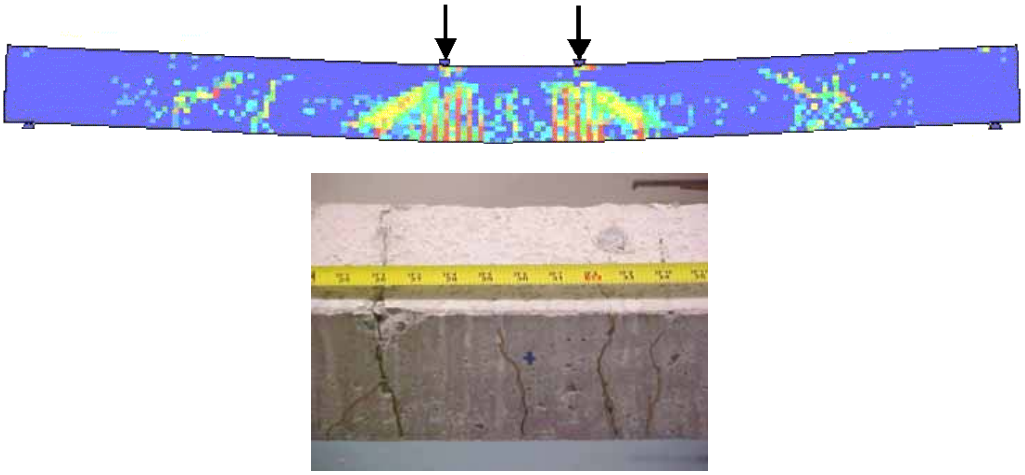

a) Damage patterns for over-reinforced beam

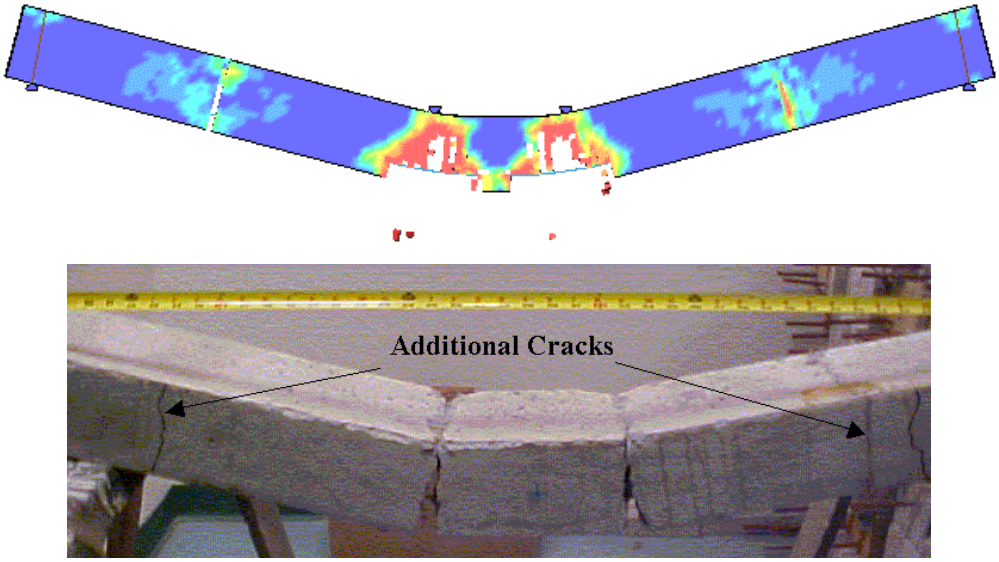

b) Damage patterns for under-reinforced beam

Fig. 2.16 Numerical and experimental damage mode of RC beams under impact (Murray et al. 2007)

The collision impact tests carried out by Murray (2007) were conducted on full-scale beams of 4.9m long with a shear span of 1.8 m. The beam cross section was 203 mm×343 mm. The beams were made of 46 MPa concrete and singly reinforced with two No.6 steel bars making a reinforcing ratio of 1%. The beams were tested with different impact speeds from a bogie vehicle. The failure mode under the lower speed loading (4 m/s) was dominated by a rather concentrated plastic/damage zone at the middle of the beam, whereas the failure mode under

the higher impact speed (9.2 m/s) involved a punching shear failure starting from the impact zone, The damage subsequently developed into extended shear failure mode together with tearing/debond failure throughout the entire shear

a) Experimental results (V_0=4.4 m/s) b) Numerical results (V_0=4.4 m/s)

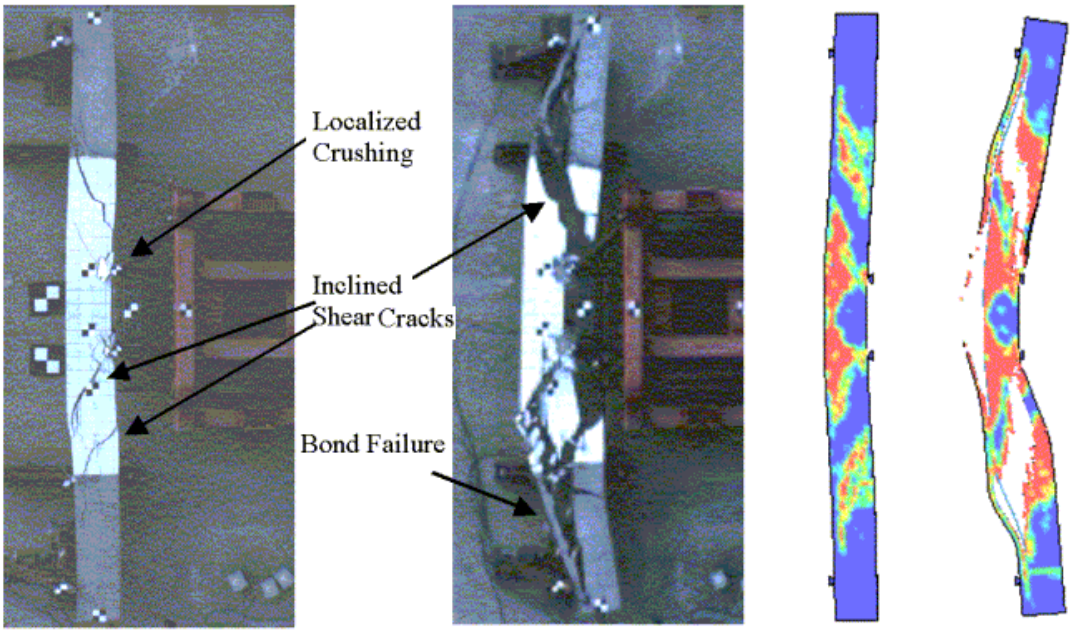

c) Experimental results (V_0=9.2 m/s) d) Numerical results (V_0=9.2 m/s)

Fig. 2.17 Numerical and experimental damage mode of RC beam under vehicle collision (Murray et al. 2007)

span on both side of the beam. The numerical simulation was able to reproduce the main shear and tearing/debond failure. However the numerical model appeared to indicate spalling on the back side of the impact zone, which did not seem to occur in the actual test. This should be noted as spalling is also an indicator of the tension fracture behaviour of the material model.

Jiang et al. (2012, 2015) modelled impact tests of RC beams conducted by Fujikake et al. (2009) using CSC model. The test beam was 1.7m long and had a shear-span-to-effective-depth ratio of 3.9 and cross-section of 250 mm×150 mm. The longitudinal and transverse reinforcing ratio was 1.3% and 1.4% respectively. The FE simulation generally captured the overall damage patterns from tests with different drop heights, with a tendency of varying from distributed flexural cracking to increasingly concentrated shear cracking and local punching failure as the drop height increased. It should be noted that in the flexural response case the global deflection was rather small (less than 10 mm), whereas the much larger deflection (~35 mm or 2.3% to the span length) in the shear-failure case was due to concentrated plastic deformation around the mid-span. It is also worth noting from the comparison of the deflection time histories that the simulation tended to return much less permanent plastic deformation than in the actual test, a trend that appears to be opposite to the observations from using KCC model. In fact when the drop height was greater than 0.3 m, significant shear cracking was developed at mid-depth of quarter span position and then propagated towards the loading head and supports; however, FE results indicated much less such shear cracking. All of these echo the present study concerning CSC model as will be discussed later in Chapter 3 and 4.

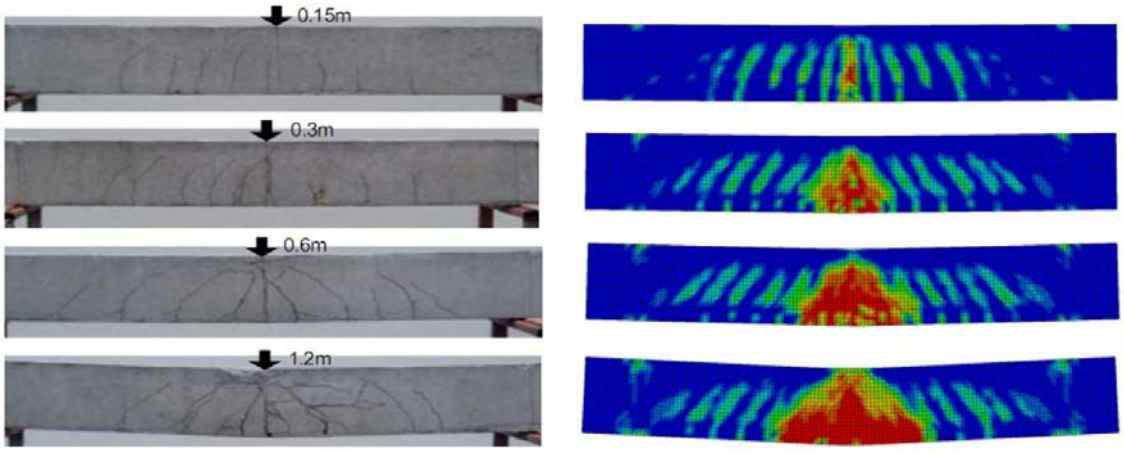

a) Test crack profile b) Simulated damage pattern

Fig. 2.18 FE analysis for RC beam at varied drop height, after Jiang et al. (2015)

A few papers from the same group of researchers (Williams and Williamson 2011; Williams 2009; Williams et al. 2008) modelled filed blast tests of RC bridge columns. The tested column were made in half scale and had the same height of 3.4 m. It is noted that most of the column specimens were lightly damaged and thus only the two most severely damaged cases are discussed here. The first column had a circular cross-section with a diameter of 460mm and the second was a square column with side width of 760 mm. Both columns were made by concrete with a compressive strength of 27 MPa, and had a longitudinal reinforcement ratio of around 1.1% and #4 transverse stirrups was placed at a spacing of 150 mm. The charges were placed very close to or in contact with the tested columns and the response was expected to be local. Complete shear failure near the support were evident in both specimens and little flexural cracking was observed. The circular column showed a diagonal cracking rising up and to the right from the failed region, and transverse shear slip was noticed at the support of the square column, indicating direct shear type of failure. The measured residual displacement for the two columns were 127 mm and 76.2 mm, respectively.

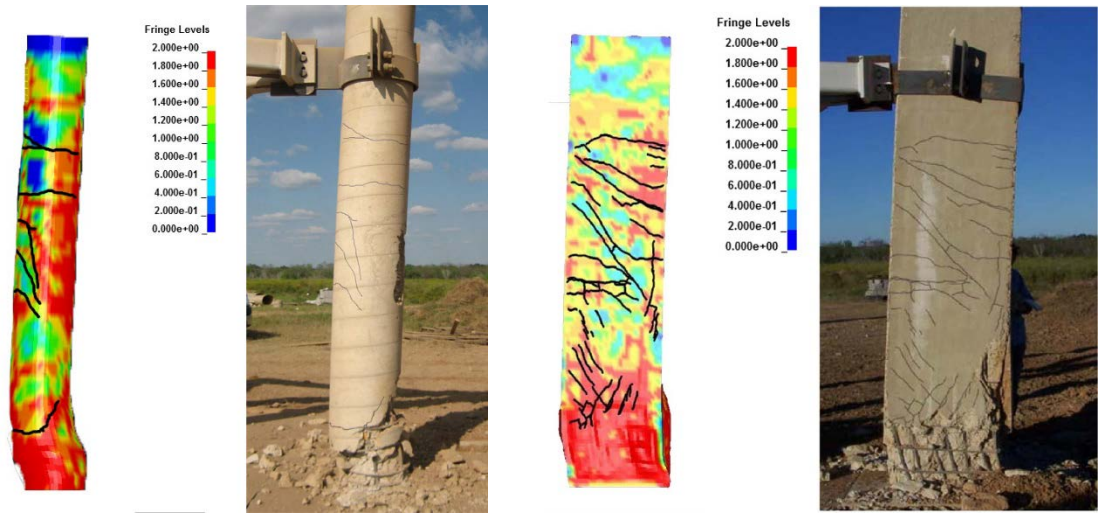

a) 460 mm circular column b) 760 mm square column

Fig. 2.19 Comparison of post-blast deflected shapes and damage patterns (after Williams 2009)

In the FE model, KCC model and simplified Johnson-Cook model were used to model concrete and rebars, respectively. The authors suggested a mesh size between 2.1 mm to 2.4 mm corresponded best to the experimentally measurements. The numerical damage contours appeared to match the overall damage pattern. Apart from distributed damage, concentrated damage and plastic deformation of the material was visible in the column region near the base, indicating local failure both at the structural and material levels.

The numerical results under-predicted the residual deflection and produced displacements of 109 mm and 66.0 mm for the two columns, equivalent to about 86% of the experiment residual deflection. The authors indicated that this was due to an over-ductile KCC softening curve for confined concrete undergoing extensive compression and shear. In fact, as the mesh size was refined and the softening curve of KCC material become relatively flattened, under high rate load there was limited time for cracking and plastic deformation to be fully developed, and this combined effect contributed to the overprediction of concrete ductility.

Kyei (2014) modelled the response of 300×300×3000 mm RC columns subjected to field blast tests, using CSC model. The square columns were cast by 41 MPa concrete and reinforced by four 400 MPa steel rebars of a diameter of 25mm. 10 mm size rebars were used for transverse reinforcing and spaced at 150mm which was reduced to 75 mm spacing in the plastic hinge regions. Charge masses were placed at a stand-off distance of 2.5 mm, respectively. The

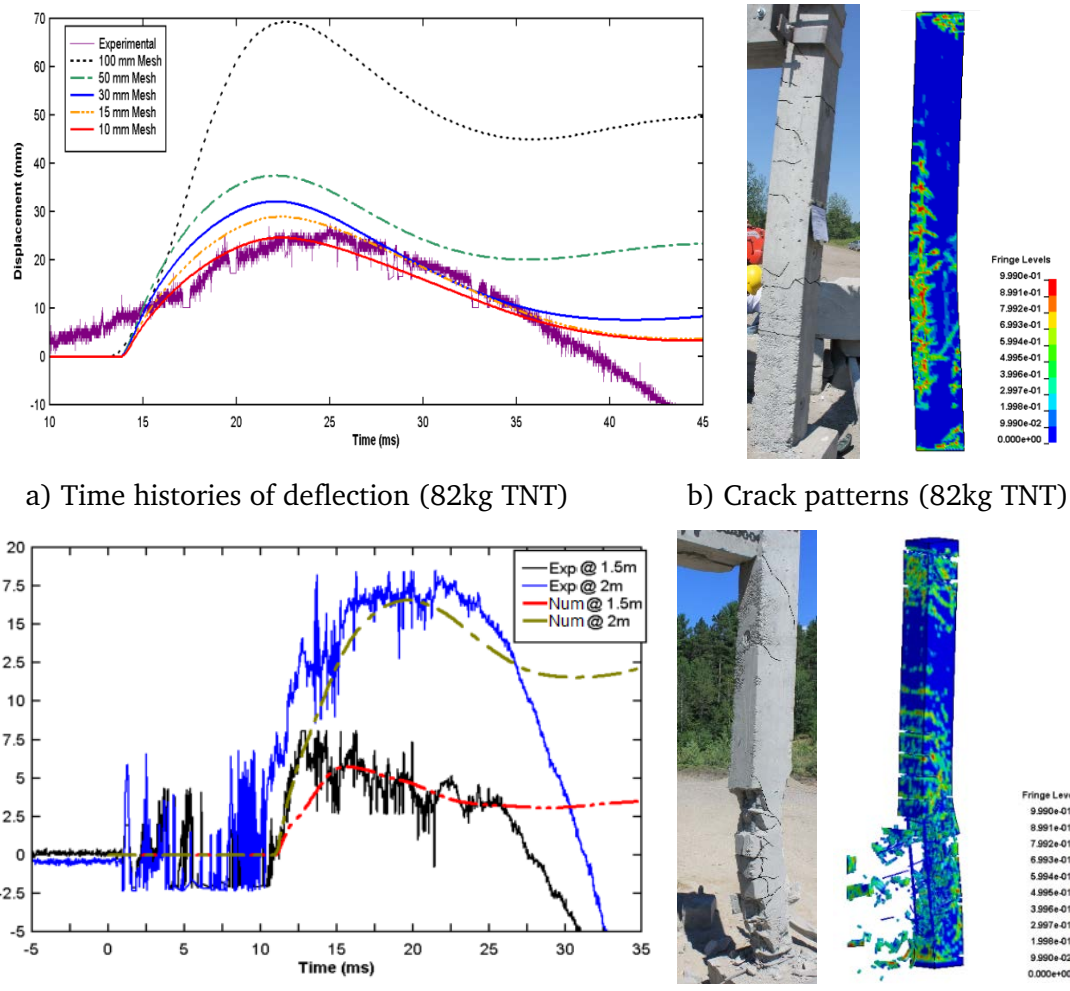

a) Time histories of deflection (82kg TNT) b) Crack patterns (82kg TNT)

c) Time histories of deflection (132kg TNT) d) Crack patterns (132kg TNT)

Fig. 2.20 Comparison of mid-span time histories and damage profiles for 132kg equivalent TNT test (after Kyei 2014)

RC column experienced a flexure failure under small charge equivalent to 82 kg of TNT explosive, and when a larger 123 kg TNT explosive was denoted the

column failed due to severely localised concrete damage near the bottom support.

The RC columns, were modelled with mesh sizes ranging from 10 mm to 100mm, and it was found that maximum displacements decrease with decreasing mesh size, converging to the experimental displacement at a mesh size of 10 mm. The numerical results captured well the overall deflected shape and the peak deflection in both load scenarios, while the damage pattern revealed that CSC model tended to predict much more tensile cracking than experiment. In the flexural failure case, severe damage appeared along the longitudinal reinforcement, suggesting that the steel-concrete interaction was damaged more severely in the numerical model that experiment.

A comparative numerical study has been done by Abu-odeh (2008) to analyse the response of RC safety barrier impact test by a 2.3 ton bogie vehicle (Williams et al. 2007). The tested barrier was casted by 27 MPa concrete and #4∼#6 rebars were used as reinforcement with the details given in Fig. 2.21a. Both KCC and CSC models were used to model the concrete, and rebars were modelled by beam elements that were coupled to the concrete continuum by using the keyword “Constrained_Lagrane_in_Solid” in LS-DYNA.

At a low impact velocity of 24 km/h, the barrier showed no failure but developed minor cracks. When the velocity increased to 32 km/h, severe local punching failure was found around the impact region, as shown in Fig. 2.21. Numerical analysis using the CSC model showed a comparable damage pattern in the low velocity impact case but did not catch the severe punching failure in the high velocity impact. However in both impact cases KCC model showed a rather larger damaged area and the deformation was more pronounced. In the region where no damage occurred in the test, severe damage was produced in the KCC result and it developed along the reinforcement, suggesting an unexpected deterioration of concrete-rebar interaction.

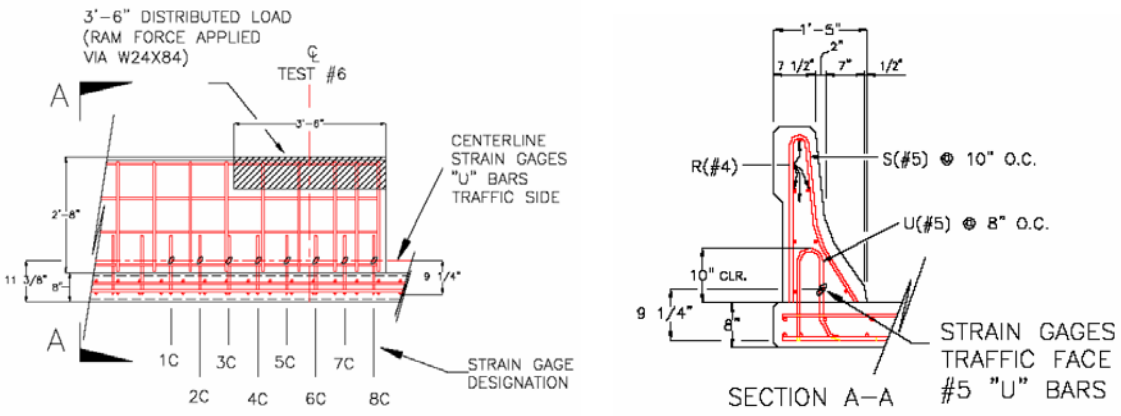

a) Reinforcement plan for the RC barrier

b) Test (v= 24 km/h)

c) Test (v= 32 km/h)

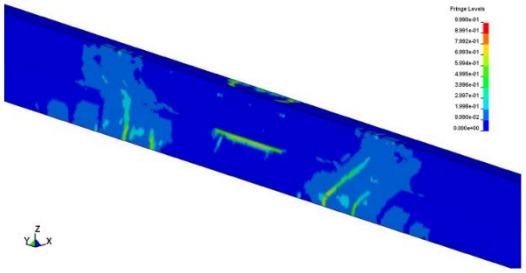

d) CSC damage pattern (v= 24 km/h)

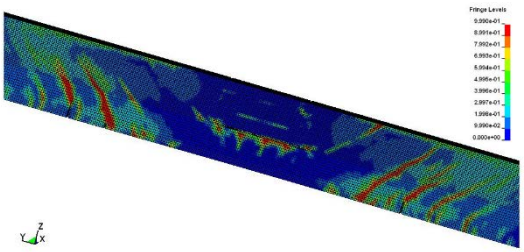

e) CSC damage pattern (v= 32 km/h)

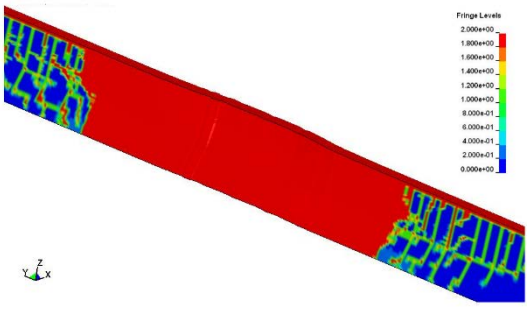

f) KCC damage pattern (v= 24 km/h)

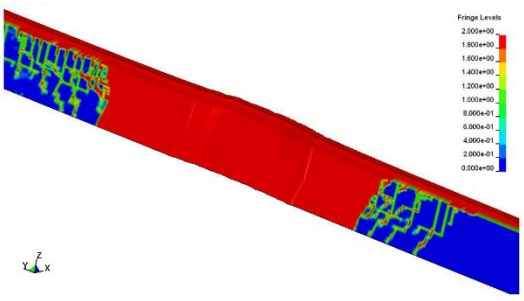

g) KCC damage pattern (v= 32 km/h)

Fig. 2.21 Damage pattern of FE simulation and test under different impact velocities (after Abu-odeh 2008)

Wu et al. (2011a; b) also used KCC model to simulate the response of RC column subjected to contact explosive. The tested column had a cross-sectional dimension of 400 mm×400 mm and a vertical height of 2400 mm. Concrete strength was 30 MPa, and the longitudinal and transverse reinforcement ratio was 1.57% and 0.12%, respectively. A charge equivalent to 25 kg of TNT was placed at stand-off distance of 500 mm.

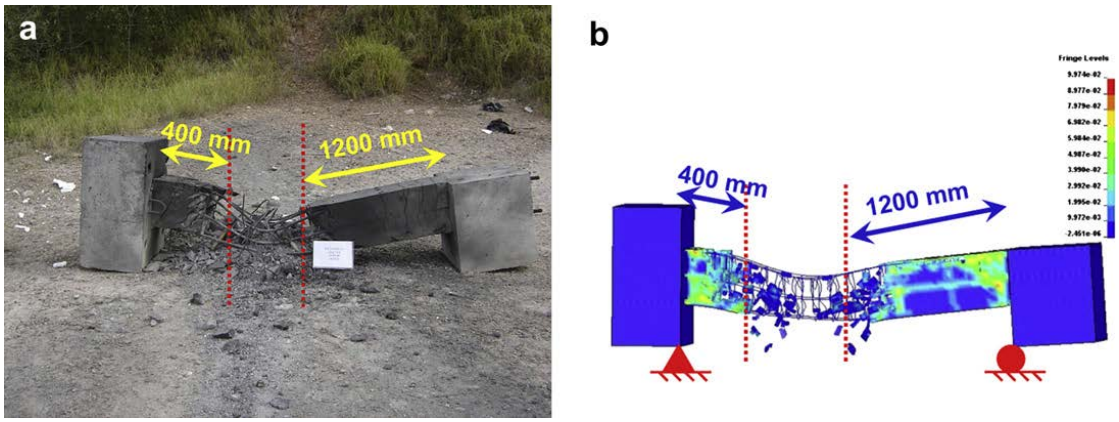

a) Post-blast failure b) Numerical damage pattern

Fig. 2.22 Simulation of RC column subjected to contact explosive (after Wu et al. 2011)

In the numerical model, erosion was enabled and the criterion was set at a cut-off value of 10% principle strain. The deformed shape, deflection value and breaching zone (by erosion) were simulated rather accurately for columns subjected to the effects of contact or near-field explosives. In the meantime, significant flexural cracks were found in the blast side of the column, which was not captured by the FE model. Instead, severe damage was seen along the longitudinal rebars at mid-depth and corners of the cross-section. The same modelling approach was also applied by some other researchers (Bao and Li 2010; Li et al. 2012) for numerical simulation of severely damaged RC columns under blast loading.

2.4.3 Concluding remarks

From the above review, it can be seen that the performance of KCC and CSC models varied in different applications under different loading conditions. Both KCC and CSC models seem to work satisfactorily in scenarios where damage is dominated by localised material failure, such as in close-in blast and higher rate impact. However, when the (global) structural response becomes more important, both models tend to exhibit deficiencies but in somewhat opposite directions; while KCC model tends to result in accelerated damage in tension/shear and rebar anchorage, and hence a premature global failure, CSC model tends to over-estimate the tension/shear capacities leading to over-prediction of the residual strength capacity and underestimation of the plastic deformation.

As most of the studies have been concerned about the direct response and damage due to the blast or impact load, the above mentioned issues regarding mis-representation of the structural state have gone largely un-noticed. Since such representation is essential in an assessment of the structural integrity and the residual capacities, a comprehensive evaluation of the relevant modelling requirements and specific demands on the concrete material models is crucial. At issue will be the soundness of the concrete material models in the tension and shear dominant regimes, and a realistic and unified representation of the concrete-rebar interaction in different modelling schemes. These will be the key questions the present study is intended to address.

Chapter 3: Numerical modelling of RC structural response to blast loading: common practice and issues

3.1 Introduction

The behaviour of concrete material and reinforced concrete structures under impact and blast loads has attracted much renewed research interest in recent years. A distinctive trend in the latest research effort on this subject is an ever increased use of high fidelity numerical simulation approaches. The tendency towards computer simulation has been promoted by the availability of advanced dynamic analysis codes and the growing computer power, which have made it possible to carry out rather sophisticated numerical analyses with a desktop computer.

It is generally understood that the response of concrete structures to impact and blast loads is complicated and involves a number of challenges in terms of the rigour and reliability of modelling considerations, for example appropriate handling of pressure and rate dependence of materials, stress wave phenomenon, damage evolution and softening, as well as large deformations. Although these capabilities have mostly been incorporated in various general-purpose computational analysis software, e.g. LS-DYNA (LSTC 2012), Autodyn (ANSYS 2009) and ABAQUS/Explicit (Dassault Systèmes 2007), whether or not the underlying mechanics during the dynamic process may be adequately represented still depends on the soundness of the constitutive material

descriptions and the interactions among the constituent materials under the complex structural and loading environment. Handling such complex modelling analysis certainly also requires an analyst to be able to comprehend the model behaviours as well as the underlying physical processes.

Different computational techniques exist for the analysis of concrete structures under high dynamic loading (Tu and Lu 2009). Nonetheless, the majority of the numerical simulation studies in this field are conducted using a finite element approach. In a traditional continuum FE framework, fracture of concrete is simulated in a smeared manner using the so-called macroscopic material models, in which classical continuum mechanics based considerations, e.g. damage evolution, plastic flow, failure surfaces and so on are implemented at the local element level. Mesh-objective softening (i.e. preservation of the fracture energy) may be achieved by incorporating a mesh-adjusted softening rule (e.g. Malvar and Crawford 1997; Murray et al. 2007).

As introduced in the literature review in Section 2.4, numerous studies have been carried out recently to examine and verify numerical models developed under such a general FE framework for high impulsive loading analysis. It has been found that the outcome of a numerical simulation is closely related to the capacity of the concrete models in dealing with the nonlinear behaviour of the material under complex loading conditions, and the performance of a particular material model could vary in different structural and loading conditions. Therefore continued research effort is needed to understand more comprehensively the demands a rigorous simulation may impose on a modelling approach and thereby the needs for improvement in the model formulation.

This Chapter is mainly concerned about the performance of concrete material models when applied in the simulation of reinforced concrete (RC) structures under blast loading. Two representative concrete models, namely Karagozian & Case concrete damage model (also known as KCC model) and Continuous

Surface Concrete Model (known as CSC model), both available in LS-DYNA, are employed and examined. The overall structural response in such a loading scenario is understood to be primarily monotonic, and consequently the performance of these material models are expected not to differ significantly from what have been observed in other reported simulation studies. However, it has been discovered, rather surprisingly, that the KCC model could not maintain a satisfactory result especially in the later stage of the response, whereas the CSC model exhibits reasonable performance throughout the entire response.

Securitisation of the detailed response in relation to the basic behaviour of the material model behaviour suggests that the root cause of the problem tends to originate from the faster descending of the material model behaviour towards an effectively zero strength state following a tension/shear dominated damage process, and the consequent diminish of the interaction capacity between the steel rebar and the surrounding concrete. In contrast, the CSC model retains a certain level of residual capacity which enables a minimum connection between the rebar and the surrounding concrete at the severely cracked but not entirely fragmented state. In a broader sense, necessary rectification would need to be considered when it comes to using the KCC type model in simulating the response of RC structure concerning both local and global responses, which will be further discussed in Chapter 4.

3.2 Overview and general discussion on the KCC and CSC models

The concrete material models used in hydrocode simulation of the dynamic response under high rate loadings generally need to accommodate a wide range of pressure, stress states, strain rate, and levels of damage. Most of such material models are formulated in a similar damage plasticity framework. The KCC and

CSC models employed in the present study, available in LS-DYNA, are well documented in previous publications (Crawford et al. 2012; Magallanes et al. 2010; Malvar et al. 2000; Schwer and Malvar 2005) and have been subjected to extensive scrutiny and validation studies (Magallanes 2008; ARUP 2009; Tu and Lu 2009, 2010; Crawford et al. 2012; Wu et al. 2012). For the purpose of present discussion, an overview and discussion of some of the key features that relate closely to the behaviour in a typical reinforced concrete simulation environment is provided.

3.2.1 Strength surfaces and damage definition in KCC model

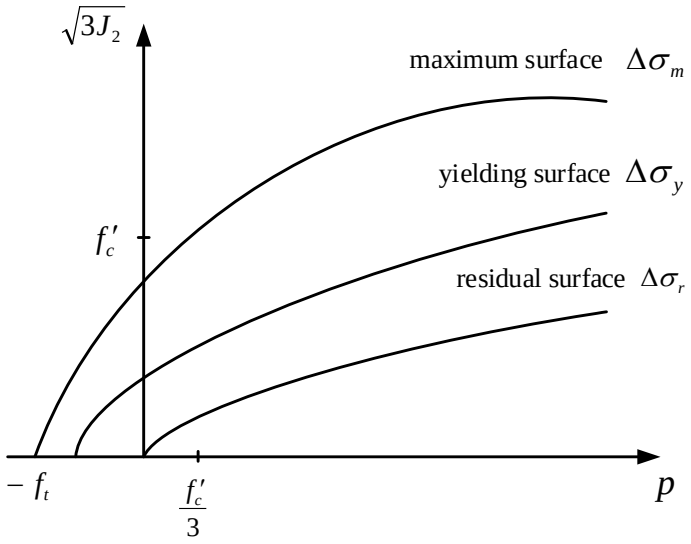

Fig. 3.1 Failure surfaces defined in KCC model

In KCC concrete model, three independent strength surfaces are defined for yield, maximum and residual strength, respectively, as shown in Fig. 3.1. All these strength surfaces are pressure sensitive, and a complete definition requires eight material parameters which are determined from standard material tests (Crawford et al. 2012). At any state of damage, the prevailing strength surface is defined as a linear interpolation between the maximum and either the yielding or residual failure surfaces, depending on the cumulative damage level:

$$\Delta\sigma(=\sqrt{3J_2}) = \begin{cases} \eta\Delta\sigma_m + (1-\eta)\Delta\sigma_y & for \quad \lambda < \lambda_m \\ \eta\Delta\sigma_m + (1-\eta)\Delta\sigma_r & for \quad \lambda \geq \lambda_m \end{cases} \tag{3.1}$$

where $\Delta\sigma_m$, $\Delta\sigma_y$ and $\Delta\sigma_r$ represent the maximum, yielding and residual surfaces respectively, and are defined by a set of eight parameters:

$$\begin{cases} \Delta\sigma_m = a_{0m} + \dfrac{p}{a_{1m} + a_{2m}p} & maximum \quad surface \\ \Delta\sigma_y = a_{0y} + \dfrac{p}{a_{1y} + a_{2y}p} & yielding \quad surface \\ \Delta\sigma_r = \dfrac{p}{a_{1r} + a_{2r}p} & residual \quad surface \end{cases} \tag{3.1a}$$

The interpolation factor η is a function of the modified effective plastic strain measure λ, as shown in Fig. 3.2, and it varies from 0 (before yielding) to 1 (when λ equals to λ_m) to allow the strength surface to move between yielding to the maximum strength surface, then from 1 to zero to allow softening to develop between the maximum and residual surfaces.

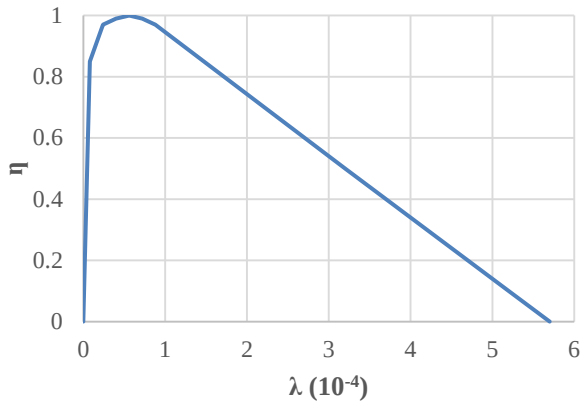

Fig. 3.2 Default η-λ curve defined in KCC model

The modified effective plastic strain λ is defined as

$$\lambda = \begin{cases} \int_0^{\overline{\varepsilon^p}} \dfrac{d\overline{\varepsilon^p}}{r_f(1+p/r_f f_t)^{b_1}} & for \quad p \geq 0 \\ \int_0^{\overline{\varepsilon^p}} \dfrac{d\overline{\varepsilon^p}}{r_f(1+p/r_f f_t)^{b_2}} & for \quad p < 0 \end{cases} \tag{3.2}$$

where the effective plastic strain increment is given by

$$\overline{\varepsilon^p} = \sqrt{(2/3)\varepsilon_{ij}^p \varepsilon_{ij}^p} \tag{3.3}$$

f_t, r_f and ε_{ij}^p are the tensile strength, rate scaling factor and total plastic strain component, respectively. b_1 and b_2 are exponential weighting factors to control different rate of accumulation of incremental plastic strain in the hydrostatic compression ($p \geq 0$) and tension regime ($p < 0$), and in this way the softening phase develops in distinctive manners under compression and tension, respectively, while the same η-λ curve is employed.

For an illustrative purpose, let the rate scaling factor be unity (no strain rate effect) and the multiplier of the incremental plastic strain in Eq. 3.2 may be written as:

$$d\lambda = \begin{cases} (\beta_1) d\overline{\varepsilon^p} & for \quad p \geq 0 \\ (\beta_2) d\overline{\varepsilon^p} & for \quad p < 0 \end{cases} \tag{3.4}$$

where $\beta_1 = \dfrac{1}{(1+p/f_t)^{b_1}}$, $\beta_2 = \dfrac{1}{(1+p/f_t)^{b_2}}$.

With KCC default values of b_1=1.6 and b_2=1.35, the variation of β_1 and β_2 with pressure are plotted in Fig. 3.3. It can be seen that with the default b_1 and b_2 values, the rate of damage accumulation is greatly accelerated in negative (tension) pressure regime and decelerated in positive (compression) pressure regime and a smooth transition is enabled at zero pressure point.

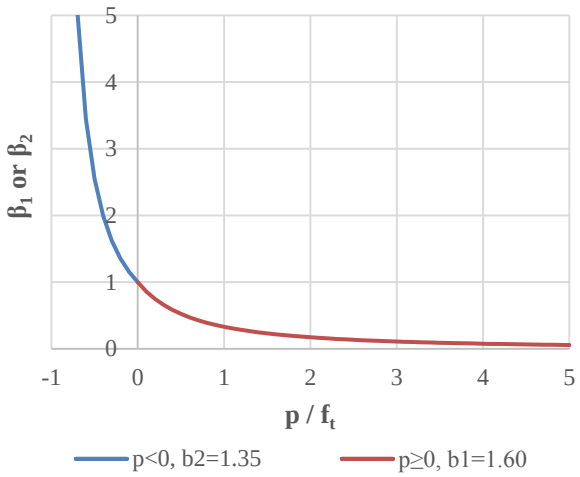

Fig. 3.3 Incremental plastic strain multiplier vs. hydrostatic pressure

It is also noted that the actual values of b_1 and b_2 themselves control the rate of accumulation of the incremental plastic strain into the total λ, thus different shapes (slopes) of the softening branch may be realised by adjusting the b_1 (for compression) and b_2 (for tension) values.

In the KCC model, the damage level is directly related to the modified effective plastic strain. For post-processing, a nominal damage scalar called *SDF* (scaled damage factor) is further introduced and it is defined as follows:

$$SDF = \frac{2\lambda}{\lambda + \lambda_m} \tag{3.5}$$

As λ is a positive non-decreasing variable, *SDF* varies from 0 to 2. In the pre-peak phase $0<SDF<1$, and when concrete enters softening phase, $1<SDF<2$. *SDF* eventually approaches 2 as λ increases to infinity, which ultimately represents a total damage state. A more detailed look into the variation of *SDF* with the accumulation of damage will be given later in comparison with the damage index adopted in the CSC model.

3.2.2 Strength surfaces and damage definition in CSC model

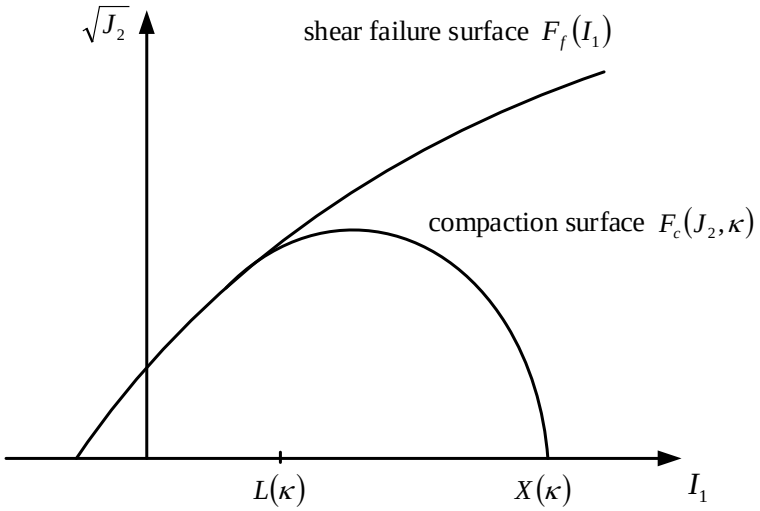

Fig. 3.4 Failure surfaces defined in CSC model

In CSC model the failure surface is defined as a smooth intersection between a shear failure surface $F_f(I_1)$ and a hardening cap $F_c(J_2,\kappa)$, in the low to high confining pressure regimes, as shown in Fig. 3.4. The overall failure surface is expressed in Eq. 3.6.

$$f(I_1,J_2,J_3,\kappa)=J_2-\Re^2F_fF_c \tag{3.6}$$

where F_f is the shear failure surface, F_c is the hardening cap of compaction, and $\Re$ is a Rubin factor. Multiplying the cap function F_c and shear failure function F_f allows the cap and shear surfaces to take on the same slope at their intersection. The shear surface is defined along the compression meridian:

$$\sqrt{J_2}=F_f(I_1)=\alpha-\lambda\exp^{-\beta I_1}+\theta I_1 \tag{3.7}$$

where parameters α , β , λ and θ are calibrated from material tests of plain concrete (Murray 2007).

The compaction cap surface is expressed in an ellipse shape to model plastic volume change related to compaction due to pore collapse, and the function is defined as

$$\sqrt{J_2} = F_c(I_1, \kappa) = \begin{cases} 1 - \left(\dfrac{I_1 - \kappa}{X - \kappa} \right)^2 & I_1 > \kappa \\ 1 & otherwise \end{cases} \tag{3.8}$$

where κ is the intersection of the shear surface and the cap, and $X(\kappa)$ is the intersection of the cap with I_1 axis. The cap moves to model the plastic volumetric change. It expands for volume compaction, as $X(\kappa)$ and κ increases, and contacts to simulate the dilation based on a hardening rule. Without cap motion, the pressure-volumetric relation would be perfectly plastic.

With failure surfaces defined above, the model uses a scalar damage index d to transform the undamaged stress tensor into damaged one:

$$\sigma_{ij}^{damaged} = (1 - d)\sigma_{ij}^{damaged} \tag{3.9}$$

Damage index d ranges from 0 for no damage to 1 for complete failure, and is defined in accordance with two strain-based energy terms, namely, brittle and ductile damage index d_b and d_d for tensile and compressive stress state respectively,

$$d = \begin{cases} \max(d_b, d_d) & p < 0 \\ d_d & p > 0 \end{cases} \tag{3.10}$$

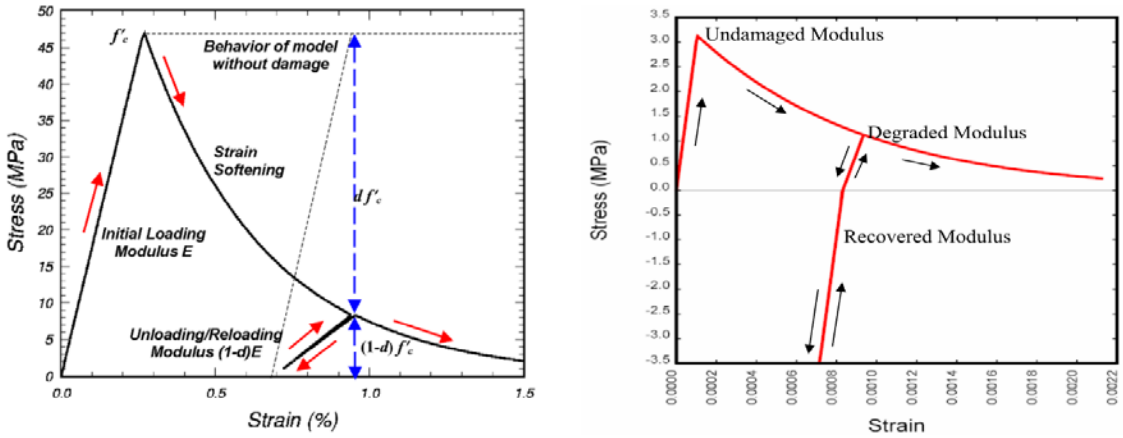

Fig. 3.5 Strain softening and stiffness reduction due to damage accumulation in CSC model (after Murray 2007)

To simulate the crack opening and closure, the brittle damage index drops to zero whenever the hydrostatic pressure enters compression, such that the residual compressive strength and stiffness is recovered as crack closes. Once the pressure switches from compressive to tensile again, the previous maximum value of the brittle damage index is reactivated. The softening function of d_b and d_d are defined as a function of the damage threshold τ, which is a term used to describe the current strain and energy accumulation,

$$d_b = \frac{1}{D}\left[\frac{1+D}{1+D\exp^{-C\tau_b}} - 1\right]$$
$$d_d = \frac{d_{\max}}{D}\left[\frac{1+B}{1+B\exp^{-A\tau_d}} - 1\right] \tag{3.11}$$

Parameter A, B, C and D control the shape of the softening function. The brittle damage threshold τ_b is defined by the maximum principal strain, whereas the ductile damage threshold τ_d depends on the total strain components, as follows:

$$\tau_b = \sqrt{E\varepsilon_{\max}^2}$$
$$\tau_d = \sqrt{\frac{1}{2}\sigma_{ij}\varepsilon_{ij}} \tag{3.12}$$

3.2.3 Consideration of fracture energy and mesh convergence

The general considerations of crack softening in both KCC and CSC models stem from the crack band theory (Bažant and Oh 1983). To enable a mesh-objective solution and general mesh convergence, both KCC and CSC models essentially incorporate a length factor, albeit in a different manner, which relates the strain energy over a characteristic "band width", L_c, in the softening phase of the material response to target fracture energy, G_f, which is considered as a material property (CEB-FEP 1990). In a general form, this requirement transpires to satisfying the condition expressed in Eq. 3.13:

$$\int_{\varepsilon_m}^{+\infty} \sigma d\varepsilon = \frac{G_f}{L_c} \tag{3.13a}$$

$$\text{or} \qquad \int_{\varepsilon_m}^{+\infty} \sigma (L_c d\varepsilon) = \int_{\delta_m}^{+\infty} \sigma d\delta = G_f \tag{3.13b}$$

In CSC model, L_c is simply tied to the characteristic element size L_e (cubic root of the element volume), implying that the softening (crack) is always localised within a single layer of elements. On the other hand, KCC model provides a possibility of dealing with softening to spread (in the band width direction) over multiple elements, and this is achieved by introducing a user specified localisation width L_w. When the element size L_e is larger than L_w, the standard treatment prevails such that the characteristic length L_c in Eq. 3.13a is made equal to the element size L_e. In case the element size is smaller than L_w, the stress-strain relation is then adjusted based on the assumption that the facture energy is dissipated within the localisation width L_w rather than a single element length L_e. In short, the handling of the softening and consideration of the strain energy through a characteristic band width in KCC and CSC may be summarised in Eq. 3.14.

$$L_c = \begin{cases} L_e & for \quad CSC \\ \max(L_e, L_w) & for \quad KCC \end{cases} \tag{3.14}$$

To better demonstrate the treatment on mesh objectivity in the KCC and CSC models, single-element numerical tests are conducted to demonstrate the concrete response under uniaxial tension and compression. Single cubic elements with lengths varying from 100 mm to 12.5 mm, and a compressive strength of 30 MPa are chosen.

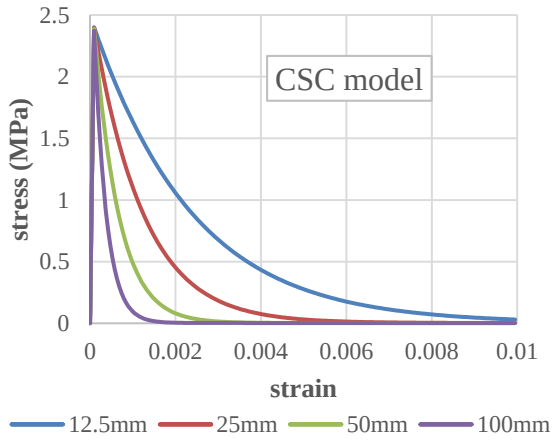

a) Stress-strain curve (CSC model)

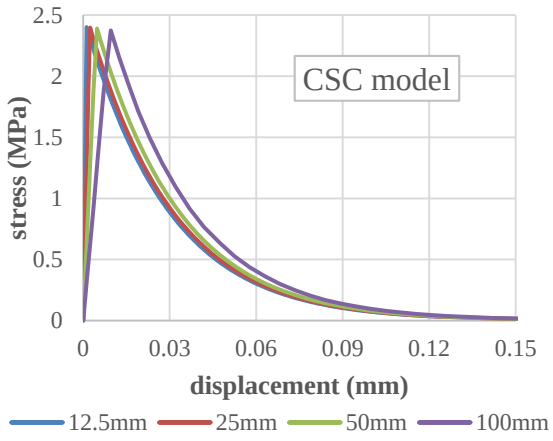

b) Stress- displacement curve (CSC model)

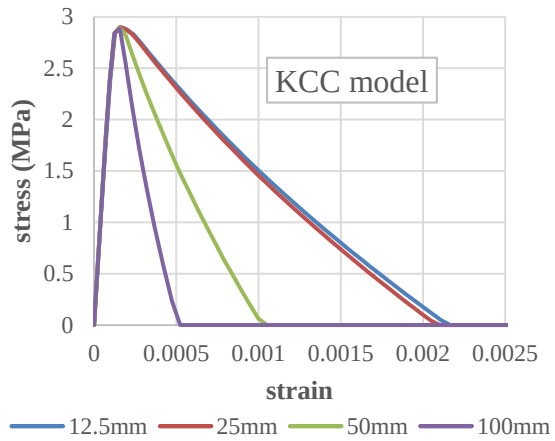

c) Stress-strain curve (KCC model)

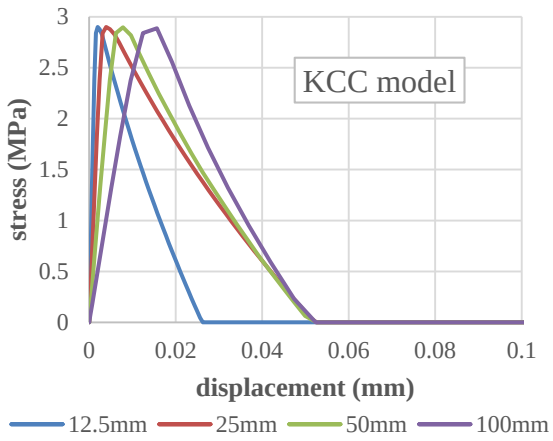

d) Stress-displacement curve (KCC model)

Fig. 3.6 Tensile response of singe element with varied element sizes

Stress-strain and stress-displacement curves under uniaxial tension are shown in Fig. 3.6. It can be seen that in the softening regime, the strain decreases with increasing element size, while the overall displacement is independent of element size for CSC model. As for KCC model, constant displacement is found when element size is larger than the pre-defined localisation width L_w of 25 mm. In the case of 12.5 mm, the assumption is to achieve a same displacement over the localisation width, which consists of two 12.5mm-wide elements, and the actual displacement in one single element is halved. This treatment has also been applied in the compressive softening regime, as shown by responses of single element under uniaxial compression in Fig. 3.7.

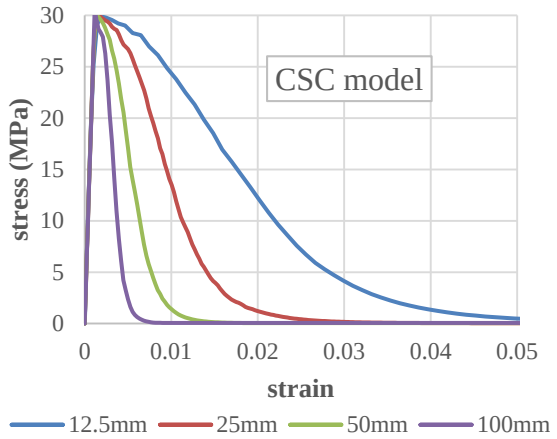

a) Stress-strain curve (CSC model)

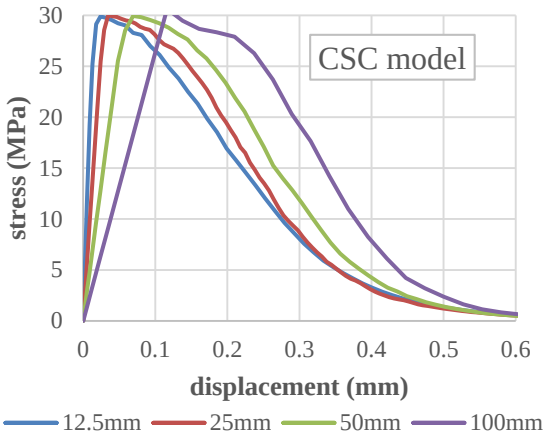

b) Stress-displacement curve (CSC model)

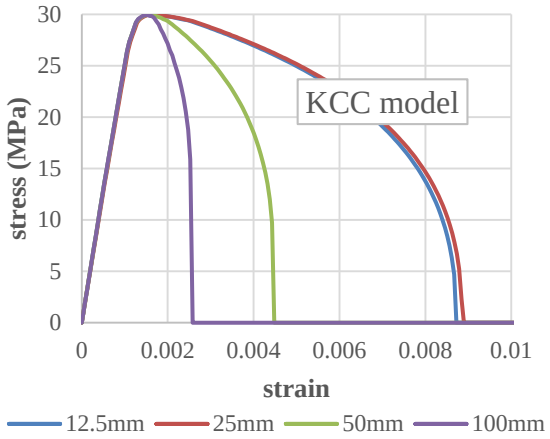

c) Stress-strain curve (KCC model)

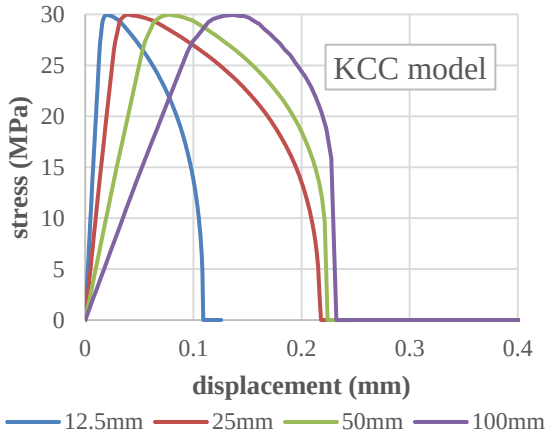

d) Stress-displacement curve (KCC model)

Fig. 3.7 Compressive response of singe element with varied element sizes

For FE analysis in relatively simple tension-dominated loading conditions, localisation will inevitably occur along a single row of elements perpendicular to the primary tension direction. In such situations it is obvious that the localisation width should be tied to the element size, which means L_w in KCC model should be given a value equal to the characteristic element size L_e.

However, when the stress state becomes complicated in a damage zone, the localisation width could spread across more than one element in the FE model, particularly in the case of a refined mesh, and consequently the setting of L_w would become a complicated issue and an appropriate choice could be case-dependent. Further discussion along this line is beyond the scope of this study. In the present analysis, the standard option that the target fracture energy is realised over a single element width is adopted.

3.2.4 Further discussion on interpretation of the damage indices

In view of the different ways that the damage scalars are defined in the KCC and CSC models (similarly in other damage plasticity models), single-element numerical tests are further conducted to demonstrate the concrete response and the computed values of damage under uniaxial tension and compression. A single cubic element with a length of 25mm and compressive strength of 30 MPa is chosen.

The uniaxial tension and compression stress-strain curves produced from the KCC and CSC models, respectively, are shown in Fig. 3.8 along with the indication of the damage scalar values. Note that the absolute strain values in a single element test is element-size dependent, so the strain values need to be read with the element size in mind. On the other hand, the total deformation of the element, which in the tension case would represent the “crack width”, would

be independent of the element size. The scale of deformation values are also indicated on the top axis in Fig. 3.8.

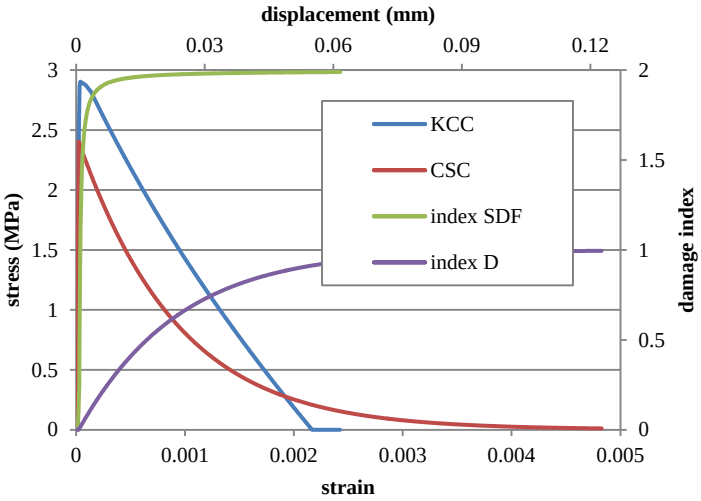

a) Uniaxial tension response

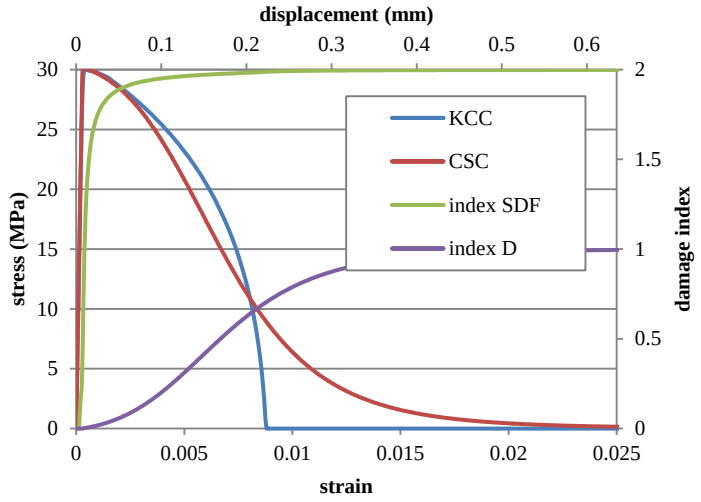

b) Uniaxial compression response

Fig. 3.8 Uniaxial stress-strain curves and damage indices produced by the two models

From Fig. 3.8 it can be seen that slight difference in the tensile strength exists between the two models for the same target compressive strength. More remarkably, however, the shapes of the softening curves are different in characteristics. Taking the tensile curves for example, while both KCC and CSC

curves tend to cover a similar area (thus indicating similar fracture energy), the KCC model has a terminate strength cut-off at a strain level of about 2.3×10^{-3}, or a “crack width” level of about 0.06 mm, beyond which the material would have zero strength. On the contrary, the CSC model has a more gradual descending phase. The patterns of the curves in compression are similar to the respective tensile curves. Further discussion about the potential effect of the KCC model having a strength termination point will be given later.

With regard to the damage scalars, aside from the fact that the SDF factor in KCC has a scale range of 0～2 while the damage index in CSC has a range of 0～1, which may be unified easily if needed, the SDF factor tends to exhibit a narrow effective range as it is already greater than 1.5 before reaching the maximum strength. In comparison, the damage index in CSC model tends to exhibit a more gradual increase while the material softening accumulates. The D index appears to closely relate to the (descending) stress state and the absolute strain, which seems to be physically more meaningful.

Fig. 3.9 further illustrates the relationship between the SDF and D indices. Form the whole range perspective, the two indices do not appear to get along with each other. But upon a loser look, they are reasonably correlated in the medium to severe damage states. In the D index case, this marks a range of 0.3 to 1.0, but the corresponding SDF is in a very narrow range of 1.97～2.0. This effective range of the SDF values for severe material damage needs be particularly noted when it comes to interpreting the severe damage or crack patterns with the SDF factor.

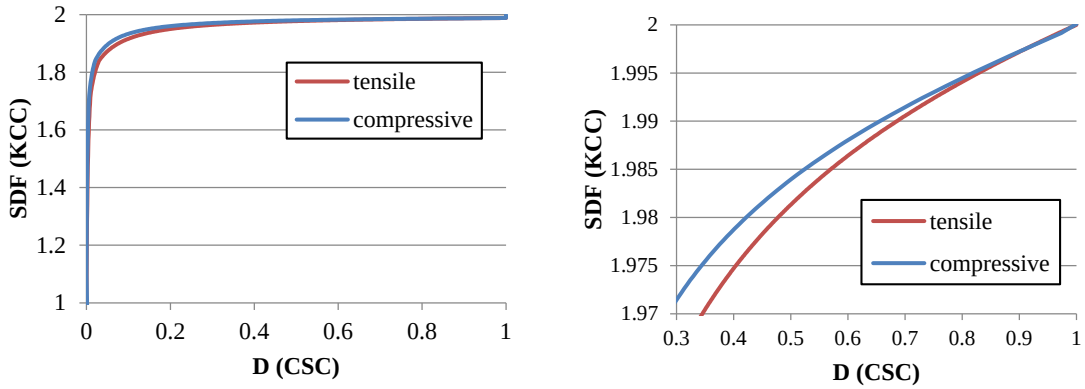

Fig. 3.9 Relationship between SDF in KCC and D in CSC model

3.3 Numerical simulations with the two concrete models and comparison with experimental results

A full scale investigation into the performance of hydrocode concrete material models in a reinforced concrete structure analysis was partially motivated from the experiences attempting to numerically simulate the benchmark experiment available from a blind blast contest (Thiagarajan 2013; Thiagarajan et al. 2011, 2014). The overall structural response in such a loading scenario was primarily of a monotonic process, and consequently the performance of these material models was expected not to differ significantly. However, the modelling turned out to suggest, rather surprisingly, that the KCC model could not produce a sensible result especially in the later stage of the response, whereas the CSC model exhibits reasonable performance throughout the entire response.

The numerical investigation is then extended to the simulation of a quasi-static RC beam test to further examine the material model performance without the involvement of the dynamic effects.

3.3.1 Simulation of RC slab response to blast load

The simulation being discussed here is concerned with the normal strength RC slab tested by Thiagarajan (2013). The RC slab, along with other specimens, was originally tested at the University of Missouri Kansas City (UMKC) using a blast loading simulator, which is capable of simulating a uniform pressure pulse on the loading face. The slab was supported against two strong steel box beams on the rear side of the slab at the two ends of the main (longitudinal) direction, and the response of the slab was measured by accelerometers and a laser measurement device attached to the rear face of the slab, as shown in Fig. 3.10.

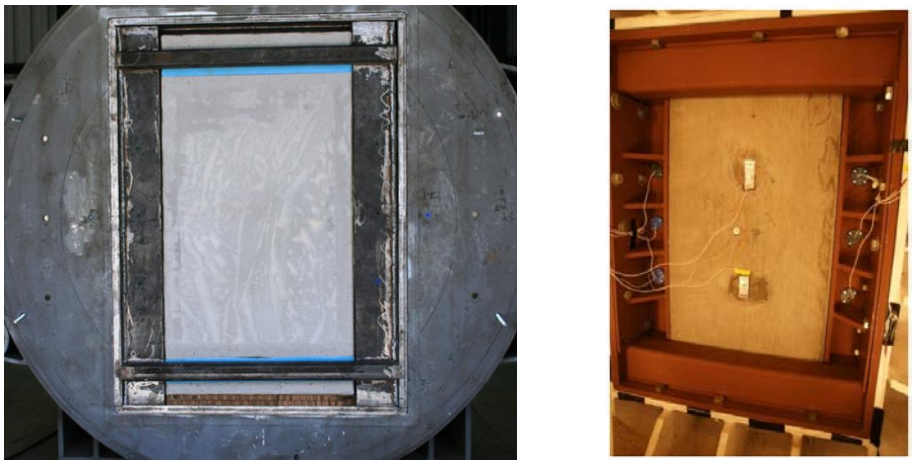

Fig. 3.10 Outside and inside view of the slab from the pressure tube (Thiagarajan 2013)

The support arrangement (Fig. 3.11b) effectively made the RC slab as a one-way slab, with a net span of 1320 mm and a thickness of 101.6 mm. The longitudinal reinforcement consisted of 9 #3 steel bars of diameter 9.525 mm, and nominal transverse reinforcement consisted of 5 #3 steel bars. All the reinforcing bars were placed on the bottom side (opposite to the loading face) of the slab. The normal strength RC slab was cast using concrete with a compressive strength of 34.5 MPa. The reinforcing bars were of Grade 60.

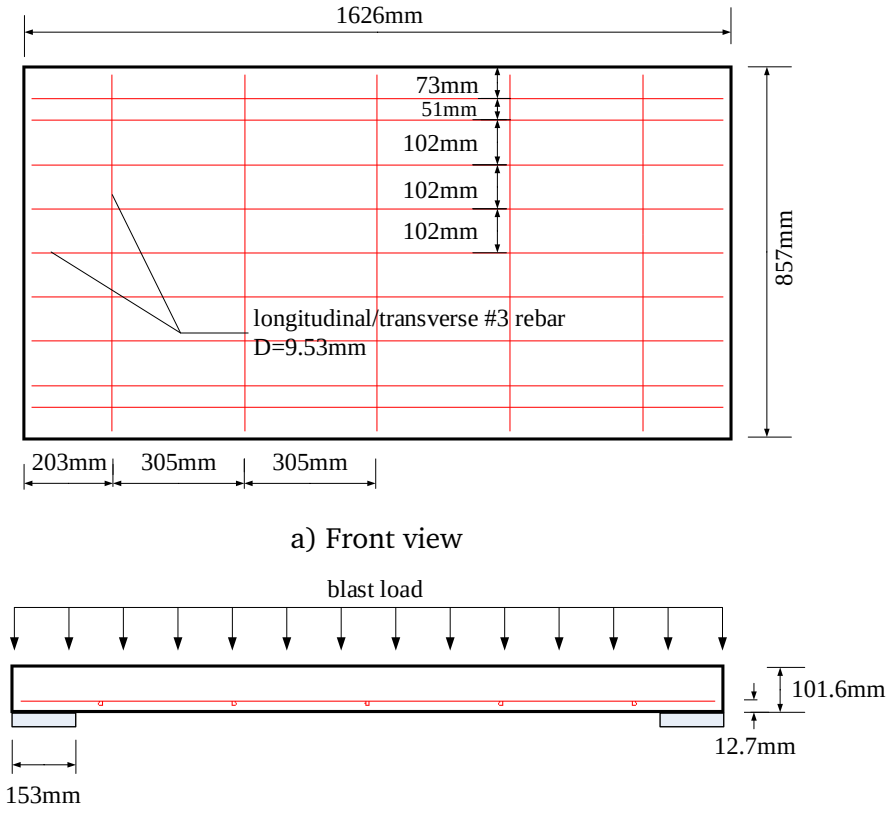

Fig. 3.11 Details of tested RC slab (after Thiagarajan 2013)

The numerical simulation is carried out using LS-DYNA. In the FE model for the slab, 8-node solid elements are used for concrete whilst 2-node beam elements are used for longitudinal and transverse reinforcements. The rebar elements are embedded in the solid elements such that they connect to the concrete elements with shared nodes, mimicking a perfect bond condition. To preserve the support condition, the profile of the support box beam was retained in the model and the RC slab is placed on the support beam via surface to surface contact. Considering the symmetry, only ¼ of the test RC slab needs to be modelled, as depicted in Fig. 3.12.

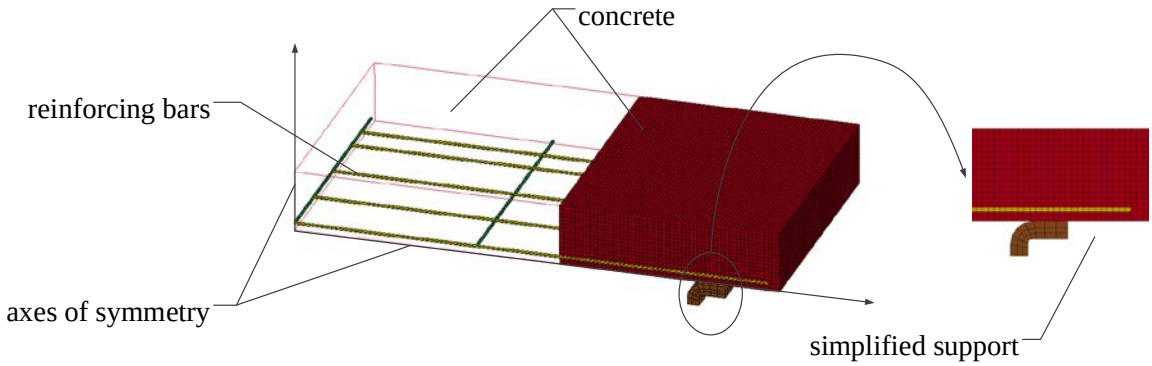

Fig. 3.12 Layout of the ¼ FE model for the slab and the end support beam

The concrete in the RC slab is modelled by KCC and CSC material models in two different FE models, respectively. In both models, the automatic generation of material model parameters is adopted by specifying only the unconfined compressive strength, which is 34.5 MPa based on the experimental data. A mesh convergence study was conducted and according the results a nominal mesh grid size of 6.35 mm was adopted in both FE models for the detailed simulations. This offers a resolution of 16 solid elements along the slab thickness, with a total of about 140,000 elements. Correspondingly, a localisation width (L_w) of 6.35 mm (equal the average element size) is employed in the KCC model.

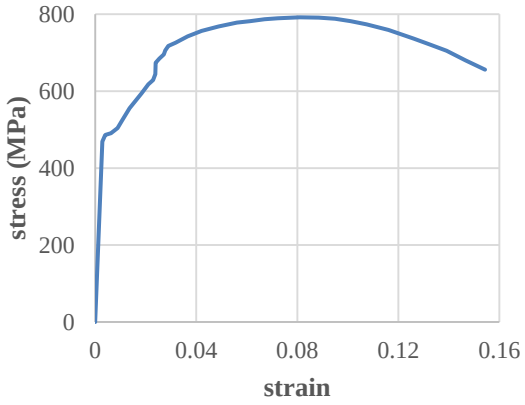

Fig. 3.13 Stress-strain curve of rebar

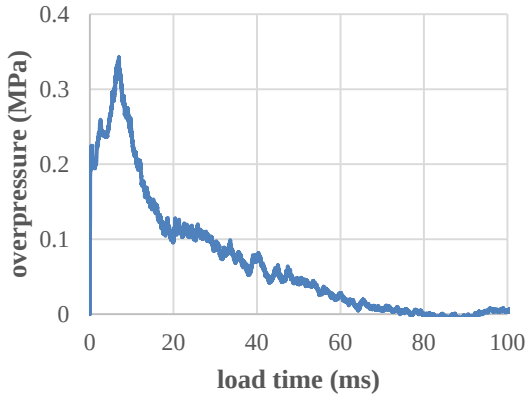

Fig. 3.14 Time history of applied pressure

In the FE model, the rebar elements are modelled by the material model *MAT_PIECEWISE_LINEAR_PLASTICITY, which allows a piece-wise definition of the stress-strain relationship to match closely the actual post peak stage of the test result as presented in Fig. 3.13. Blast load is simulated by uniformly distributed pressure pulse onto the loading face of the RC slab, using the pressure history recorded from the actual experiment, as presented in Fig. 3.14.

Fig. 3.15 shows the time histories of the central deflections and reaction forces in the ¼ models using KCC and CSC model, respectively. The experimental blast force is calculated based on the pressure pulse applied onto the one-quarter model of the slab.

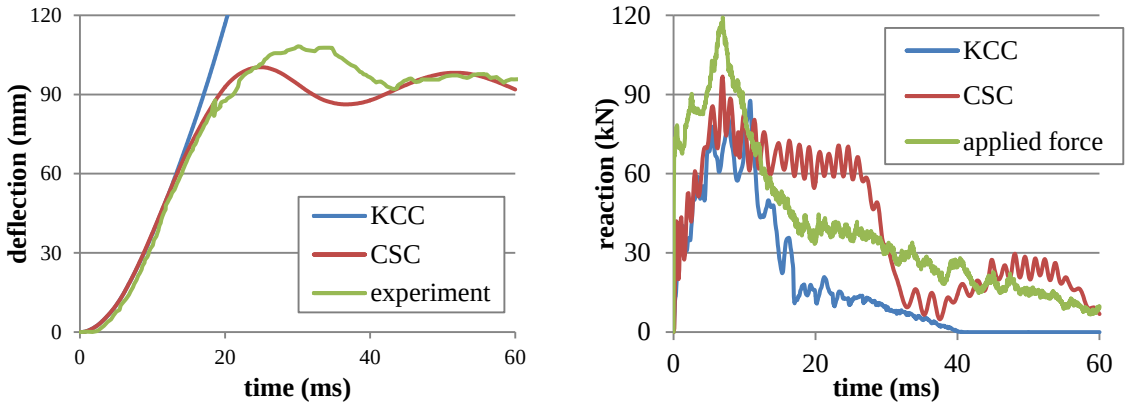

Fig. 3.15 Time history of central deflection and reaction

As can be seen from Fig. 3.15, the deflection predicted by the CSC model agree well with the experimental results, and it exhibits an increasing phase until about 100 mm (7.6 % of the span), followed by a stable oscillation around a permanent plastic deformation, as observed from the actual experiment. In contrast, the deflection time history from the KCC model shows an unstable (diverging) response following the initial increase of the deflection. It is noteworthy that the slab appears to have failed globally in the KCC model at about 13ms when a central deflection reaches only about 60 mm (4.5% of the

net span), which is well below the peak deflection experienced in the experiment.

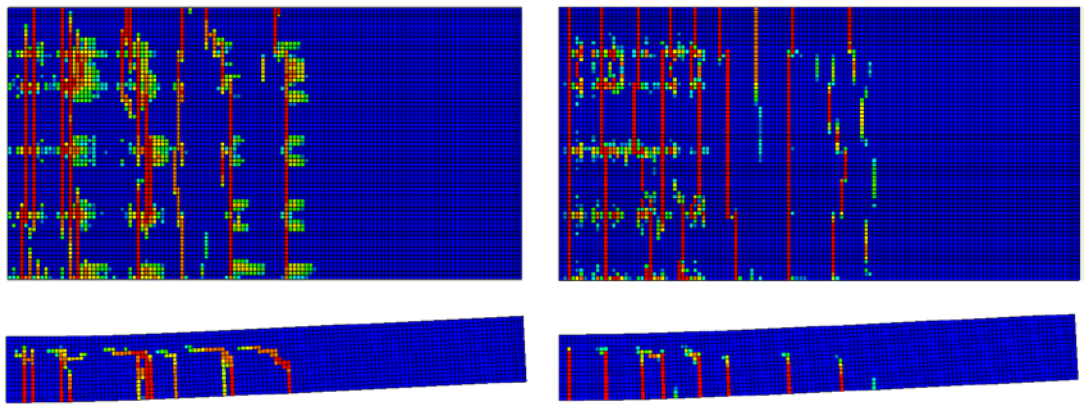

a) KCC model (t=8ms) b) CSC model (t=8ms)

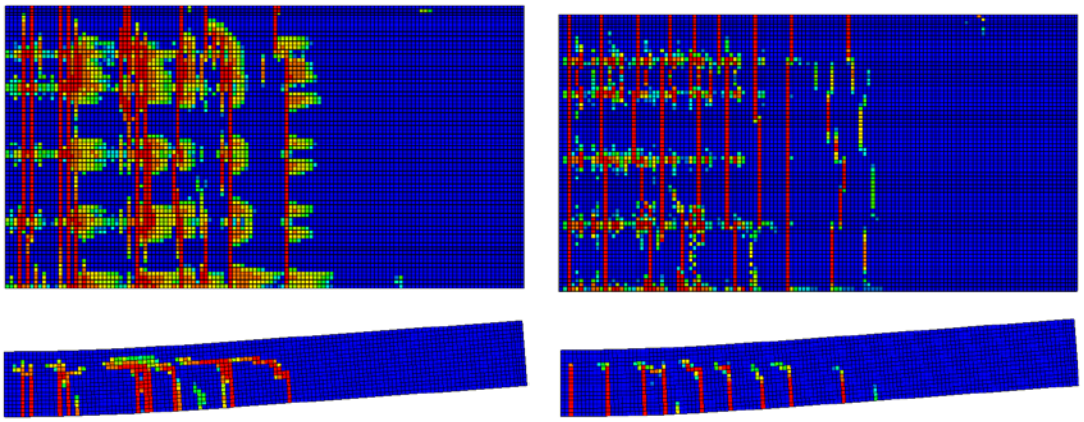

c) KCC model (t=10ms) d) CSC model (t=10ms)

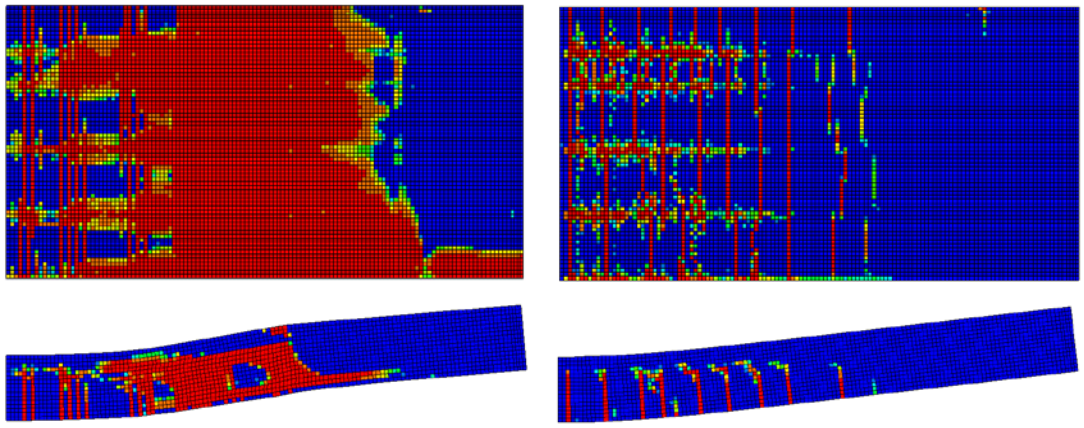

e) KCC model (t=14ms) f) CSC model (t=14ms)

Fig. 3.16 Damage distribution in the slab surface and over cross-section (KCC: 1.97~2.00; CSC: 0.3~1.0)

Fig. 3.16 shows the damage patterns along the rebar and over the slab depth at selected time instants as obtained using the KCC (left) and CSC model (right). The final crack patterns of the experimental RC slab, as reported in Thiagarajan (2013) and Thiagarajan et al. (2014), are reproduced in Fig. 3.17 for a comparison. Note that in order to make the damage comparable, the scale of the SDF in KCC model is narrowed to a range of 1.97∼2.00 against a range of 0.3∼1.0 in CSC model in accordance with the calibration results shown earlier.

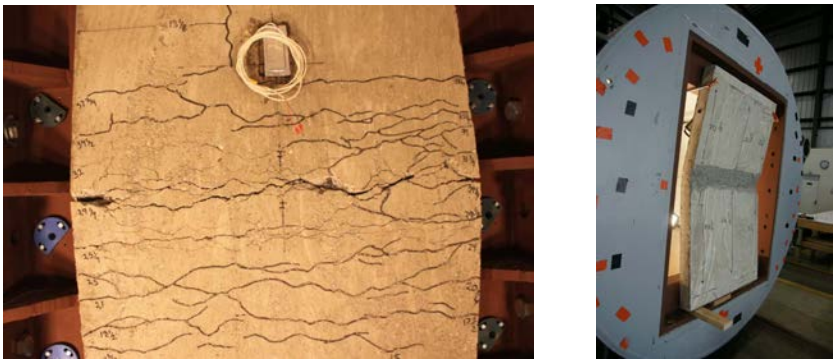

Fig. 3.17 Experimental crack distribution after blast (courtesy of Thiagarajan 2013)

It can be observed from both KCC and CSC models that at the initial stage, damage develops as bending cracks, starting from the mid-span region and then propagating towards the support. However, upon reaching the peak resistance at around 10ms, the model with KCC concrete exhibits a rapid spread of damage in concrete surrounding the longitudinal reinforcing bars and in the high shear region. The spread of failure in concrete in the KCC model appears to eventually result in the longitudinal rebar detaching from the surrounding concrete alongside loss of shear capacity over the depth of the slab at about 14ms, leading to a complete loss of the global resistance of the slab.

In contrast, the damage in the model with CSC tends to stabilise with a final crack pattern featured by distributed lateral cracks together with longitudinal cracks along the main reinforcing bars, which agree favourably with the experimental result.

Fig. 3.18 presents the evolution of the axial stress distribution in rebar at selected time instants. At the early stage of the response up to about 8ms, the axial stress in the rebar develops in a similar fashion in both KCC and CSC models, and is consistent with a flexure-controlled response under a distributed load. The shear-bond stress in the concrete elements to which the rebar elements are attached is correlated to the slope of the longitudinal distribution of the axial stress in the rebar. From Fig. 3.18 it can be observed that when the global response reaches a certain limit, herein at about 10ms, the stress in the rebar stops increasing in the KCC model, indicating that the shear and the rebar anchorage region (closer to the end support) starts failing, while displacement increases uncontrollably. Comparing to the KCC model, the axial stress in the CSC model exhibits a consistent but globally increasing pattern as the response develops to reach the peak deformation. There is no sign of extensive bond or shear failure in the concrete.

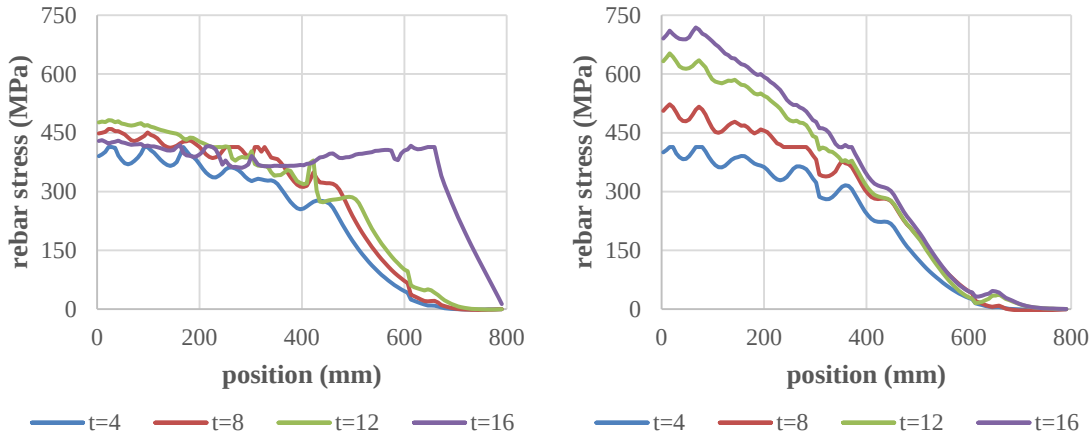

a) KCC model b) CSC model

Fig. 3.18 Development of axial stress distribution along longitudinal rebar

To further examine the process of the KCC concrete failure in shear (or “bond”) around the longitudinal rebar, a column of concrete elements immediately surrounding a longitudinal rebar is taken out from the slab to expose the path to failure in the interaction between steel rebar and adjacent concrete.

A check of the responses among the four concrete elements at the same cross-section has found that the two elements on the left and right of the rebar generally have a similar stress/strain level, so the mean values are taken between these two elements. On the other hand, elements above and below the rebar show slightly more different stress/strain states.

Fig. 3.19 shows the development and distribution of damage in these concrete elements along the length of the rebar, for the KCC and CSC models, respectively. The general development paths confirm the observations made in earlier based on the rebar stress, in that a total (shear) failure eventually develops in the concrete elements along the rebar length in the KCC model, resulting in the loss of rebar effect on the concrete slab response and the global failure of the slab. Such a problem does not occur in the CSC model.

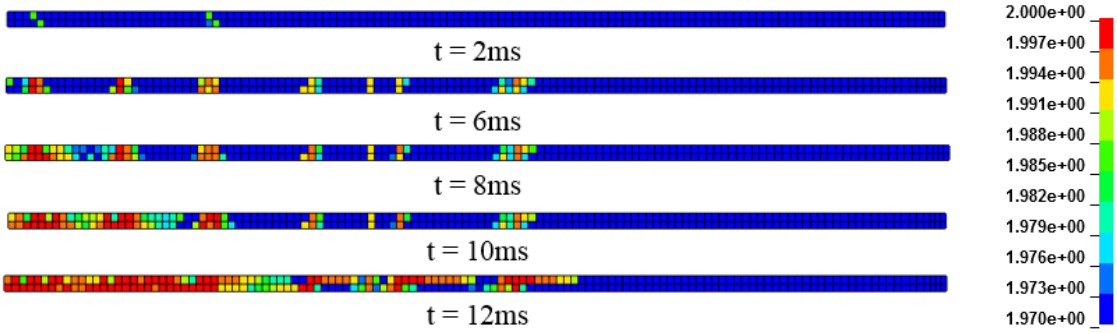

a) KCC model (fringe range: 1.97~2.00)

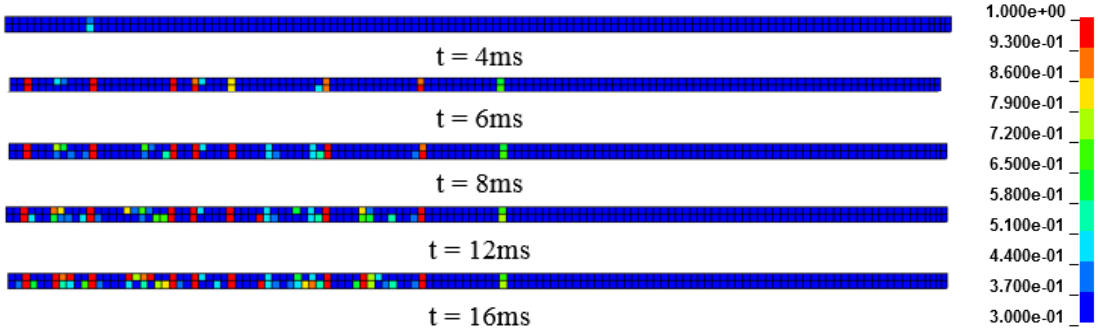

b) CSC model (fringe range: 0.3~1.0)

Fig. 3.19 Development and distribution of damage in concrete elements connected with rebar

In an attempt to explain what aspects in the KCC model have contributed in the abnormal simulation phenomenon, the shear and principal tensile strains in the concrete element connected to the rebar are extracted for different response levels. The results for the principal tensile strain are shown in Fig. 3.20. The limiting tensile strain at which the KCC model would completely lose its strength (thus becomes stress-less) for the size of the elements under a uniaxial tension condition is also shown on the plots for a benchmark purpose.

From the shear/principal strain development, it can be observed that in the early stage of the response up to about 8ms, both the magnitudes and distributions of the strains do not differ significantly between the two models. However, with further increase of the shear/principal strains, the magnitude of the strains at the peak locations reach and exceed the KCC total failure limit, rendering the respective concrete elements to be totally stress-free. This in turn accelerates the increase of the strains in the concrete elements in general as the global response increases, and at the same time the peak strain bands widen much more quickly as compared to the CSC model. Finally, almost the entire set of the concrete elements connected to the rebar exceeds the total failure strain limit and thus enters into a stress-less state, leading to the collapse of the slab.

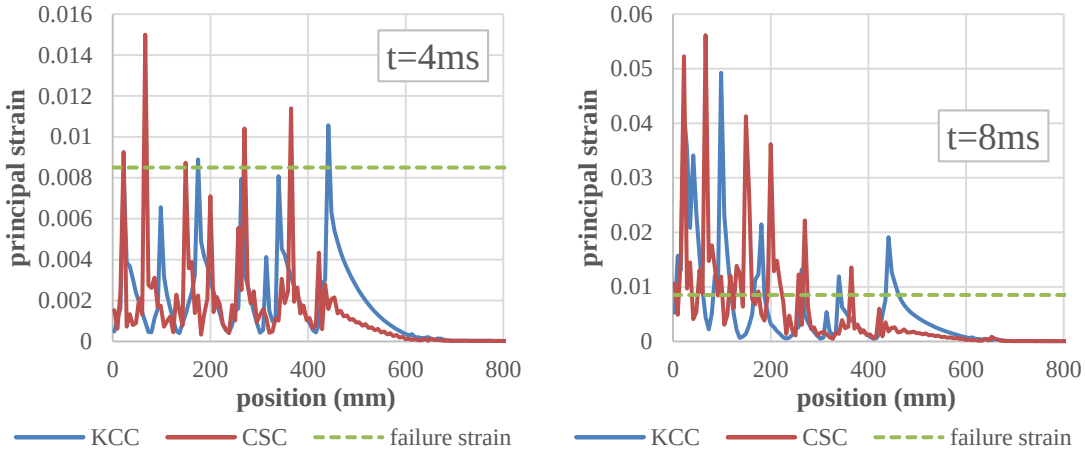

a) t = 4ms

b) t = 8ms

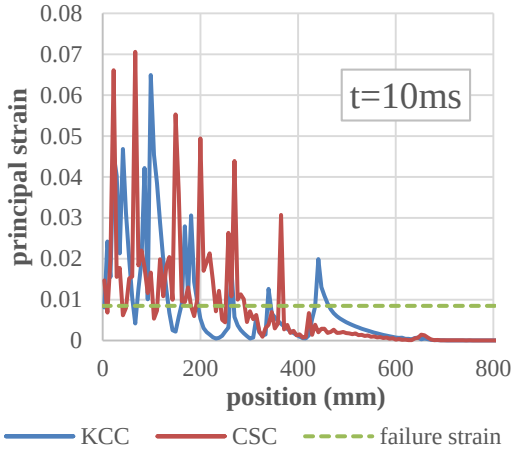

c) t = 10ms

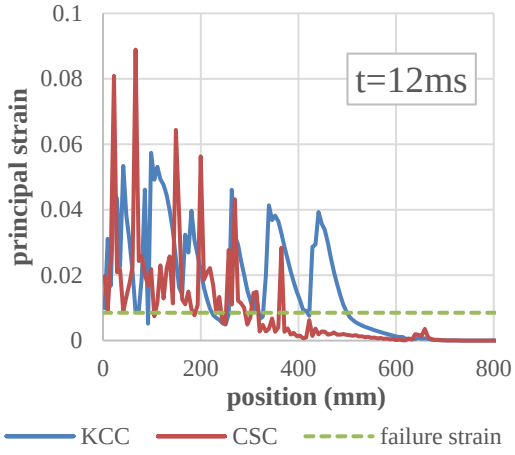

d) t = 12ms

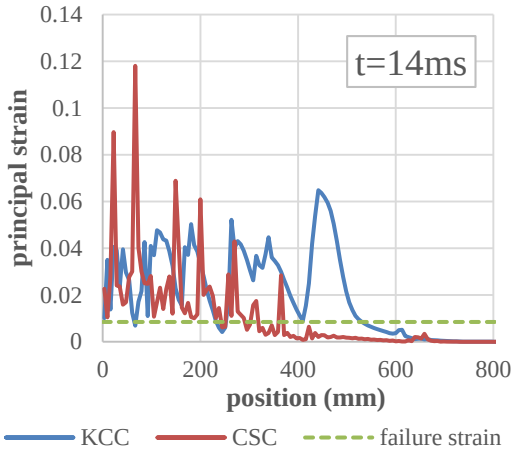

e) t = 14ms

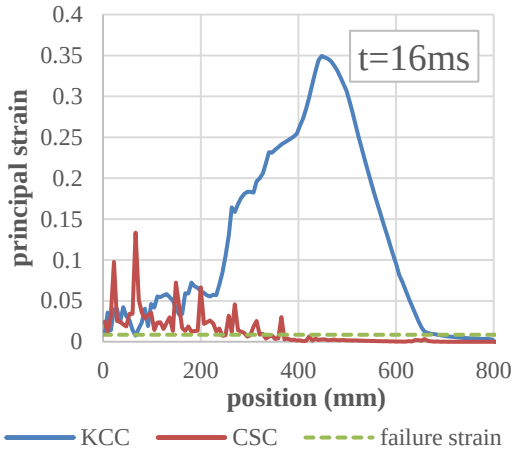

f) t = 16ms

Fig. 3.20 Principal (tensile) strain in concrete elements connected to rebar

3.3.2 Simulation of RC beam under quasi-static load

In recognition of the fact that the significant differences in the simulation results between the two models occur in the global deformation phase of the response, and in particular the KCC model appears to exhibit a premature global failure, it was considered necessary to carry out a simulation on a static RC beam to further examine the material behaviour in a global deformation mode of response, but without any complications from transient dynamic influences.

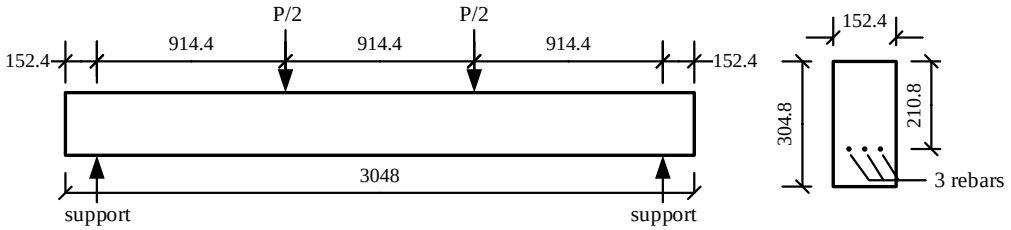

a) Dimensions of specimen (unit: mm, adapted from Janney et al. 1956)

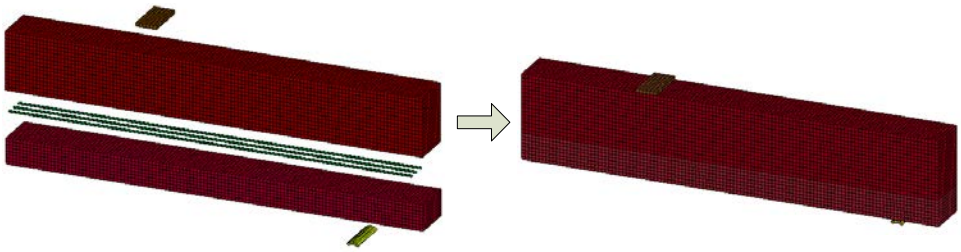

b) Geometric layout of numerical model

Fig. 3.21 Experimental RC beam and its FE model

As mentioned before, to fully expose the behaviour of the concrete material model in interacting with the main reinforcing bars, it is desirable that the RC specimen involves only a simple layer of main reinforcing bars, especially without stirrups which would otherwise dilute the problem of loss of cone rete/ rebar interaction. For this reason, the RC beam tests conducted by Janney et al. (1956) are selected. The particular test beam considered for the present simulation is shown in Fig. 3.21a. The beam had a net span of 2743 mm, it had

only longitudinal reinforcement without any stirrups. The longitudinal reinforcement consisted of 3 #5 steel bars giving rise to a reinforcement ratio of 1.87%. The beam was tested in a four point-load bending configuration. The length to thickness ratio was about 13, similar to the RC slab presented earlier. The concrete used in the test beam had a compressive strength of 36.2 MPa with tensile strength assumed to be 2.82 MPa, and the reinforcing bars had a yield strength of 333 MPa.

As reported in the experiment by Janney et al. (1956), the beam developed about five cracks in the region of pure flexure. After yielding occurred in the tension rebars, the flexural deformation developed in a ductile manner without much increase of the loading capacity. Finally the beam failed in a flexural mode without any apparent shear or bond problem.

Similar FE model set-up as used in the simulation of the RC slab is employed here, as depicted in Fig. 3.21b. The steel bars are modelled by beam elements while concrete is modelled by solid elements. Concrete model parameters are generated automatically for the 36.2 MPa class concrete. According to experimental observation no apparent hardening stage existed in the stress-strain relation of the steel bars thus the rebar is assumed to be elasto-plastic in the numerical model.

A mesh convergence study was conducted to identify an acceptable mesh size while maintaining a manageable computational time, which is generally much longer due to the test being quasi-static. Finally an average element length of 6.35 mm is chosen for the beam simulation using both the KCC and CSC models.

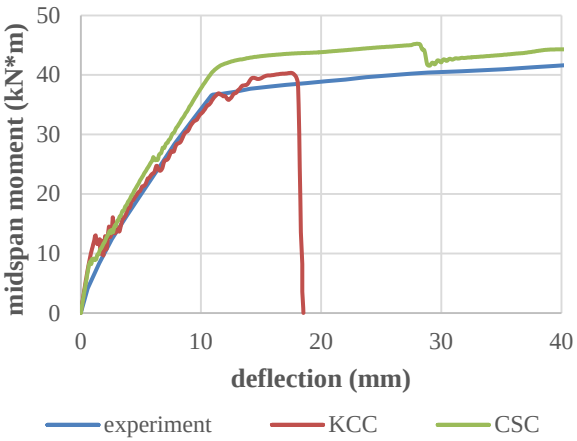

Fig. 3.22 Comparison of central deflection vs. mid-span moment curves

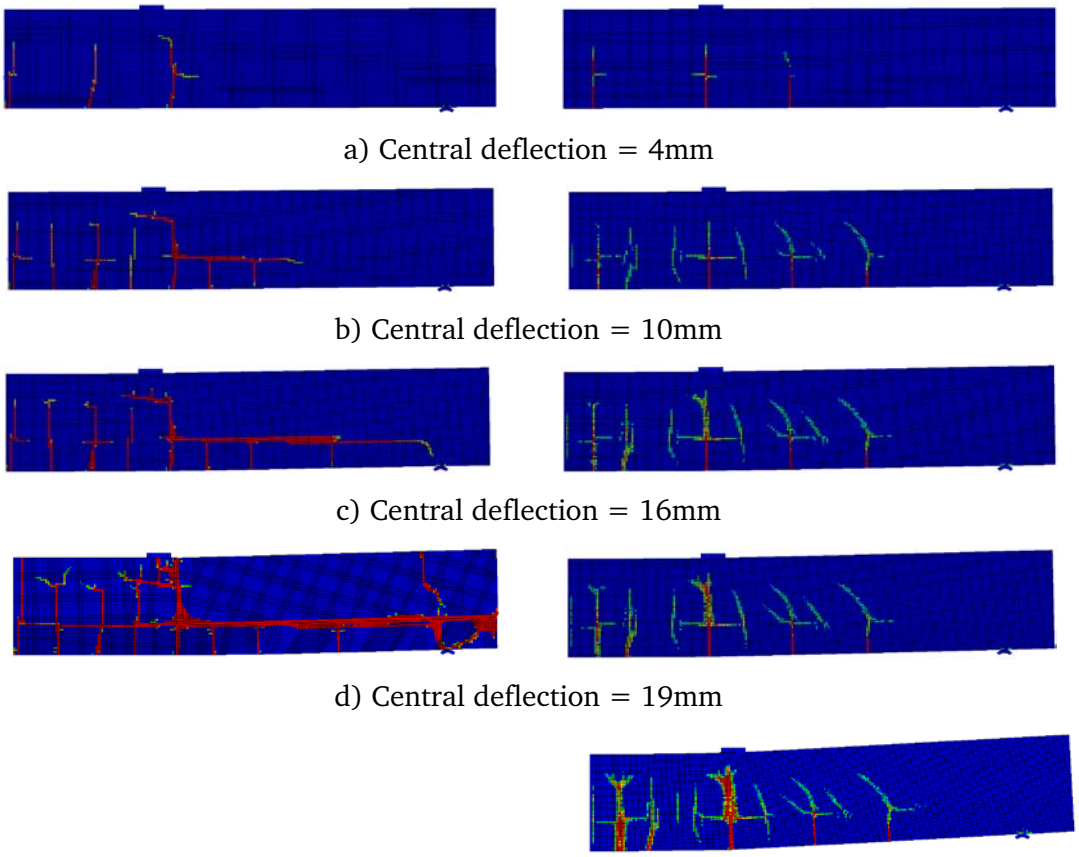

a) Central deflection = 4mm

b) Central deflection = 10mm

c) Central deflection = 16mm

d) Central deflection = 19mm

e) Central deflection = 50mm

Fig. 3.23 Damage pattern of RC beam under quasi-static load (KCC: 1.97~2.00; CSC: 0.3~1.0)

The predicted load (mid-span moment) vs. central deflection relationships using the two models are compared with the experimental result in Fig. 3.22. It can be clearly observed that the results generally repeat what have been observed in the RC slab blast simulation shown in Fig. 3.15. For the particular RC beam herein with no shear links or stirrups, the KCC model tends to fail prematurely with an abrupt loss of the global resistance at a deflection of 18 mm (or approximately 1/150 of the net span). On the other hand, the CSC model appears to match well the experimental curve with a slightly higher strength. It is noted that the experimental failure point was recorded at around 42 mm.

The development of the damage (crack) patterns at selected deflection levels are shown in Fig. 3.23. The failure pattern in the KCC model also suggests that the premature and abrupt failure in this model is attributable to the failure of concrete elements to which the rebar elements are attached in the high shear/anchorage region (between the point load and the support), essentially resulting in the loss of the reinforcement effect (analogous to the rebar being pulled out or sliding in the concrete). The CSC model also developed damage along the longitudinal rebar but the effect is not catastrophic and the overall behaviour matches well the experiment as mentioned earlier.

In a closer inspection at the failure process of rebar and concrete interaction, the evolution of axial stress distribution in rebar, together with the principle strain (tensile positive) in the concrete elements connected to the rebar at selected deflection levels are presented in Fig. 3.24 and Fig. 3.25, respectively. The corresponding strain limits at which the KCC/CSC model would completely lose its strength under uniaxial tension and compression are also shown as a benchmark.

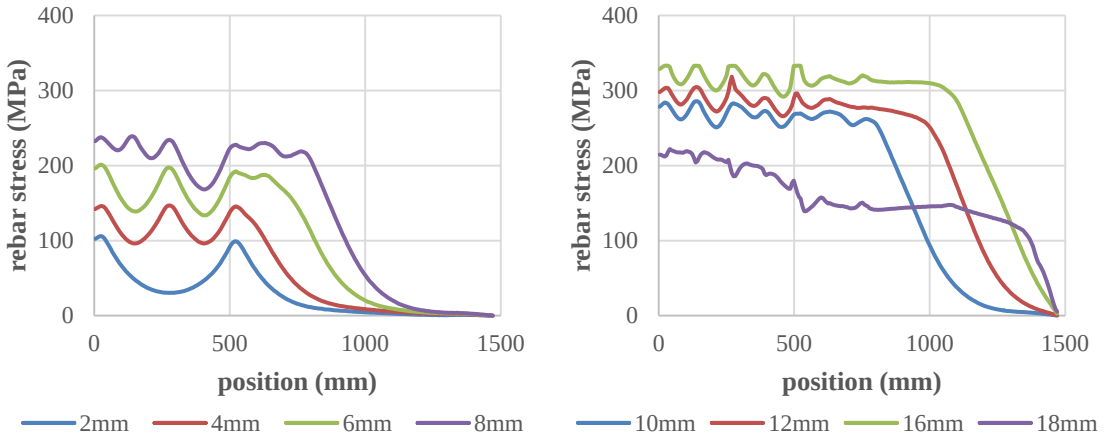

a) KCC model

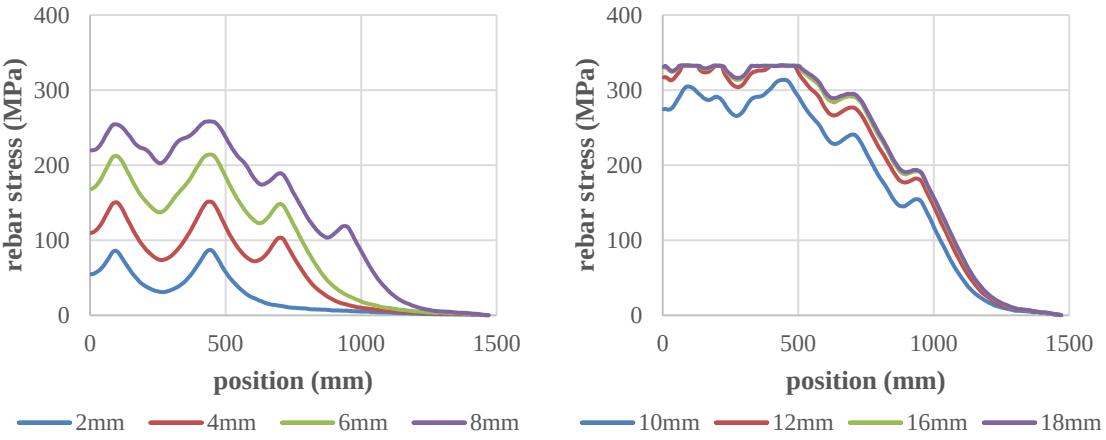

b) CSC model

Fig. 3.24 Axial stress distribution along the length of rebar

It can be seen from the model with KCC that as early as a deflection of 4mm, strain begins to increase drastically at the flexural crack 500mm from the mid-span. It immediately exceeds the strain limit and becomes stress-less, and results essentially in the loss of stress transfer between the concrete and the rebar at this point. This renders an accelerated spread of "bond" failure in the shear span towards the support. When the global response reaches 18mm, almost the entire set of the concrete in the shear span exceeds the total failure strain limit and becomes "stress-less" in the KCC model. Comparing to KCC model, the strain in the concrete connected to the rebar develops considerably below the strain limit

in CSC model, thus no significant connection failure takes place and the axial stress in the rebar exhibits a consistent but globally increasing pattern as the beam deflects.

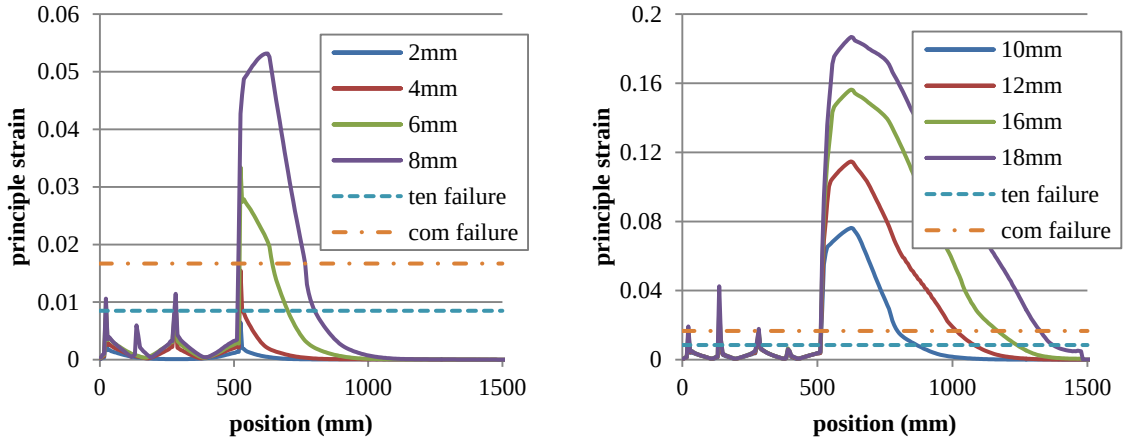

a) KCC model

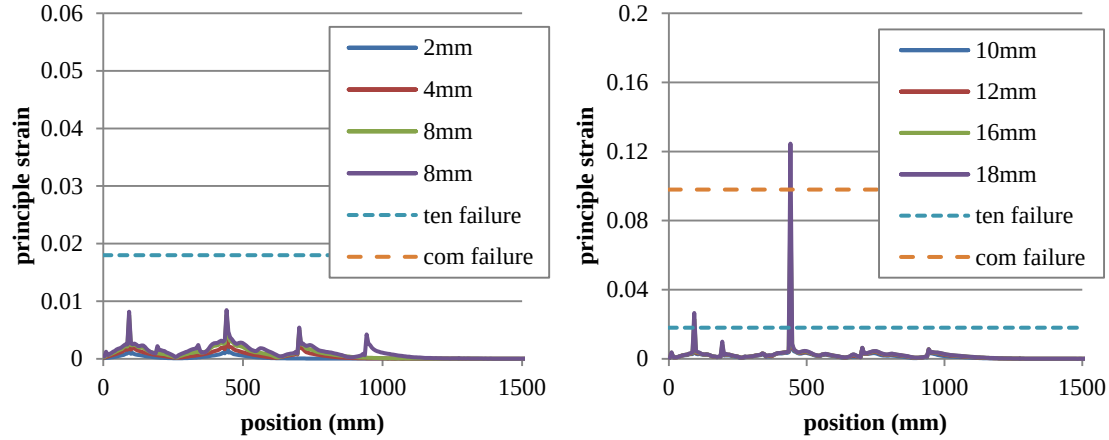

b) CSC model

Fig. 3.25 Principle strain in concrete elements connected to rebar

Based on the above results in conjunction with the comprehensive observations of the failure processes in the two models presented in the previous section, it may be concluded that the deterioration rate of tensile/shear strength in the softening stage in the KCC model, particularly the progress into a zero stress state, tends to be too quick and too early. This feature may not pose any significant problem in high pressure applications, but could be problematic in

lower pressure applications where tension and shear failure generally plays a governing role. The problem will tend to get worsened in reinforced concrete members such as the RC slab in the present investigation, where premature failure of concrete in shear and “bond” will result in an unrealistic elimination of the reinforcement effect, leading to a premature collapse of the RC member as if it was un-reinforced in the late stage of the response.

3.3.3 Discussion on the abnormal over-ductile tensile behaviour of CSC model

The performance of the CSC material model in the simulation of the global bending dominated RC slab and beam responses as presented in Section 3.1 and 3.2 has been satisfactory and no abnormal behaviour due to premature failure of the material has been observed. However, there have been signs of overly ductile response for the material model as evidenced in the RC beam analysis. The result there tends to indicate that the material model produces an extremely flat softening curve in the bond-slip relation thus greatly overpredicts the shear/tension of concrete in the rebar interaction zone. This suggests that the CSC model is likely to be unable to represent realistically the “bond” behaviour of concrete when this region does develop into critical and failure state, which the model presents a problem in the opposite direction of the KCC model.

The results from the single element tests under a uniaxial stress condition, as presented in Fig. 3.8, do not show any apparent problem with the CSC model in the softening stage. However, further examination reveals that the problem actually arises when lateral pressure, even at a small magnitude, is involved.

We shall take a look at the damage formulation in the CSC model first. In addition to the definition of the confinement (pressure) dependent failure surface, an extra equation is introduced to factor down the maximum possible damage level d_{max} in compressive situations:

$$d_{\max} = \begin{cases} \left(\dfrac{\sqrt{3J_2}}{I_1} \right)^{1.5} & \text{for} \quad \dfrac{\sqrt{3J_2}}{I_1} < 1 \\ 0.999 & \text{otherwise} \end{cases} \tag{3.15}$$

The non-dimensional term in the brackets is a stress invariant ratio that is equal to 1.0 in unconfined compression and less than 1.0 under confined compression. This effect may be illustrated in Fig. 3.26, and it is activated only when the stress condition falls into the shaded area. The exponent 1.5 is set by default.

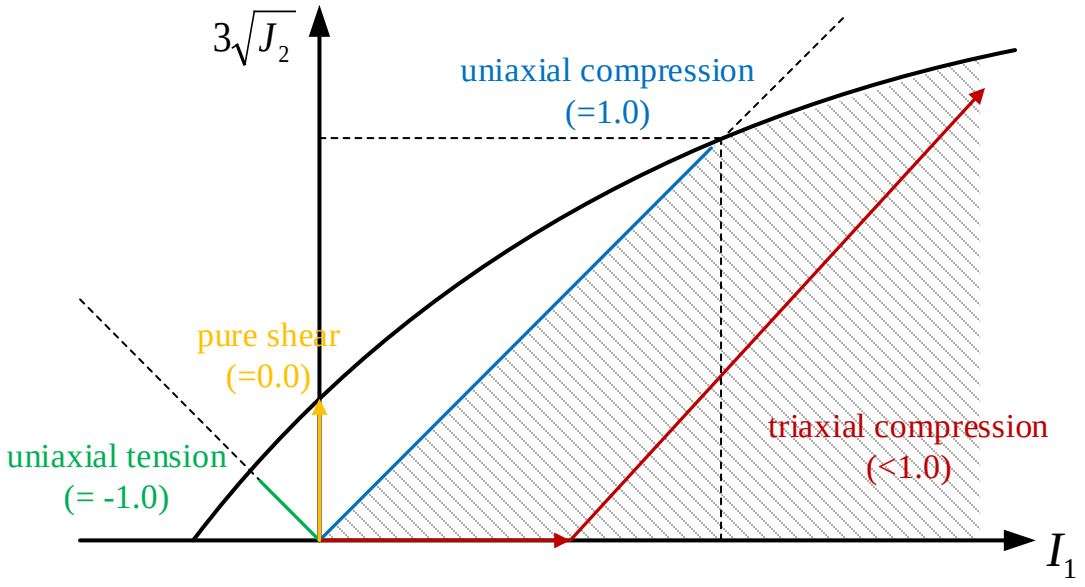

Fig. 3.26 Different stress paths and correspondent stress invariant ratios

As shown in Fig. 3.26, for an element under uniaxial compression, the principle stresses are $\sigma_1 = \sigma_c < 0$ and $\sigma_2 = \sigma_3 = 0$. The stress invariants are calculated as $I_1 = \sigma_c$ (compressive is positive) and $J_2 = \frac{1}{3}\sigma_t^2$, so the ratio $\frac{\sqrt{3J_2}}{I_1} = 1.0$. Similarly, it can be deduced that the ratio $\frac{\sqrt{3J_2}}{I_1} = -1.0$ for uniaxial tension and $\frac{\sqrt{3J_2}}{I_1} = 0.0$ for pure shear state. When the element is subjected to triaxial

(confined) compression, the ratio is less than 1.0, and stress path therefore lies in the shaded area to right side of the line $\frac{\sqrt{3J_2}}{I_1}=1.0$, and Eq. 3.15 would take its effect.

However in the case of confined tension, in which the stress state falls in the region of $\frac{\sqrt{3J_2}}{I_1}<1.0$ but the deformation state is still in expansion, the above

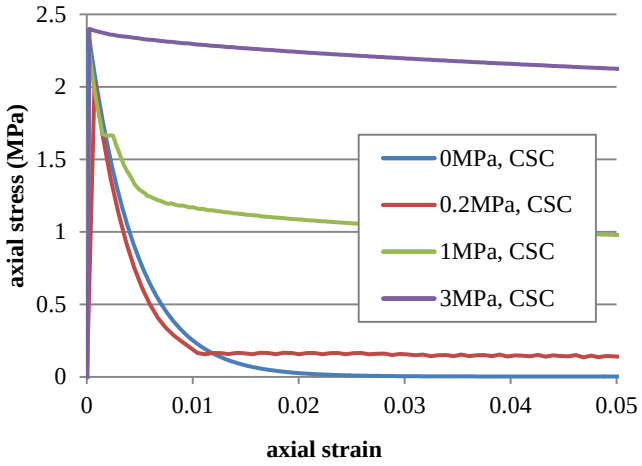

a) Stress-strain curves under confined tension

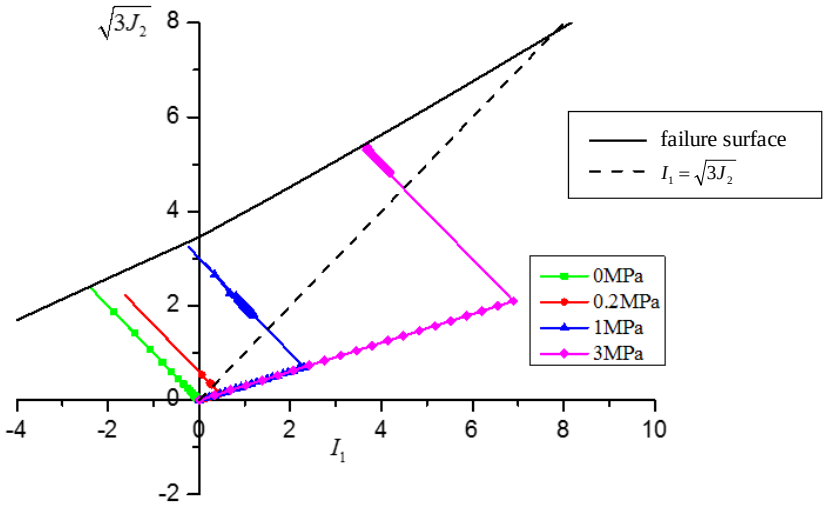

b) Graphical explanation of the stress paths

Fig. 3.27 Behaviour of CSC material model under confined tension

CSC implementation of confinement effect becomes problematic, which can be demonstrated by a single element stress test under tension, and the results are illustrated in Fig. 3.27a. As can be observed, in the tension softening regime a fully damaged state can never be reached in the CSC if the element is under a hydrostatic pressure condition, even with a small confinement of just 0.2 MPa. When the pressure increases, the tension behaviour becomes more ductile. With a confinement of 3 MPa, the tensile stress-strain response becomes extremely flat almost like elasto-plastic.

An examination of the stress paths is illustrated in Fig. 3.27b. It can be seen that the stress starts to decrease through the original path once it meets the tensile meridian; however due to reduced maximum possible damage level, the stress is always prevented from unloading across to the right side of the straight line of $I_1 = \sqrt{3J_2}$, and thus the strength is restrained and never deteriorates to a zero stress state. The persist existence of a minimum stress state may not be of a problem by itself; however, such mechanism of consideration of the confinement effect by an extra reduction to the damage index can cause unrealistic over-ductile tensile response when an appreciable level of pressure (e.g. 2~3 MPa) is present, which is often possible in areas surrounding a reinforcing bar. With this deficiency in mind and considering the fact that the CSC model is originally not designed to cover an intensive stress wave response, no further attempt in rectifying this issue with the CSC model will be pursued in the present study. However the potential problem with the CSC as discussed here is worth noting while we use this model to check against the performance of KCC in the global response regimes.

3.4 Conclusions

Numerical simulation of reinforced concrete structures under impact and blast loadings requires the material models to be able to accommodate a wide range of stress, strain rate and deformation conditions. Although extensive calibration and validation studies have been conducted for typical concrete material models under a variety of loading conditions, the performance and demands of the material models in a reinforced concrete environment and under a global deformation dominated response regime is relatively less explored. The study presented in this chapter examined the performance of KCC model in comparison with the CSC model in the application of RC slab and beams for impact and blast loading with involvement of significant global response features.

The benchmark experiment being modelled is generally in a global flexure regime and the response is primarily of a monotonic character. For such a classical modelling situation, however, the two models exhibit very distinctive performances. The simulation on the blast response of the RC slab demonstrates that with the default KCC model the simulated response tends to fail prematurely due to a rapid loss of the shear and tensile strength of concrete, particularly in the elements to which the reinforcing bars are attached and effectively eliminate the reinforcement effect and cause the collapse of the slab. Further simulation on an RC beam under a quasi-static loading shows a similar phenomenon.

The aspects of the KCC material model behaviour that may be linked to the abnormal performance of the RC slab simulation are deemed to include, primarily, the rapid descending rate in the later softening phase and an earlier entry into a stress-less state. While this feature may not pose a significant problem in high pressure applications, it becomes problematic in low pressure situations, especially in a reinforced concrete structure such as in the RC slab

under investigation where premature failure of concrete in shear and “bond” will accelerate unrealistically the failure process towards a premature collapse. The problem with too steep a descending rate into a zero-stress state therefore requires rectification, and this is a topic which will be investigated in detail in Chapter 4.

On the other hand, the CSC model, although seemingly exhibiting good performance in the simulation of the same benchmark problem, actually tends to produce an overly conservative behaviour at the rebar interface that would become problematic in situation where shear and interface do become critical.

A closer examination of the model performance reveals that CSC model is inclined towards the opposite direction of KCC model in a tension or shear dominated response subjected to low pressure regime, in that it tends to be excessively ductile in tension with the presence of a limited amount of confining pressure. The cause of this abnormal phenomenon is deemed to originate from the use of a reduction of damage in a confined stress condition. Such a phenomenon has not been well calibrated in the literature, and should be treated with care before an appropriate resolution is available. Thus the primary focus has been focused on rectifying the KCC model in terms of a holistic modelling for high impulsive loading.

Chapter 4: Modification to KCC model and holistic modelling of RC flexural and shear response

4.1 Introduction

The extensive analysis of the failure processes in the simulation results in Chapter 3 has revealed that the global failure in the RC members with the KCC model tends to be premature, and this phenomenon is deemed to be resulting from a premature and complete loss of “bond” strength in the concrete elements surrounding the rebar. The premature failure of these concrete elements will equate elimination of the reinforcement effect, leading to a premature collapse of the RC member as if it was un-reinforced in the late stage of the response.

In this Chapter, the behaviour of the material models is firstly further examined in a classical pull-out scenario, and two possible rebar modelling schemes, namely the conventional one-dimensional line/beam model and a solid element model, are considered for an evaluation on the degree to which different rebar models may contribute in any abnormal interaction behaviour. The main objectives are to investigate into the root cause of the premature failure of KCC model, and subsequently to propose and demonstrate possible remedies. The two rebar model schemes of rebar in concrete are examined. The possible influence of transverse reinforcement on reducing the “bond” demand, are also examined and discussed.

Rectification of the KCC model problem is then focused on realising a more gradual softening (descending) phase of the tensile and shear behaviour, including in the conditions where an appreciable hydrostatic pressure is involved. The proposed modification includes a modified damage function, i.e. the η -λ curve, as well as an adjustment of the plastic strain accumulation factor b_1 of the KCC model. With the proposed modification, the KCC model is found to behave rather satisfactorily in modelling the RC slab and beam responses under both impulsive dynamic and quasi-static load situations.

The overall modelling framework for RC components and the modification of the KCC model are further validated for their performances in capturing the global structural behaviour of RC members against some recent experiments of RC beams conducted at University of Edinburgh, with a special focus on the prediction of global shear failure mechanism and shear resistance.

4.2 Further investigation on the premature failure of interaction between concrete and rebar

As a commonly adopted approach in modelling structural or component response of RC structures subject to blast type of loads, the reinforcing steel bars are usually embedded in the concrete with shared nodes between the rebar and concrete elements along the length of the rebar. This is equivalent to assuming a perfect bond between concrete and rebar. The basic rationale is that the response during the blast loading phase is so fast that there is no time for “slip” to develop, whereas in the subsequent phase bond failure and “slip” may be reasonably represented through the softening and failure of the concrete to which the rebar is attached to.

Besides simplicity, a prevailing justification for this approach is based on a recognition that “bond” failure between steel reinforcement and concrete can

always be replicated by the failure of the concrete elements, which are attached to the rebar elements. Indeed in a real RC environment involving deformed steel bars, “bond” failure can often be attributed to eventual failure of concrete surrounding the rebar. Therefore ignoring a physical bond interface is not expected to change the failure mode in the interface region, whereas the possible “slip” deformation, as commented earlier, is not regarded as important in a blast type loading scenario. By rendering failure to be governed by the surrounding concrete, the macroscopic reinforcement-concrete composite effect and the global response of the RC member is maintained.

What is less recognised, however, is the fact that the stress condition in the layer of concrete attached to the rebar is altered, particularly in the beam-element model scheme for rebar. The implied requirement on the concrete material model is that it should not be very sensitive to a certain degree of variation of the stress condition in a damaged tension-shear state around the steel rebar. Depending upon the loading and structural conditions, this factor may or may not introduce a noticeable effect. Therefore, this potential issue has not been discussed openly in the numerical simulation community.

For blast related simulation, steel rebar is often modelled as one-dimensional 2-node beam or link element (Lowes et al. 2004; Ben Romdhane and Ulm 2002; Salari and Spacone 2001; Shi et al. 2009); less often is the rebar modelled using solid elements (e.g. Magnusson et al. 2010) due to computational cost. An example of the RC section with beam-element rebar modelling setting is represented in Fig. 4.1a, in which the one-dimensional rebar is represented by a yellow node with its actual perimeter highlighted by the dashed circle. Fig. 4.1b gives an example of the cross-section with rebar modelled by solid elements.

a) Rebar modelled by beam elements b) Rebar modelled by solid elements

Fig. 4.1 Different modelling approaches for rebar in FE models

The major difference between the two rebar modelling approaches lies in the geometrical description of the rebar. Under a beam-element rebar assumption, the rebar is represented by a string of one-dimensional elements without the actual perimeter, while under a solid-element rebar assumption the boundary between the steel rebar and adjacent concrete is explicitly defined. Besides, solid-element rebar normally requires refiner mesh resolution to describe the circular rebar shape and preserve flexural stiffness of the rebar, therefore longer computational time will result.

Naturally in a FE configuration, the deformation and deterioration caused by the rebar-concrete interaction would largely be localised in the first layer of concrete elements adjacent to the rebars. In a beam-element rebar setting, the original space occupied by the actual rebar is allocated into concrete material. This may not generate significant issue in an FE model where the concrete element size is much larger than the rebar size. However, when the mesh size is relatively small (comparable to the radius of rebar), which is often required in a blast response simulation due to the need to capture the stress wave effect, the concrete elements in the original rebar space actually represents none of the physical material involved. From this point of view, it is not fair to require a concrete material model to be fully capable of catering to the stress condition in this fictitious concrete region while behaving like normal concrete. It is only by the

fact that the gross transfer of stress from the line/beam rebar to the surrounding concrete should generally remain like in the actual concrete-rebar interaction region that the fictitious layer of concrete may still be handled using a concrete material model. The detail of the force transfer and a possible use of an equivalent (concrete) material for the fictitious layer of concrete will be discussed in Chapter 5.

In typical reinforced concrete configuration, transverse shear links and stirrups are usually present to ensure the shear resistance and overall integrity. On the other hand, the steel cages formed by longitudinal and transverse reinforcements will inevitably reduce the demand on bond and anchorage in the longitudinal rebar. From the perspective of numerical modelling, this could effect to mask the problems in the performance of the concrete model such that the local bond failure might not result in a gross loss of concrete-rebar interaction. The extent of such an effect is also worth clarifying.

In this section, the performance of KCC model under the two rebar modelling approaches are examined via a pull-out simulation. This is followed by a FE investigation on the effect of transverse reinforcement in masking the “bond” problems with this concrete model.

4.2.1 Examination of the two rebar models using a pull-out test

With questions from the simulation for RC slabs and beams aroused regarding the modelling of concrete-rebar interaction, it is reasonable to take a close look at the behaviour of the concrete and rebar models in a pull-out test, where a simple but representative shear load transfer condition is readily present. With a quantitative comparison with available experimental data, it also helps to give a clear idea about the extent to which the post-peak “bond” interaction should

withhold. Insight will also be gained with regard to the effect of using the two different rebar models on the interaction simulation.

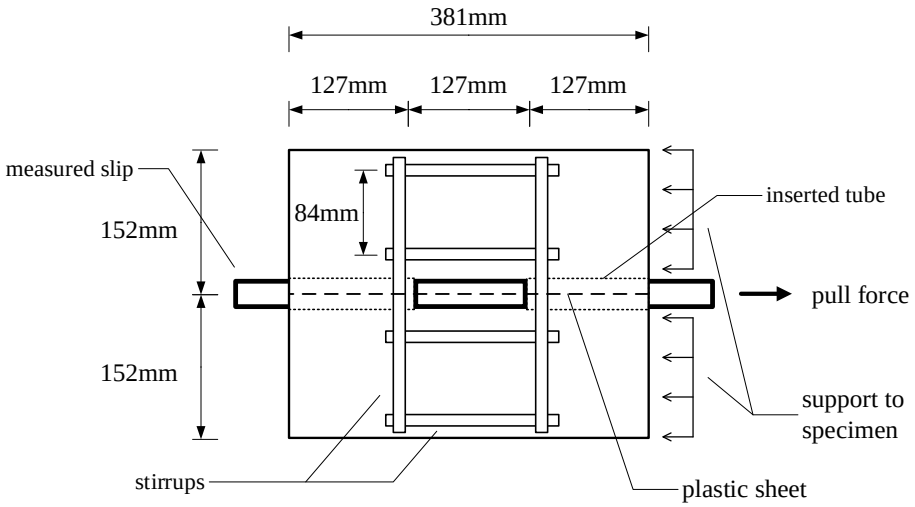

a) Side view

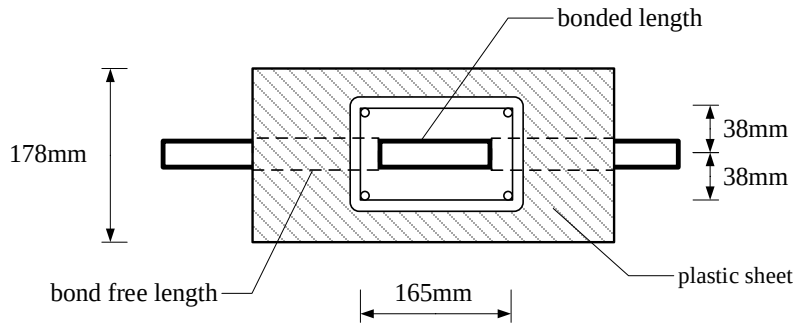

b) Cross-sectional view

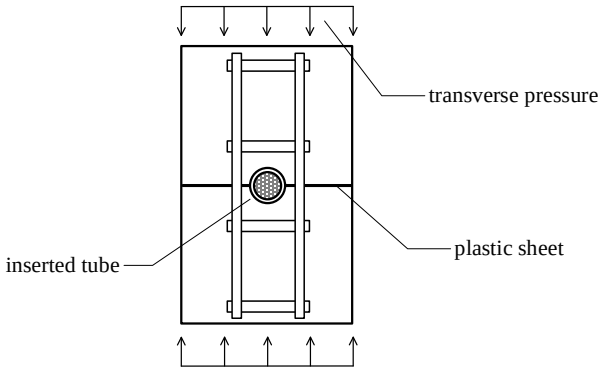

c) Front view

Fig. 4.2 Test specimen and pull-out setup (after Eligehausen et al. 1982a)

The classical pull-out tests conducted by Eligehausen et al. (1982a; b) are modelled. The basic setup and specimen configuration are presented in Fig. 4.2. The test specimen represented a confined region of a typical beam-column joint. The gross dimensions of the specimens were approximately 300 mm by 180 mm by 380 mm, and grade of concrete was 30 MPa. The longitudinal rebar was Grade 60, #8 (25.4 mm in diameter), and the stirrups were of #4 (12.7 mm in diameter) bars. Only a short bond length of 5 times of rebar diameter was created in the test specimen. A specimen with the same dimensions but without stirrups was also tested for comparison purpose. Load was applied using a displacement controlled procedure such that the intended development of slip was achieved. The net slip was measured at the unloaded end of the main bar. The bond stress was calculated from the applied force by the following equation:

$$\tau = \frac{F}{\pi \cdot D_b \cdot l_b} \tag{4.1}$$

where F is the rebar force, D_b is the diameter of the rebar, and l_b is the embedded bond length. In this case $l_b = 5D_b$. The bond-slip relation was obtained by pairing the bond stress so calculated with the corresponding slip from the measurements.

In the numerical model, one-quarter the specimen is modelled considering the symmetry. Two modelling approaches for the longitudinal rebar, i.e., beam-element and solid-element, are investigated. Concrete is simulated by solid elements and stirrups by beam elements, as shown in Fig. 4.3. In the numerical simulation, load is also applied at one end of the longitudinal rebar in a displacement controlled manner. Due to the explicit scheme used in the analysis, the rate of applying the displacement was made sufficiently slow (10mm per second) to avoid any unwanted transient effect while at the same time avoid excessive computational time.

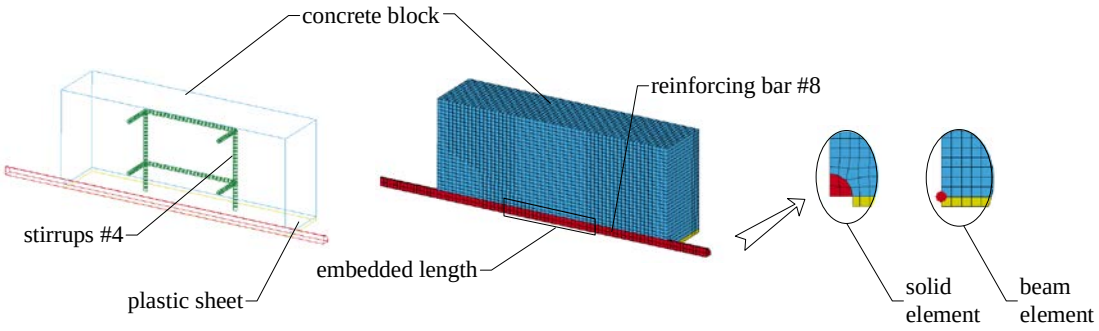

Fig. 4.3 Numerical model setup of the pull-out specimen

In the experiment, a plastic sheet was inserted into the cross-sectional plane of the RC specimen and only concrete inside the steel cage (140 mm×127 mm) was bonded. This was for the purpose to result in a controlled splitting area while simulating a realistic bond environment in a joint region. In the FE model, this arrangement is modelled by placing an extra rigid-body plate (highlighted in yellow) and surface-to-surface contact is defined between the sheet and concrete. Similarly, contact surfaces are defined in the bond-free region between the longitudinal rebar and concrete, and leave a 127 mm length of bonded region, which equals to the length of 5 times of rebar diameter, as shown in Fig. 4.4.

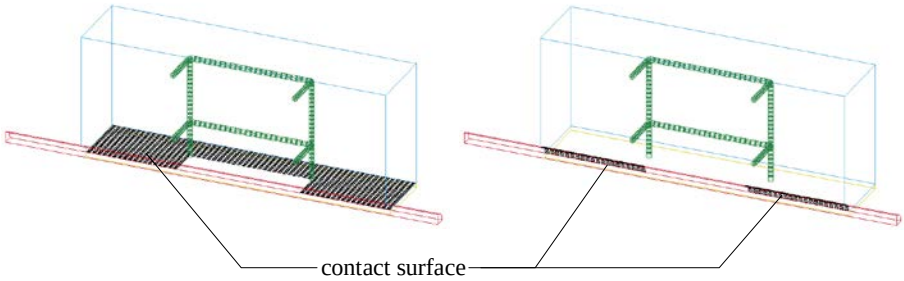

Fig. 4.4 Simulation of the bond-free length and inserted plastic sheet by contact surface

According to the paper (Eligehausen et al. 1982a), a splitting crack was developed prior to failure in both specimens, in the plane of the longitudinal axis of the bar. After developing this crack, load dropped rapidly in the specimen

without stirrups and failed in splitting, as shown in Fig. 4.5a. When concrete was confined by stirrups, the resistance had further increase while the bond stiffness gradually decreased. The final failure was caused by pull-out of the bars, and the concrete between lugs was completely sheared off and almost pulverised, as shown in Fig. 4.5b.

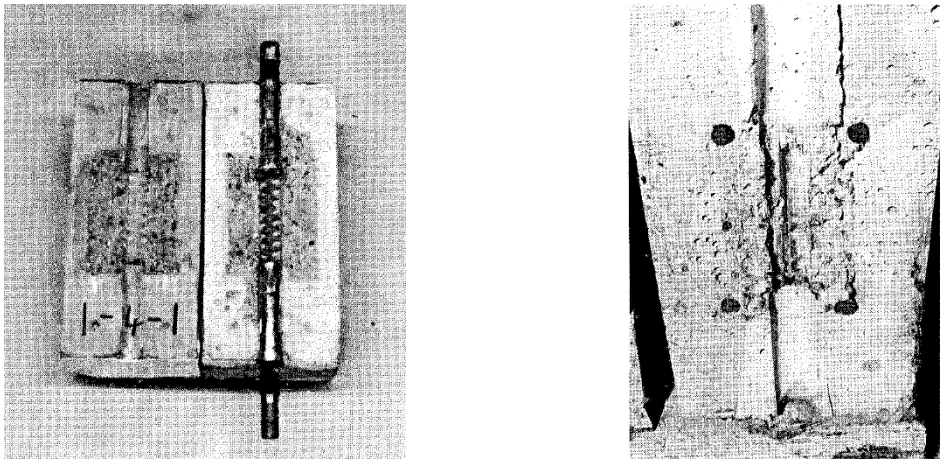

a) Specimen without stirrups (splitting) b) Specimen with stirrups (pulled out)

Fig. 4.5 Cross-sectional photo of specimens after failure (Eligehausen et al. 1982a)

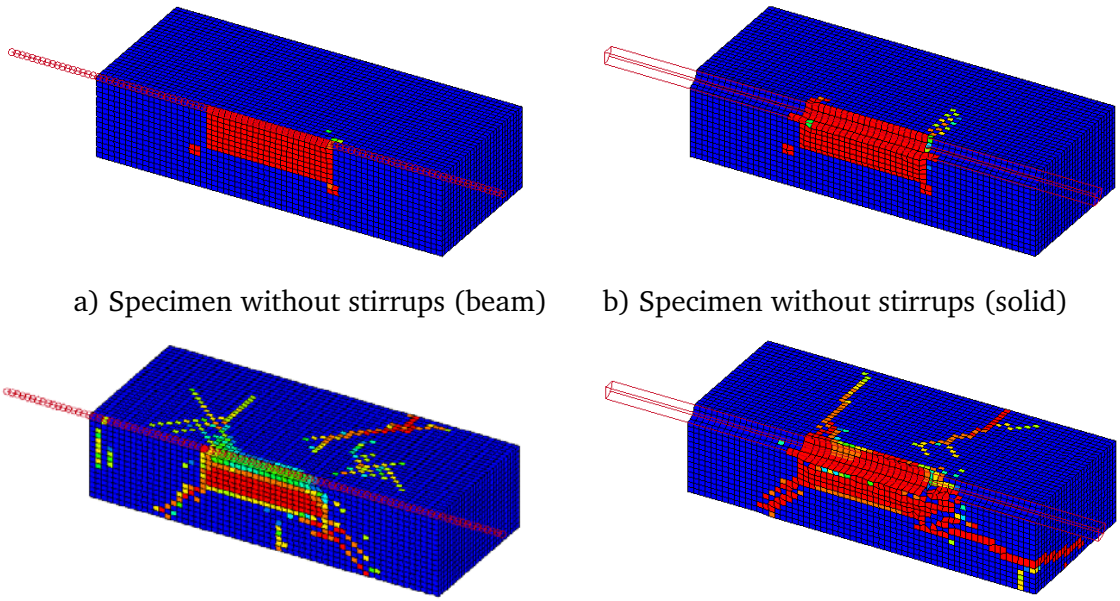

a) Specimen without stirrups (beam) b) Specimen without stirrups (solid)

c) Specimen with stirrups (beam) d) Specimen with stirrups (solid)

Fig. 4.6 Damage contour of pull-out specimen at failure modelled by KCC model (SDF: 1.97~2.00)

Fig. 4.6 gives the damage contour of the specimens simulated by KCC model at failure. The failure patterns of beam- and solid-element models are similar, and consistent with the experimental observations for both pull-out specimens.

Fig. 4.7 shows a comparison of the simulated bond stress – slip displacement curves using beam- and solid-element rebars with KCC model, in comparison with the experimental curves. An extra case with rebar modelled by solid-element and concrete modelled by CSC model is also included. Clearly, in both models KCC exhibits again overly brittle bond-shear behaviour and the specimen fails rather steeply when the maximum bond stress was attained. This observation is consistent with the results from the RC slab and beam simulations presented in the previous chapter. Results also reveal that the bond strength of the beam-element rebar is greatly under-predicted and is only half of the bond strength in solid-element rebar setting.

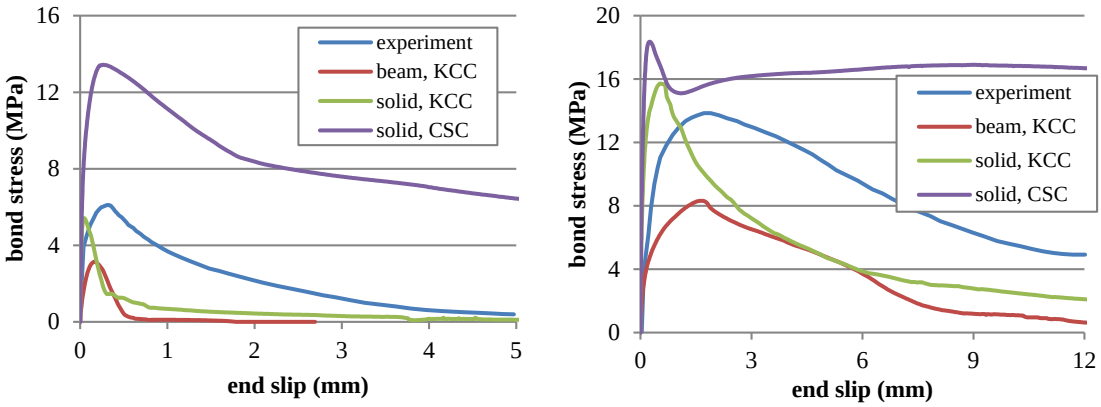

a) Specimen without stirrups b) Specimen with stirrups

Fig. 4.7 Comparison of global bond-slip relation

It is noteworthy that the CSC model, while still withholds a reasonable trend in the overall behaviour, tends to over-predict significantly the bond strength as well as the overall slip deformability. This phenomenon echoes with the discussion on overly ductile behaviour of CSC model in Chapter 3.

4.2.2 Effect of transverse stirrups in reducing the "bond" demand in RC members

As mentioned earlier, the presence of stirrups, especially in numerical models in which the stirrups are usually rigidly connected to longitudinal rebar, would effect to somewhat dilute the demand on the performance of a concrete model at the interaction region with rebar. This situation is suspected to have at least partially contributed to the fact that the potential problems with popular concrete material models such as KCC in this respect is less recognised in the blast response simulation field.

Herein such a "diluting" effect is demonstrated from a simulation of a quasi-static RC beam test, originally carried out by Miyamoto, et al. (1989). The test RC specimen had a rectangular cross-section of 160 mm×150 mm and a span of 1200 mm, and it was simply supported as plotted in Fig. 4.8a. The beam was subjected to a concentrated load acting at the mid-span. The reinforcement consisted deformed bars of 10mm in diameter, two in the compression side and three in the tension side. Stirrups were made from steel bars of 6mm in diameter. The reinforcement was of Grade SD30 steel which had a yield and ultimate strength of 352 MPa and 468 MPa, respectively. The compressive strength of concrete was 29.4 MPa. The tensile reinforcing ratio was just around 1.12%.

The FE model setup is similar to the simulation of the RC slab, as depicted in Fig. 4.8b. Two FE models are used, one using beam-element for the main steel bars, and the other using solid-element rebar for a comparison. Besides, for the FE model with beam-element main rebar, a further model is set up in which the stirrups are purposely removed, again for a comparison purpose. In all three models, the stirrups are always modelled by beam elements. The concrete is modelled by KCC and the model parameters are generated automatically for the

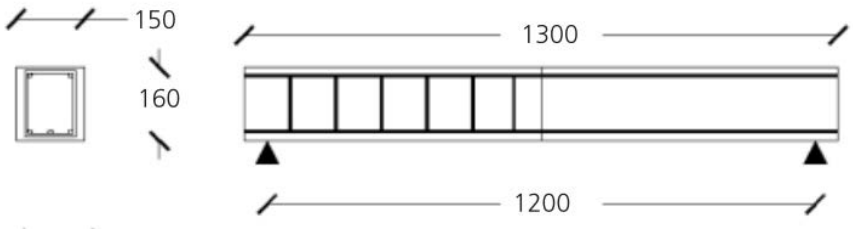

a) RC beam configuration

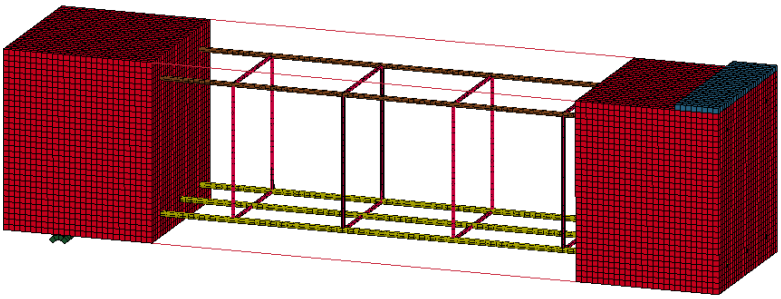

b) FE model

Fig. 4.8 Dimensions of doubly reinforced RC beam specimen

C30 class concrete with default values. In the FE model, the beam is simply supported as in the experiment, and loaded in the mid-span in a deformation-controlled way.

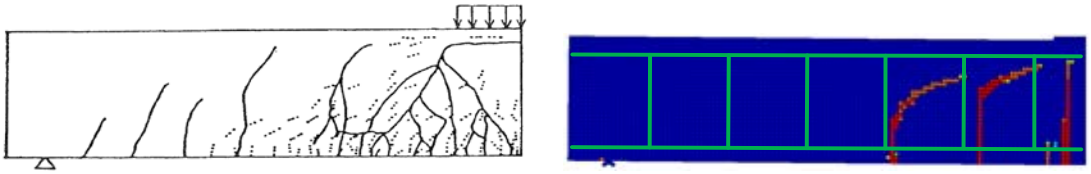

a) Experiment crack file (Miyamoto, et al. 1989) b) Beam-element rebar

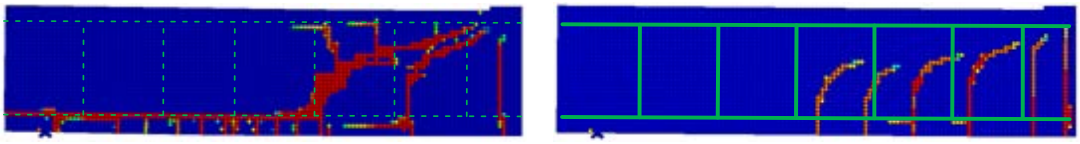

c) Beam-element rebar (stirrups removed) d) Solid-element rebar

Fig. 4.9 Experimental and numerical crack patterns of Miyamoto's beam test

Fig. 4.9 shows the damage patterns of the simulated RC beams, in which the positions of stirrups are highlighted by green lines, as compared with experimental crack profile. The simulated and experimental load-displacement

curves are presented in Fig. 4.10. As reported by Miyamoto, et al. (1989), the tested beam experienced significant flexural plateau stage, and collapsed at the deflection of 5mm due to the propagation of diagonal cracks towards the loading plate, as shown in Fig. 4.10a.

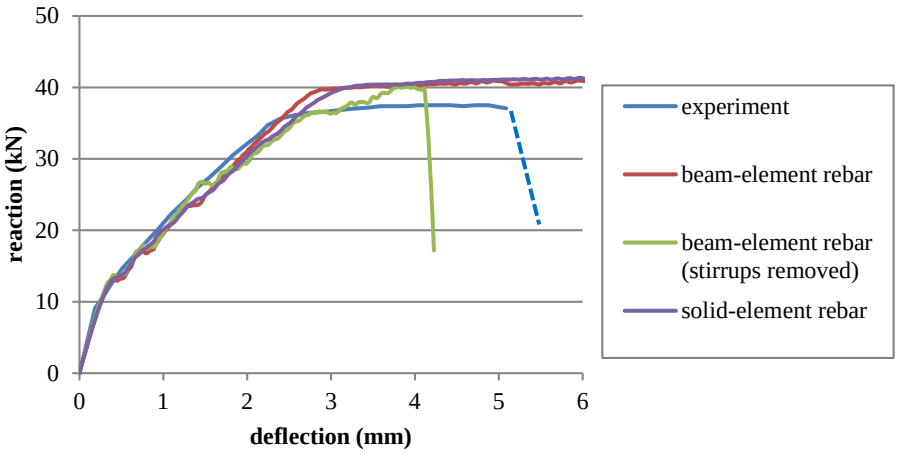

Fig. 4.10 Load-displacement curves of Miyamoto's beam test

Note that the tested beam has a span-to-depth ratio of 4.6. From the simulation result in Fig. 4.10, it can be seen that the model with beam-element rebar experienced typical flexural behaviour with an obvious plateau stage and a slightly higher resistance. Although the beam does not collapse after a deflection of 6mm, its propagating cracks towards the loading plate clearly indicates a similar diagonal tension failure which agreed well with the experiment, as shown in Fig. 4.9b.

It is noteworthy that when the stirrups are purposely removed, the beam reaches the same flexural resistance but without an obvious plateau stage, and suddenly collapses at a deflection of 4.6mm. It is found that the failure is not caused by shear, but due to loss of anchorage near the support and splitting of concrete cover layer along the tension rebar, as shown in Fig. 4.9c. A closer inspection at the distribution of axial force in the tension rebar, as presented in Fig. 4.11, suggests that when the deflection reaches 2mm the rebar force stops further

increasing and the rebar anchorage region starts failing. On the contrary, in the model with stirrups the rebar force increases persistently, with no sign of extensive bond failure in the concrete.

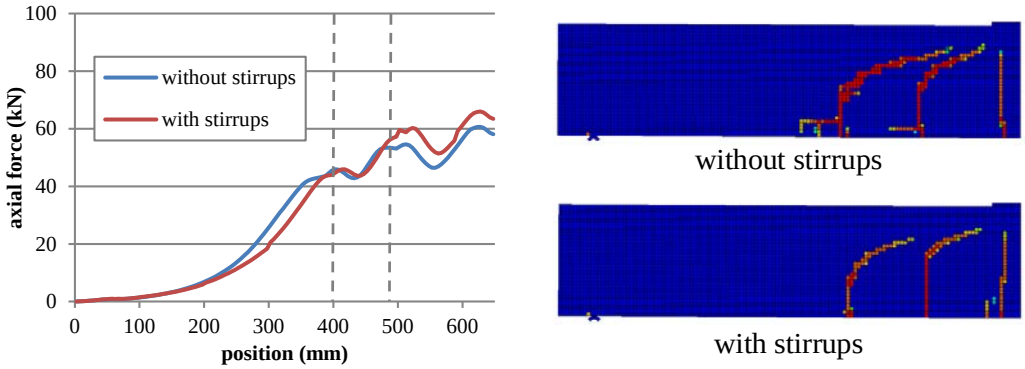

a) Deflection = 2mm

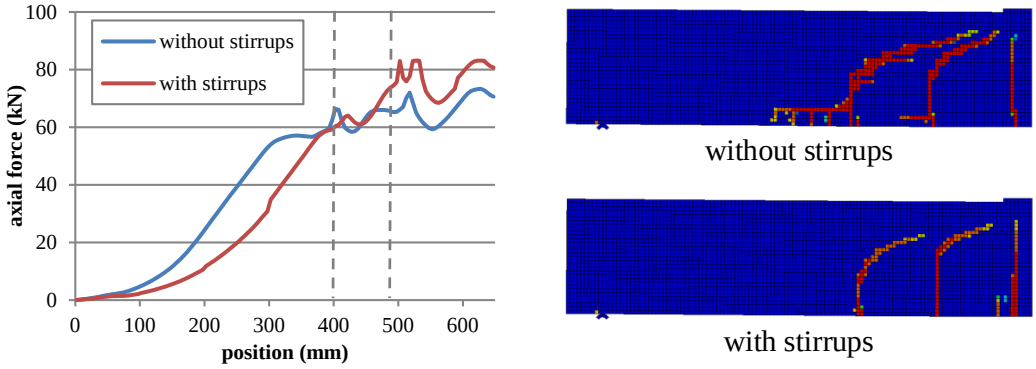

b) Deflection = 3mm

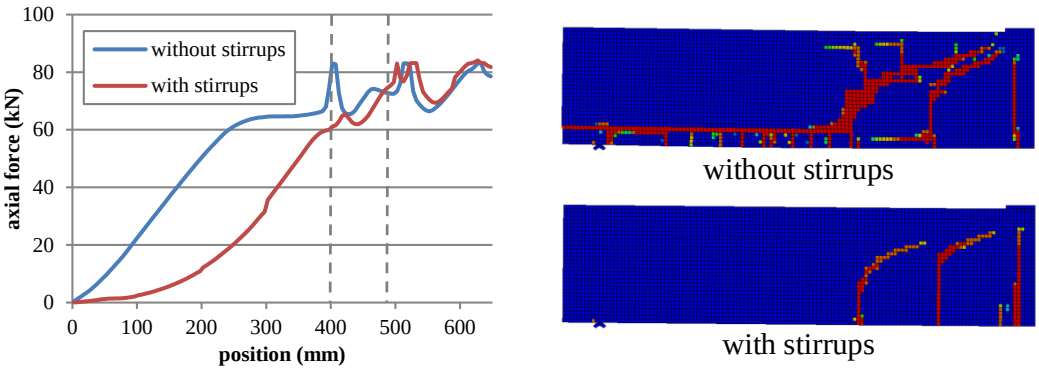

c) Deflection = 4mm

Fig. 4.11 Distribution of rebar force and cracking development at different deflection levels (beam-rebar models)

It is also useful to compare the performance of the two rebar modelling approaches in this typical RC beam with normal transverse reinforcement. Although no obvious difference is observed in the load-deflection curves (Fig. 4.10), the damage patterns shown in Fig. 4.9b and Fig. 4.9d clearly reveal that more flexural cracks develop in the solid-rebar model. This is an indication that the solid-element rebar provides better “bond” interaction between rebar and concrete, thus resulting in more distributed cracks.

From the above analyses it can be generally established for finite element modelling of a RC component, the transverse reinforcements, originally designed for shear resistance, would in effect help alleviate the demand on direct bond between concrete and the longitudinal reinforcement. As a result, the problem with the concrete material model in terms of under-representing the interaction strength between rebar and concrete could be somewhat diluted. However, this does not mean that the abnormal phenomenon in KCC model can be simply ignored. On the contrary, failing to address this issue could lead to misrepresentation of the true failure mechanism in a RC member.

Based on above results in conjunction with the comprehensive observations of the failure process in the simulation for pull-out tests in Section 4.2.1, it can be concluded that the use of beam-element rebar can introduce increased complication and lead to less realistic behaviour in the concrete layer surrounding the rebar. This could manifest as underestimation of the concrete interaction strength especially when a small mesh size is employed. Further discussion on this problem and a substitute equivalent transitional layer model will be proposed in Chapter 5. For the following part of this Chapter and the primary numerical simulation studies presented in subsequent chapters, a solid-element rebar modelling setting is used.

4.3 Proposed modification to the standard KCC model

4.3.1 General discussion of the modification strategy

The extensive analysis of the failure processes in the simulated results reveal that the global failure in the RC members with the KCC model tends to be premature in the FE model, and this phenomenon is deemed to be resulting from an early loss of strength in the concrete elements surrounding the rebar. The early failure of these concrete elements will equate the elimination of the interface and therefore the reinforcement effect, leading to a premature collapse of the RC member in the FE model as if it was un-reinforced in the late stage of the response. This has been shown to unrealistic comparing to the physical experiment.

The concrete elements surrounding the rebar are generally in shear and tension dominated stress state, while a certain level of hydrostatic pressure can always be present in this area. To rectify the problem of premature failure of concrete in such a primary tension and shear condition, it would be rational to seek ways to prolong the softening or descending phase of the material model behaviour under tension and prevent the model to enter into a zero strength state prematurely. The ability to maintain a minimum level of resistance can be particularly important for KCC like models that adopt an iso-damage approach in which a concrete element failed completely in tension would not possess any strength when the stress condition is reverted to compression.

The above objective of allowing a more gradual softening and avoiding abrupt and early termination of strength may be achieved via modification to the relevant material model formulation. In the present study, we look into achieving such an effect may by examining the damage accumulation law in conjunction with an adjustment to the plastic strain weighting treatment.

4.3.2 Modifications to the softening law in KCC model

As discussed earlier, in KCC model the damage accumulation or softening rate are controlled by a softening law which is realised through the η-λ curve. The rates of softening is also controllable by the exponential factors b_1 and b_2 in the damage accumulation formulas. In particular, the η-λ curve affects directly the shape of softening curve, whereas the factor b_1 and b_2 control the rate of damage accumulation under tension and compression respectively, based on the equivalent plastic strain. In combination these parameters give rise to a desired softening stress-strain relation and guarantee a certain fracture energy level.

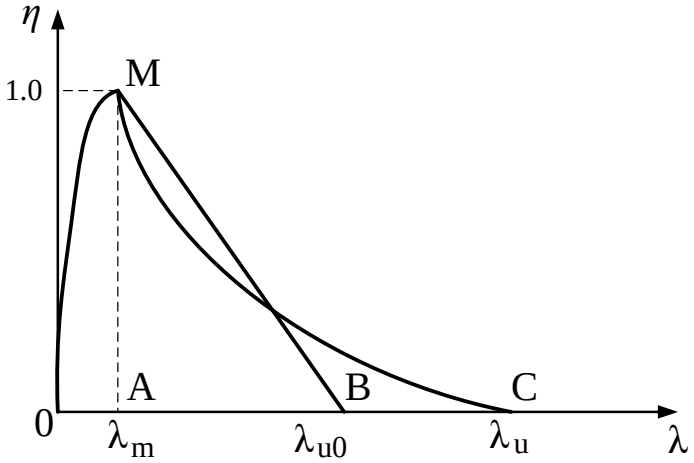

Fig. 4.12 Modification to η-λ curve

As demonstrated earlier in Fig. 3.2 and re-sketched in Fig. 4.12, the default η-λ relation (OMB portion in Fig. 4.12), is approximately a linear function in its softening portion. Assume that it is linear and can be written in the form of Eq. 4.1.

$$\eta(\lambda)_{old} = \frac{\lambda - \lambda_m}{\lambda_{u0} - \lambda_m} \quad (\lambda \geq \lambda_m) \tag{4.1}$$

The default value of λ_m when $\eta = 1$ is 5.6×10^{-5}, and for λ_{u0} when η returns 0 is 5.7×10^{-4}, which represents a fracture energy $G_f = \sim$100 kN/m (Crawford et al.

2012). It generates a uniaxial stress-strain curve with a very steep softening response under both uniaxial tension and compression, with a clear strain (or deformation) limit beyond which the strength will become and remain zero. The area AMB under the η-λ curve, which conceptually represents the facture energy, can be calculated by

$$A_{\lambda-0} = \frac{\left(\lambda_{u0} - \lambda_m\right)}{2} \tag{4.2}$$

A more gradual accumulation of the damage, and hence the more gradual softening and delayed total loss of strength, may be achieved by modifying the softening branch of the η-λ function into an exponential form (e.g. OMC in Fig. 4.12). The specific form of the adopted function may vary, and here for demonstration purpose, a simply form is adopted by introducing a power factor of k:

$$\eta(\lambda)_{new} = \left(\frac{\lambda - \lambda_m}{\lambda_u - \lambda_m}\right)^k \quad (\lambda \geq \lambda_m) \tag{4.3}$$

Similarly the area AMC under the η -λ curve in Fig. 4.12 can be calculated via integral as

$$A_{\lambda-n} = \frac{\left(\lambda_u - \lambda_m\right)}{k+1} \tag{4.4}$$

One may easily find that when $k = 1$, the η-λ function returns to the default value. By equating Eq. 4.2 and 4.4 to ensure a same fracture energy, for a new termination limit of the λ_u value, the power factor k can be expressed as

$$k = \frac{2\lambda_u - \lambda_{u0} - \lambda_m}{\lambda_{u0} - \lambda_m} \tag{4.5}$$

It should be noted that the determination of the fracture energy for concrete is still a subject of continued study and for the same type of concrete the variation range of the fracture energy could be rather significant. For this reason, in the

present proposal of modifying the softening behaviour of the KCC model we do not confine ourselves to a specific fracture energy quantity. For larger fracture energy, process similar to Eq. 4.3-4.5 can be employed to deduce the k value for any termination limit of the λ_u.

Based on the above considerations, a set of the exponential functions with a different termination limit of the λ_u values, as shown in Fig. 4.13, are proposed to yield different degrees of gradual softening behaviours and retain a certain level of residual strength within a certain strain range.

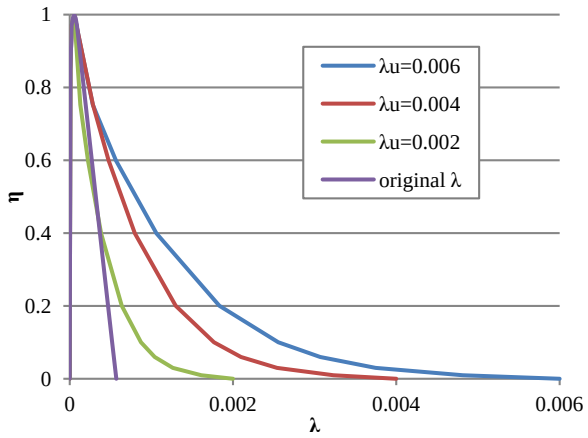

Fig. 4.13 Modified η-λ curve

As also discussed earlier, in KCC model the same η-λ law is used for both tension and compression regimes. Now that the η-λ curve is modified with an explicit aim to achieve a gradual softening in tension, there is no reason to accept a by-product of a significantly altered compression behaviour because of this modification.

Recalling the formulation of KCC model outline in Section 3.2.1, Eq. 3.2-3.3, different softening features in compression and tension can be controlled, separate from the damage accumulation law, by the plastic strain factor b_1 and b_2 respectively. Therefore the b_1 factor, which takes effect when the stress conditions comes into the (hydrostatic) compression regime, can be adjusted in

accordance with the modification of the η-λ law to generally offset the effect on the compression behaviour.

4.3.3 *Parameterisation of η-λ curve and b_1 factor*

The responses of single element using modified KCC model with different λ limits, under varied load conditions, namely uniaxial tension and uniaxial compression, are given in Fig. 4.14a and 4.13b. Fig. 4.14c and 4.13d presents

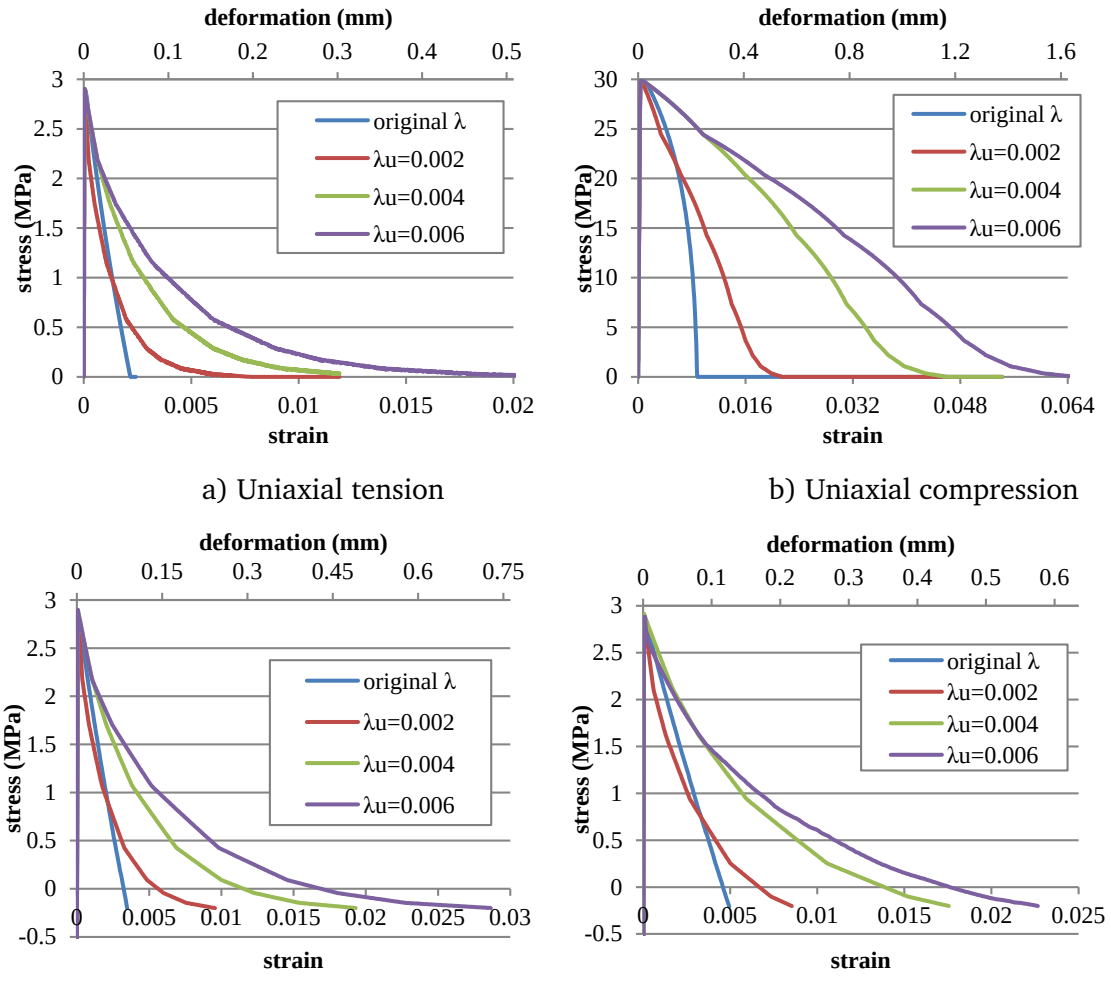

a) Uniaxial tension b) Uniaxial compression

c) Confined tension (1.5MPa) d) Confined tension (3.0MPa)

Fig. 4.14 Influence of η-λ law on stress-strain curves (element size = 25.4mm)

the behaviour of the material element under a confined tension, which is identified to be a representative stress state in the concrete elements surrounding the rebar.

It can be immediately observed that the softening branch of the uniaxial tension is markedly affected by the modification of the η-λ function and softening becomes increasingly gradual as the limiting value of λ_u is increased, and this effect also holds in the two examples of confined tension scenarios. However, as mentioned in previous paragraph the effect from the modified η-λ curve carries over to affect the compressive stress-strain relationship as well, making the material unrealistically ductile in compression as can be seen from Fig. 4.14b.

The compressive plastic strain factor b_1 is therefore adjusted to offset the unwanted effect on the compression behaviour from modifying the η-λ curve. It is also worth noting from the RC slab and beam simulation experiences that the concrete elements interfacing with the rebar are often in a “confined” tension state with a positive (compressive) hydrostatic pressure. In such cases the tension behaviour of these concrete elements are effectively controlled by the b_1 factor rather than b_2, and this adds another layer of consideration in the choice of the b_1 factor (or a similar parameter in other damage-plasticity category of models).

Take the modified η-λ curve with λ_u=0.004 as an example, a range of different b_1/b_2 values are examined and results are plotted in Fig. 4.15. Clearly (as obvious from Eq. 3.2), the influence of b_1 to the stress-strain response gets larger when the hydrostatic pressure increases, and the stress-strain relation is rather sensitive to the b_1 value under uniaxial compression.

Taking the various factors into account, it appears that using the exponential η-λ curve with λ_u=0.004 and an adjusted b_1=1.2 are suitable to achieve a balanced effect, both physically and numerically. The corresponding behaviour of the

resulting material model under general confined compression is checked and the results are shown in Fig. 4.16. The comparison with the original KCC model in the confined compression region do not differ significantly, indicating that the recommended modifications for rectifying the tension/shear softening behaviour would not introduce significant side effect when it comes to general compression regime.

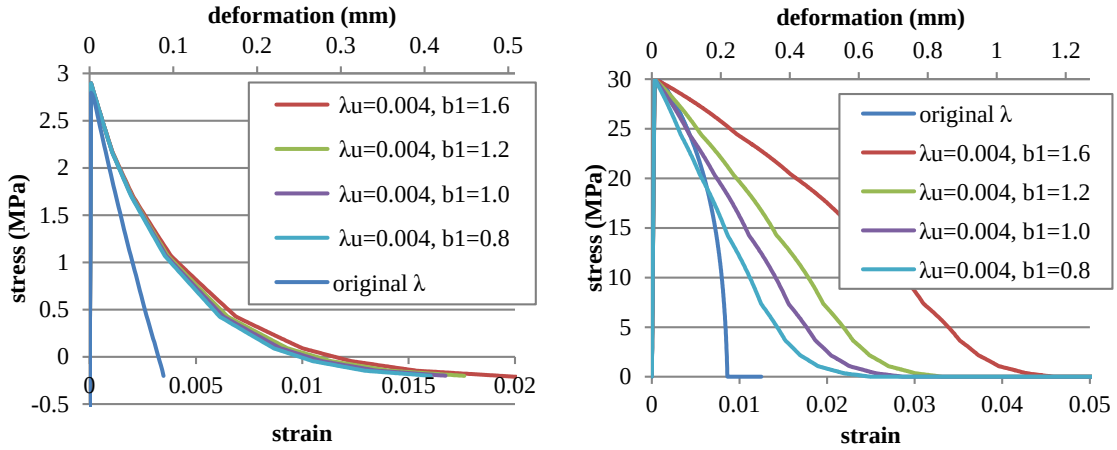

a) Confined tension (pressure = 1.5MPa) b) Uniaxial compression

Fig. 4.15 Influence of b_1 value on stress-strain curves (element size = 25.4mm)

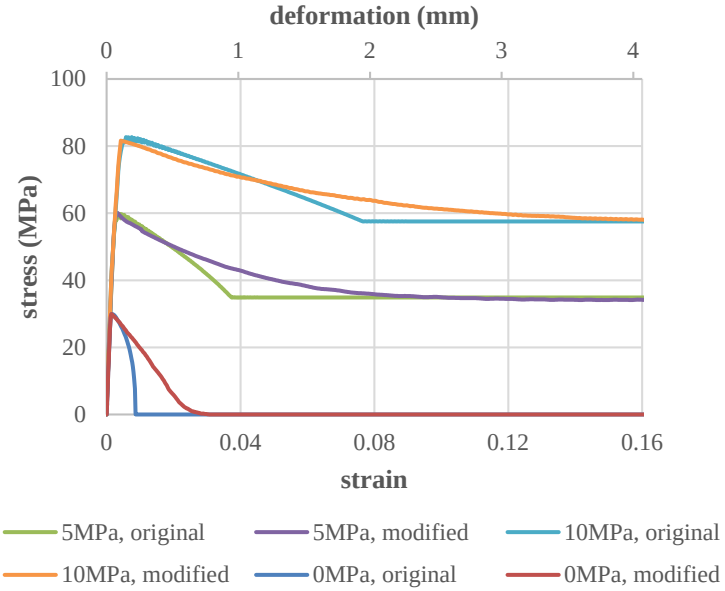

Fig. 4.16 Stress-strain curves under confined compression after modification (element size = 25.4mm)

4.4 Simulation of RC response using modified KCC model

The modification proposed in Section 4.3 has shown to work well in rectifying the tension-softening behaviour while maintaining the original model behaviour in general compression regimes. In this section, the modification to KCC model is further verified through the numerical simulation of pull-out test and response of RC members discussed earlier.

4.4.1 Validation of the proposed modification in a pull-out setting

Fig. 4.17 presents the bond-slip relation for the pull-out tests analysed in Section 4.2.1, using the modified KCC model with b_1 being modified to 1.2 and λ_u set as 0.004.

As can be observed, both the maximum bond strength and subsequent softening branch of the bond-slip displacement curves are greatly improved by the proposed modification to the material model. The renewed simulation results, especially in the post-peak softening portion, compare favourably with the experiment results.

The proposed modification is also applied to the beam-element rebar model in the same pullout experiment, and the simulated results confirms previous finding that the beam-element modelling for rebar is not suitable for such problems where shearing/tension around the rebar plays a governing role in the overall response. As shown in Fig. 4.17c and Fig. 4.17d, despite some obvious improvement in the post-peak softening portion of the bond-slip curves, the maximum “bond” strengths in both cases remain to be significantly under-predicted as compared to the experimental results.

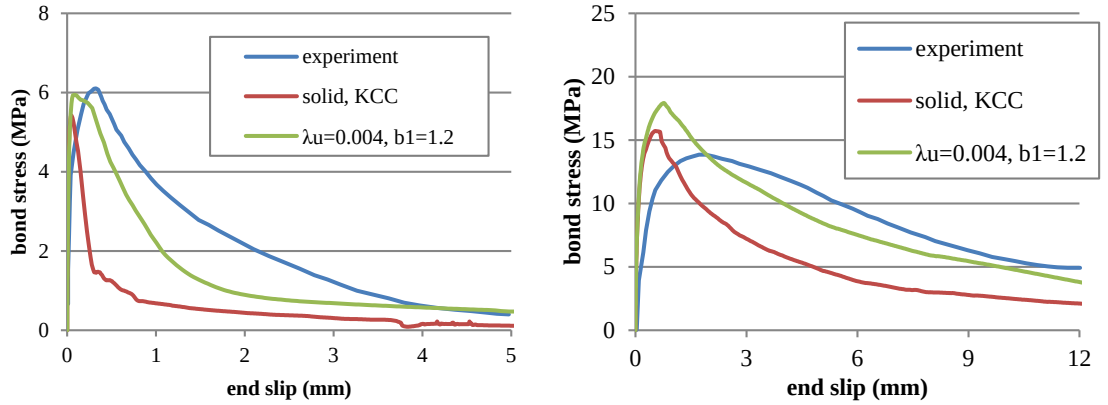

a) Specimen without stirrups (solid-rebar) b) Specimen with stirrups (solid-rebar)

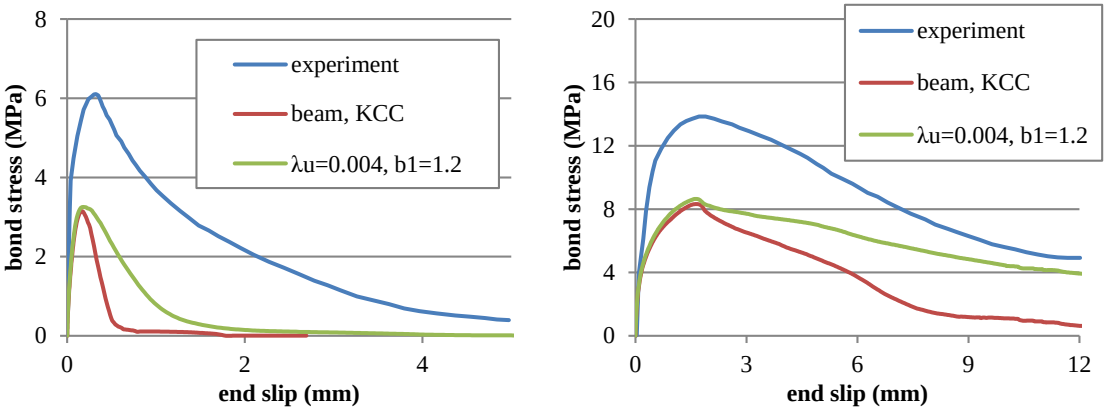

c) Specimen without stirrups (beam-rebar) d) Specimen with stirrups (beam-rebar)

Fig. 4.17 Bond-slip relations using modified KCC model

4.4.2 Simulation of the RC beam and slab response using the modified KCC model

Fig. 4.18 shows the updated load-deflection response for the RC beam using the modified η-λ curve with λ_u being 0.004 while b_1 is modified to 1.2. It can be observed that the simulated response using the modified material model improve drastically as compared to the original model and the predicted response now agrees satisfactorily with the experimental result.

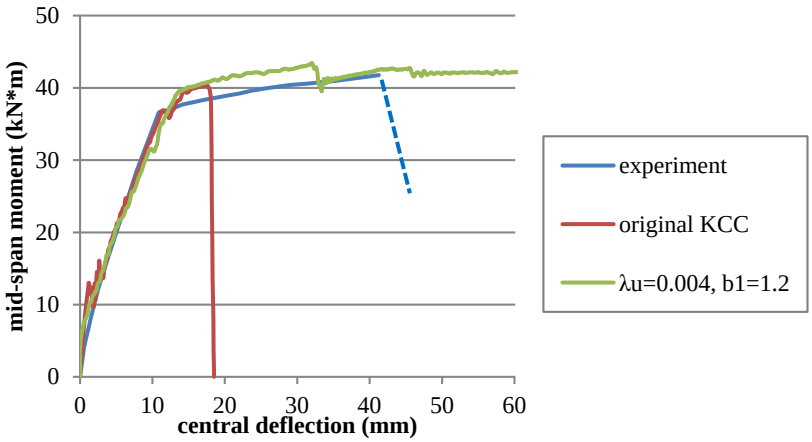

Fig. 4.18 Central deflection – mid-span moment curves of RC beam under quasi-static load using modified KCC model

The modified KCC model is also employed to simulate the RC slab response to the blast load described in earlier section. The same modification to the η-λ curve with λ_u=0.004 and the setting of b_1=1.2 is used. Fig. 4.19a shows the new deflection response time histories. The simulation results using the modified KCC model again shows a characteristic improvement. The simulated maximum deflection is 113.2 mm, which is very close to the measured 108.2 mm. From the damage (crack) patterns presented in Fig. 4.19b, it can be seen that with the modified KCC model the abnormal damage along the rebar and in the shear span disappear. The simulated crack distribution is similar to that obtained with the CSC model shown in Fig. 3.16, and both agree favourably with the experimental observations.

From the above analyses it can be generally established that for a general damage-plasticity concrete material model like KCC to extend its satisfactory performance into applications where the response in the relatively low pressure regime may play an important role, an appropriate description of the softening behaviour in shear/tension can be crucial. As far as the KCC model is concerned, a modification to the η-λ law in conjunction with adequate control of the softening factor (b_1) are deemed to be necessary, and the recommended

modifications prove to work out fairly satisfactorily in the cases under considerations.

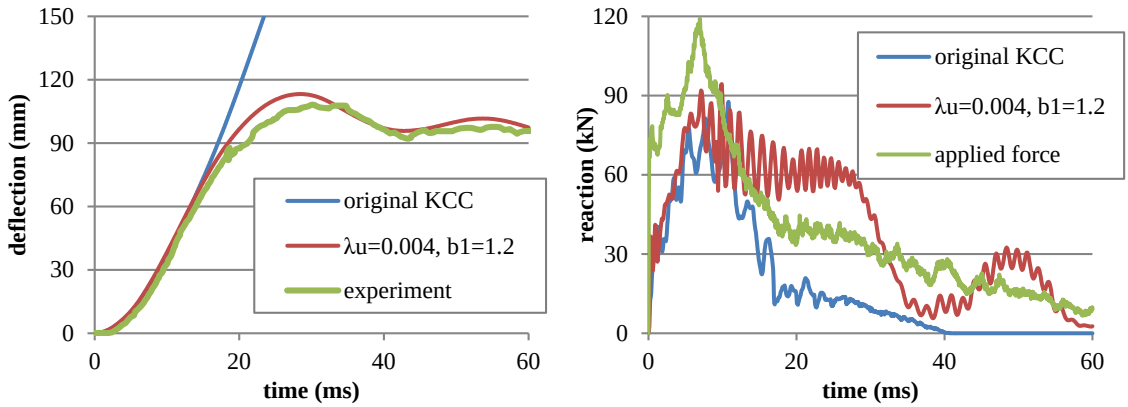

a) Deflection and reaction force time history

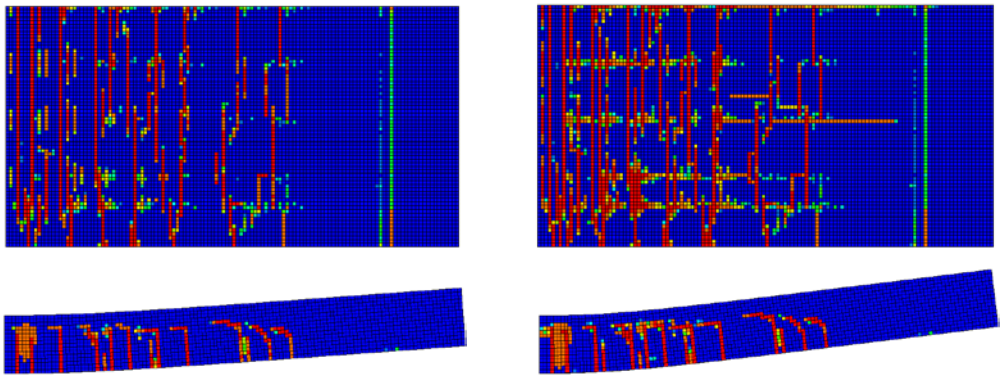

t=10ms t=14ms

b) Damage pattern with modified KCC model (SDF: 1.97~2.00)

Fig. 4.19 Re-calculated RC slab response to blast load using modified KCC model

4.5 Further validation against RC beam experiments tested at University of Edinburgh

The overall modelling framework for RC components and the modification of the KCC material model are further validated for their performances in capturing the global structural behaviour of RC members against some recent experiments of RC beams conducted at University of Edinburgh. One of the specific purposes of

the experiments was to generate benchmark data for RC beams with relatively well defined concrete to steel rebar bond conditions, including cases where no stirrups were provided. The experiments were conducted under quasi-static loading, but as far as validation of the FE model in terms of their ability of representing the global structural behaviour, comparison to the response under a quasi-static load would be sufficiently instructive.

4.5.1 Experimental programme and numerical modelling

A series of RC beams were tested at the Structure Lab at the University of Edinburgh. The tested beams had the same length of 2m and a cross-section of 200 mm×100 mm. Four-point loading scheme was adopted and the clear span was kept as 1.7 m, and the shear span was 0.57 m, which left an overhang length of 150 mm on side, while the pure bending middle segment was also 0.57 m. Fig. 4.20 illustrates the test specimens.

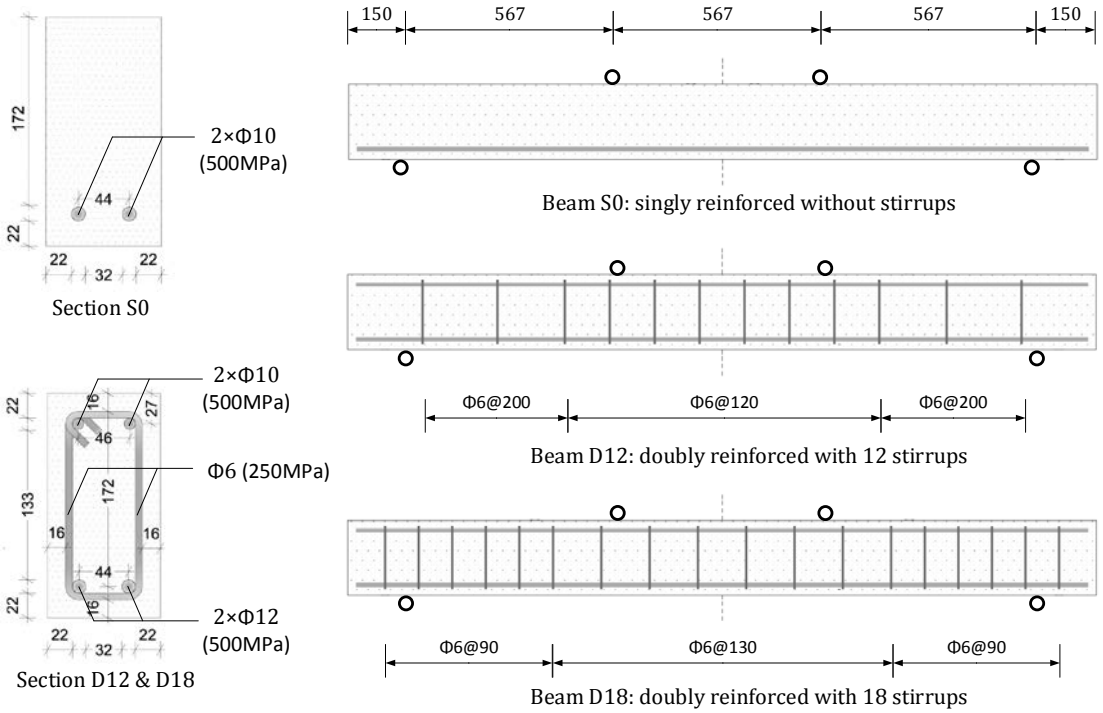

Fig. 4.20 Dimensions and cross-section of the RC beam specimens

One singly-reinforced beam, marked as S0, was reinforced by two British 500C deformed rebar that has a diameter of 10 mm. Two doubly-reinforced beams, marked as D12 and D18, were reinforced by two 10 mm rebar in compression and two 12 mm rebar in tension. The transverse rebar was made of plain 250 MPa steel, and the difference between beam D12 and D18 lies in the spacing of stirrups, as identified in Fig. 4.20. The material properties of the concrete are given in Table 4.1.

Table 4.1 Properties of concrete in the RC beam test

Material property	*Value*
Density	2480 kg/m3
Compressive strength (cubic)	44 MPa
Compressive strength (cylinder)	36 MPa
Tensile strength (MPa)	3.32 MPa

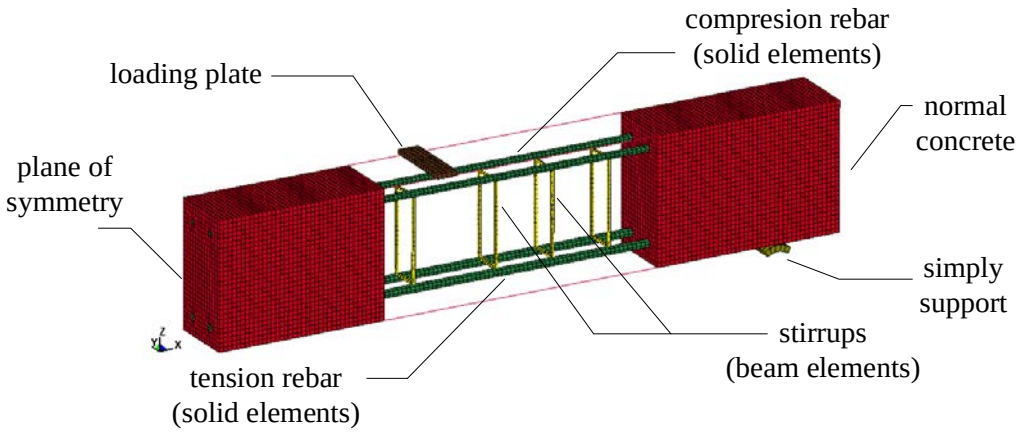

Fig. 4.21 Schematic view of FE model for RC beam

The RC beam is modelled in a similar way as in the modelling of the RC slab and beam simulation described in Section 3.3, and only half of the specimen is modelled because of symmetry. The longitudinal steel rebar is modelled by solid elements while the transverse stirrups are modelled by beam elements. Concrete is modelled by solid element using the modified KCC model. The mesh size is

chosen to be 7 mm and all together around 61,000 elements are involved in the FE model.

4.5.2 Beam S0 & D12: diagonal tension failure

The Beam S0, which has no transverse shear links and was loaded at a shear-span-to-effective-depth ratio of 3.2, experienced a typical diagonal tension shear failure during the tests, as shown in Fig. 4.22a. The load-displacement curves as predicted by numerical simulation is presented in Fig. 4.22b. Despite it gives a similar load-displacement curve, the FE model with original KCC model actually failed at an earlier stage, due to loss of anchorage and "tunnelling" of concrete along the tension rebar, as shown in Fig. 4.22c. The model with proposed modified KCC model, on the other hand, gives a reasonable prediction of the diagonal tension failure, as shown in Fig. 4.22d.

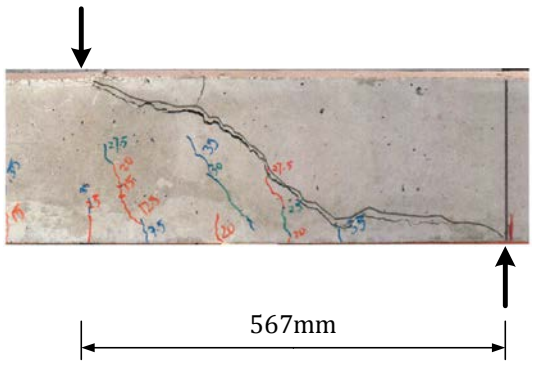

a) Crack pattern in test

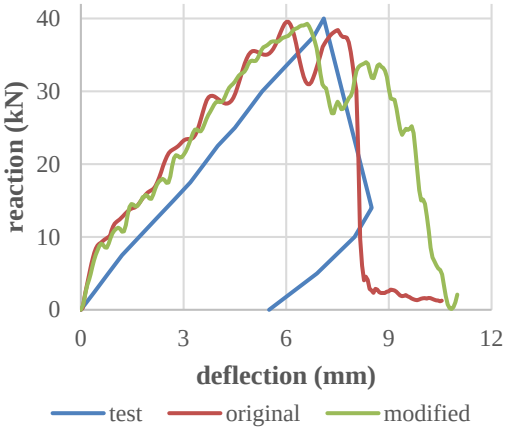

b) Load-displacement curves

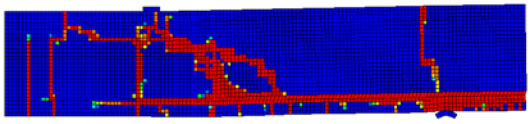

c) Damage contour (original KCC)

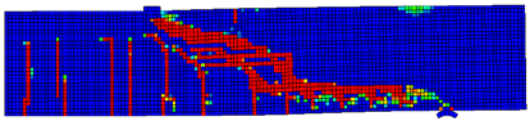

d) Damage contour (modified KCC)

Fig. 4.22 Comparison between numerical response and test data for beam S0

The Beam D12, which was transversely under-reinforced with stirrups placed at a spacing of 200 mm, also failed in a diagonal tension mode during the experiment, as shown in Fig. 4.23a. The FE model results are shown in Fig. 4.23b-d. Comparing to the original KCC and modified KCC results, the overall resistance is generally the same but the original KCC model apparently exhibited a much reduced deformability. The modified KCC model shows a favourable comparison with the experiment curve (note that in the experiment the test was terminated after the peak was reached, hence no post-peak stage of the response). The damage pattern at failure with modified KCC model, as presented in Fig. 4.23d, agrees quite favourably with the experimental observations.

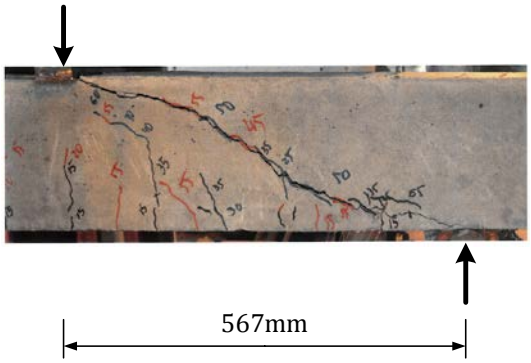

a) Crack pattern in test

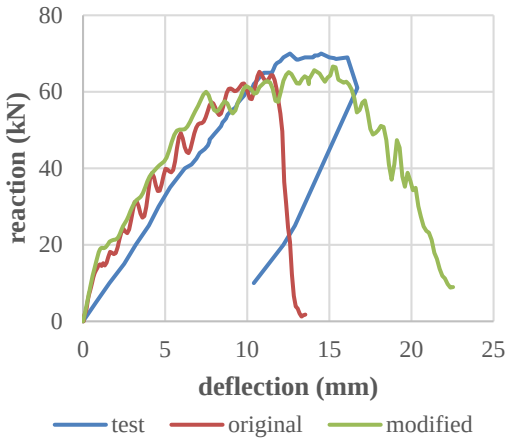

b) Load-displacement curves

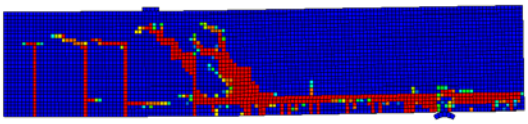

c) Damage contour (original KCC)

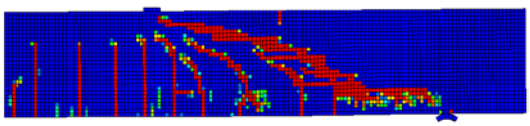

d) Damage contour (modified KCC)

Fig. 4.23 Comparison between numerical response and test data for beam D12

4.5.3 Beam D18: flexure failure

The Beam D18, which was designed to have sufficient transverse reinforcement and was loaded at a shear-span-to-effective-depth ratio of 3.2, experienced flexural failure during the test, as shown in Fig. 4.24b. This is successfully simulated by the model with the modified KCC model. Again, the original KCC model tended to fail due to premature loss of the "bond" interaction between concrete and rebar.

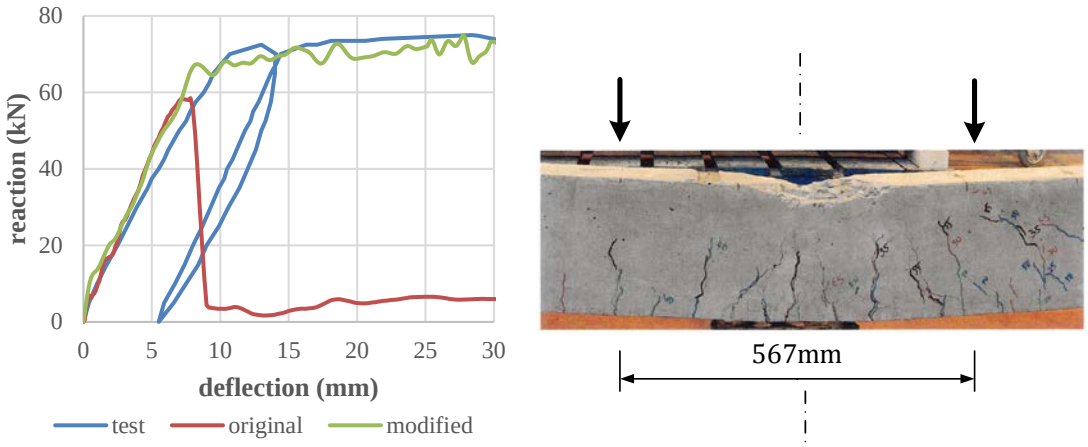

a) Load-displacement curves b) Crack pattern in test

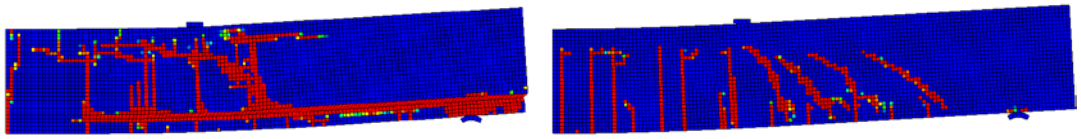

c) Damage contour (original KCC) d) Damage contour (modified KCC)

Fig. 4.24 Comparison between numerical response and test data for beam D18

4.5.4 Overall comment on the performance of simulating RC shear failure

For typical RC structures, before shear failure the state of stress in the shear region of a cracked RC member differs considerably from what is predicted by the theory of linear elasticity. It is well acknowledged (ACI 445R-99, 2000) that the following mechanisms play vital parts in the shear transfer: 1) shear stresses

in uncracked concrete, i.e., the flexural compression zone; 2) aggregate interlock and crack friction; 3) dowel action of the longitudinal reinforcing bars; and 4) arch action.

As demonstrated in Section 3.2, it is generally understood that the KCC model can predict soundly the concrete behaviour under uniaxial and bi-axial compression, as well as simple shear and tension scenarios. In the meantime, with the proposed modification, the KCC performance of dealing with complex stress conditions, such as interaction between rebar and concrete, has been significantly enhanced.

Although current FE modelling framework does not cater to aggregate interlock and dowel action in an explicit way, the proposed modification to KCC model incorporates a prolonged softening curve which is capable of maintaining a minimum residual strength. The fact that there is a significant descending (softening) branch after the peak tensile stress is reached also improves the modelling of the interaction between concrete and rebar in anchorage region. The satisfactory comparisons in terms of the shear resistance for all the specimens which failed in global shear in the experiments are a testament that the FE model with the modified KCC is competent for explorations into the dynamic shear resistance mechanisms, which will be presented in the subsequent chapters.

4.6 Conclusions

An examination of the model behaviour in a classical pull-out scenario confirms that with the default KCC model the premature failure mode due to loss of rebar-concrete interactions tends to be inevitable. Securitisation of the detailed pull-out response suggests that the particular issue with the KCC model indeed originates from the abrupt descending of the material towards a zero strength

state, and as such in a tension/shear dominated response phase the interaction between the steel rebar and the surrounding concrete can diminish quickly causing premature total failure.

By examining the two rebar model schemes it is also found that modelling rebar with a line/beam element will not fundamentally change the stress condition in the concrete in the interface region, however it can become problematic when a refined mesh size is adopted and it also tend to render the behaviour of concrete material adjacent to the rebar to be more sensitively influenced by the mesh size. Further analysis leads to the observation that the transverse reinforcements in RC components would in effect help alleviate the demand on bond interaction between concrete and the longitudinal reinforcement.

Rectification of the KCC model problem is then focused on realising a more gradual softening (descending) phase of the tensile and shear behaviour, including in the conditions where an appreciable hydrostatic pressure is involved. The proposed modification includes a modified damage law, i.e. the η -λ curve, as well as an adjustment of the plastic strain accumulation factor b_1 of KCC model. With the proposed modification, the KCC model is found to behave rather satisfactorily in modelling the pullout behaviour, as well as in the modelling of the RC slab and beam responses under blast and quasi-static load situations.

The overall FE modelling framework, together with the proposed modification for KCC model, are further validated against quasi-static RC beam experiments. Results suggest satisfactory comparisons in terms of the shear resistance for all the specimens which failed in global shear in the experiments.

Chapter 5: An equivalent transitional layer model for modelling concrete-rebar interaction

5.1 Introduction

As discussed in Chapter 4, the basic rationale behind the perfect-bond hypothesis is that the deterioration of interaction between rebar and concrete to a large extent can be replicated by the failure of concrete elements attached to the rebar elements. The stress state and damage process of these elements can be influenced by the conditions in the interaction zones, and as such it requires the material model, especially the shear and tension behaviour, to be less sensitive to a certain variation of the stress conditions. With the proposed modification in Chapter 4, the performance of KCC model is found generally satisfactory when the rebar and concrete are simulated by solid elements.

However, in a more practical application scenario, the rebar is often simulated by one-dimensional beam or link elements embedded in the concrete. The stress state of the elements attached to the rebar is greatly distorted, and the material in such elements is actually fictitious and may not be represented well if a normal concrete material model is employed straight away.

In this chapter, an equivalent transition layer (ETL) model is proposed to provide a numerical description of the phenomenological interaction between the rebar and adjacent concrete. This model is built from the existing KCC model framework, and is aimed to be capable of predicting both pull-out and splitting failures in cases where the main rebar is modelled as a one-dimensional element.

5.1.1 Characteristic of bond interaction between concrete and rebar

The mechanism of bond interaction between deformed rebar and surrounding concrete is comprised of three major factors: chemical adhesion at the interface, mechanical interlock of ribs, and friction. Except in the adhesion stage, the use of the term 'bond' is generally accepted in a broader sense to describe the gross interaction between rebar in concrete.

The bond transfer mechanism generally occurs in a finite zone surrounding the rebar. Many researchers (Cox and Herrmann 1998, Eligehausen et al., 1982) have defined a cylindrical volume around the rebar as the "bond process zone", the radius of which bounds the crushing and transverse cracks produced by the mechanical interaction, and is chosen in the range of 1~2 times of the rebar diameter. From an experimental point of view, this means a process zone surrounding the rebar needs to be defined, and the so-called "slip" actually includes the deformation of this zone. If an analytical model of the interface has zero thickness, its characteristics will have to be derived indirectly by reproducing the measured bond-slip at a specific distance from the rebar.

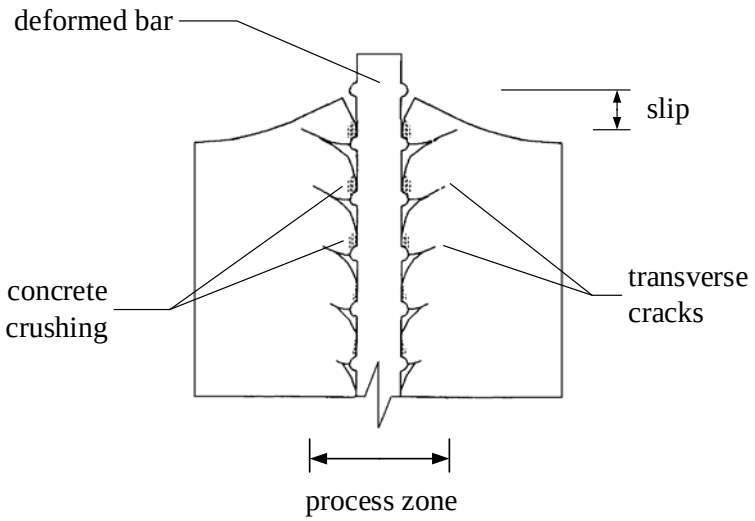

Fig. 5.1 Transfer mechanism of bond interaction between concrete and rebar

At the early loading stage, chemical adhesion is the main load-transfer mechanism at the interface. It quickly breaks down as interfacial cracks initiate, and is then replaced by the wedging action concentrated around the rib faces, as shown in Fig. 5.1. As the rebar force increases, the bond interaction reaches its maximum value and concrete adjacent to the contact area will start to fail in two possible ways: a) crushing due to concentrated compression, and b) transverse cracking initiated from tip of the ribs. The extent of such cracks defines a region of process zone, as illustrated in Fig. 5.1.

The concrete in front of the ribs continues to crush gradually, which explains the non-linear softening behaviour as shown in Fig. 5.2. Once enough crushing has occurred, the concrete between rugs is completely sheared off and the rebar is then pulled out from the concrete. The only mechanism at this stage is frictional resistance between rough concrete at the cylindrical surface.

As the loading processes, tangential splitting force can also be developed due to increasing radial pressure caused by the wedging action and the crushed concrete. Without adequate constraint, longitudinal splitting failure can occur at a much earlier stage, as presented in Fig. 5.2.

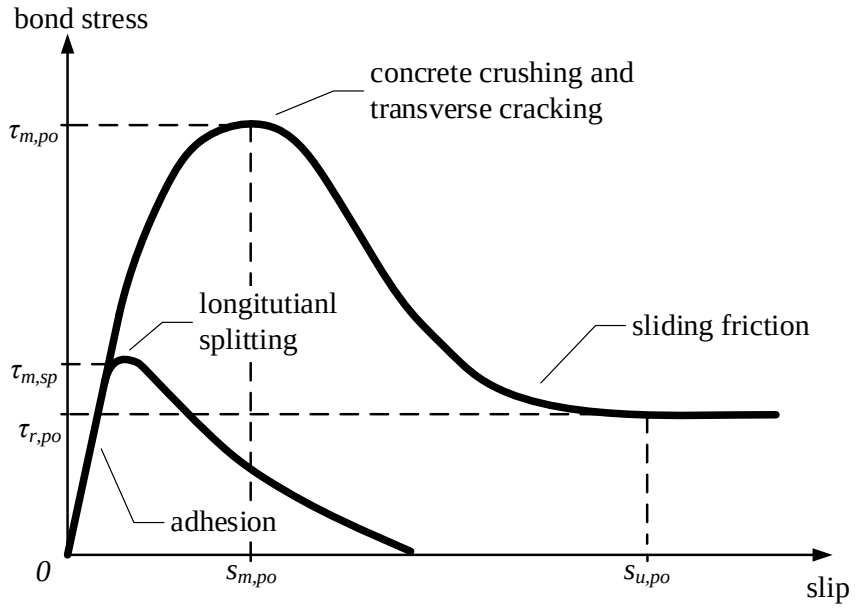

Fig. 5.2 Analytical monotonic bond stress-slip relationship

A number of researchers have investigated the influence of various system parameters on bond response. According to the ACI state-of-the-art report (ACI Committee 408, 1992), parameters that determine bond strength and slip history include concrete strength, bar size, bar spacing, concrete cover and the deformation pattern on the surface of the rebar. Typical bond-slip relations for splitting and pull-out failure as recommended by CEB Mode Code 2010 is given by:

$$\begin{cases} \tau_{m,po} = 2.5\sqrt{f_{ck}} \\ \tau_{r,po} = 0.4 \cdot \tau_{m,po} = 1.0\sqrt{f_{ck}} \\ s_{m,po} = 1mm \\ s_{r,po} = c_{clear} \end{cases} \qquad \begin{cases} \tau_{m,sp} = 7.0 \cdot \left(\frac{f_{ck}}{20} \right)^{0.25} \\ s_{m,sp} = s\left(\tau_{m,sp}\right) \\ s_{r,sp} = 1.2 \cdot s_{m,sp} \end{cases} \tag{5.1}$$

where f_{ck} is the compressive strength of concrete, and c_{clear} is the clear distance between ribs in rebar.

5.1.2 Modelling scales and numerical approaches

Considering a finite element modelling framework for reinforced concrete, the cumulative effect of the bond mechanisms has generally been modelled based on three different observation scales (Cox and Herrmann 1998), namely rib-, bar- and member-scale, as shown in Fig. 5.3.

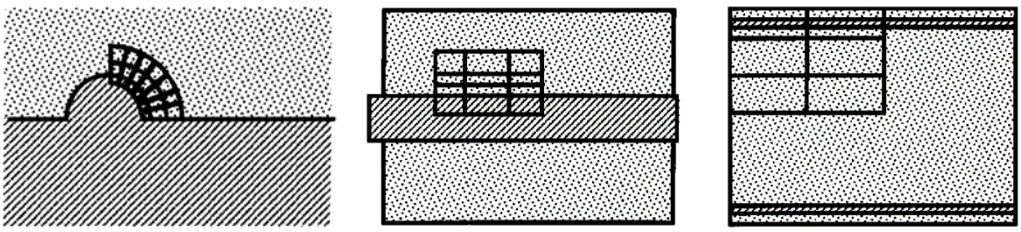

a) Rib-scale b) Bar-scale c) Member-scale

Fig. 5.3 Three scales of bond simulation (after Cox and Herrmann 1998)

In the structural level i.e. the “member-scale”, steel rebar is considered as one-dimensional, and treated as discrete, embedded or smeared in the concrete matrix, which is common treatment for modelling either a structural component or complete structure (Lowes et al. 2004; Ben Romdhane and Ulm 2002; Salari and Spacone 2001; Mutalib and Hao 2011; Magnusson et al. 2010; Shi et al. 2008, 2009). The bond law is normally established in one-dimensional stress relation (i.e. relating bond shear stress to slip), which inevitably neglect the influence of concrete damage state and confining pressure.

At the intermediate bar-scale, both the rebar and concrete are treated as continuums, and the ribs are often seen as homogenised and idealised as an interface, without explicitly including discontinuity between the rebar and concrete (e.g., Casanova et al., 2012; Cox and Herrmann, 1998; Luccioni et al., 2005, to name a few). Compared with member-scale scale, phenomenological representation of radial bond zone response is particularly critical for simulating of splitting-type bond failure and may be necessary for representation of passive confinement provided by transverse reinforcement.

The high-fidelity “rib scale” (or more generally mesoscale) analysis usually includes an explicit discretisation of the ribs on the rebar, and a significantly smaller mesh grid. Some applications include research by Ingraffea et al., (1984), Ozbolt and Eligehausen (1992), Reinhardt et al., (1984), and Rots (1988). In the meantime, simulating bond for large slip at rib scale also requires proper description of material damage state (e.g. post-crushing behaviour) and interface properties, and often involves complexity related to availability of experimental data and computational costs.

The objective of the present research is to develop and validate a model that will characteristically represent the effect in the interface zone including the effect due to the elimination of the rebar space (by using line element), to suit for the needs of withholding realistic member level responses.

5.2 Basic framework and parameter generation for equivalent transitional layer

In the following sections, an equivalent transitional layer model, following the node-sharing assumption, between one-dimensional rebar (beam-element) and the surrounding concrete, is established. The key components of the equivalent transitional layer model include the equivalent stress and strain state, yield criterion and flow rule. Each component is briefly discussed, and how it is implemented in the basic KCC material model framework is explained.

5.2.1 The equivalence objective of the transitional layer between concrete and rebar

The mechanical interaction of the rebar ribs with the surrounding concrete results in a very complex behaviour that includes fracture, crushing and friction,

as depicted in Fig. 5.4a. Under a node-sharing assumption, the overall bond-slip interaction between concrete and rebar is actually represented in an average sense by the local deterioration and failure of the material in the bond zone, as illustrated in Fig. 5.4b.

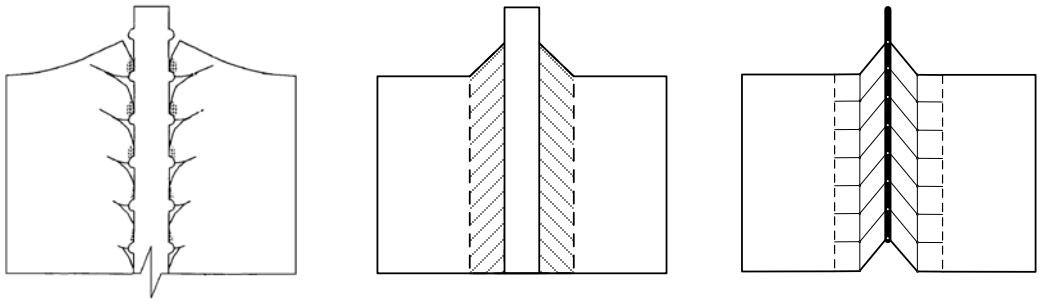

a) Actual bond failure b) Equivalent transitional layer c) FE formation

Fig. 5.4 Schematic representation of equivalent transitional layer

In the meantime, without geometric description of rebar diameter and physical interface with concrete, the material within the bond zone can no longer be regarded as normal concrete. In the context of FE modelling, it is necessary to be considered as an equivalent transitional layer made of artificial material to represent the overall behaviour of the bond zone, and it therefore needs to be applied over the layer of element adjacent to the beam-element rebar, as shown in in Fig. 5.4c. As discussed in Section 5.1.1, this zone, constituted by a local damage region with finite radius surrounding the rebar, is defined in this study as 0.5 d~1.0 d.

The conceptual region called the "bond zone" bounds the crushing and transverse cracks produced by the mechanical interaction but does not contain: a) all longitudinal cracks, some of which can split a test specimen or the cover of a flexural member, or b) transverse cracks that produce a local failure such as a pull-out cone. In the modelling approach taken here, the latter type of cracks must be represented by the deterioration of the equivalent layer, while the former cracks can naturally develop due to the fracture of plain concrete matrix.

In the context of FE modelling, as demonstrated in Fig. 5.4c, the deformation and failure would largely be concentrated within the nearest layer of elements in the equivalent layer. In addition to the idealisation of bond process zone, the transitional layer is also approximated as axisymmetric. So its fully three-dimensional stress state, normally described in the hydrostatic-deviatoric plane, can be represented by axisymmetric tangential and normal stress components.

5.2.2 Equivalent stress state in the transitional layer

The proposed transitional layer model is specially suited for three-dimensional FE analysis, where the reinforcement is modelled by one-dimensional beam elements and concrete modelled by solid elements. It must be noted that the elements in the transitional layer that are effectively pulled by a string of nodes at one edge, is in a severely distorted state.

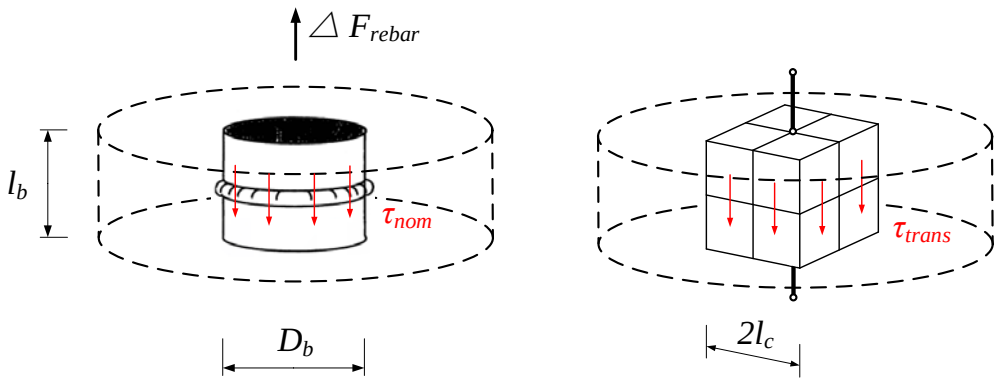

a) Physical representation of bond zone b) FE with beam-element rebar

Fig. 5.5 Equivalent transitional layer between concrete and rebar

Consider a segment of reinforcing bar of diameter of D_b and segment length of l_b, as shown in Fig. 5.5a. In the concrete within a vicinity of the actual rebar surface, the nominal bond stress can be calculated from the differential rebar force over the length l_b and the interfacial area between the rebar and concrete:

$$\tau_{nom} = \frac{\Delta F_{rebar}}{\pi \cdot D_b \cdot l_b} \tag{5.1}$$

Fig. 5.5b gives a typical FE modelling of bond zone as simulated by beam-element rebar and brick-element concrete. It can be seen that the embedded rebar is represented by a string of one-dimensional beam elements, and its interaction with the matrix material is through a column of 2×2 brick elements. So the "bond" stress being transferred through this column of "bond" layer can be expressed by the differential rebar force and the total shear area at the outer side of the layer:

$$\tau_{trans} = \frac{\Delta F_{rebar}}{8 \cdot l_c \cdot l_b} \tag{5.2}$$

where l_c is the size of the brick element. Equating the stress in Eq. 5.2 to the stress in Eq. 5.1, the relation between the nominal "bond" stress τ_{nom} and the shear stress in the transfer layer τ_{trans} can be established as:

$$\tau_{trans} = \frac{\pi D_b}{8 l_c} \tau_{nom} \tag{5.3}$$

Eq. 5.3 suggests that the relation between the shear stress in the transfer layer of the FE model and the nominal (real) bond stress is dependent on both the element size and the rebar diameter.

Besides the shear stress, to describe the full stress state in the transitional layer we also need to look at the radial stress (pressure) that develops as the material expands or contracts laterally. To examine this we can take a cylinder of concrete that encompasses the physical bond process zone, and let the radius of this cylinder be r_c. We examine the equivalence of the pressure-induced stress state between the original rebar scenario and the equivalent one-dimensional rebar with a transitional layer scenario, as illustrated in Fig. 5.6. We assume a generic pressure exists at the outer side of the cylinder, as p_c.

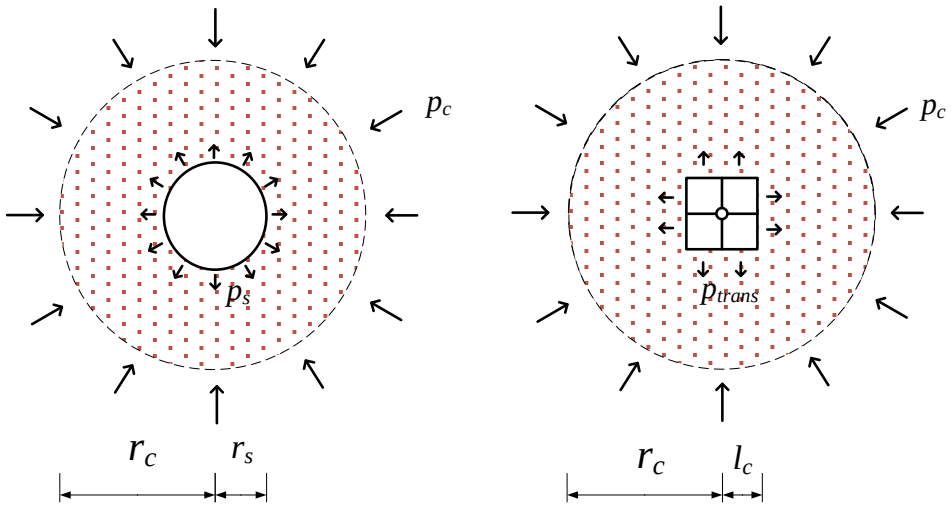

a) Before cracking (actual bond) b) Before cracking (beam-element rebar)

Fig. 5.6 Determination of confining pressure in the transitional layer (pre-cracking stage)

Prior to cracking, the process layer can be regarded as a linear elastic thick-walled cylinder with a core of steel rebar. The outer diameter is r_c and internal diameter is r_s. Assuming the pressure developed at the rebar-concrete interface is p_s. Thus, the cylinder of concrete can be treated as a hollow cylinder subjected to an external pressure of p_c and internal pressure of p_s, for which the hoop and radial stresses have been given by Timoshenko (1976):

$$\begin{cases} \sigma_{r,r}(r) = \dfrac{r_s^2 p_s - r_c^2 p_c}{(r_c^2 - r_s^2)} - \dfrac{(p_s - p_c)\cdot r_s^2 \cdot r_c^2}{(r_c^2 - r_s^2)\cdot r^2} \\ \sigma_{t,r}(r) = \dfrac{r_s^2 p_s - r_c^2 p_c}{(r_c^2 - r_s^2)} + \dfrac{(p_s - p_c)\cdot r_s^2 \cdot r_c^2}{(r_c^2 - r_s^2)\cdot r^2} \end{cases} \tag{5.4}$$

At the surface of rebar ($r = 0.5D_b$) these become:

$$\begin{cases} \sigma_{t,s} = \dfrac{p_s\left(4r_c^2 + D_b^2\right) - 8p_c D_b^2}{4r_c^2 - D_b^2} \\ \sigma_{r,s} = -p_s \end{cases} \tag{5.5}$$

The inner radius (interfacing with rebar) of the concrete cylinder changes by (assuming increase or expansion as positive):

$$\begin{aligned}\Delta r_c &= \frac{D_b(\sigma_t - \nu_c\sigma_r)}{4E_c} \\ &= \frac{D_b p_s}{E_c(4r_c^2 - D_b^2)}[r_c^2(1-\nu_c) + \frac{D_b^2(1-\nu_c)}{4} - \frac{2r_c^2 p_c}{p_s}]\end{aligned} \tag{5.6}$$

where E_c and ν_c is the Young's modulus and Poisson's ratio of concrete.

On the other hand, with a pressure of p_s, the steel rebar undergoes a contraction in radius by (again with positive value as expansion):

$$\Delta r_s = -\frac{D_b p_s(1-\nu_s)}{4E_s} \tag{5.7}$$

where E_s and ν_s is the Young's modulus and Poission's ratio of steel rebar.

The radial deformation of rebar and concrete at the interface (surface of rebar) must be compatible, meaning the change of radius in the inner face of the concrete cylinder and the change (reduction) of the radius of the rebar must be the same, i.e.,

$$\Delta r_c = \Delta r_s \tag{5.8}$$

Substituting Eq. 5.6 and Eq. 5.7 into Eq. 5.8 yields,

$$\frac{p_c}{p_s} = \alpha_e = \frac{1}{2}\left[(1+\nu_c) + \frac{4D_b^2}{r_c^2}(1-\nu_c) + \frac{E_c}{E_s}(1-\nu_c)\left(1 - \frac{4D_b^2}{r_c^2}\right)^2\right] \tag{5.9}$$

Eq. 5.9 applies for elastic range of concrete before cracking. For the case of normal strength concrete and rebar, assuming $E_c \cong 0.1E_s$, ν_c =0.15, ν_s =0.3, and considering the depth of process layer is one time of the rebar diameter, r_c=1.5D_b, the ratio becomes

$$p_s = \frac{p_c}{\alpha_e} = 1.53 p_c \tag{5.10}$$

For the FE model scenario where rebar is modelled by one-dimensional beam element, as shown in Fig. 5.6b, the material inside the cylinder is effectively homogenous. Eq. 5.9 can also be applied to the relation between pressure p_{trans} at the transitional layer and pressure p_c at the outer surface of cylinder, and it reduces to

$$p_{trans} = p_c \tag{5.11}$$

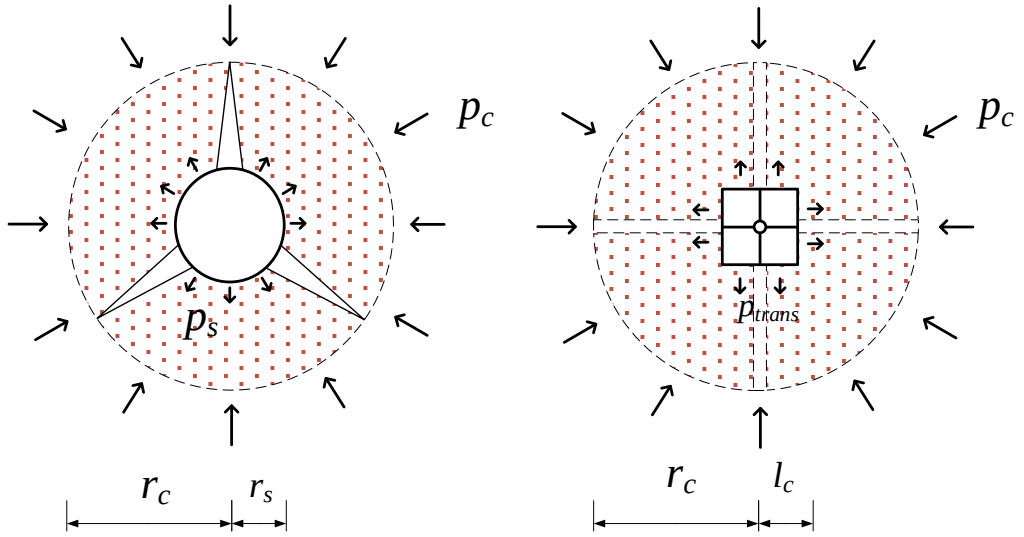

a) After cracking (actual bond) b) After cracking (beam-element rebar)

Fig. 5.7 Determination of confining pressure in the transitional layer (post-cracking stage)

In the post-cracking stage, the stress conditions associated with the pressure can be illustrated in Fig. 5.7a. Assuming cracking happens longitudinally along the rebar (splitting type), the circumferential tensile stress vanishes within the process zone. By equilibrium of a cracked block in the radial direction, we can establish that the pressure is inversely proportional to the radius within the cylinder, and at the rebar position the relation becomes:

$$p_c \cdot r_c = p_s \cdot r_s \tag{5.12}$$

and the ratio between the pressure at the edge of the process zone and at the surface of the rebar is

$$\frac{p_c}{p_s} = \alpha_p = \frac{r_s}{r_c} \tag{5.13}$$

for r_s=0.5D_b and r_c=1.5D_b,

$$p_s = \frac{p_c}{\alpha_p} = 3p_c \tag{5.14}$$

Similarly, when the rebar is described by one-dimensional beam-element as presented in Fig. 5.7b, the pressure in the first layer of elements within the process cylinder, i.e. the transitional layer, is

$$\frac{p_c}{p_{trans}} = \frac{l_c}{r_c} \tag{5.15}$$

Combining Eq. 5.10-11 and Eq. 5.14-15, the relation between the actual pressure at the rebar surface and the pressure in the equivalent layer can be established as:

$$p_{trans} = \begin{cases} \alpha_e \cdot p_s & pre-cracking \\ \dfrac{D_b}{2l_c} \cdot p_s & post-cracking \end{cases} \tag{5.16}$$

As implemented in most FE based damage-plasticity model, the stress state is described in three-dimensional stress space via hydrostatic and deviatoric planes. The alteration of the pressure as indicated in Eq. 5.16 implies that the (shear) strength for the transitional layer of “concrete” material will need to be altered accordingly so that the stress being transferred through the equivalent transitional layer to the rest of the concrete domain will be similar to the situation as through the actual rebar and the bond process zone.

Considering that the transitional layer may be treated as axis-symmetric, the shear stress expressed in the Cartesian coordinates can be written as

$$\begin{cases} \tau_{xy} = 0 \\ \tau_{yz} = \tau_{zx} = \tau_{trans} \end{cases} \tag{5.17}$$

where *z* defines the longitudinal direction of the rebar, and *xy* defines its cross-section. As the transitional layer is in a tri-axial compressive state, assuming the hydrostatic pressure is the same as the radial normal stress. So the hydrostatic pressure $\left(-I_1/3\right)$ and deviatoric stress $\sqrt{3J_2}$ is then calculated as

$$\begin{cases} p = \dfrac{I_1}{3} = p_{trans} = \dfrac{D_b}{2l_c} \cdot p_s \\ \sigma_{dev} = \sqrt{3J_2} = \sqrt{6}\tau_{trans} = \dfrac{\sqrt{6}\pi D_b}{8l_c}\tau_{nom} \end{cases} \tag{5.18}$$

5.2.3 Definition of failure surfaces for the equivalent transitional layer

The three pressure-dependent failure surfaces defined in the standard KCC model can be fitted with suitable parameters to readily result in a pressure-dependent shear stress vs. shear deformation (equivalent of the gross bond-slip) relationship, as schematically illustrated in Fig. 5.8. The three strength surfaces here are made to correspond to the yielding, maximum and residual strength in a gross bond-slip relation.

As an equivalent layer the properties will be defined such that all the mesoscopic effect including the rebar size and deformed surface patterns will be represented through the equivalent strength surfaces. Similar to the evolution of the strength in the standard KCC model, at any state of damage, the prevailing surface is obtained via linear interpolation between the maximum and either the yielding or residual failure surfaces, depending on the accumulated damage level, which

is expressed in the form of plastic strain, which due to the particular load transfer and the resulting stress conditions will be mostly developed through the shearing (slip) deformation.

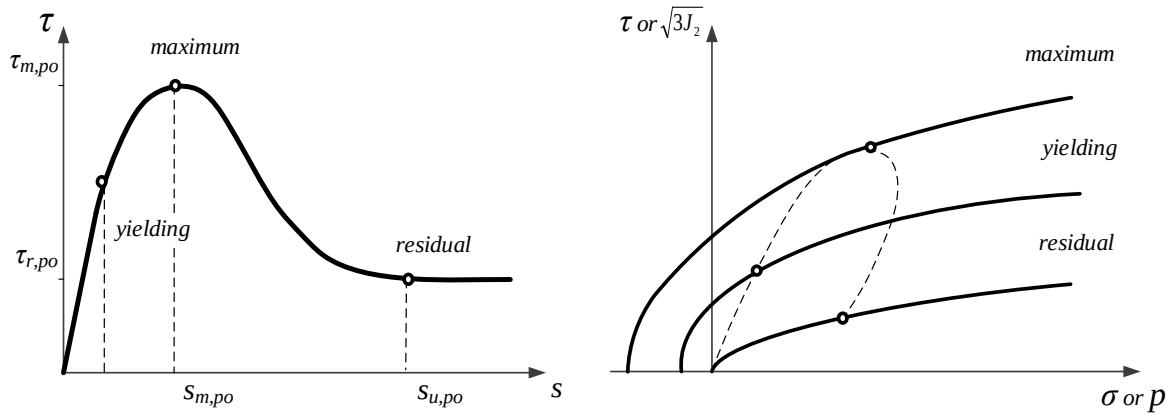

a) Gross bond-slip relation b) shear-normal stress relation

Fig. 5.8 Failure surfaces representing gross bond-slip behaviour of the transitional layer

The experiments performed by Malvar (1991), in which the nominal bond stress at various level of pressures at the rebar surface were derived, are adopted to construct the yield criterion. Fig. 5.9 presents the failure surfaces at the yielding, maximum and residual stages of evolution, as extracted from the experiment of Malvar (1991) by Cox and Herrmann (1998). The “confinement stress” represents the normal compressive stress at the bar-concrete interface assuming the specimen carries no hoop stress, similar to a state illustrated in Fig. 5.7. The tangential and normal stresses are non-dimensionalised by the tensile strength of concrete.

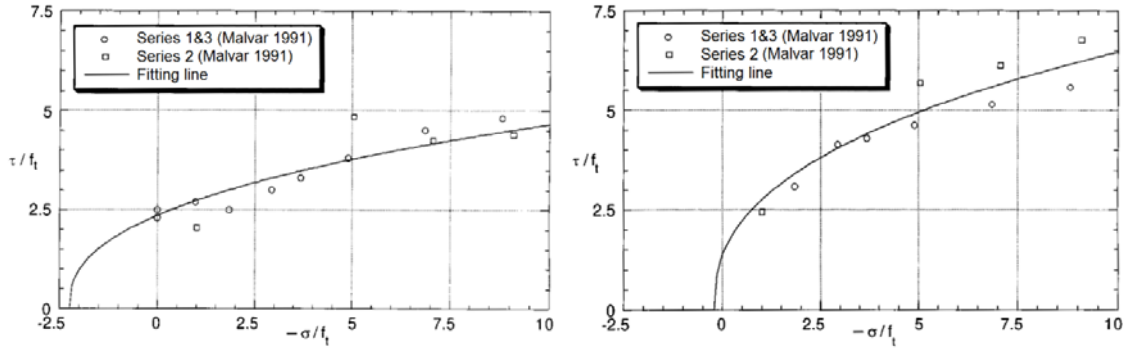

a) Yielding surface b) Maximum surface

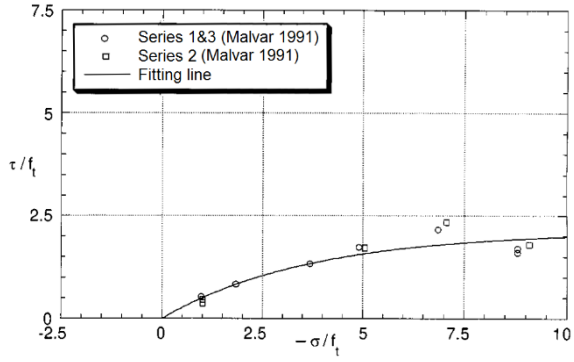

c) Residual surface

Fig. 5.9 Failure surfaces extracted from Malvar's pull-out tests (after Cox and Herrmann 1998)

Following the basic form of failure surface functions as defined in Eq. 3.2, the relation between nominal tangential stress (bond stress) and normal stress (pressure at the rebar surface) presented in Fig. 5.9, can be fitted in the following form:

$$\left(\tau_{nom}\right)_n = a_{0n\_0} + \frac{p_s}{a_{1n\_0} + a_{2n\_0} p_s} \tag{5.19}$$

in which subscript "n" represents "m", "y" or "r" in Eq. 3.2. The eight parameters are then determined as follows:

$$\begin{cases} a_{0m\_0} = 4.5; \\ a_{1m\_0} = 0.6; \\ a_{2m\_0} = 0.04; \end{cases} \quad \begin{cases} a_{0y\_0} = 8.2; \\ a_{1y\_0} = 2.0; \\ a_{2y\_0} = 0.08; \end{cases} \quad \begin{cases} a_{1r\_0} = 2.0; \\ a_{2r\_0} = 0.07; \end{cases} \tag{5.20}$$

The modified failure surfaces with proposed parameters in Eq 5.20 is plotted in Fig. 5.10, and the default parameters in KCC model is also presented for comparison purpose.

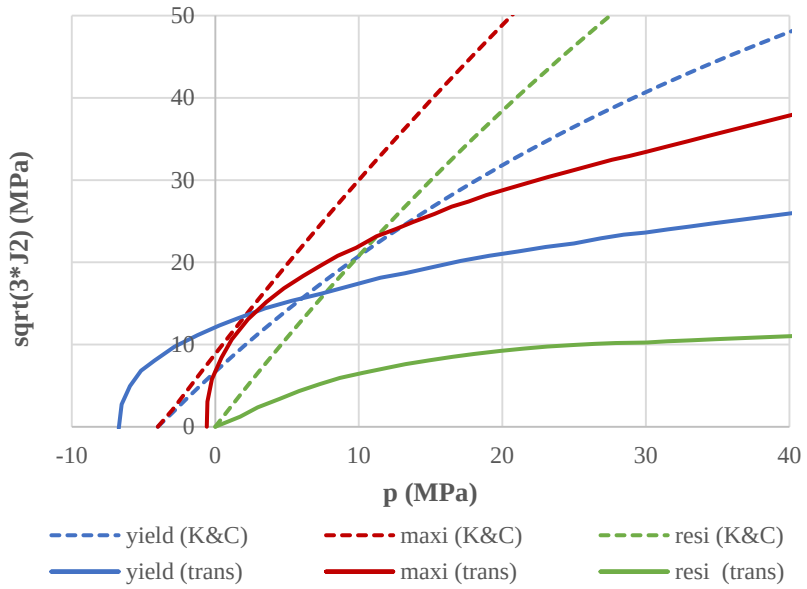

Fig. 5.10 Modified failure surfaces for equivalent transitional layer

The parameters presented in Eq. 5.20 applies to normal concrete with a compressive strength of 30 MPa. If a new concrete with known unconfined compressive strength is to be modelled, a new set of parameters can be scaled from the existing data following the process described in the following.

Considering the mesh size of element l_c, rebar diameter D_b and concrete compressive strength f_{ck}, the relation between the hydrostatic pressure p_{trans} and deviatoric stress $\left(\Delta\sigma_{trans} = \sqrt{3J_2}\right)$ in the equivalent layer, can be determined from the nominal bond stress and pressure at rebar surface. Rewriting Eq.18, a scaling factor can be defined:

$$\begin{cases} r_p = \dfrac{p_{trans}}{p_s} = \dfrac{D_b}{2l_c} \\ r_t = \dfrac{\Delta\sigma_{trans}}{\tau_{nom}} = \dfrac{\sqrt{6}\pi D_b}{8l_c} \cdot \sqrt{\dfrac{f_{ck}}{f_{ck\_0}}} \end{cases} \tag{5.21}$$

where f_{ck_0} is the benchmark concrete compressive strength. Substituting Eq. 5.21 into Eq. 5.20, one can obtain:

$$\left(\frac{\Delta\sigma_{trans}}{r_t}\right) = a_{0n\_0} + \frac{\left(\dfrac{p_{trans}}{r_p}\right)}{a_{1n\_0} + a_{2n\_0}\left(\dfrac{p_{trans}}{r_p}\right)} \tag{5.22}$$

and it can be further expressed as:

$$\begin{aligned} \Delta\sigma_{trans} &= a_{0n\_0} \cdot r_t + \frac{p_{trans}}{\dfrac{r_p}{r_t} a_{1n\_0} p + \dfrac{1}{r_t} a_{2n\_0}} \\ &= a_{0n} + \frac{p_{trans}}{a_{1n} p_{trans} + a_{2n}} \end{aligned} \tag{5.23}$$

So the new coefficients can be expressed as:

$$\begin{cases} a_{0n} = r_t \cdot a_{0n\_0} \\ a_{1n} = \dfrac{r_p}{r_t} \cdot a_{1n\_0} \\ a_{2n} = \dfrac{1}{r_t} \cdot a_{2n\_0} \end{cases} \tag{5.24}$$

in which subscript "*n*" is "*m*", "*y*" or "*r*", representing maximum, yielding and residual surfaces.

5.2.4 Equivalent strain state and "slip" deformation

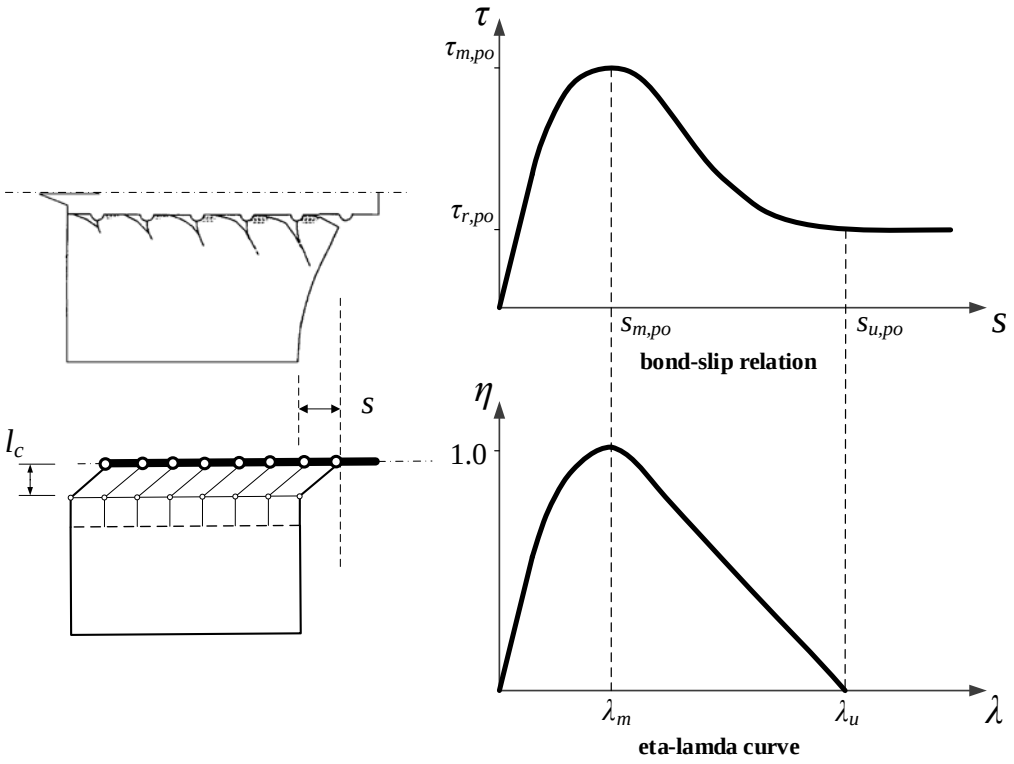

a) Slip deformation in transitional layer b) Damage accumulation in bond-slip

Fig. 5.11 Equivalence of "slip" deformation and modifications for "bond-slip" curves

For the transitional layer, the overall slip displacement is mainly represented by shear deformation in a single layer of elements attached with the beam-element rebar, as shown in Fig. 5.11a. As the shear strain approximately equals to the slip divided by characteristic length, for different mesh size, the shear strain is inversely proportional to the characteristic length.

$$\gamma_{tran} \approx \frac{s}{l_c} \tag{5.25}$$

As discussed earlier in Chapter 3, in KCC model the damage accumulation or softening rate are controlled by the η - λ curve in conjunction with the exponential factor b_1 and b_2 in a comprehensive manner. In particular, the factor

b_1 and b_2 control the rate of damage accumulation under tension and compression respectively. These two factors are set to zero here, so that λ value equals to the effective plastic strain as defined in Eq. 3.3.

To achieve a mesh-independent deformation, the hardening and softening curves are adjusted accordingly to ensure a constant slip displacement. This is realised by modifying the η - λ function in KCC model to match with the bond-slip curve, at two key states, i.e., maximum bond strength state, subscripted by "m", and the residual bond strength state, subscripted by "u", as shown in Fig. 5.11b.

The modification to the η - λ function involves scaling of the λ value. As discussed in Section 5.1.1, the slip at the maximum bond strength and the slip at the starting point of the friction are related to rebar properties and can be determined by Eq. 2.1 in Chapter 2. The modification to λ value can be divided into the hardening part $0 \sim \lambda_m$ and the softening part $\lambda_m \sim \lambda_u$.

For the hardening part, the λ_m can be calculated via the slip $s_{m,po}$ at the maximum bond strength as defined in Eq. 2.1 and a mesh size of l_c,

$$\lambda_m = \frac{s_{m,po}}{l_c} \tag{5.26}$$

For the softening part, as introduced in Section 3.2.3, the tensile/shear softening curve in KCC model is defined with a view to keep a constant fracture energy independent of the mesh size. According Crawford et al. (2012), the original parameterisation was based on a calibration to the tension tests of 100mm (4 inch) specimens, so the portion λ_m - λ_u in the function can be expressed as:

$$\lambda_u - \lambda_m = \frac{s_{u,po} - s_{m,po}}{l_{c100}} \tag{5.27}$$

where l_{c100} = 100 mm, $s_{m,po}$ and $s_{u,po}$ are the slip values at the maximum and residual bond strength as defined in Eq. 2.1. For this study, the adopted values for $s_{m,po}$ and $s_{u,po}$ is based on recommendation of the CEB codes given in Eq. 2.1.

To help understand the modification process, the modified η - λ curves calibrated from the sample test (details given in next section) for varied mesh sizes are presented in Fig. 5.12. The pull-out specimen uses D10 rebar, and the slip displacements $s_{u,po}$ and $s_{m,po}$ are 1 mm and 5 mm, the mesh size is 10 mm. It can be seen from the curves that the hardening part of η - λ is adjusted with mesh size, while the softening portion remains mesh-independent.

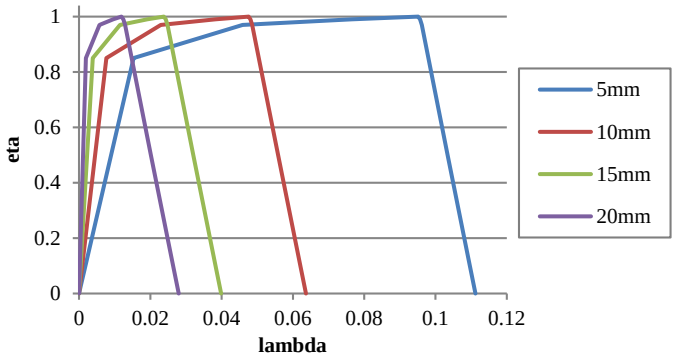

Fig. 5.12 Modified η - λ curves to varied mesh sizes (s_m=1mm, s_u=5mm)

5.3 Validation studies with experiment

In this section the validation of the equivalent transitional layer model for "bond" interaction between rebar and concrete is presented. The performance of the proposed parameter generation method for the KCC model framework in fitting for rebar properties and concrete is verified. The scope of the validation was limited to pull-out type specimens that had relatively short embedment lengths and conducted under displacement control. Experimental data from two different research groups are considered in the validation effort.

5.3.1 Validation with Baena's test

The pull-out tests by Baena et al. (2009) were conducted according to Eurocode 2 and ACI 44.3R-04 standards, to address the influence of rebar surface and diameter on the bond-slip relationship. The concrete specimen was 200 mm cube, with normal strength concrete of a mean compressive strength of 28.6 MPa. The tested steel bars were of diameters 12mm and 16mm, respectively, and the steel bars were embedded by a length of five times of the diameter and placed at the bottom of the concrete cube. A schematic of the specimen is shown in Fig. 5.13a. The pull-out test setup is shown in Fig. 5.13b.

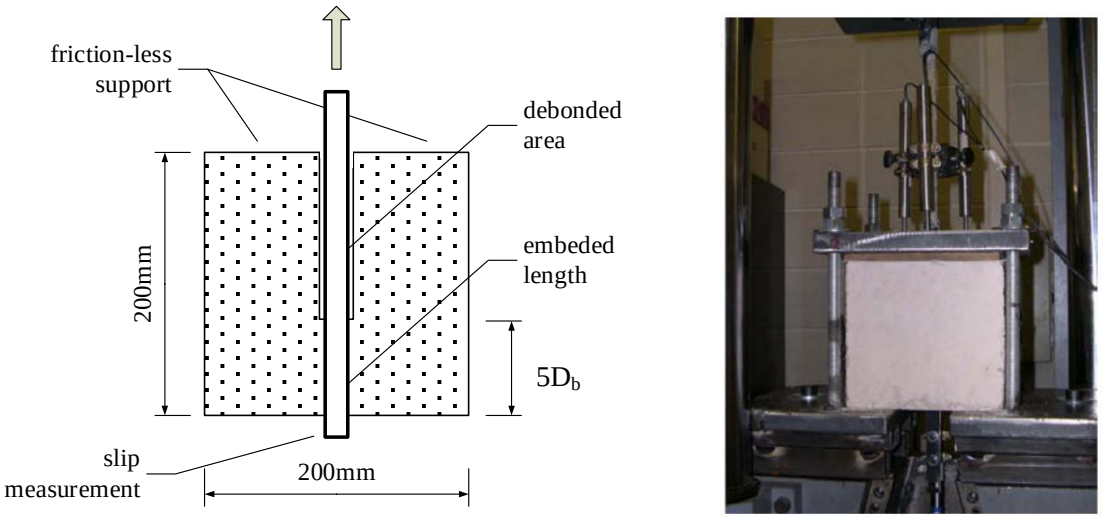

a) Specimen dimensions b) Loading setup

Fig. 5.13 Pull-out test specimen and setup (after Baena et al. 2009)

Fig. 5.14 presents the FE model of the pull-out specimens with the transitional layer model. The width of transitional layer is defined to be $3D_{b,}$ and the mesh sizes of 18 mm, 9 mm and 6 mm are chosen. The parameters for failure surfaces are generated via Eq. 5.21 based on the compressive strength provided in the paper (Baena et al. 2009). The η - λ function is modified according to Eq. 5.26 -

27 based on CEB recommended values of targeted slip at maximum bond resistance and failure.

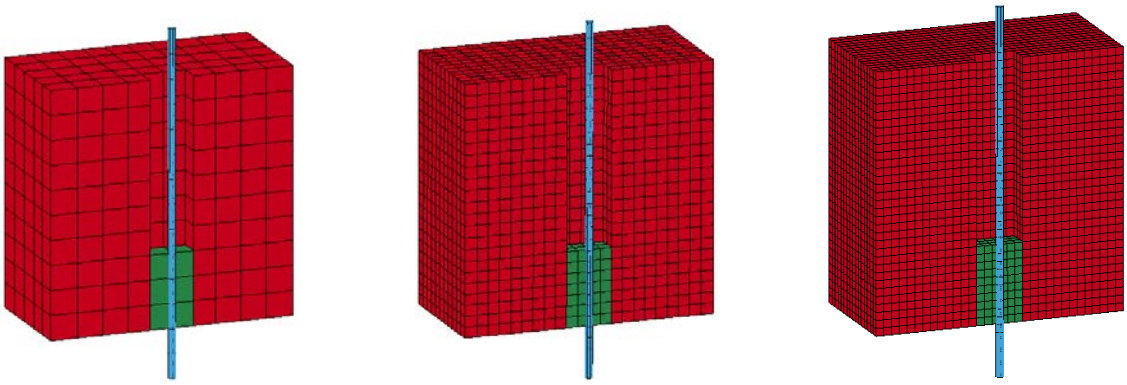

a) Mesh size = 18 mm b) Mesh size = 9 mm c) Mesh size = 6 mm

Fig. 5.14 FE model using transitional layer with varied mesh sizes

Fig. 5.15 and Fig. 5.16 present the simulation results of the bond-slip relations of the steel bars with two different diameters using the transitional layer model, with comparison to the test results. It can be seen that the simulated bond-slip curves from different mesh sizes are almost identical, and the predicted maximum bond strengths in all cases are around 13 MPa, suggesting that the proposed parameter generation is capable of reproducing mesh-independent results.

The predicted bond-slip relations presented in Fig. 5.15 for the rebar with D_b = 16 mm agrees quite well with the experiment result, while in the case where D_b = 12 mm the transitional layer model tends to underpredict the residual bond resistance in the friction stage. This could be further improved by calibration to the residual failure surface in Eq. 5.20, but given that the real behaviour in the "bond" softening stage can involve large uncertainty, the results from the proposed transitional layer model may be regarded as satisfactory in both types of rebar cases.

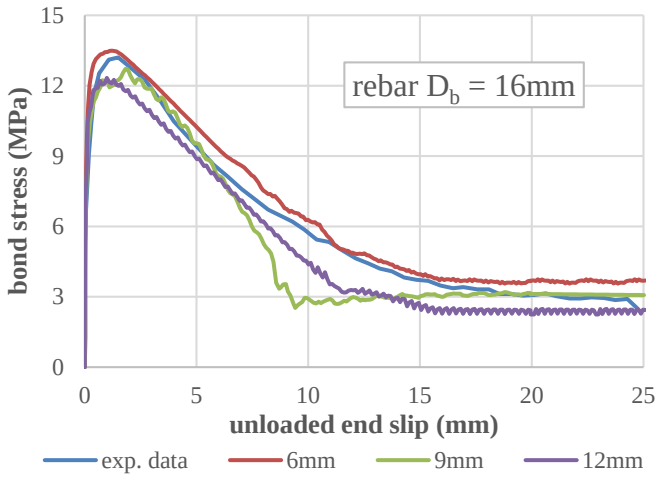

Fig. 5.15 Numerical bond-slip curves for rebar with a diameter of 16 mm

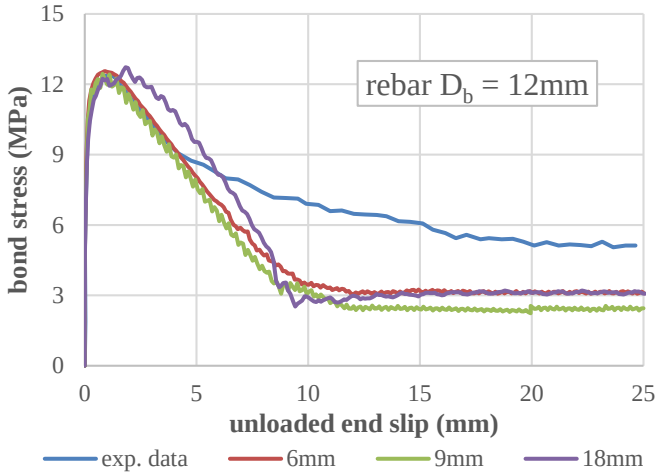

Fig. 5.16 Numerical bond-slip curves for rebar with a diameter of 12 mm

5.3.2 Validation with Eligehausen's test

The pull-out tests conducted by Eligehausen et al. 1982, as discussed earlier in Chapter 3, is re-visited and further employed here to verify the proposed transitional layer model. The experiment was designed to represent the stress history found in the highly confined region of a beam-column connections. Details of the experiment plan can be found in Section. 4.2.1.

The FE model of the pull-out specimen is built in a way similar to Section. 4.2.1, with the rebar being simulated by beam elements and the proposed transitional layer is applied, as presented in Fig. 5.17. The transitional layer is considered to be 64 mm wide ($2.5D_b$) for the whole specimen (shown as 32 mm in the quartier model shown in Fig. 5.17a). The mesh size is set as 5.6 mm. The parameters for

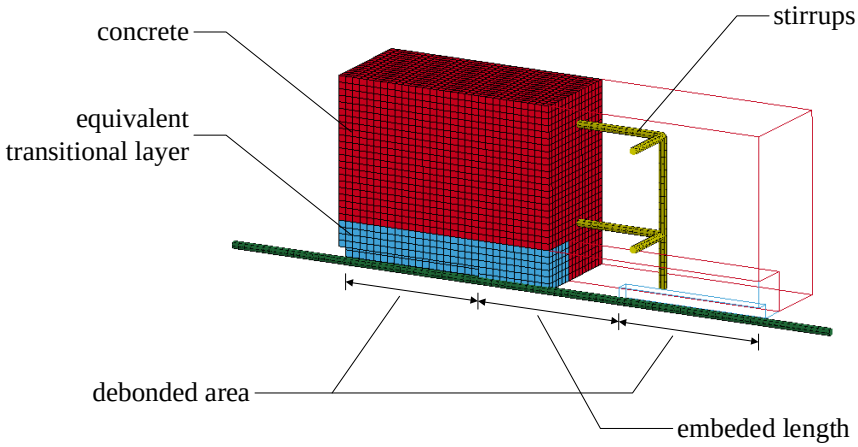

a) Pull-out specimen with equivalent transitional layer

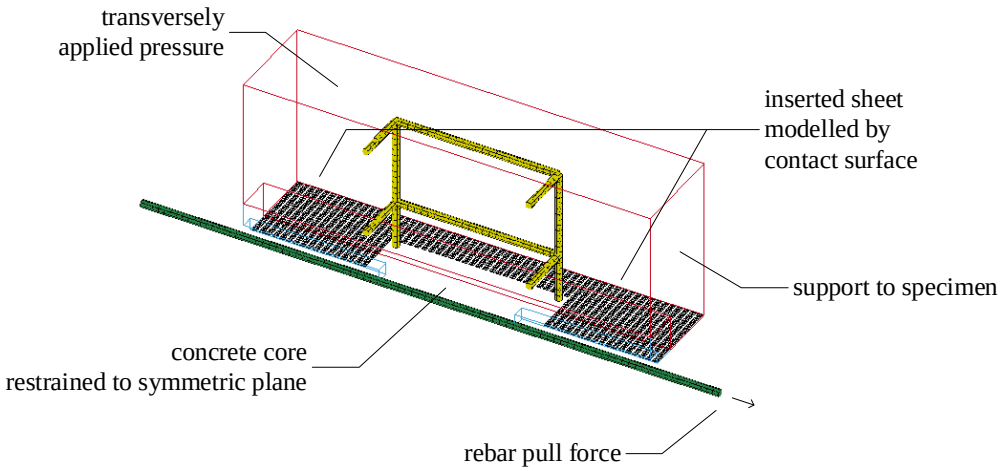

b) FE implementation of the plastic sheet

Fig. 5.17 Numerical implementation of the plastic sheets

failure surfaces are based on normal concrete with a compressive strength of 30 MPa and the slip value $s_{u,po}$ in Eq. 5.27 is set as the length of the diameter. The

simulation of the plastic sheet used in the original experiment (Eligehausen et al. 1982) is shown in Fig. 5.17b.

The cases of RC specimen with and without extra stirrups, previously discussed in Section 4.2, is re-checked here. The comparison among FE results using the original approach in Section 4.2.1, and the proposed transitionally layer model, together with the experimental data, is presented in Fig. 5.18. It can be seen that, the bond-slip relations predicted by the transitional layer model have improved markedly from the original simulation, and agree favourably with the experiment result.

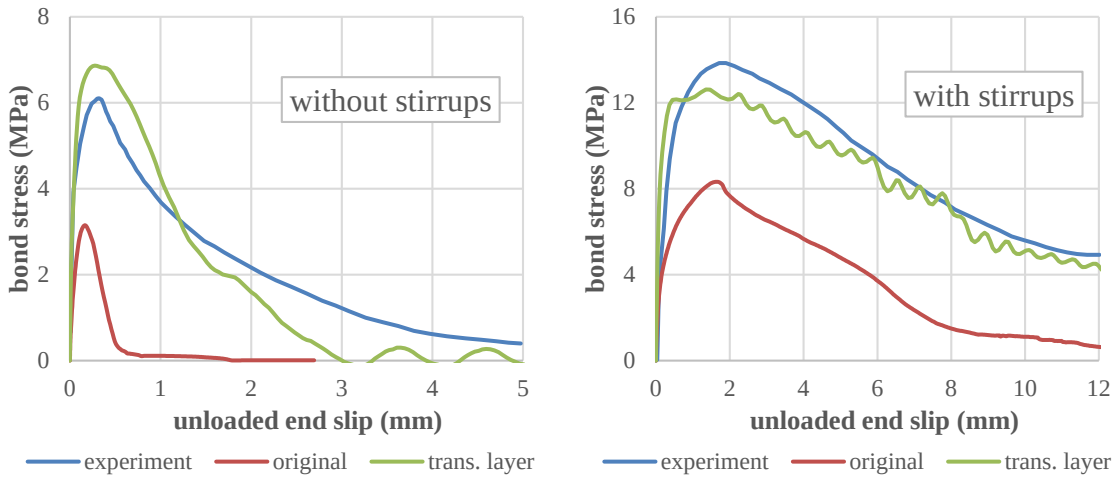

a) Splitting failure b) Pull-out failure

Fig. 5.18 Modelling bond-slip relationship with transitional layer

The effect of confining pressure on the bond-slip relation is investigated in Fig. 5.19. The pressure is externally applied on the surface of the concrete specimen, as presented in Fig. 5.17b. As can be observed from the results, the general trend of overall bond strength increase with the confining pressure is captured by the proposed equivalent transitional layer. The key slips at the peak and ultimate residual strength, which are determined by the η - λ relation, remain constant.

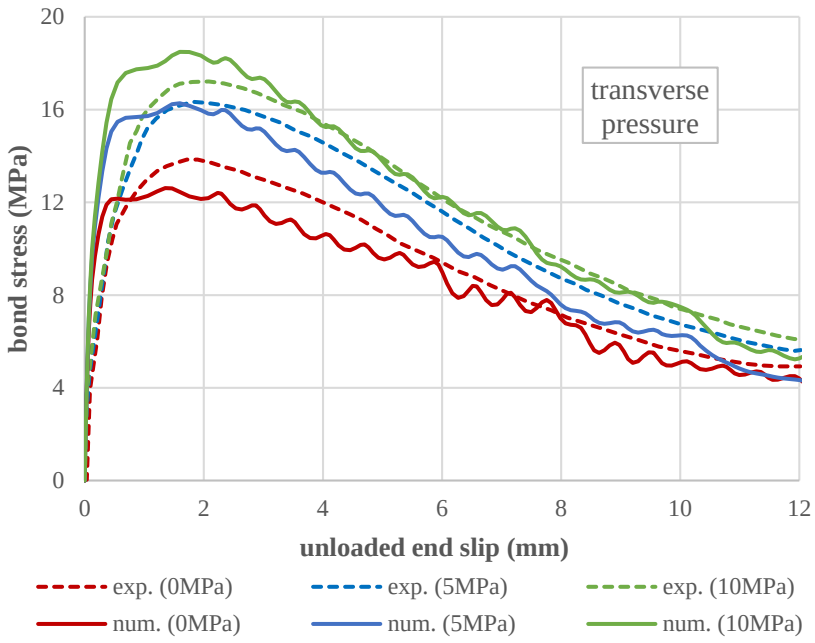

Fig. 5.19 Modelling effect of transverse pressure on bond-slip relationship with transitional layer

5.4 Conclusions

An equivalent transitional layer model is proposed to simulate the bond interaction between rebar and concrete, to cater for the needs of modelling such interaction in a realistic manner while the rebar is modelled with one-dimensional line (beam) elements in a RC member response analysis. The proposed transitional layer model is capable of capturing the gross “bond” and “slip” behaviour while the one-dimensional rebar is perfectly tied to the concrete matrix.

The equivalent stress state in the equivalent layer is derived through a simplified theoretical model taking into account the effect of the pressure that can develop around the rebar space. On this basis, the yield surfaces are established by modifying the basic failure surfaces employed in the standard KCC model. The

generalised strains and internal variables include characteristic length measures related to the rebar properties.

Comparisons of the FE modelling results using the proposed transitional layer model with the experimental data show good agreement across different experimental conditions.

Chapter 6: Transient high shear phenomenon and transition of response modes of RC members subjected to blast load

6.1 Introduction

When a structural component is subjected to impulsive load, the response of RC components will always undergo firstly a shock and stress wave phase within the body of material due directly to the shock load, and this is followed by the structural response involving shear and bending due to the energy imparted by the load impulse (Lu 2013).The structural response can be further divided into three consecutive stages according to the dominant dynamic modes of response, namely intense concentrated shear near support, intense shear over a relatively small shear span, and global bending stage.

It is generally understood that, depending on the intensity of the shear forces that may develop in the first two consecutive stages, direct shear and diagonal shear failure may occur, leading to partial or total failure of the structural member at these stages. If the member can survive from the above shear-

dominated stages, global flexural response can then develop which will largely depend upon the impulse of the blast load.

So far in practice, the majority of the blast response analysis methods and the assessment criteria have been based on a global bending mode of responses. The transient high shear phenomena, although recognised to some extent (Krauthammer et al. 1986; Ross and Krawinkler 1985), have not been dealt with in a systematic way. On the one hand, there is a lack of generally accepted method for the analysis of the high transient shear forces; on the other hand, there is essentially a total lack of understanding about the dynamic shear resistance mechanisms and how they should be appropriately analysed.

In terms of the general shear phenomena, it has been observed experimentally that RC components could fail at the positions near the support due to direct shear slip failure (Krauthammer 1984; T. Ross 1983; Slawson 1984), when subjected to a distributed load of extremely short duration. The phenomenon is also reproduced and studied by means of FE modelling (Li et al. 2012; Magnusson et al. 2010; Shi et al. 2008; Xu et al. 2014). On the analysis of the direct shear, a Timoshenko beam model has been employed to analyse RC member response incorporating the direct shear failure (Gong and Lu 2007; Krauthammer et al. 1993a; b; T. J. Ross 1983). SDOF approaches were utilised by several authors to analyse the transition between direct shear and flexure failure (Dragos and Wu 2014, Krauthammer 1986,1994, and Low and Hao 2002). Studies have also been conducted on the analysis of generic beams involving direct shear failure using rigid-plastic beam models (Li and Jones 1995; Ma et al. 2007), where a fully coupled analytical approach was used to determine both the direct shear and midspan flexural deflection responses. None of these studies has dealt with the dynamic effects on the resistance side of the equation, such as the loading and strain rate effects, the timescale of development of the shear modes in relation to the shock duration, as well as the

possible variation of the shear span (and hence the effect on the shear resistance).

This study is aimed to provide a comprehensive treatment of the high shear phenomena in the blast response of RC components as represented by typical RC beams. In this chapter, a simplified beam model is utilised to look into and demonstrate the key phenomena associated with the development of high shear forces, especially when the blast pulse duration gets very short. The process of the beam response moving through the high shear stages to global bending is examined and the dominant deformation modes are characterised. The propagation of the transient shear force and the contributions of high modes are discussed.

For this purpose, a simplified numerical analysis using an FE model with beam elements is employed. For a convenient comparison, the blast load is simplified as a triangle pulse with zero rise time and the magnitude of blast impulse is assumed to be constant. Different loading rates can be achieved by scaling the load duration t_d and the peak overpressure p_m, while keeping the overall impulse level I_0 constant. The development of shear force in the early response phase (transient high shear stage) prior to the global bending stage, in terms of the amplitude and distribution, is scrutinised. The increasing demand on the shear resistance as loading rate increases is examined and discussed.

6.2 Numerical analysis with beam elements

6.2.1 RC beam specimen and characteristic flexural period

For this analysis, a reinforced concrete beam specimen with typical dimensions is considered, as presented in Fig. 6.1. The beam is 3m long and has a cross-section of 200 mm× 100 mm. The cross-sectional arrangement is adopted from the RC

beams discussed in Section 4.5, in which two D12 rebars and two D10 rebars are placed in the tension and compression sides, respectively. Material properties of concrete and steel rebar are listed in Table 6.1.

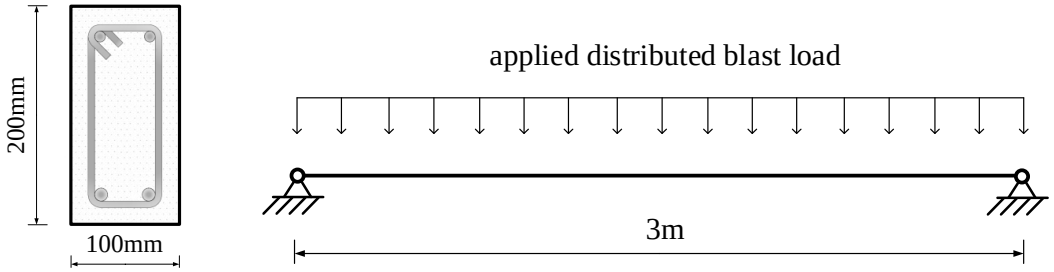

a) Cross-section b) Beam layout

Fig. 6.1 Considered RC beam specimen

Table 6.1 Material properties for RC beam

Concrete		*Steel rebar*	
f_c'	36 MPa	f_y	500 MPa
E_c	28 GPa	E_s	200 GPa
ρ_c	2300 kg/m^3	ρ_s	780 0kg/m^3

Using a classical SDOF-based method, as will be discussed in more detail in Chapter 8, the first natural period of the flexural mode of the beam with simply-supported and fixed-supported conditions, respectively, can be calculated using the following expressions:

$$T_f = 2\pi\sqrt{\frac{M_{eq-f}}{K_{eq-f}}} = 2\pi\sqrt{\frac{K_{M-f}M}{K_{L-f}K_f}} = \begin{cases} 2\pi\sqrt{\dfrac{5K_{LM}mL^4}{384EI}} & \text{simply-supported} \\ 2\pi\sqrt{\dfrac{K_{LM}mL^4}{384EI}} & \text{fixed-supported} \end{cases} \quad (6.1)$$

where m and L are the mass per length and span length respectively. EI is the flexural rigidity, and K_{LM} is the load-mass factor. Detailed deduction of Eq. 6.1 is given later in Section 8.2.1. Assuming a cracked section for generality, the flexural rigidity can be calculated using a standard method, herein using a UFC

recommended method (UFC 3-340-02 2008) as will be explained in detail in Chapter 8. In the case herein the cracked EI_a is found to be about 70% of the uncracked reinforced section.

For the given RC member, the first flexural period is 35.0 ms for the simply-supported case and 15.6 ms for the fixed-supported case. In the discussion that follows, these natural period values will be employed as a reference base in the characterisation of the timescales of the load durations.

6.2.2 Numerical model with beam elements and material properties

Fig. 6.2 illustrates the finite element model for the RC member. The one-dimensional Belytschko-Schwer resultant beam element (Belytschko et al. 1977) in LS-DYNA (LSTC 2006) is chosen to carry out the numerical analysis. For element formation, the internal forces are updated directly from the nodal displacement vs. force relations so that no integration point is required, which yields considerable benefits in computational efficiency. Considering the high shear phase of the response which tends to present large fluctuation along the beam length, 200 beam elements are used for the whole beam to ensure an appropriate resolution, resulting in a mesh grid size of 15 mm.

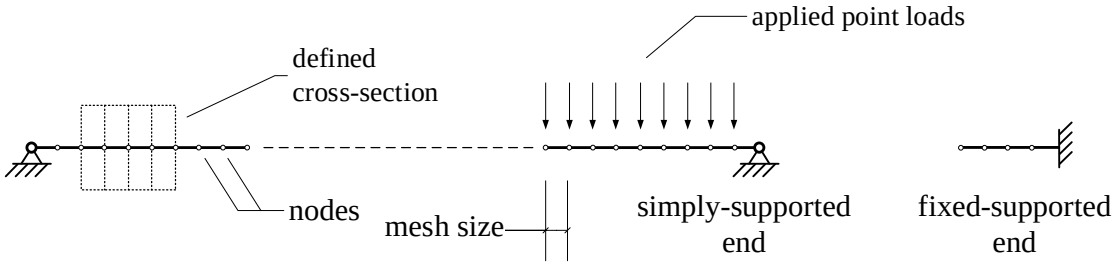

Fig. 6.2 Schematic view of beam element model for RC beam

The primary purpose of this analysis is to examine the development of the shear forces (thus the shear demands) at different response stages, and in particular to

compare the maximum shear forces during the high shear phase with the shear force that is associated with the global bending. Such a comparison will demonstrate the potential for a shear failure to develop before the response settles into the usual global bending stage. For the above analysis, a simple elastic analysis would appear to suffice; however, considering the fact that the shear force that can develop during the global bending is subject to the limit imposed by the bending strength, it is meaningful to include a flexural strength in the analysis.

For the flexural strength, the elasto-perfect-plastic moment-curvature relation is assumed. This will limit the shear force that can develop in global bending but will not affect the shear force to develop elastically before the response enters into the global bending phase. This is achieved by using material model *MAT_SEISMIC_BEAM (MAT_191) in LS-DYNA. This material enables lumped plasticity to be developed at the ends of each beam element, and defines a plastic yield surface that allows interaction between moment and axial force, which is expressed by

$$\psi = \left(\frac{M_s}{M_{ys}}\right)^2 + \left(\frac{M_t}{M_{yt}}\right)^2 + 2.0 \times \left(\frac{N}{N_{yc}}\right)^2 - 1.0 \times \left(\frac{N}{N_{yt}}\right)^4 - 1 \qquad (6.3)$$

where M_s, M_t and N are the current moment about local s and t axes and axial forces respectively. M_{ys}, M_{yt}, N_{yc} and N_{yt} are the yield moments in s and t axes and yield forces in compression and tension, respectively. The multiplier and exponential parameters are presented with default values.

For the RC beam analysed in this section, the flexural resistance M_{yt} is set as 17 kN·m as referred from Section 4.5, and perfect plasticity is assumed. In order to provide a more realistic stiffness, the cracked flexural rigidity EI_a and shear rigidity GA_{eq}, the latter being in a partial shear-damaged state as will be derived in Chapter 8, are adopted here. Calculation shows that the reduced EI_a and GA_{eq}

are about 70% and 24% of their original value for the intact section, respectively. For the remaining parameters, the cross-section and material properties listed in Table 6.1 are adopted.

6.2.3 Blast loading

The blast load is simplified as a triangle pulse with zero rise time, as shown in Fig. 6.3 and expressed in Eq. 6.4.

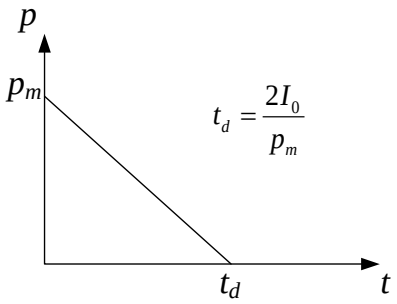

Fig. 6.3 Simplified triangular shaped blast load

$$p(t) = \begin{cases} p_m\left(1 - \dfrac{t}{t_d}\right) & 0 < t \le t_d \\ 0 & t > t_d \end{cases} \tag{6.4}$$

where p_m is the peak overpressure of the blast, t_d is the duration. It follows:

$$t_d = \frac{2I_0}{p_m} \tag{6.5}$$

In the beam analysis model, the blast loading is simulated by point loads applied directly onto the beam nodes. For simplicity, the loading area is considered as the net beam top face, thus for each point load, the amount of load can be calculated by:

$$P_{node}(t) = p(t) \cdot b \cdot l_e \tag{6.6}$$

where $p(t)$ is the blast overpressure, b and l_e are the width and length of each beam element, respectively.

Different types of blast loads are considered by varying the duration of the load, from relatively long to very short duration with respect to the natural bending period T_f, and the relative significance of the shear and bending modes are examined with respect to the blast duration. As mentioned before, for the convenience of comparison, the impulse level of blast is kept constant at $I_0 = 4$ kPa·s to allow for a direct comparison. To give an idea, an explosion of 100 kg TNT at a distance of 1.5 m would yield a reflected blast impulse of this magnitude.

6.3 Shear response of simply supported RC member

6.3.1 Response under blast load in quasi-static regime ($t_d \approx T_f$)

Fig. 6.4 shows the time histories of global deflection and forces under a blast impulse of 4 kPa·s with duration of 32 ms, which is in the same order as the flexural period. As can be read from Fig. 6.4a, the time interval between the two deflection peaks are about 33.5 ms, suggesting a match between the theoretical and numerical prediction of the flexural mode period. Fig. 6.5 gives the distribution of deflection and internal forces at key time instants.

As can be observed from both the time history and the distribution plots, under such blast load of enough long duration, the response is mainly dominated by first-order flexural deformation mode, and the development of the shear force and bending moment generally follows the pattern of a quasi-static loading

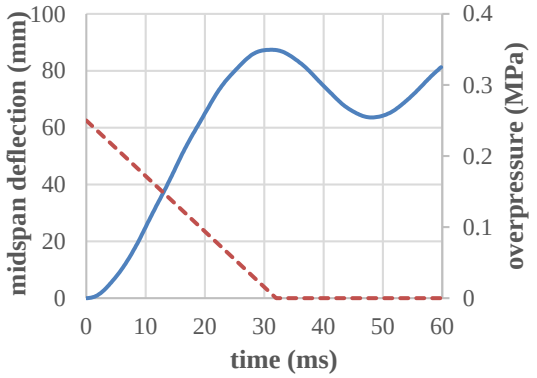

a) Mid-span deflection

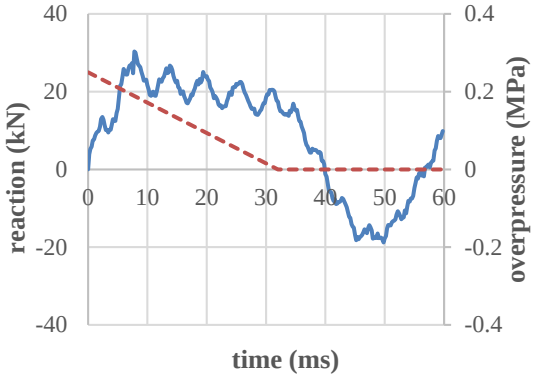

b) Reaction force / shear force at support

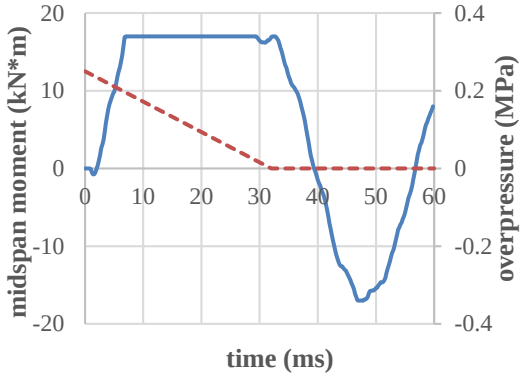

c) Mid-span bending moment

Fig. 6.4 Time histories of simply-supported RC beam under blast in quasi-static regime (I_0=4 kPa·s; p_m=0.25 MPa; t_d=32 ms)

scenario, in close association with the deflected shape. The level of shear force is limited by the maximum moment resistance, as seen from Fig. 6.4c; in fact, a simple calculation for the simply-support beam with a yield moment of 17kN*m under a uniform static load yield a maximum shear force of 24kN, which tallies with the maximum shear force observed from Fig. 6.4b and Fig. 6.5b.

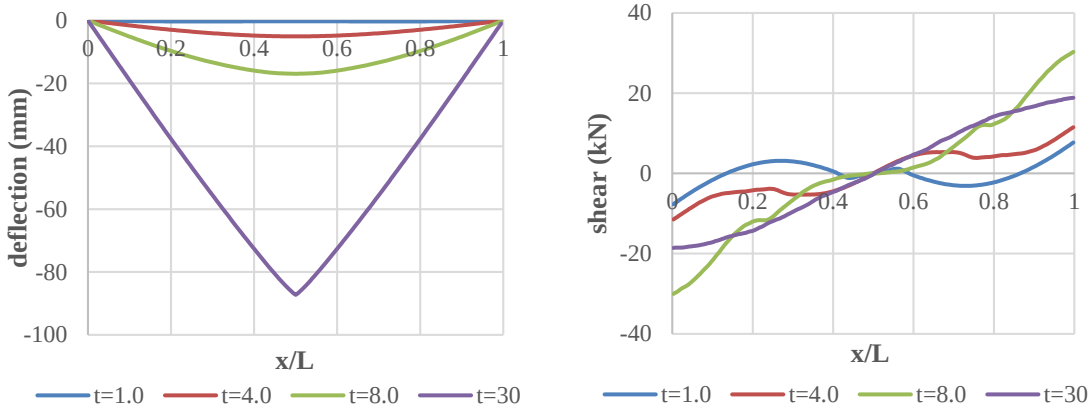

a) Deflection distribution

b) Shear force distribution

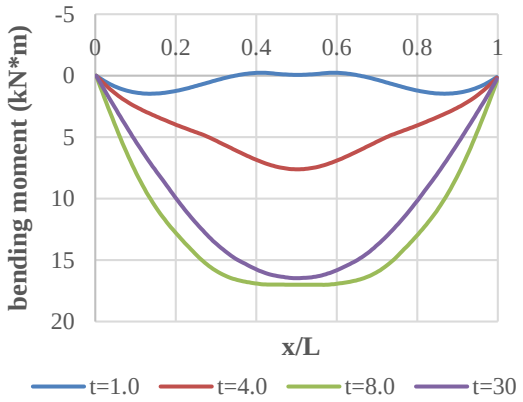

c) Bending moment distribution

Fig. 6.5 Deflection and force distribution of simply-supported beam under blast in quasi-static regime (I_0=4 kPa·s; p_m=0.25 MPa; t_d=32 ms)

6.3.2 Response under blast load in impulsive regime (e.g. $t_d = 1\ ms \approx T_f/40$)

Fig. 6.6 gives the time history of deflection and forces of RC beam under the same blast impulse of 4 kPa·s but a much shorter duration of 1.0 ms, which is about 1/40 of the flexural period. The deflection shapes, distributions of the shear force and bending moment at representative time instances are plotted in Fig. 6.7.

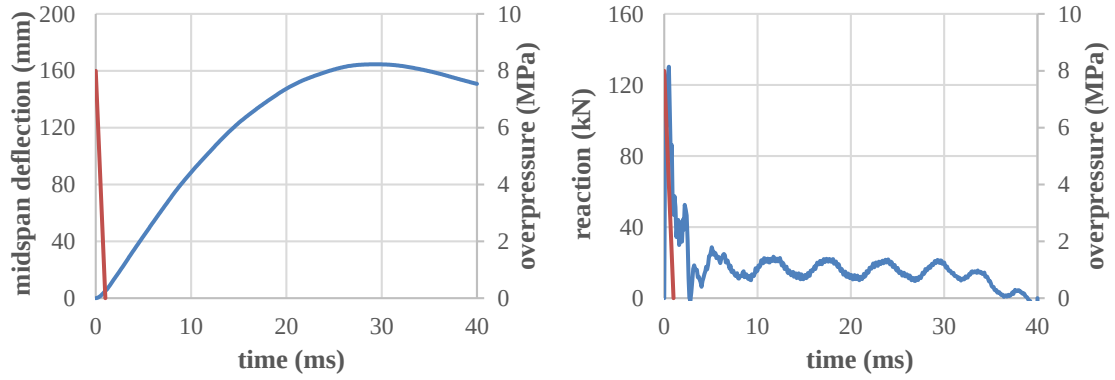

a) Mid-span deflection

b) Reaction force / shear force at support

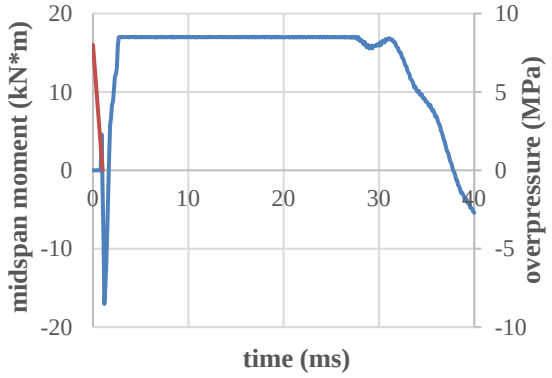

c) Mid-span bending moment

Fig. 6.6 Global response of simply-supported beam under blast in impulsive regime (I_0=4 kPa·s; p_m=8 MPa; t_d=1 ms)

From the time histories, it can be seen that very large reaction and shear forces develop during the pulse load duration (1 ms herein), while the global deflection is still very small. The de-coupling between the shear force and the global deformation is also evident from the distributions of the deflection and shear force over the length of the beam in Fig. 6.7a and Fig. 6.7b (t=0.5 ms, 1.0 ms). In fact the deflection shape at t=0.5 ms exhibited a clear direct shear deformation mode dominated by concentrated shear deformation over a small region near the supports. A closer look at the deformation and force distribution shown in Fig. 6.7 reveals that, at the initial stage of the blast pressure (t=0.5~1.0 ms), the member acts as a rigid body moving downward and high shear force concentrates in a very short length near the supports.

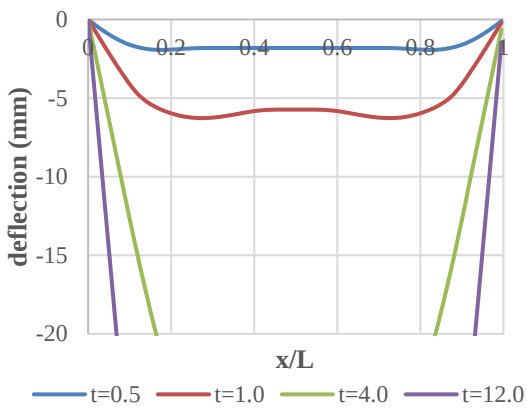

a) Deflection distribution

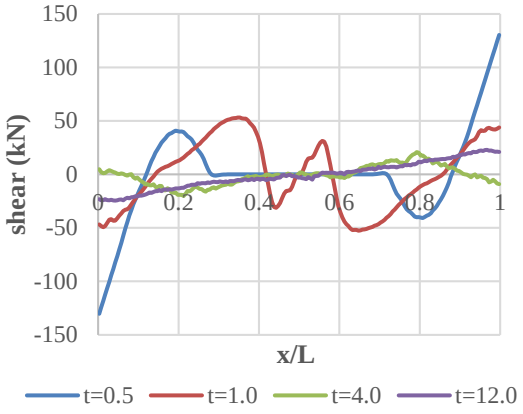

b) Shear force distribution

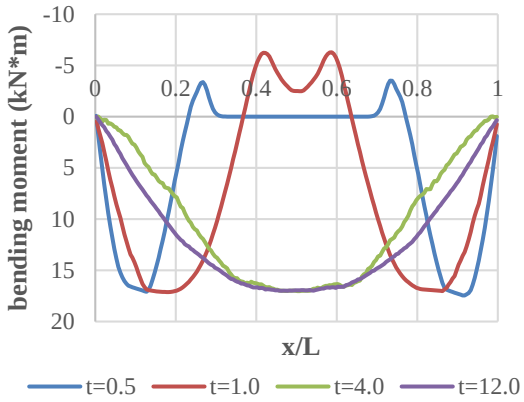

c) Bending moment distribution

Fig. 6.7 Deflection and force distribution of simply-supported beam under blast in impulsive regime (I_0=4 kPa·s; p_m=8 MPa; t_d=1 ms)

It can be understood that due to the zero rise time of the loading, the maximum reaction and hence the maximum shear force occur almost at the onset of the blast load; however at this moment the shear peak occupies only a very small length and hence will not generate significant shear deformation (despite a large local shear strain). The precise damage zone width in the case of direct shear is a subject of debate and there in no particular experimental evidence to support a robust definition, and it will depend on the sectional properties. But for reinforced concrete beams, one may consider that it would be at least a couple of times the size of a main steel bar, as otherwise the dowel action could be too

large for the surrounding concrete to sustain. For this reason, herein we propose a reference direct shear zone length to be 0.5*d* with *d* being the section depth.

In this connection, it is reasonable to use an "effective" shear force, defined as the average shear force over the above zone length, as a measure of the effective shear force with respect to the direction shear failure. Further discussion on the concept of shear zone length and the effective shear force will continue in Chapter 7.

It can be seen from the shear force distributions in Fig. 6.7b that the maximum direct shear force that develops in the transient high shear stage amounts to about 120 kN; this is in contrast to the maximum shear force of about 24 kN that can develop in the global bending phase of the response. Of course the high shear phase quickly diminishes and the shear dropped into the normal shear as associated with the global bending, which is in turn limited by the available moment strength. Meanwhile global bending deformation develops into full shape.

6.3.3 Response under blast load in dynamic regime ($t_d \approx T_f/5$)

Fig. 6.8 shows the time histories of global deflection and forces under the same impulse but a duration equal to around 1/5 of the flexural mode period. The deflection shapes, distributions of the shear force and bending moment at selected time instances are plotted in Fig. 6.9.

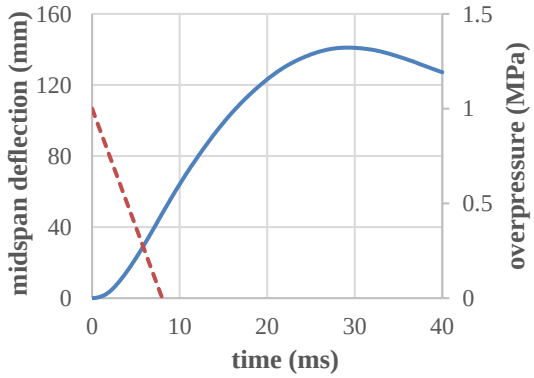

a) Mid-span deflection

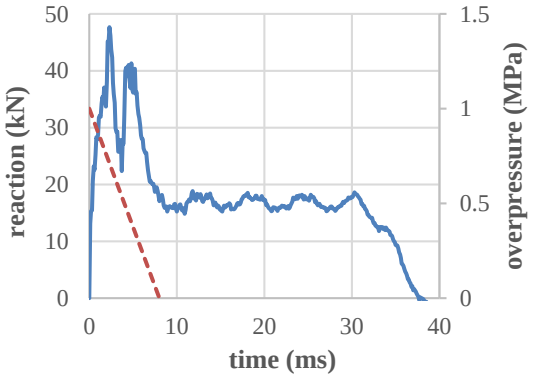

b) Reaction force / shear force at support

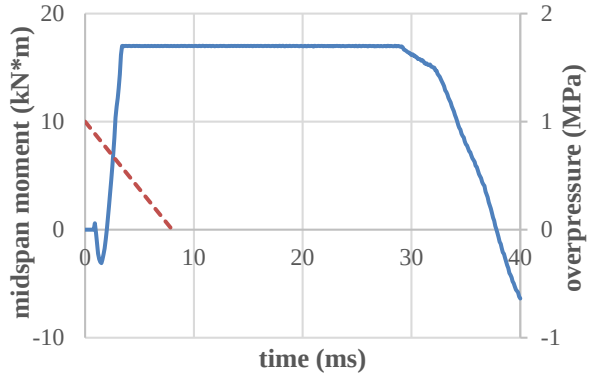

c) Mid-span bending moment

Fig. 6.8 Global response of simply-supported beam under blast in dynamic regime (I_0=4 kPa·s; p_m=1 MPa; t_d=8 ms)

Under such load duration, the developed shear force reaches around 50 kN, which is much smaller than the shear force experienced in the direct shear mode scenario but still significantly higher than the maximum static shear of ~24 kN. From the time history it can be seen that the peak shear appears at a slightly later stage (2~4 ms) than the direct shear mode, and this indicates clearly a dynamic effect, which is actually associated with a diagonal shear mode of response as will be discussed later in Chapter 8.

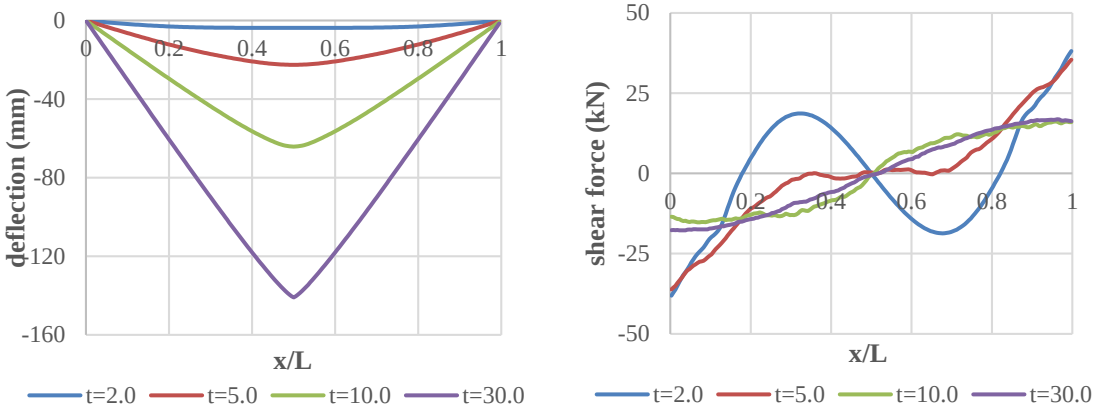

a) Deflection distribution

b) Shear force distribution

c) Bending moment distribution

Fig. 6.9 Deflection and force distribution of simply-supported beam under blast in dynamic regime (I_0=4 kPa·s; p_m=1 MPa; t_d=8 ms)

As shown in the force distribution in Fig. 6.9b, at the maximum shear force, the width of developed shear span has increased into around one-half of the effective depth, indicating a diagonal-shear dominated deformation mode, which will also be discussed further in Chapter 8.

6.3.4 Influence of loading rate on simply supported beams

The time histories of central deflection and shear force under the same impulse but varied load durations are compared directly in Fig. 6.10. Common to all

cases, the flexural responses as represented by the mid-span deflections show a similar pattern, but the maximum deflection tends to increase as the load duration decreases before reaching an asymptotic limit (note that total impulse remains constant). This can be explained by the basic dynamic response of the global system. On the other hand, the maximum shear force tends to increase with the decrease of the load duration, and this trend becomes almost exponential in the short duration range. The maximum shear forces derived from Fig. 6.10, after normalisation with respect to the quasi-static maximum shear force $4M_y/L$, are plotted in Fig. 6.11 against load duration, which is normalised by the flexural period.

The achieved maximum shear force in the short duration range is significantly larger than what may be predicted from the flexural mode of response, which is governed by the static equilibrium $4M_y/L$, as plotted by dashed line in Fig. 6.10b. This limiting shear force corresponds to the maximum shear force when the beam reaches its yielding moment at mid-span under quasi-static uniformly distributed load.

It can also be observed that the time at which the maximum shear force is reached decreases, indicating that the shifting from a flexure-dominated mode to a shear-dominated mode of response. This, together with the inability of a simplified bending mode analysis to capture the high shear phenomenon, suggests a simplified analysis incorporating the shear mode of the beam will be needed, and this will be discussed in detail in Chapter 8.

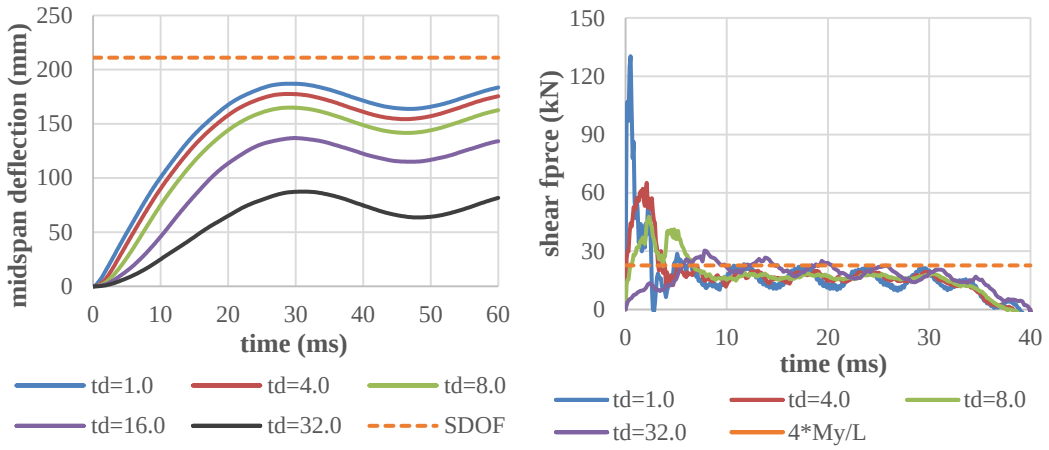

a) Mid-span deflection b) Shear force

Fig. 6.10 Time histories of midspan deflection and shear force under different load durations (I_0=4 kPa·s)

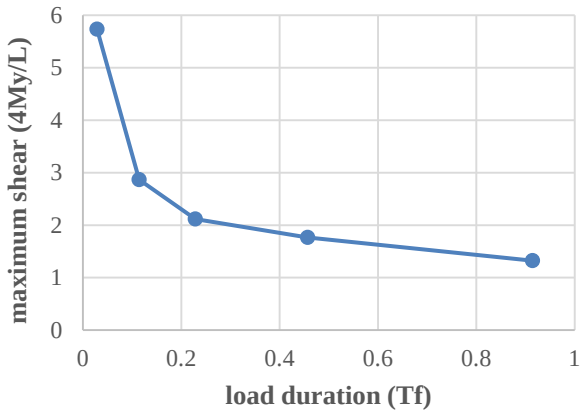

Fig. 6.11 Maximum shear force of simply-supported beams under different load durations (I_0=4 kPa·s)

The distributions of the shear force and bending moment at key time instants, after normalisation with respect to the quasi-static maximum shear force $4M_y/L$ and yield bending moment M_y respectively, are plotted in Fig. 6.13. It can be found that in the early stages, the general shape of the shear force diagram is not affected by the load duration, but the amplitude of shear force, especially within the short shear span near the supports, is considerably increased. For the short duration cases, travelling shear wave is also evident but the maximum

shear force takes place consistently at the support region before significant travelling shear wave occurs.

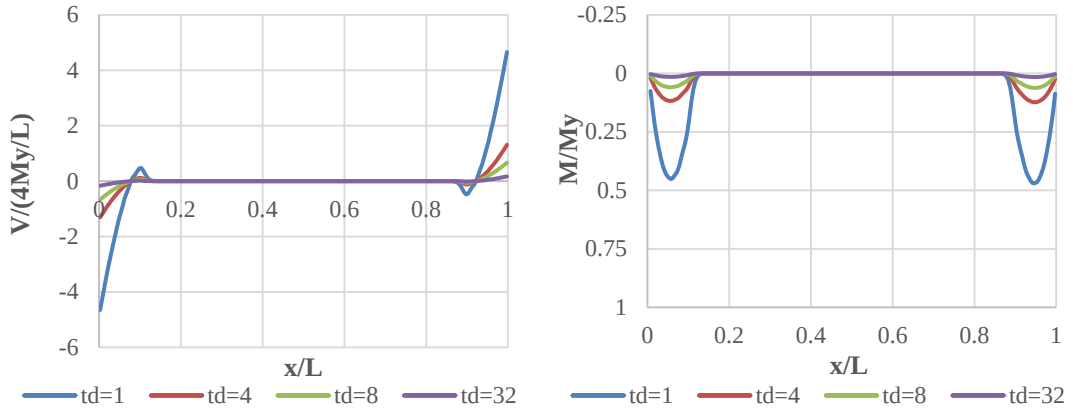

a) t=0.2 ms

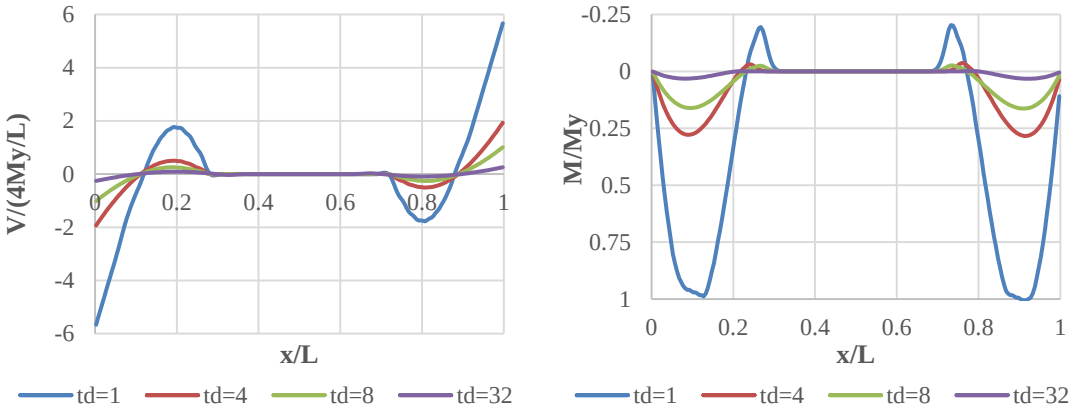

b) t=0.5 ms

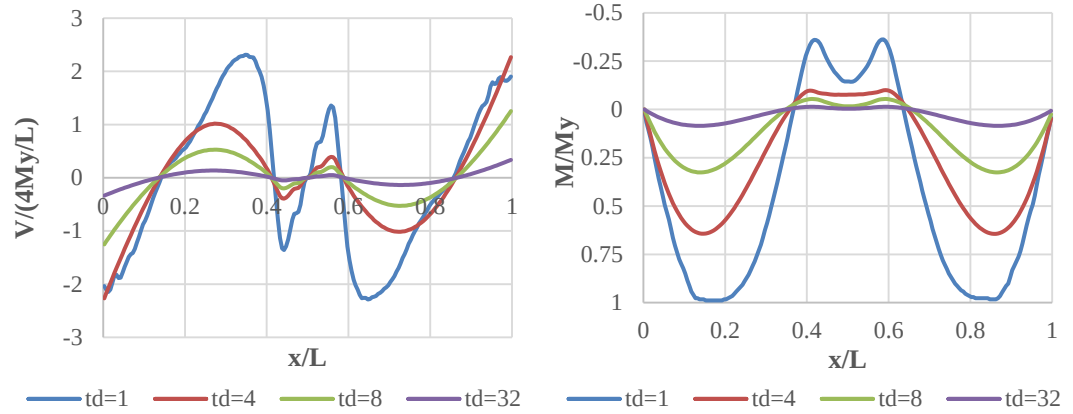

c) t=1.0 ms

Fig. 6.12 Normalised SFD and BMD of simply-supported beam under different load durations (I_0=4kPa·s)

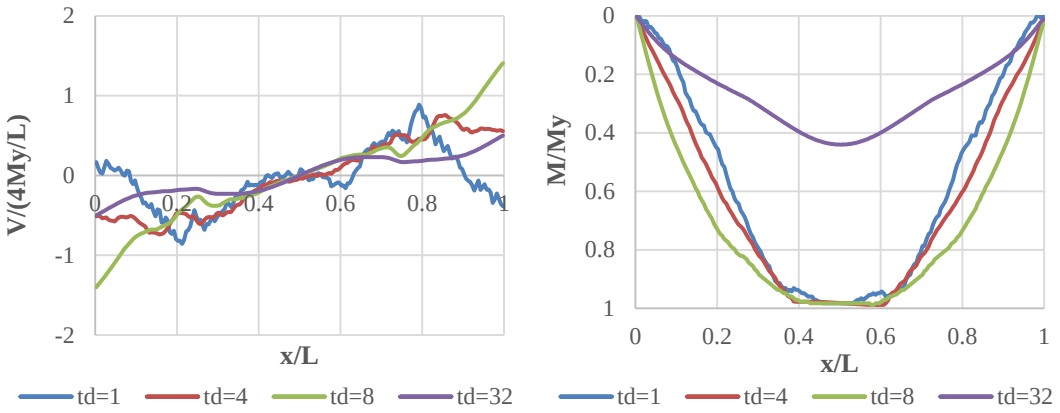

d) t=4.0 ms

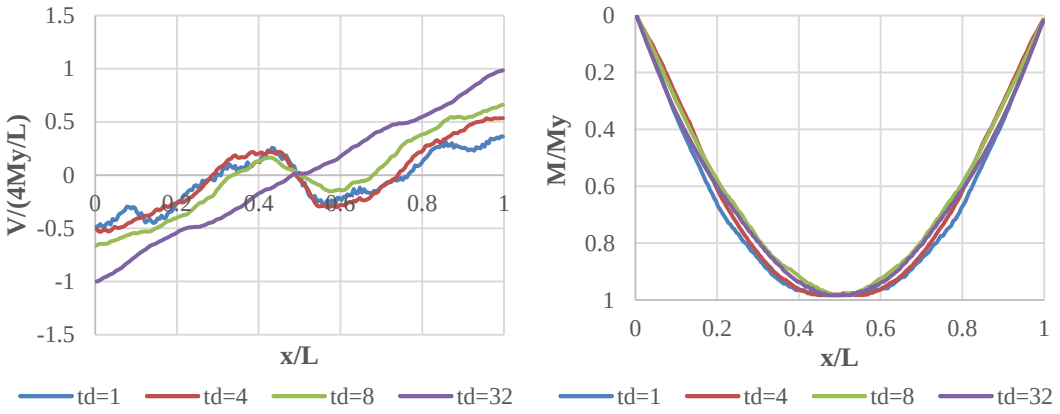

e) t=12.0 ms

Fig. 6.13 Normalised SFD and BMD of simply-supported beam under different load durations (I_0=4 kPa·s) (continued)

Now confining our attention to the high shear phenomenon at the support region, it can be reasonably deduced that a) if the shear strength is reached while high shear force develops, shear failure could occur, and b) in that case, the shear failure zone or the "shear span" could be much shorter than in a quasi-static shear scenario. The quicker high shear force and shear failure develops, the shorter the shear span, and ultimately the shear failure could enter into a direct shear scenario with very short shear span.

While the high shear phenomenon may readily be predicted using even a relatively simple beam model, the dynamic shear strength, on the other hand, is

not well understood. In fact there is very little information in the literature regarding the shear resistance in a high dynamic response environment. Based on the general analysis described in this section, it can be anticipated that the factors influencing the dynamic resistance will include the variation of the shear span, in addition to the possible enhancement of the material strength due to the high strain rate. As has been demonstrated, the shear span tends to decrease with decrease of the loading duration, and this implies an increase in the shear strength even without any material enhancement due to the strain rate. This is to be investigated thoroughly in Chapter 7.

6.4 Shear response of fixed-supported RC member

While the characteristics of the transient high shear phenomenon are not expected to change because of different boundary conditions, the relative magnitudes and the timescale can differ. In this section RC beam with fixed supported is examined following a similar procedure as in the above analysis of the simply-supported beam.

6.4.1 Response under blast load in quasi-static regime ($t_d \approx T_f$)

Fig. 6.14 shows the time histories of global deflection and forces for a fixed supported RC member under a typical quasi-static blast load. It has an impulse of 4 kPa·s, an overpressure of 0.5 MPa and duration of 16ms, which is slightly longer than the flexural mode period of the beam. As seen in Fig. 6.14a, the interval between the two peaks of the midspan deflection in the free vibration stage is around 16 ms, which agrees well with the predicted flexural mode period.

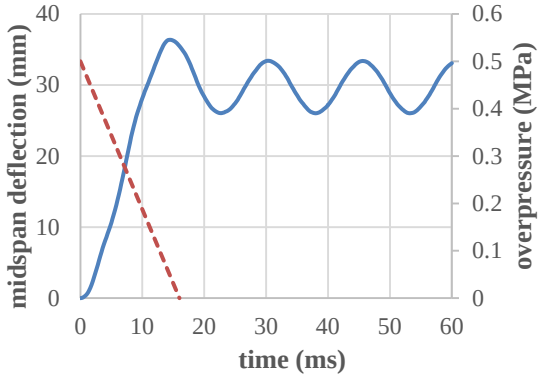

a) Mid-span deflection

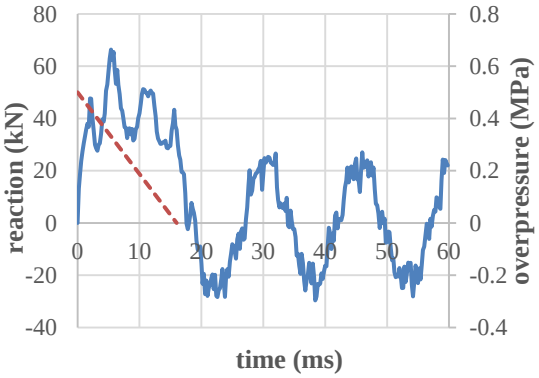

b) Reaction force

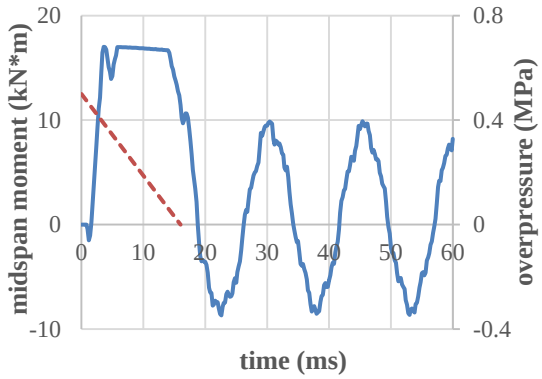

c) Mid-span bending moment

Fig. 6.14 Global response of fixed-supported beam under blast in quasi-static regime (I_0=4 kPa·s; t_d=16 ms)

Fig. 6.15 gives the distributions of deflection and internal forces at key time instants. Similar to what has been found in the simply-supported beam case, the response is mainly flexure-dominated and the shear force and bending moment distributions follow closely the patterns under a quasi-static uniformly distributed load. The highest shear force achieved is around 65 kN. Note that the maximum shear force that can be achieved when a full plastic mechanism is formed, under a uniformly distributed static load, is found to be 34 kN using a simple plastic mechanism analysis. The above results suggest that the maximum shear that can be achieved in a fixed support beam under a dynamic load with duration of around the flexural period is still related the maximum static shear; however, as the flexural period is about halved comparing to the pinned support

case, an appreciable dynamic shear amplification (by a factor of 1.9) also emerges.

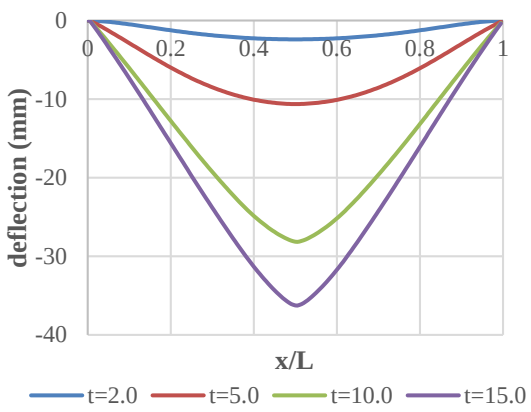

a) Deflection distribution

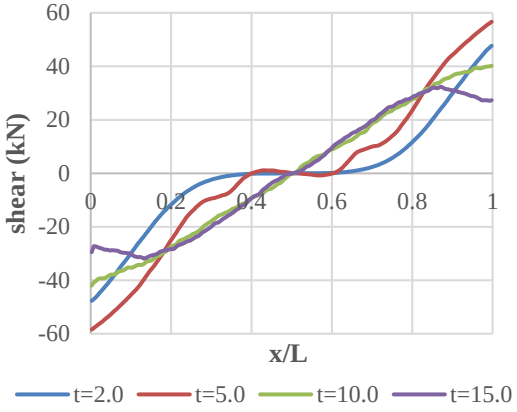

b) Shear force distribution

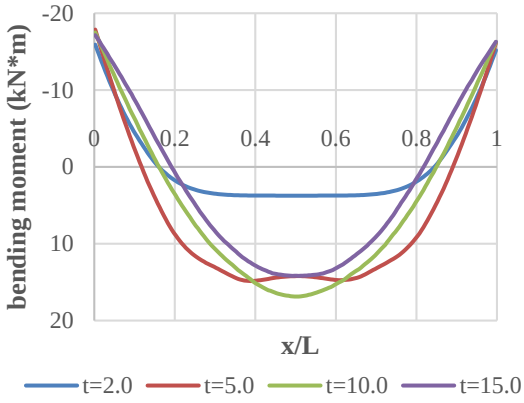

c) Bending moment distribution

Fig. 6.15 Deflection and force distribution of fixed-supported beam under blast in quasi-static regime (i=4 kPa·s; td=16 ms)

6.4.2 Response under blast load in impulsive regime (t_d=1ms ≈T_f/16)

The response time histories when the load duration is shortened to 1ms (same for the simply supported beam) which is around 1/16 of the flexural period are shown in Fig. 6.16. Fig. 6.17 gives the deflection distribution, shear force and bending moment diagram at key time instants in the early stage of the loading.

As can be seen, under such a short duration loading, the beam undergoes a similar direct shear response as previously discussed in the simply-supported case, with extremely high shear force occurring almost immediately after the peak load. The maximum shear force under such load duration is around 195 kN, which is more than three times of the magnitude reached in the quasi-static loading case.

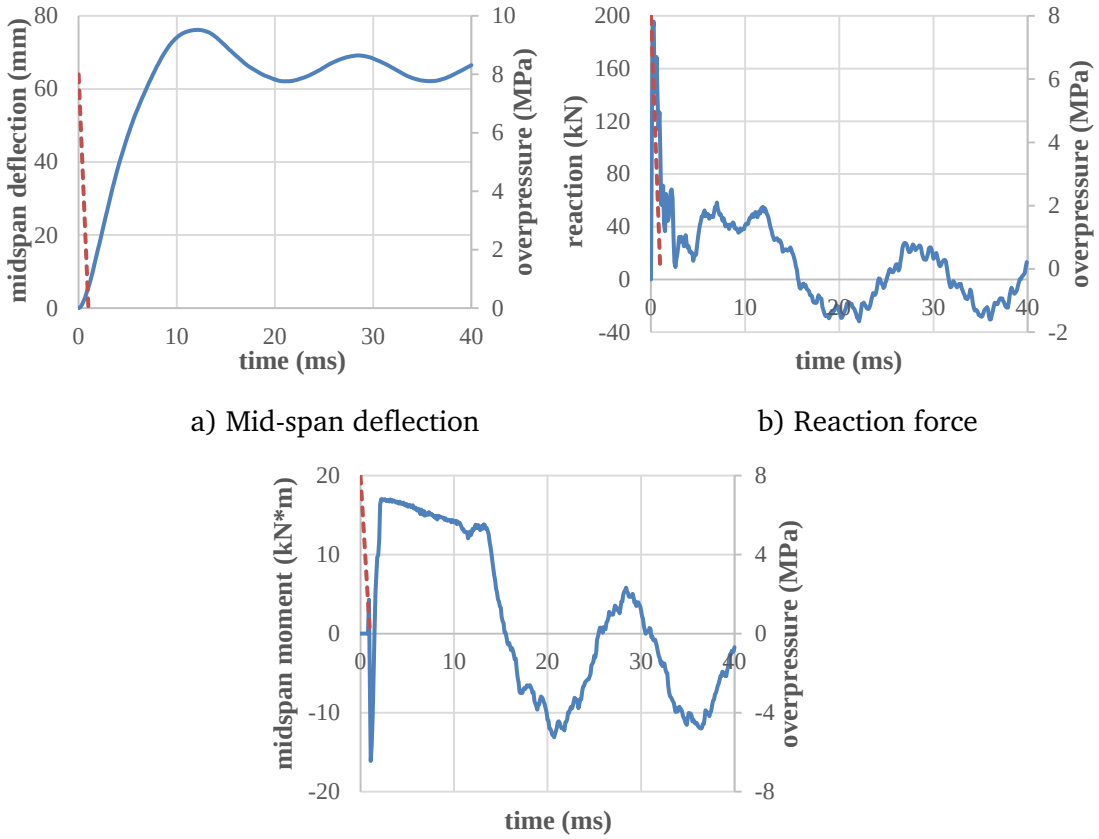

a) Mid-span deflection

b) Reaction force

c) Mid-span bending moment

Fig. 6.16 Global response of fixed-supported beam under blast in impulsive regime (I_0=4 kPa·s; p_m=8 MPa; t_d=1 ms)

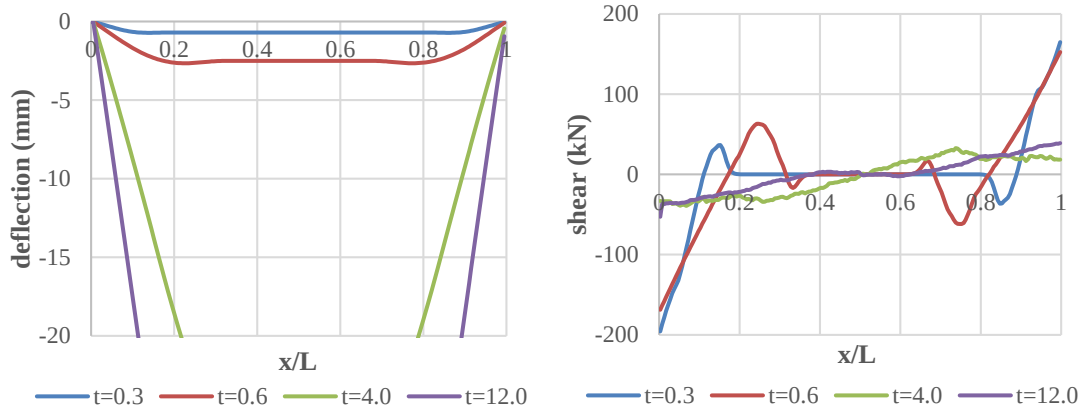

a) Deflection distribution

b) Shear force distribution

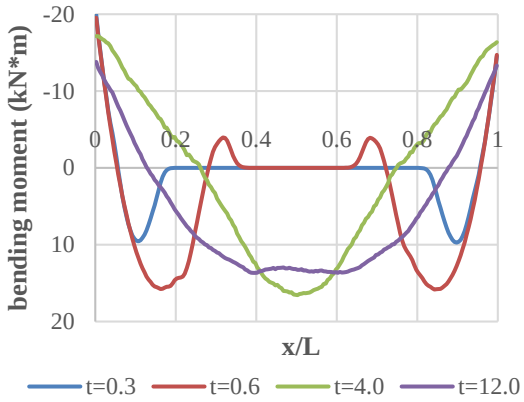

c) Bending moment distribution

Fig. 6.17 Deformation and force distribution of fixed-supported beam under blast in impulsive regime (I_0=4 kPa·s; p_m=8 MPa; t_d=1 ms)

6.4.3 Response under blast load in dynamic regime ($t_d \approx T_s/4$)

Fig. 6.18 and Fig. 6.20 give the response time histories and distribution profiles of the fixed-supported when the blast load duration is set at 4 ms, keeping the same impulse of 4 kPa·s. The general trend is similar to the simply-supported case.

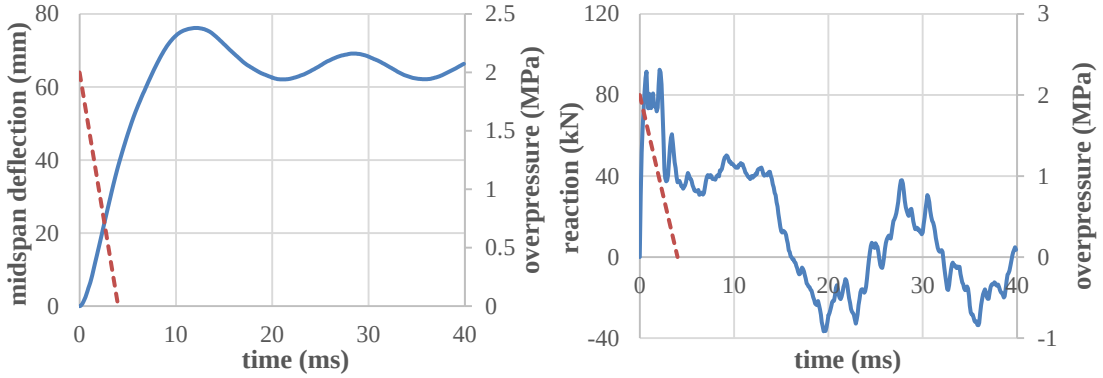

a) Mid-span deflection b) Reaction force

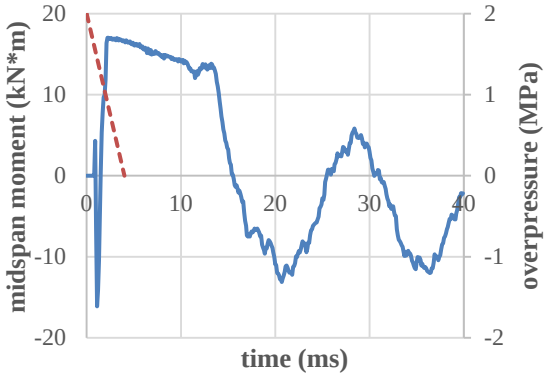

c) Mid-span bending moment

Fig. 6.18 Global response of fixed-supported beam under blast in dynamic regime (I_0=4 kPa·s; p_m=2 MPa; t_d=4 ms)

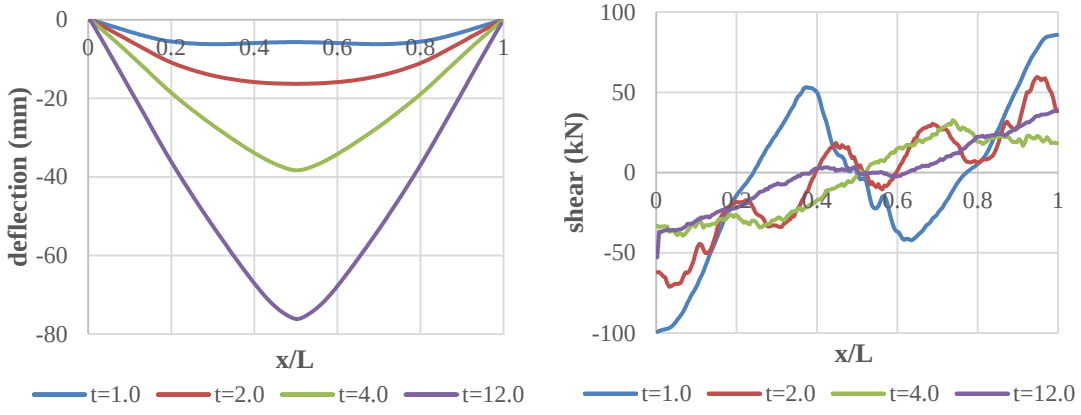

a) Deflection distribution b) Shear force distribution

Fig. 6.19 Deformation and force distribution of fixed-supported beam under blast in dynamic regime (I_0=4kPa·s; p_m=2MPa; t_d=4ms)

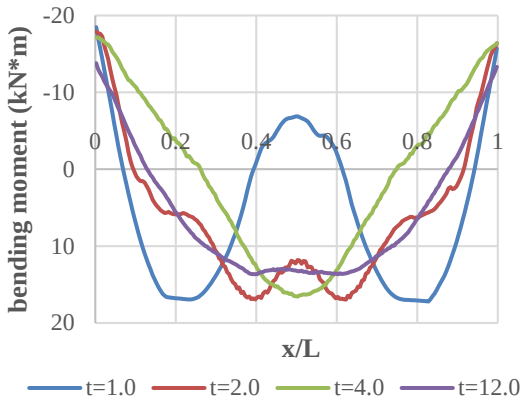

c) Bending moment distribution

Fig. 6.20 Deformation and force distribution of fixed-supported beam under blast in dynamic regime (I_0=4kPa·s; p_m=2MPa; t_d=4ms) (continued)

6.4.4 Influence of loading rate on the fixed-end beam

A set of time histories under blast load with same impulse level I_0=4 kPa·s but different load duration t_d is presented in Fig. 6.21. Observations made earlier in the simply-supported cases also hold here. The magnitude of the transient high shear response also tends to increase almost exponentially as the loading duration decreases under a constant impulse, and the time at which the maximum transient shear occurs is always at the very early stage of the response when the imposed load remains large, independent of the global bending response. This confirm that the high transient shear response is associated with a direct or diagonal shear mode, rather than the global bending mode. The high shear phase always disappears when the global bending takes shape, and the shear response becomes closely associated with the flexural mode at this stage.

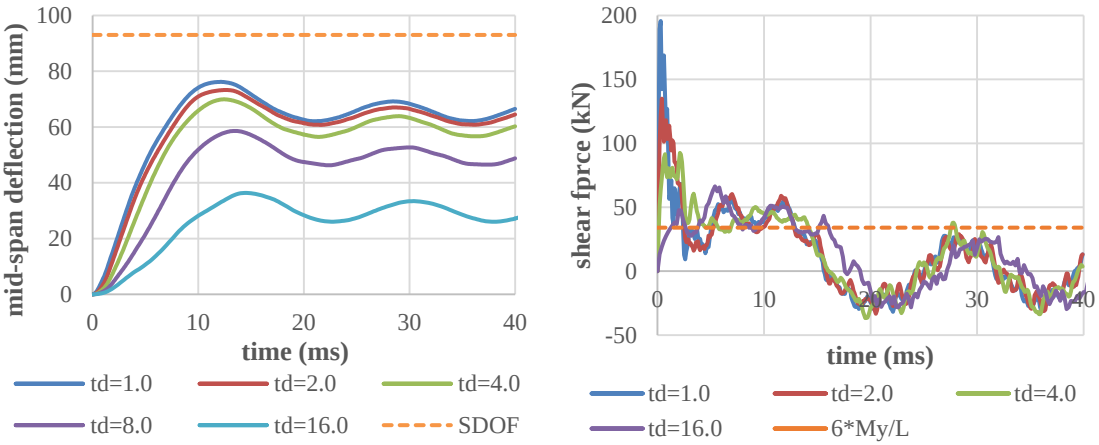

a) Mid-span deflection b) Reaction force

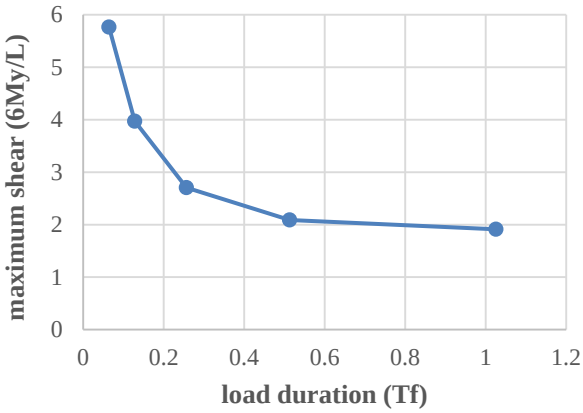

c) Maximum shear force vs. load duration

Fig. 6.21 Time histories of deflection and shear force of fixed-supported beam under different load durations (I_0=4 kPa·s)

The distributions of shear force and bending moments, after normalised by $6M_y/L$ and M_y respectively, which are the maximum shear force and bending moment that can be achieved under an equivalent uniformly distributed static load, are plotted in Fig. 6.23. As also found in the simply-supported cases, the general shape of the shear force diagram is not affected by the load duration, while the amplitude is largely increased. Meanwhile, it is noted that for fixed-supported beams, large bending moment also develops at the supports, and the combined high shear and large moment could affect the respective shear and

bending strengths. The coupled effect of flexural and shear failure at fixed supports will be discussed in Chapter 7.

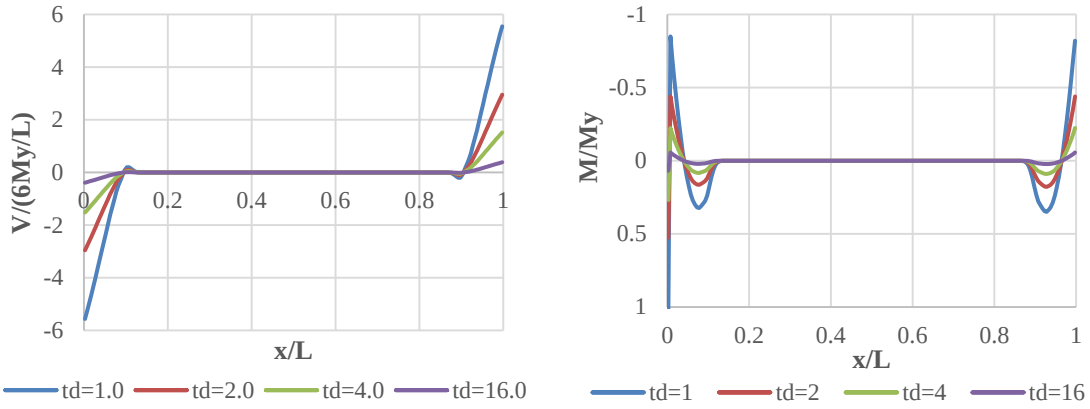

a) t=0.2 ms

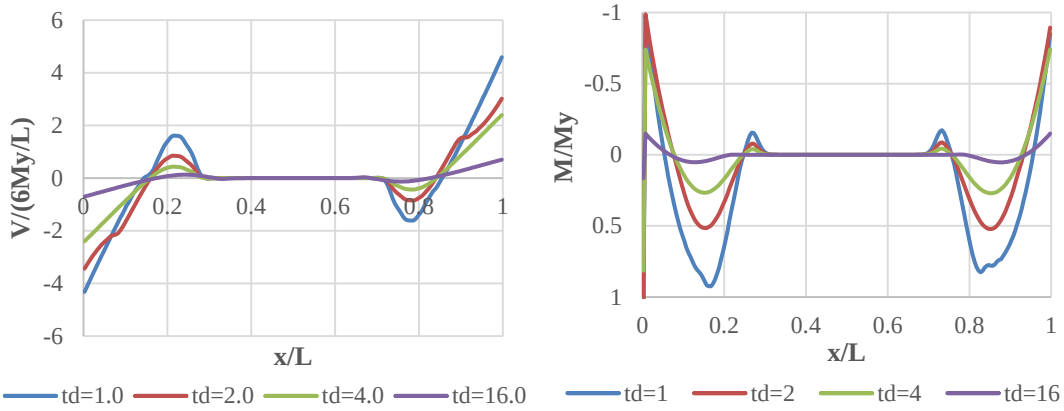

b) t=0.5 ms

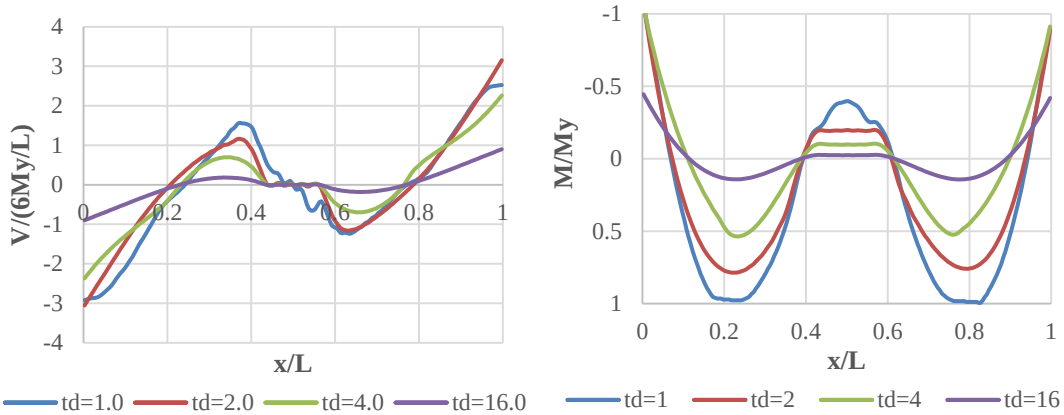

c) t=1.0 ms

Fig. 6.22 Shear force diagram of simply-supported beam under blast with different loading rates (I_0=4kPa·s)

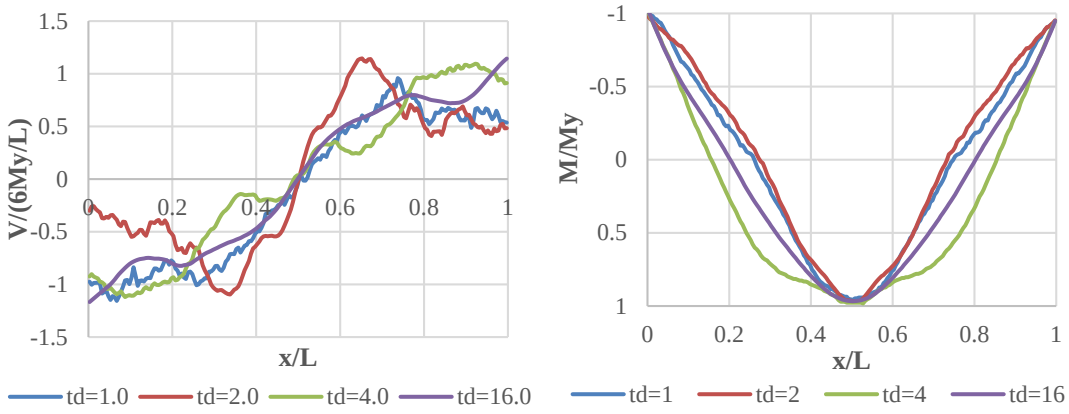

d) t=4.0 ms

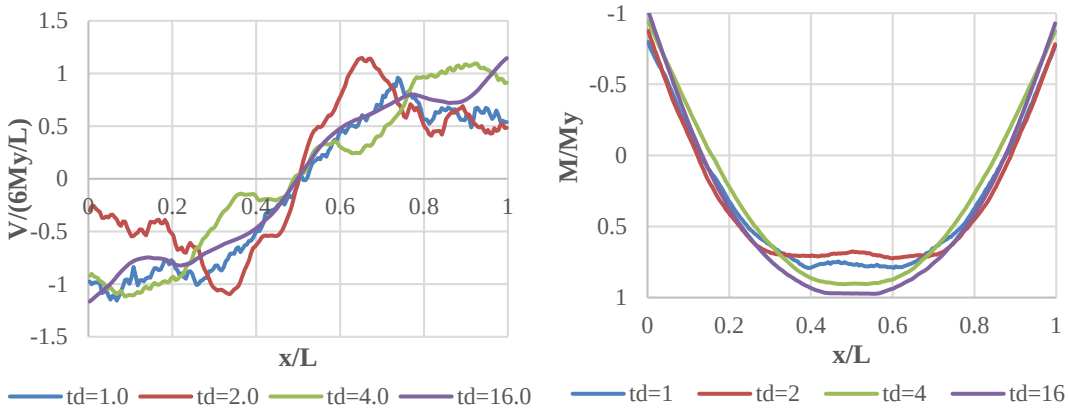

e) t=12.0 ms

Fig. 6.23 Shear force diagram of simply-supported beam under blast with different loading rates (I_0=4kPa·s) (continued)

6.5 Concluding remarks

The numerical analysis presented in this chapter reveals that, as the blast pulse duration decreases (or in other words the loading rate increases), the response of an RC member will undergo an increasingly more significant high shear phase before the response develops into a global bending mode. In the extreme situation with a pulse duration of order of 1ms, large shear force up to the magnitude of 5~6 times of the maximum shear force in the global bending stage

could develop within a timescale of around 0.5 ms. This phenomenon occurs in both simply-supported and fixed-end beam cases.

Based on the analysis results, it can be reasonably deduced that a) if the shear strength is reached while high shear force develops, shear failure could occur, and b) in that case, the shear failure zone or the “shear span” could be much shorter than in a quasi-static shear scenario. The quicker high shear force and shear failure develops, the shorter the shear span, and ultimately the shear failure could enter into a direct shear scenario with very short shear span.

The development of the high shear response is independent from the global bending mode; as a matter of fact, when high shear is reached the majority of the member remains virtually un-deformed. This indicates that the development of the high shear response is originated from the shear mode, ranging from direct shear to diagonal shear. Thus, to be able to predict the high shear using a simplified method such as a single-degree-of-freedom (SDOF) system it will be necessary to take into account the shear modes. Further discussion on the simplified predictions will be presented in Chapter 8.

Under the assumption of an elastic shear resistance, the high shear phase will quickly diminish as the response develops into a global bending mode. The shear force distribution correspondingly resumes a typical distribution as one can expect under a static loading with a uniform distributed load. The maximum shear force in the global bending stage is thus dictated by the yield bending strength of the member.

However if the magnitude of the shear force in the transient high shear phase exceeds the corresponding shear capacity, shear failure can develop before the member enters into the global bending phase. A RC member failing in shear has been frequently observed from the past blast incidents or from blast experiments, but the dynamic shear response phenomenon and the

corresponding shear resistance mechanisms have not been well understood and very limited information is available from the existing literature. Existing knowledge of blast resistance and the analysis methods are primarily limited to flexure-dominated mode. Most design methods mainly adopt a flexural mode-only hypothesis for the member and focuses in the global bending stage.

While the high shear phenomenon may readily be predicted using even a beam element model, the dynamic shear strength, on the other hand, is not well understood. In fact there is very little information in the literature regarding the shear resistance in a high dynamic response environment. Based on the general analysis described in this chapter, it can be anticipated that the factors influencing the dynamic resistance will include the variation of the shear span, in addition to the possible enhancement of the material strength due to the high strain rate. As has been demonstrated, the shear span tends to decrease with decrease of the loading duration, and this implies an increase in the shear strength even without any material enhancement due to the strain rate. This is to be investigated thoroughly in Chapter 7.

It is also worth noting that in the peak shear response phase, the time required to reach the peak shear force can be very short (unlike the global bending), thus high strain rate is involved and this implies the dynamic material behaviour and related strain rate effect can be an influential factor on the dynamic shear resistance. This adds to the effect of the change (reduction) of shear span on the dynamic shear resistance. A full investigation on the dynamic shear resistance mechanisms is presented in the next chapter.

Chapter 7: Dynamic shear resistance of RC member: shear mechanisms and influence of material rate effect

7.1 Introduction

As demonstrated in Chapter 6, the involvement of the three basic deformation modes is generally sequential in time. Depending on the intensity and rate of the blast loading, the high shear force developed in first two consecutive stages could lead to a shear failure before the response develops into the global bending mode. Since the high shear stress during the transient shear phase is rather concentrated near the support, if shear failure occurs at this stage it will tend to also concentrate within a narrow band and even become what is known as direct shear failure.

It is generally understood from the mechanics of reinforced concrete that, as the shear span narrows, the shear resistance will increase (Fenwick and Pauley 1968; Kani 1979). Therefore, one important mechanism that will need to be looked at in the investigation of the dynamic shear resistance would be the increase of the shear strength with decrease of the shear span, and how the decrease of the shear span correlates to the loading rate in the dynamic response

process. In the meantime, as the high shear response occurs within a very short timescale, on an order of milliseconds, the material could be subject to very high strain rate (unlike in the global bending stage), and hence the response and damage can also be markedly influenced by the material rate effect.

In this chapter, a numerical study is carried out to investigate the transient dynamic shear phenomenon in a more realistic reinforced concrete response environment. In particular, the dynamic shear failure mechanisms and the dynamic shear resistance will be analysed from the perspective of both the dynamic structural effect, namely the shear failure zone (shear span), and the material strain rate effect.

The numerical investigation will take advantage of the rigorously calibrated FE model for reinforced concrete, as has been discussed extensively in earlier chapters. After a brief description of the numerical model for the present analysis, a quasi-static loading analysis is carried out to establish the static behaviour of the RC member and the global resistance function. The shear strength of the member and the influence of a shortened shear span on the shear resistance are then evaluated by a four-point loading scheme, in which the shear span is purposely varied within a range of interest. The trend of increase of the shear strength with decreasing shear span is established.

The numerical study then moves into the dynamic shear resistance of the RC component under blast load by varying the pulse duration. This is realised by conducting an incremental analysis with increasing magnitude of loading until failure to obtain the ultimate shear resistance for a given load duration. The shear response and degree of damage is evaluated, in line with the discussions presented in the preceding chapter using the simplified beam model. The main difference, however, is that in the present analysis the nonlinear shear behaviour can develop and thus affect the magnitude of the shear response, even without a total shear failure. The transition of the dominant mechanisms from the

transient high shear phase to the later global bending stage is further observed, along with an examination of the effective shear span at the critical shear response stage. The results from these analyses enable the establishment of quantitative relationship between effective shear span and dynamic shear resistance with the loading rate.

In order to isolate any contributions from the material strain rate sensitivity (dynamic increase factor or DIF) from other factors in the dynamic resistance capacities, the analysis is firstly carried out assuming no dynamic increase of the material strength in concrete and steel (i.e. making the material models strain rate-insensitive). In this way, the contribution of the structural effect, chiefly the reduced shear span, towards the dynamic shear resistance can be examined more clearly.

The possible contribution of material dynamic strength increase (DIF) due to high strain rate on the dynamic structural shear resistance is then assessed by comparing the results with those without the consideration of the material rate-sensitivity. The dynamic shear and flexural resistance capacities, particularly the direct and diagonal shear resistances, from simulations with the material DIF are extracted and they are compared with their counterparts without the material DIF.

To facilitate an examination into the reasons behind the level of the material DIF contribution in the observed dynamic resistance capacities, the strain rates at critical positions during the dynamic response are extracted, from which the actual strain rate attained at the time a particular failure mode occurs can be determined, and this is anticipated to tally with the observed material DIF contribution to the overall structural resistance.

7.2 Numerical modelling

7.2.1 FE model set-up

The FE modelling approach developed in Chapter 4 is employed here to simulate the dynamic response of RC members under blast loading and investigate into the dynamic shear resistance capacities.

A typically proportioned RC member needs to be chosen as a standard case for this investigation. For this purpose, the RC beam specimen “D18” which has been validated and discussed extensively in Section 4.5, is adopted and adjusted to fit for this analysis. The cross-section of 200 mm×100 mm is kept and the length is extended to 3 m with a net span of 2.8 m. The new beam has a depth-to-span ratio of 14, and the fundamental flexural mode period of the beam for a simply-supported case and a fixed-end case, assuming cracked sectional properties, is found to be 35 ms and 15.6 ms, respectively.

The original experimental RC beam, which was tested at University of Ediburgh and used in the model validation described earlier, was casted by normal concrete with a compressive strength of 44 MPa. British 500C deformed rebar was used for reinforcement and two steel bars of 10 mm in diameter and two steel bars of 12 mm in diameter were placed in compression and tension region, respectively. The stirrups were made of plain 250 MPa steel, and a uniform spacing of 50 mm is assumed for the whole span.

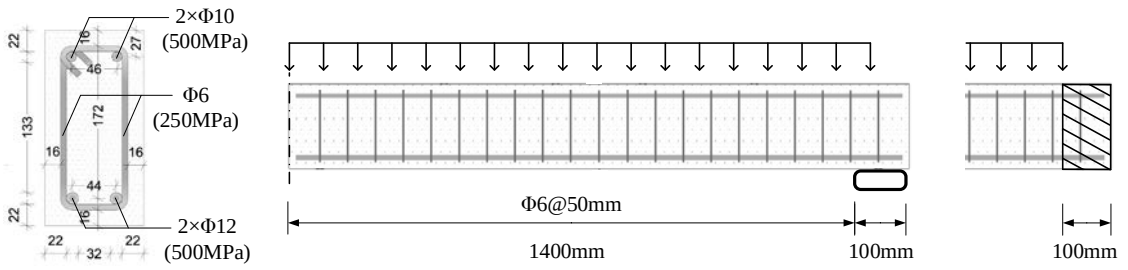

a) Cross-section b) Simply-supported c) Fixed-supported

Fig. 7.1 Layout of analysed RC beam for blast load

The basic set-up of the FE model is shown in Fig. 7.1. For simply-supported boundary, the beam is placed on a 100 mm-wide support at each end, and simple surface-to-surface contact is defined between the beam and the support, to simulate a simple support condition where axial constraint is minimal, as shown in Fig. 7.1b. The supports are made wide enough and their edges are rounded. Such treatment is simple but it is very useful in order to avoid unwanted modelling anomaly such as support failure during the numerical calculations. For fixed-supported boundary, a region of 100 mm at the end of the beam is fully restrained, which is highlighted in the dashed area in Fig. 7.1c. In the FE model, the concrete is modelled by KCC model with proposed modifications as discussed in Chapter 4.

The load is applied via uniformly distribution pressure load on the top surface of the RC beam. For the blast load, a triangular pulse shape with a zero rise time is assumed, and different blast loading rate is achieved by varying the load duration t_d while keeping a constant total impulse level I_0 as previously described adopted in Section 6.2.3.

7.2.2 Analysis of quasi-static behaviour of simply-supported RC beam

To provide a reference base for the dynamic response comparisons, the beam is firstly analysed under a quasi-static load with uniform distribution across the beam span, as shown in Fig. 7.2. This load conditions is simulated by eight 30mm-wide loading plates applied on the top surface of the beam, which are placed at equal distance apart and connected via a load-transfer mechanism to ensure the vertical force in each plate is identical. The loading plates, transfer beams and bars are assumed to be elastic and rigid. Surface-to-surface contact is defined between the loading plates and beam top surface.

The advantage of using such a loading apparatus in the numerical model is that it allows a displacement controlled process, while at the same time keeps the distribution of the loads uniform throughout the entire analysis.

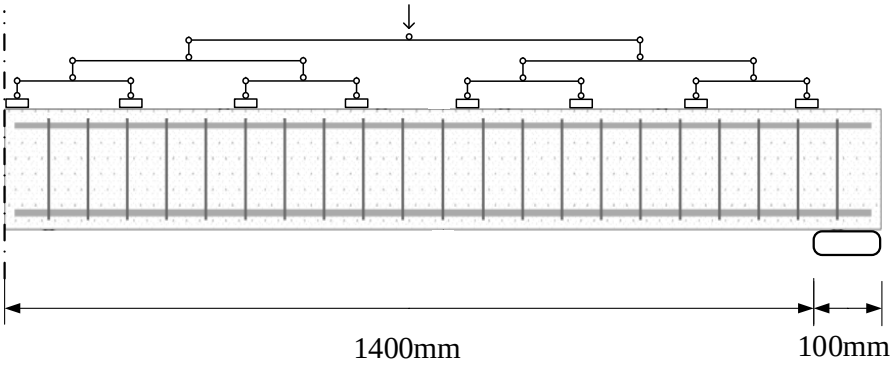

Fig. 7.2 Layout of analysed RC beam under uniformly distributed load

For the simply-supported beam, the load vs. displacement curves are shown in Fig. 7.3a and 7.3b. The damage patterns when yielding and the ultimate state (at about 75% of the maximum load post-peak) are reached, i.e., at d=24 mm and d=160 mm, are presented in Fig. 7.3c and 7.3d.

The beam exhibits a typical flexural behaviour with good ductility. The crack pattern at the peak response shows rather uniformly distributed flexural cracks. At advanced stage of the inelastic response, diagonal cracks also appear in the regions near the support, and this also rather classical. The final failure is caused by crushing of concrete, along with eventual rupture of tension rebar, at the mid-span. No further development of the shear cracks occurs, indicating that the shear strength is well on the safe side when the beam fails in flexure. Note that the maximum shear demand $4M_y / L$ is 24 kN. The above results compare well with simple predictions using standard RC analysis methods, as highlighted by dashed line in Fig. 7.3a.

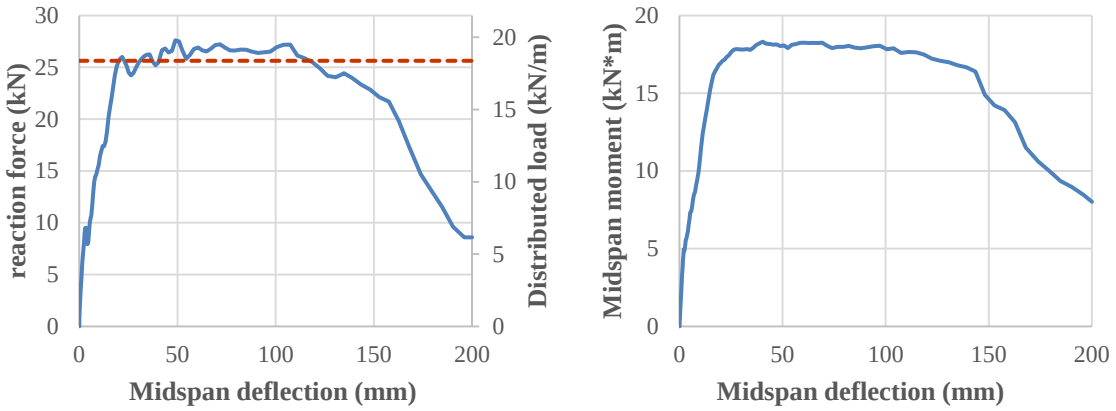

a) Reaction vs. central deflection b) Midspan moment vs. central deflection

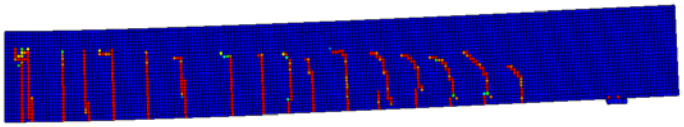

c) Damage pattern at d=24 mm

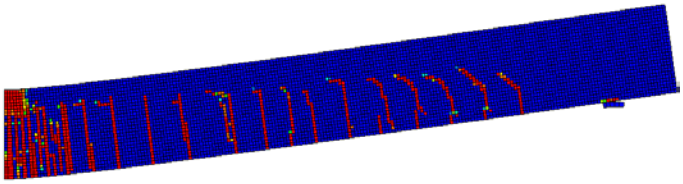

d) Damage pattern at d=160 mm

Fig. 7.3 Quasi-static performance of analysed simply-supported RC beam under uniformly distributed load

To investigate the actual shear strength of the RC beam and the trend of increase of the shear strength with a reduction in the shear span, the RC beam is subjected to a conventional four-point load test numerically, as schematically illustrated in Fig. 7.4. The point load is simulated by placing a loading plate at a distance of a to the support, and is pushed downward in a displacement controlled manner.

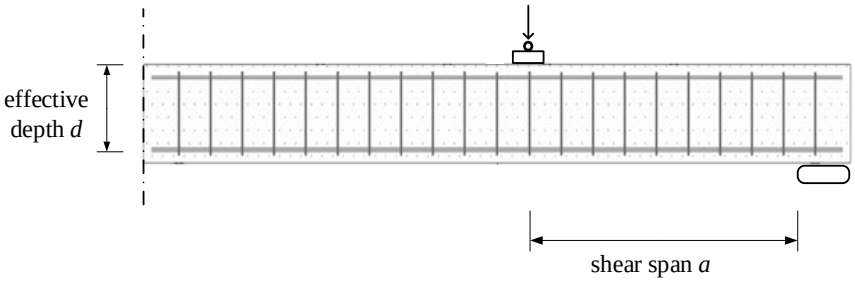

Fig. 7.4 Layout of analysed RC beam under four-point load (symmetric)

Fig. 7.5 summarise the final failure patterns for a few selected shear span cases. The shear force (equal to reaction) vs. midspan deflection relationships are shown in Fig. 7.6a. From the shear pattern, the change of the shear failure mode from a typical diagonal shear with tension (a/d = 1.5), to a diagonal shear with a compression strut (a/d = 1.0), to almost a direct shear (a/d = 0.5), is systematically demonstrated. When a/d is greater than 2.0, the failure mode is dominated by flexure for this beam.

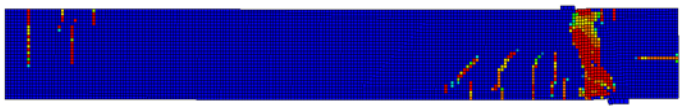

a) a/d=0.5

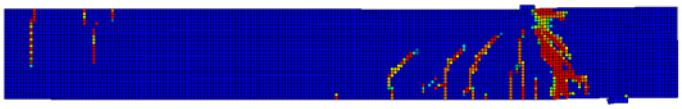

b) a/d=1.0

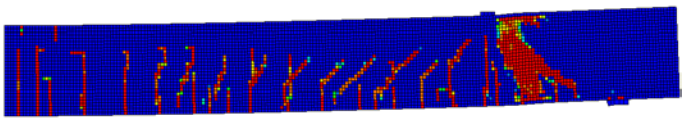

c) a/d=1.5

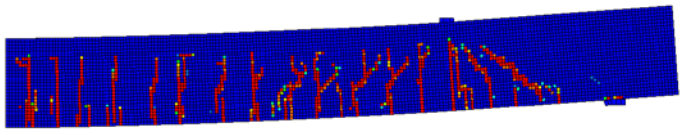

d) a/d=2.0

Fig. 7.5 Failure pattern of simply-supported RC beam under varied a/d ratios

From the shear force – deflection diagrams, it can also be observed that as the shear span reduces, the shear resistance capacity increases, and at the same time the deformability or ductility reduces. The ultimate shear resistance is plotted against the shear span ratio in Fig. 7.6b.

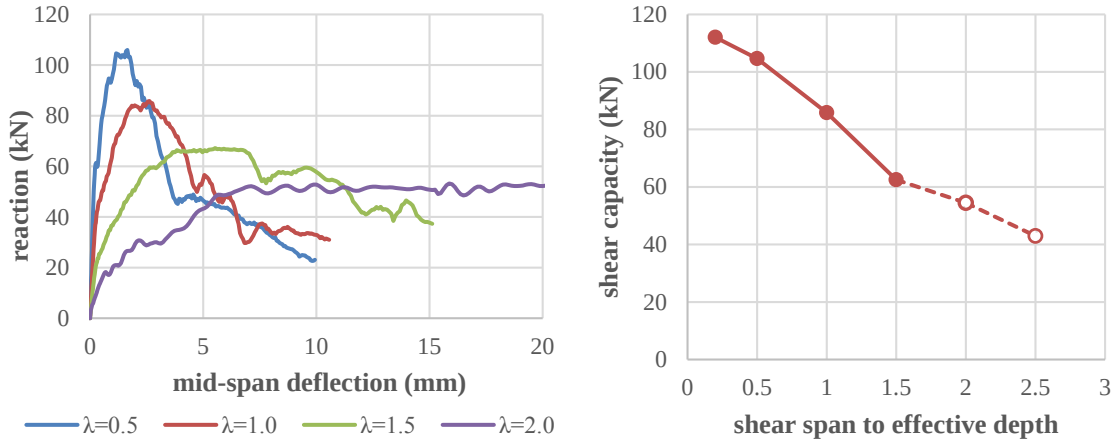

a) Load vs. displacement curve b) Shear resistance

Fig. 7.6 Shear resistance of simply-supported RC beam under varied a/d ratios

7.2.3 Analysis of quasi-static behaviour of fixed-supported RC beam

The analysis is then moved to the fixed-supported boundary. The fixed-supported beam is firstly applied by uniformly distributed load, in a way similar to the one adopted in the simply-supported cases, as illustrated in Fig. 7.2.

For the fixed-supported beam under uniformly distributed load, the load vs. displacement curves are shown in Fig. 7.7a, and the relations between bending moments at the mid-span and at the end-support, respectively, with the central deflection are plotted in Fig. 7.7b. The damage patterns when the peak moment resistance at mid-span and end-span, and the ultimate resistance are reached, i.e., at d=20 mm, d=28 mm and d=160 mm, are presented in Fig. 7.3c-7.3e.

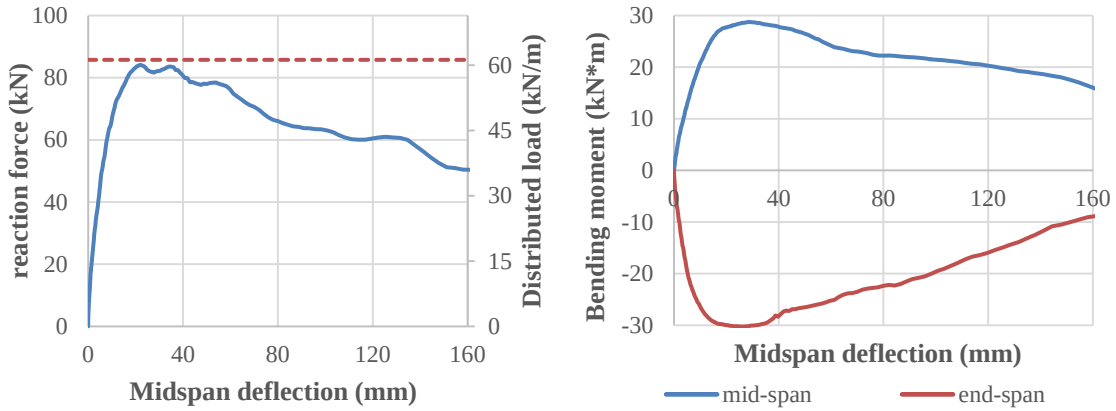

a) Reaction vs. central deflection b) Midspan moment vs. central deflection

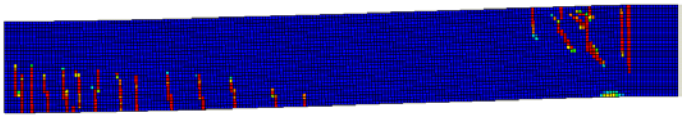

c) Damage pattern at d=20mm

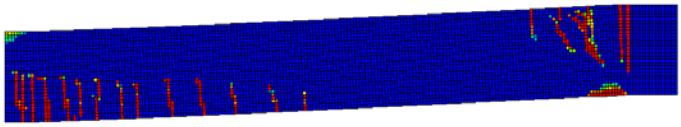

d) Damage pattern at d=28mm

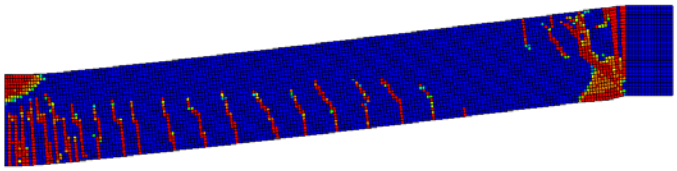

e) Damage pattern at d=160mm

Fig. 7.7 Quasi-static performance of analysed fixed-supported RC beam under uniformly distributed load

The beam exhibits a typical flexural behaviour with fairly good ductility. The final failure is caused by two plastic hinges formed at the mid-span and support, along with rebar being ruptured at the support. Minor diagonal cracks also appear in the regions near the support, but no further propagation of inclined cracks is seen.

Note that the ultimate moment capacity of the fixed-supported beam is around 30 kN·m, which is much larger than that of the simply-supported case. This is

because the stress in compression rebar can reach up to its yielding strength under the perfectly anchorage at fixed boundary. The calculated shear demand $16M_y / L$ agrees favourably with the numerical results, as indicated by dashed line in Fig. 7.7a.

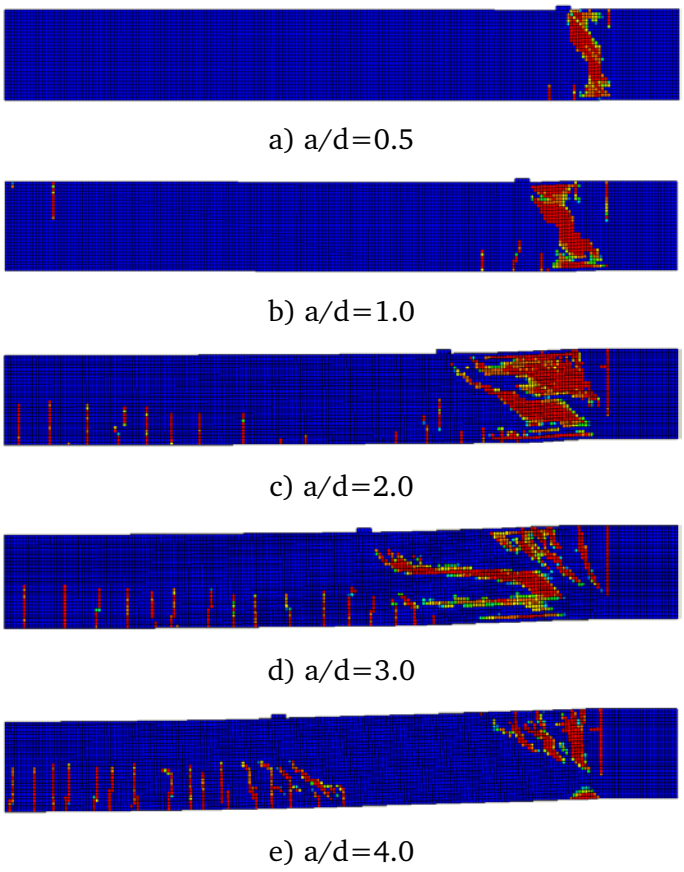

a) a/d=0.5

b) a/d=1.0

c) a/d=2.0

d) a/d=3.0

e) a/d=4.0

Fig. 7.8 Failure pattern of fixed-supported RC beam under varied a/d ratios

The fixed-supported beam is further analysed in a four-point loading scenario, similar to the one illustrated in Fig. 7.4. The failure pattern of the fixed-supported beam in four-point loading test, as under different *a/d* ratios, is summarised in Fig. 7.8. Similarly, it demonstrates the general trend of transition of failure patterns, from direct shear (*a/d*=0.5~1.0), to diagonal shear (*a/d*=1.5~3.0), to flexure (*a/d*= 4.0).

From the shear force - deflection diagrams presented in Fig. 7.9a, and the ultimate shear resistance plotted against the shear span ratio in Fig. 7.9b, it can be observed that for the same *a/d* ratio, shear resistance for fixed-supported beam is higher than that of simply-supported beam, but the failure mode is still governed by shear in small to intermediate shear span range (*a/d* <4).

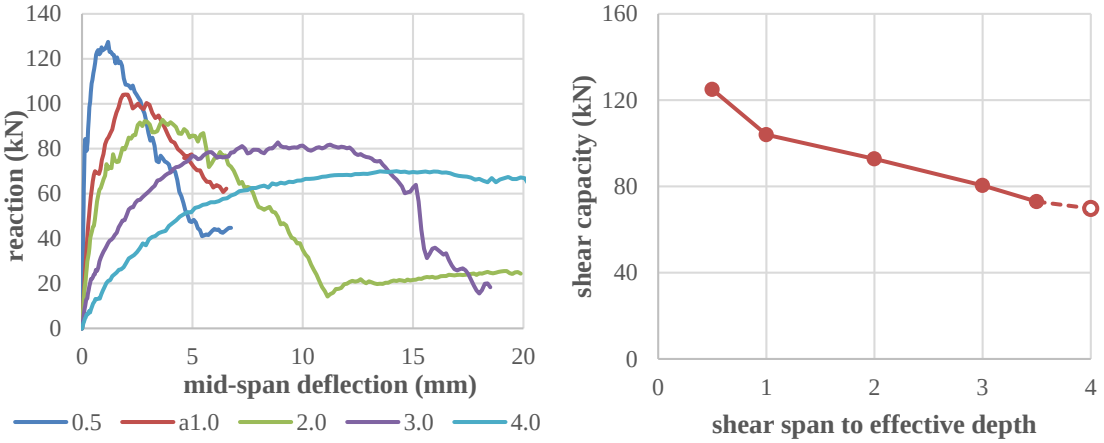

a) Load vs. displacement curve b) Shear resistance

Fig. 7.9 Shear resistance of fixed-supported RC beam under varied a/d ratios

7.2.4 Determination of effective shear span and shear resistance under distributed load

In the previous section, the relation between the reduction of shear span and the increase of shear resistance is clearly demonstrated via quasi-static four-point loading analysis. Under more complicated loads, this trend is also expected to apply such that the shear resistance would increase with the reduction of an "effective shear span" that's developed in the RC member. The terms of "effective shear span" is hereby introduced to account for the fact that the shear force within the high shear region would generally be non-uniform. This section provides some further analysis in attempt to determine the effective shear span developed in general load scenarios.

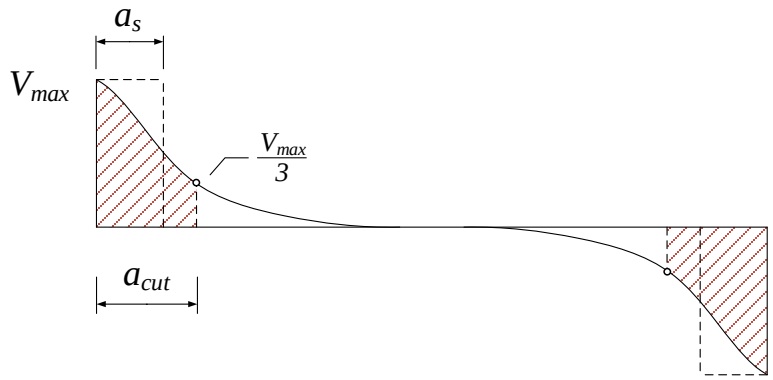

Fig. 7.10 Schematic view of practical method to determine the width of effective shear span

Fig. 7.10 illustrates a schematic diagram of shear force distribution under generalised distributed load or developed during an impulsive dynamic loading. Naturally, the shear resistance V_R is defined as the maximum shear force V_{max} that can be achieved in the RC beam, and this usually takes place at the support:

$$V_R = V_{\max} \tag{7.1}$$

The effective shear span a_s, is then calculated by following proposed method, which is based on the idea to retain the same shear failure "potential", and may be argued as retaining the same effective area of shear force diagram.

As shown in Fig. 7.10, the region highlighted by shadow indicates an "effective" shear area, which is measured from the support (maximum shear location) to a cut point of a_{cut} beyond which the level of the shear force may be considered as negligible with respect to the maximum shear force. In the absence of any physical evidence to justify a choice, herein we place the cut-off point at the level of 1/3 maximum shear. The effective dynamic shear span a_s is then calculated by equating an equivalent rectangular (uniform area) area of $\left(V_{\max} \cdot a_s\right)$, as highlighted by dashed lines, with the effective area.

$$a_s = \frac{\int_0^{a_{cut}} V dx}{V_{\max}} \tag{7.2}$$

For an example, the RC beam specimen analysed here has an overall span length of 1800 mm and effective depth of 178 mm, under uniformly distributed load the resulted effective shear span according to Eq. 7.2 would be 622 mm, giving an effective shear span ratio of a/d =3.5. This should yield a reasonable shear strength prediction for a simply-supported beam under uniformly distributed static load.

7.3 Dynamic shear behaviour and dynamic shear resistance for simply-supported RC beam

The dynamic shear behaviour and the corresponding dynamic shear resistance is analysed by subjecting the beam to simulated blast load of different duration (and hence loading rate). An incremental analysis is carried out. For each load duration, it is accomplished by performing multiple FE analyses under a suite of blast loads with the same load duration, each sees a finite increase in the impulse level until the load is sufficiently large to force the structure to a gross failure (collapse). The damage patterns are extracted to examine the change of the failure mechanisms as the loading varies. The analysis for the simply-supported RC beam case is presented in this section.

For the convenience of characterising the duration of the blast load, the load durations are set with respect to the flexural mode period, being $1.1T_f$, $0.2T_f$, and $0.03T_f$. For the short duration cases, as will be discussed later in Chapter 8, they are actually quite close to the diagonal and direct shear mode period, respectively.

7.3.1 Dynamic shear behaviour in "quasi-static" regime (blast duration on order of flexural mode period)

The RC beam is firstly subjected to a blast load of duration on the order of flexural mode period, herein in at $t_d \approx 1.1T_f$ or 40 ms, and the applied blast impulse is 12 kPa·s. This yield a peak overpressure of 0.6 MPa. For a reference this is equivalent to a reflected blast load from 71,000 kg TNT at a standoff distance of 100m accordingly to Kingery and Bulmash (1984). It could also represent blast load generated from large-scale gas explosions.

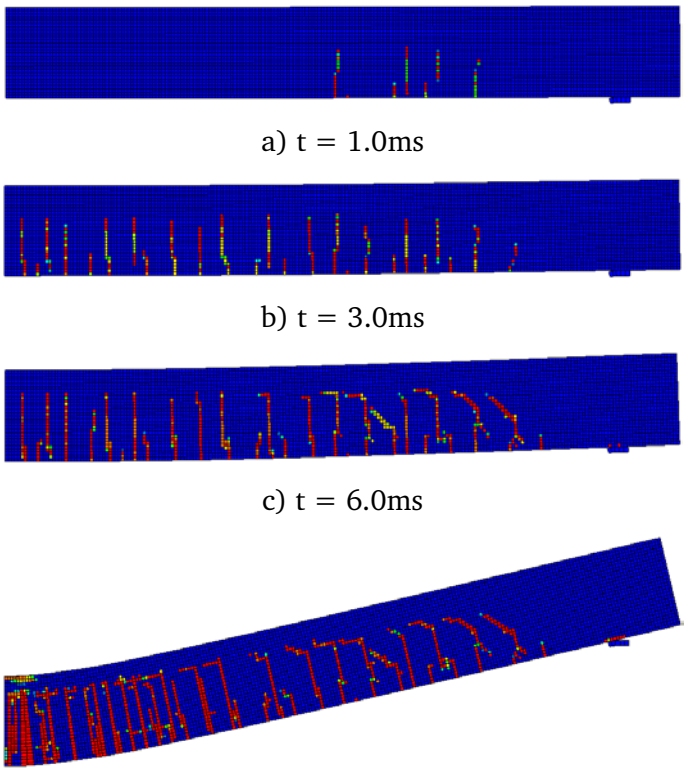

a) t = 1.0ms

b) t = 3.0ms

c) t = 6.0ms

d) t = 20ms

Fig. 7.11 Failure pattern of simply-supported RC beam under load duration t_d=40ms

Fig. 7.11 presents the intermediate and final damage patterns of the beam. The time histories of the support reaction (representing the shear force at the support region) and the midspan displacement are shown in Fig. 7.12. It can be seen

from Fig. 7.12 that the peaks of shear force and bending moment appear at around 5.7 ms. The beam experienced normal flexural cracking, and only limited diagonal cracking occurs, and finally failed due to concrete crushing and rebar rupture at mid-span. The general crack patterns are consistent with the static loading case at comparable displacement in Fig. 7.3.

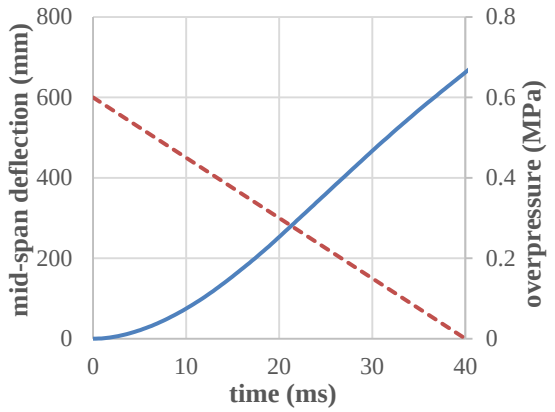

a) Mid-span deflection

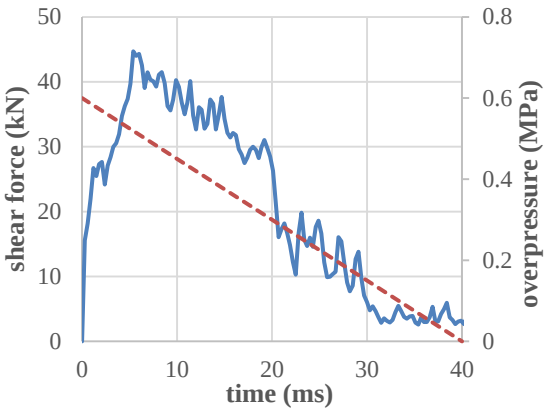

b) Reaction force

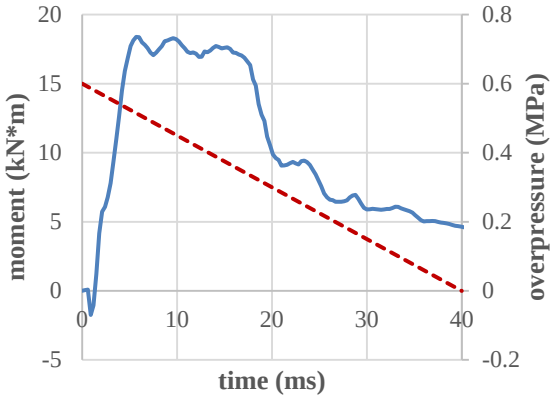

c) Mid-span bending moment

Fig. 7.12 Time history of deflection and shear force of simply-supported RC beam under load duration t_d=40 ms

Although transient shear wave phenomenon still occurs in the initial phase of the response, the magnitude of the shear force was not sufficient to cause a shear failure, and the response progresses into the global bending mode. It is noted that the maximum shear force of 47 kN developed in this case is quite

similar to the shear strength in the static loading with a normal shear span of $a/d = 2.0$, as shown in Section 7.2.2.

The distributions of shear force and bending moment at representative time instants are presented in Fig. 7.13. The shear force and bending moment, are calculated via combined effect of shear and normal stress over the cross-section, respectively. As can be seen, the diagrams at peak shear force and bending moment are generally consist with the distribution o under quasi-static load. However it must be noted that the shear force diagram does not follow exactly a triangular shape. This is because a great amount of flexural cracks have been developed near the quarter span and towards the support, which effectively create a smaller shear span.

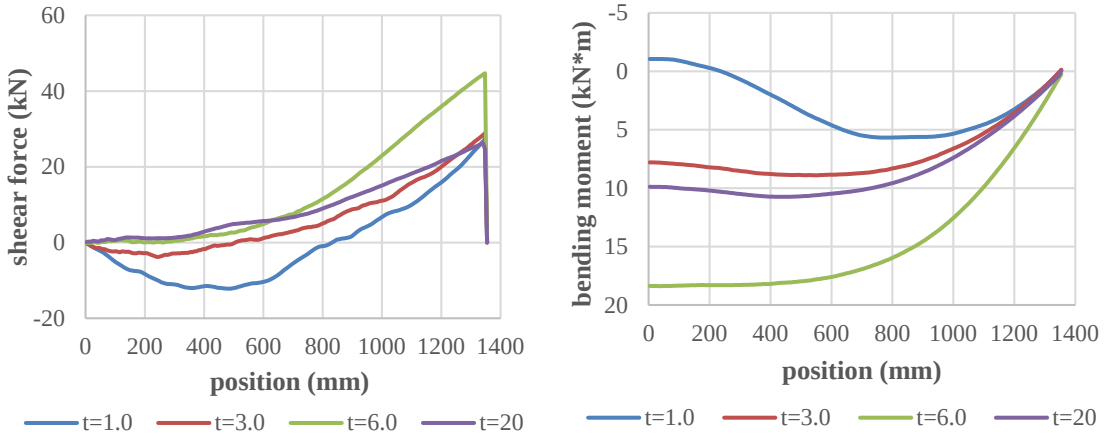

a) Shear force diagram b) Bending moment diagram

Fig. 7.13 Distribution of shear force and bending moment of simply-supported RC beam under load duration t_d=40 ms

7.3.2 Dynamic shear behaviour in "dynamic" regime (blast duration a fraction of flexural mode period)

The beam is subjected to a "dynamic regime" loading with the load duration reduced to less than 15% of the estimated flexural period, i.e.

$t_d = 4.0ms < 0.15 \cdot T_f$. The applied impulse is 10.5 kPa·s, and with the assigned duration the load is equivalent to a reflected blast load from 3100 kg TNT at a standoff distance of 17 m. Fig. 7.14 shows damage pattern at typical time instants, and the time histories of the mid-span deflection, support reaction force, and mid-span bending moment are presented in Fig. 7.15. The peak shear force is reached at around 1.5 ms and is about 105 kN, which is 2.1 times of the static shear strength under a/d = 2.0. The damage pattern indicates a typical diagonal shear failure, with a shear span of about 1.5 time of effective depth d.

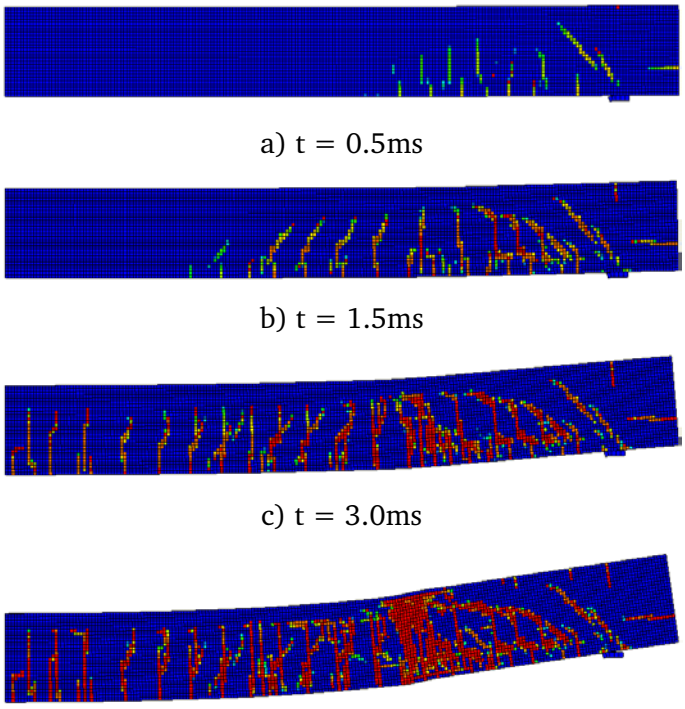

a) t = 0.5ms

b) t = 1.5ms

c) t = 3.0ms

d) t = 5.0ms

Fig. 7.14 Failure pattern of simply-supported RC beam under load duration t_d=4.0 ms

From the response time histories, it can be seen that a significant transient high shear phase develops in the first stage of the response while the overall deflection is still very small. From the damage patterns, it can be seen that multiple diagonal shear cracks are formed after 1.5ms, and tips of these cracks propagate and link with each other, and finally fails at t=5.0 ms. This shows

that in the current loading rate shear damage emerges as a result of the transient high shear response.

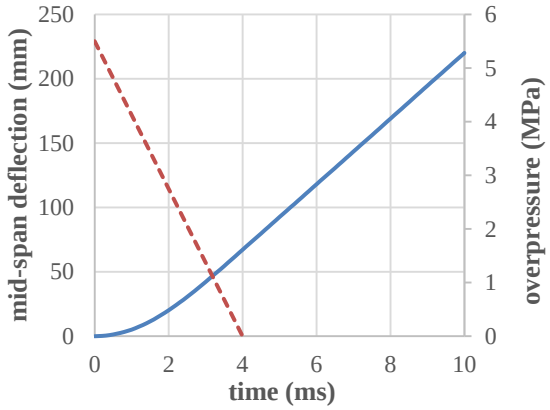

a) Mid-span deflection

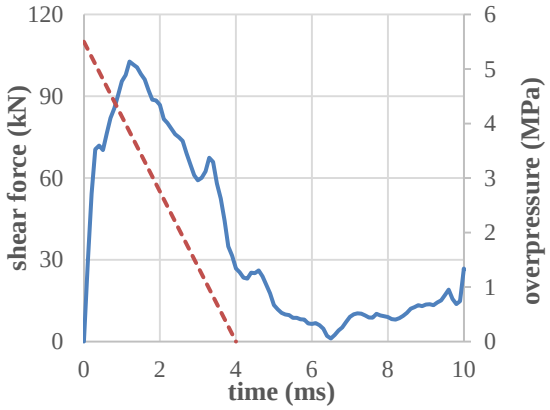

b) Reaction force

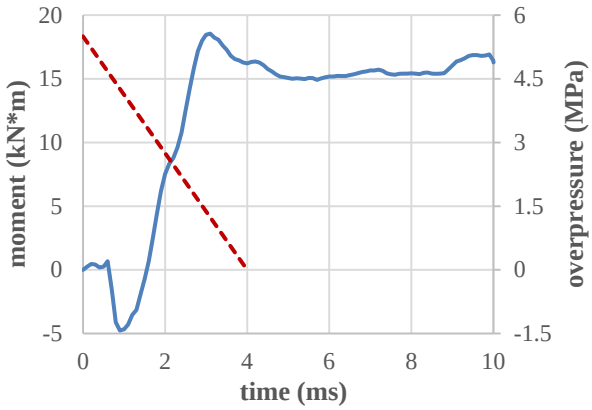

c) Mid-span bending moment

Fig. 7.15 Time histories of deflection and shear force of simply-supported RC beam under load duration t_d=4.0 ms

Fig. 7.16 show the distributions of the shear force and bending moment at key time instances. As can be seen, when shear crack develops, the high shear force tends to concentrate within a length of about 1.5 times of the effective section depth. This echoes the shear crack pattern as observed in Fig. 7.5.

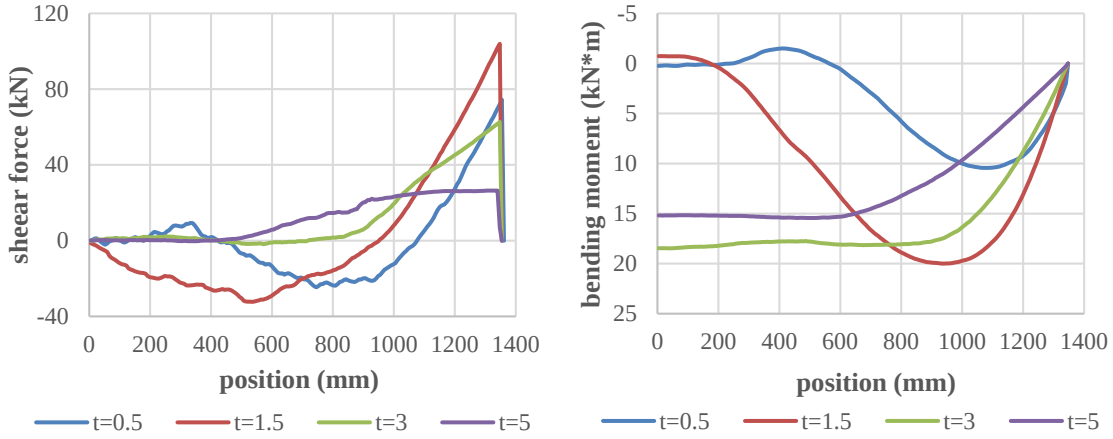

a) Shear force diagram b) Bending moment diagram

Fig. 7.16 Distribution of shear force and bending moment of simply-supported RC beam under load duration t_d=4.0 ms

7.3.3 Dynamic shear behaviour in "impulsive" regime

The RC beam is then subjected to blast load with further reduced duration, herein $t_d = 1.0ms < 0.025 \cdot T_f$, with the impulse of 7 kPa·s, which is equivalent to a reflected blast load from 220 kg TNT at a standoff distance of 5 m. Fig. 7.17-18 show the damage patterns and time histories of the beam. The peak shear force (maximum shear resistance) is found to be around 152 kN, which is 3.4 times the static shear strength and 1.5 times of that measured in the dynamic diagonal shear strength, and it occurs at 0.3~0.5 ms. The damage pattern shows clearly a direct shear mode with a shear damage zone of only about 0.5*d*. A complete vertical shear slip was formed close to the support at 1.0 ms.

The achieved dynamic shear resistance of 152 kN is clearly attributable to the small shear span. However, comparing to the static test of the shear strength at a comparable shear span, which achieved a shear strength of 106.2 kN, this is still about 45% larger. The reason may be explained by the fact that in the dynamic shear resistance the rapidly increasing shear force leaves little time for fracture

to develop in a progressive manner as would be in the case under static loading. This results in a dynamic enhancement in the whole section resistance, although the material itself is artificially made rate insensitive in the present analysis.

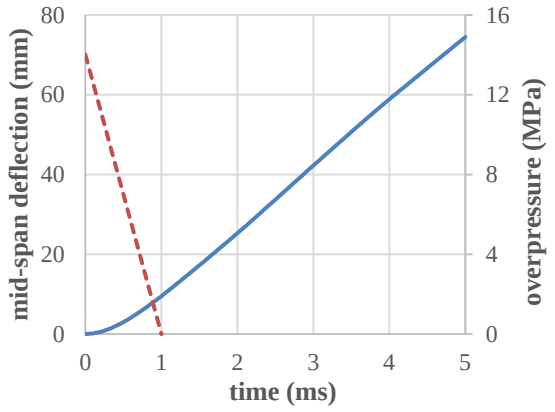

a) Mid-span deflection

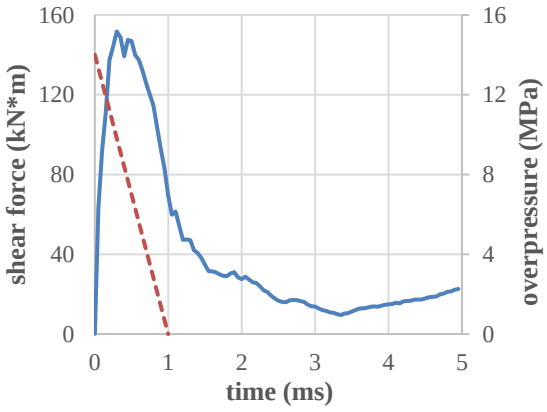

b) Reaction force

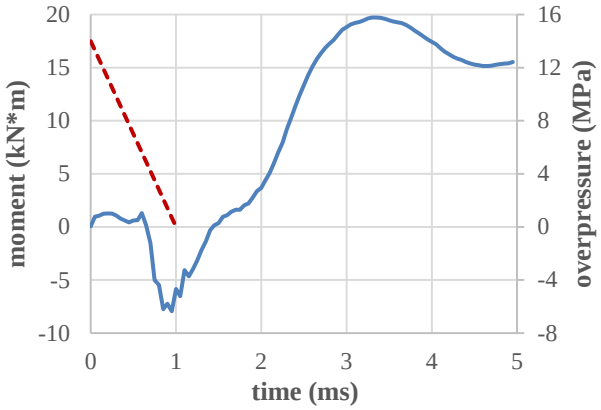

c) Mid-span bending moment

Fig. 7.17 Time histories of deflection and shear force of simply-supported RC beam under load duration t_d=1.0 ms

Fig. 7.19 shows the distributions of the shear force and bending moment at key time instances. As can be seen from the shear force diagram, when the maximum shear force is reached, the high shear force tends to concentrate within 100mm to the support, which is about 0.5 times of the effective section depth.

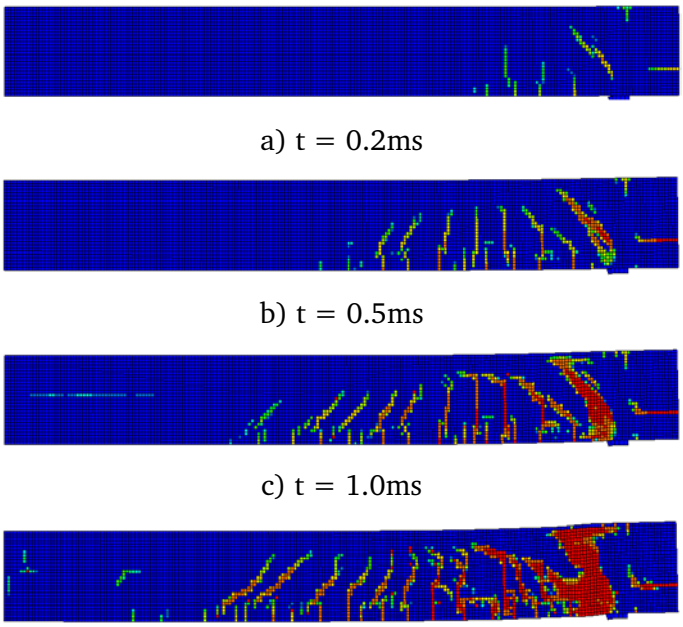

a) t = 0.2ms

b) t = 0.5ms

c) t = 1.0ms

d) t = 2.0ms

Fig. 7.18 Damage pattern of simply-supported RC beam under load duration t_d=1.0 ms

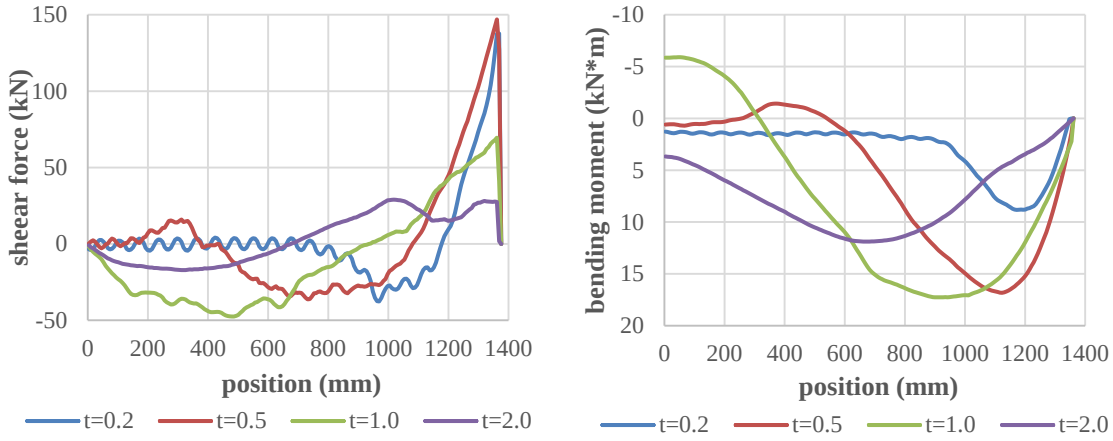

a) Shear force diagram b) Bending moment diagram

Fig. 7.19 Distribution of shear force and bending moment of simply-supported RC beam under load duration t_d=1.0 ms

7.4 Dynamic shear behaviour and dynamic shear resistance for fixed-supported RC beam

The above analysis is further extended to fixed-supported RC beams. For the convenience of characterising the duration of the blast load, the load durations are set with respect to the flexural mode period, being $1.2T_f$, $0.2T_f$, and $0.03T_f$.

7.4.1 Dynamic shear behaviour under blast duration in the order of flexural period ($t_d > T_f$)

The fixed-supported RC beam is firstly analysed under a blast impulse of 10 kPa·s and duration of 20 ms, which is about 1.2 times of the deduced flexural period. This is equivalent to a reflected blast load from 25,000 kg TNT charge at a standoff distance of 60 m accordingly to Kingery and Bulmash (1984).

Fig. 7.20 and 7.21 give the time histories and failure patterns of the beam response. Under such long pulse duration, the beam experienced normal flexural type of behaviour, and the maximum shear force is around 98 kN and reached at t=5 ms, which is close to the static shear demand under uniformly distributed load (~82 kN in Fig. 7.7a). Flexural hinges form near both support and at midspan, and diagonal cracking occurs in the vicinity of the fixed support. The beam finally failed due to concrete crushing in the compression region, as shown in Fig. 7.21. The general crack patterns are consistent with the static loading case in Fig. 7.8.

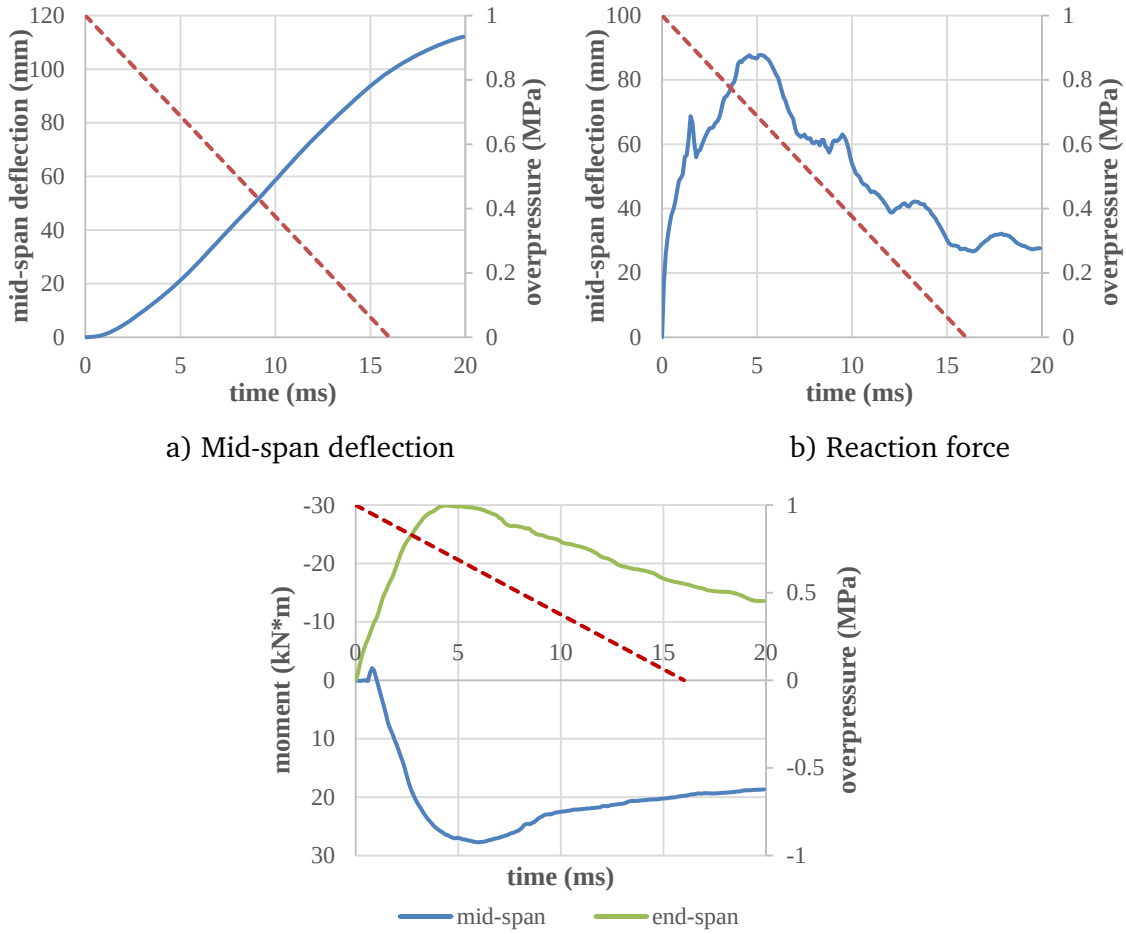

a) Mid-span deflection

b) Reaction force

c) Mid- and end-span bending moment

Fig. 7.20 Time histories of response of fixed-supported RC beam under load duration t_d=20.0 ms

The distributions of the shear force and bending moment at key time instances are plotted in Fig. 7.22. It can be seen that when the maximum shear force is reached, the shear force diagram is basically in a triangular shape, and the shape pf bending moment diagram is also quite close to the shape of that under quasi-static distributed load.

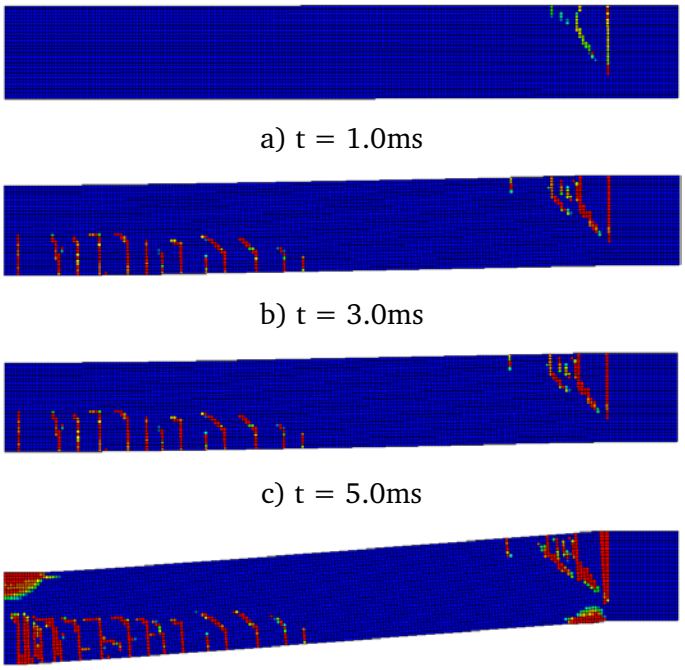

a) t = 1.0ms

b) t = 3.0ms

c) t = 5.0ms

d) t = 15ms

Fig. 7.21 Damage pattern of fixed-supported RC beam under load duration t_d=20.0 ms

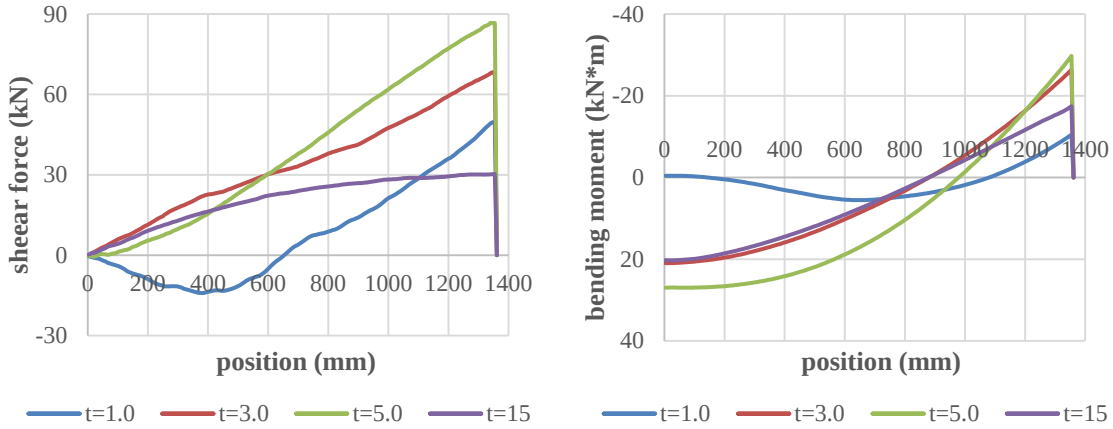

a) Shear force diagram b) Bending moment diagram

Fig. 7.22 Distribution of shear force and bending moment of fixed-supported RC beam under load duration t_d=20.0ms

7.4.2 Dynamic shear behaviour under blast duration close to dynamic regime ($t_d \approx 0.2T_f$)

The beam is then subjected to blast loading with load duration reduced to around 40% of the estimated flexural period for fixed-supported beam, i.e. $t_d = 4.0ms \approx 0.2T_f$. The critical impulse is 6 kPa·s. This is equivalent to a reflected blast load from 2,000 kg TNT charge at a standoff distance of 18 m accordingly to Kingery and Bulmash (1984).

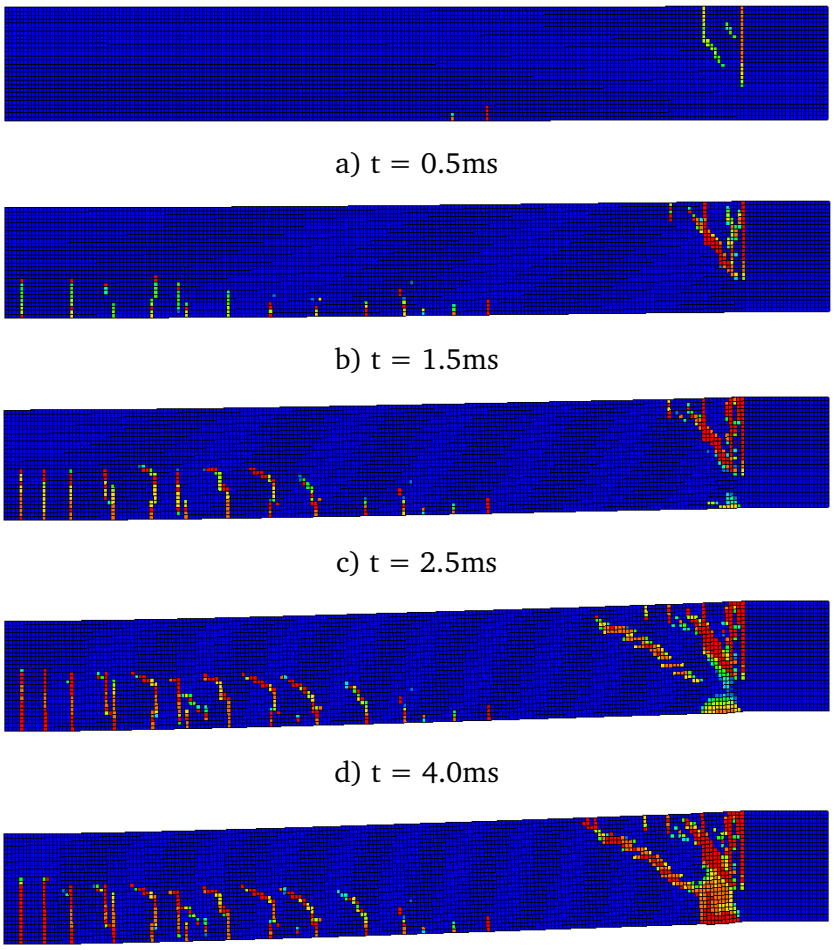

a) t = 0.5ms

b) t = 1.5ms

c) t = 2.5ms

d) t = 4.0ms

3) t = 6.0ms

Fig. 7.23 Failure pattern of simply-supported RC beam under load duration t_d=4.0 ms

Fig. 7.23 shows damage patterns at typical time instants, and the time histories of the mid-span deflection, support reaction force, and mid-span bending moment are presented in Fig. 7.24. It can be seen that the maximum shear force is as high as 109 kN and appears at around 1.5 ms. The damage pattern indicates that a critical diagonal shear crack starts to form at the mid-depth level at t=4.0 ms and lead to a diagonal shear failure, with a shear span of about 1.5 time of effective depth *d*.

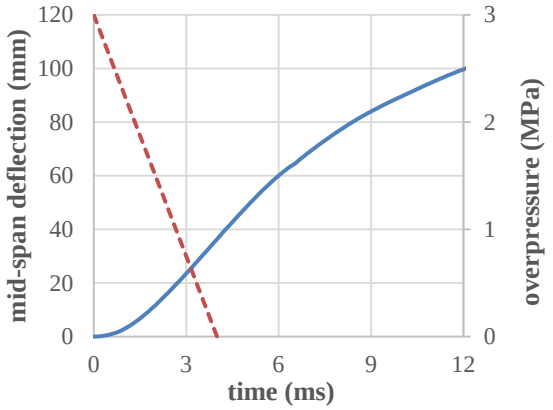

a) Mid-span deflection

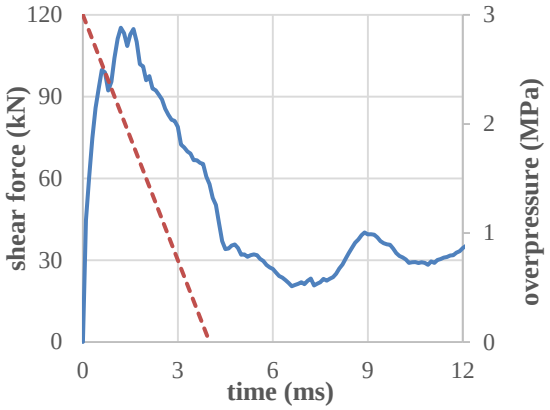

b) Reaction force

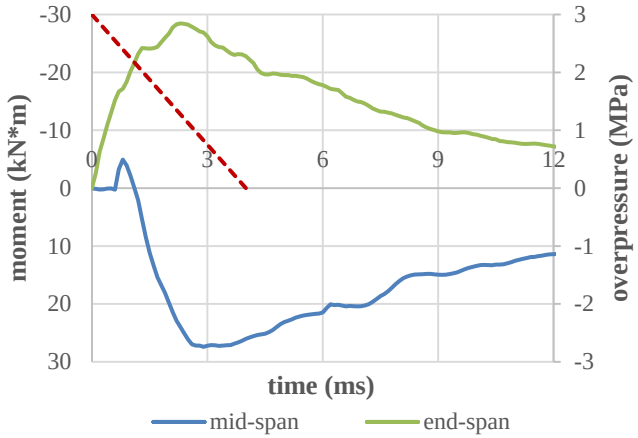

c) Mid- and end-span bending moment

Fig. 7.24 Time histories of response of fixed-supported RC beam under load duration t_d=4.0 ms

The distribution of shear force and bending moment along the span at typical time instants is presented in Fig. 7.25. As read from the diagram at t=1.5 ms

when maximum shear force is reached, the high shear force tends to concentrate within a length of about 1.5 times of the effective section depth (read from one-third point of V_{max}). This echoes the shear crack pattern as observed in Fig. 7.23.

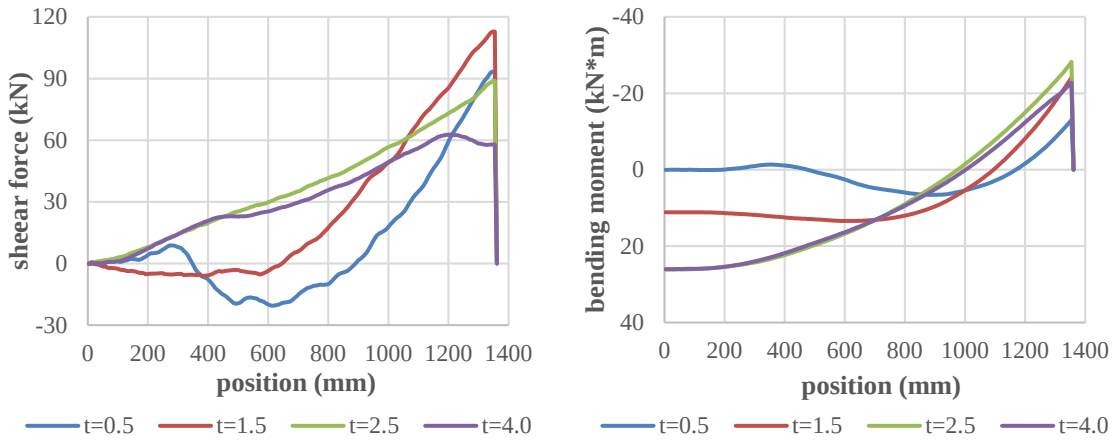

a) Shear force diagram b) Bending moment diagram

Fig. 7.25 Response of fixed-supported RC beam under load duration t_d=4.0 ms

7.4.3 Dynamic shear behaviour under blast duration close to impulsive regime ($t_d \approx 0.03T_f$)

Fig. 7.26-27 show the time histories and damage patterns of the RC beam subjected to an impulse of 5 kPa·s and a load duration of 0.5 ms. When the RC beam is subjected to such an extreme short load duration, shear force as high as 206 kN was immediately developed at 0.3 ms and deteriorated at 0.6 ms, before any significant bending moment being developed at the mid-span position, as shown in Fig. 7.26b.

The maximum negative moment at the fixed support is reached at the same time as the shear force, suggesting that the direct shear failure is caused by a combined effect of shear and flexural failure at the fixed support. This is because the perfectly anchored rebar in the compression side also contributes

significantly to the overall direct shear resistance, and the maximum shear force is higher than that in the simply-supported case. The damage pattern in Fig. 7.27 suggests that a very steep inclined crack starts to form from t=1.0 ms and results in a direct shear failure near support.

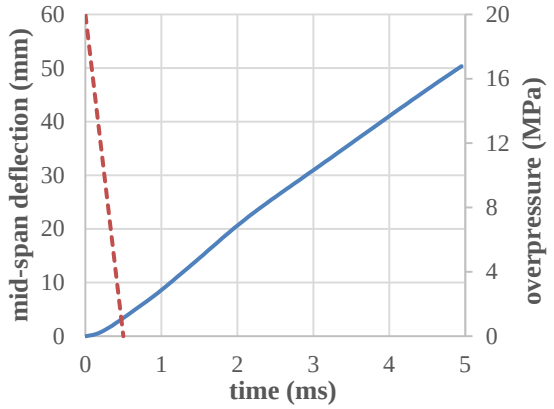

a) Mid-span deflection

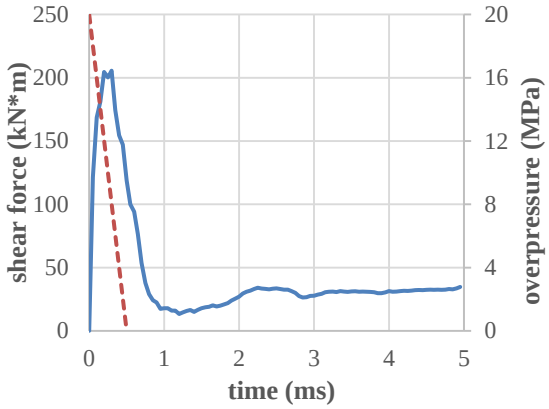

b) Reaction force

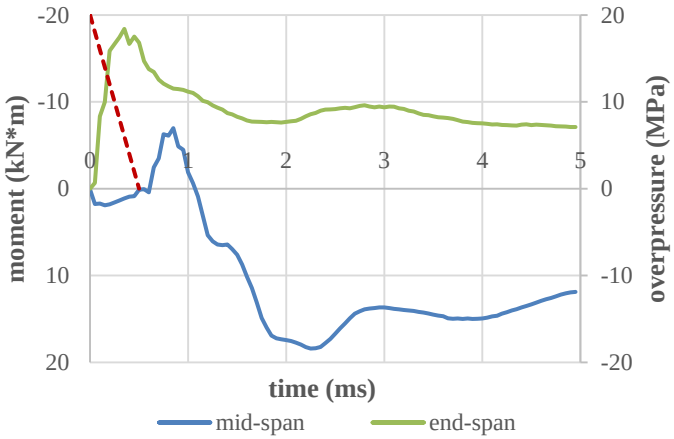

c) Mid- and end-span bending moment

Fig. 7.26 Time histories of response of fixed-supported RC beam under load duration t_d=0.5 ms

The shear force and bending moment diagrams at key time instances are presented in Fig. 7.28. The high shear force tends to concentrate within a length of 0.5*d*, when the maximum shear force is reached.

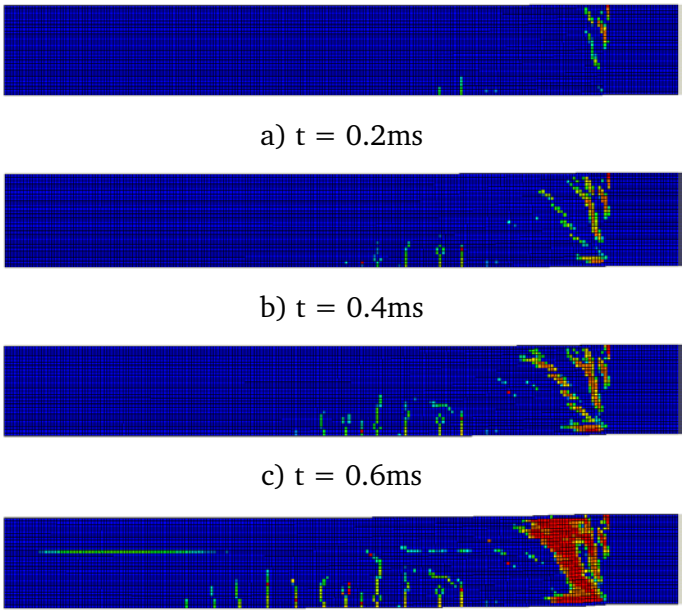

a) t = 0.2ms

b) t = 0.4ms

c) t = 0.6ms

d) t = 1.0ms

Fig. 7.27 Failure pattern of fixed-supported RC beam under load duration t_d=0.5 ms

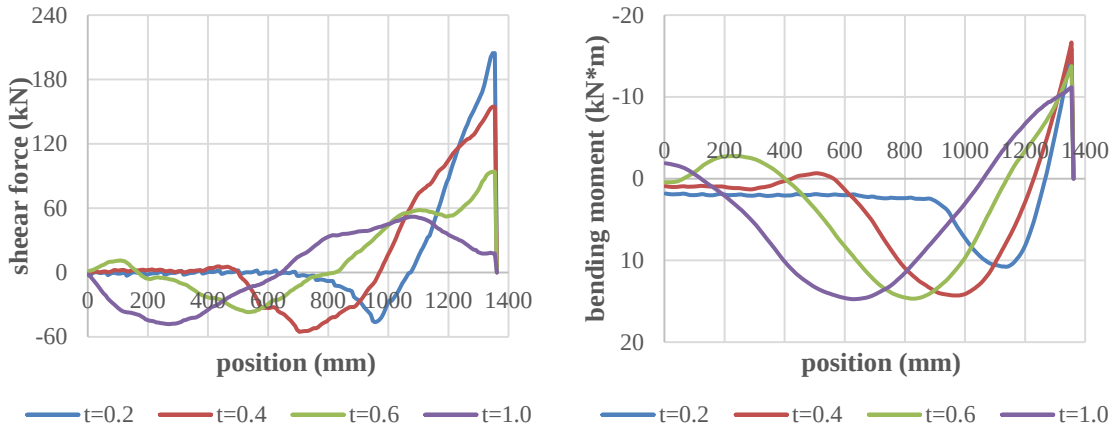

a) Shear force diagram b) Bending moment diagram

Fig. 7.28 Response of fixed-supported RC beam under load duration t_d=4.0 ms

7.5 Variation of the effective shear span in dynamic shear response

The above analysis has demonstrated clearly that in actual RC beam response, transient high shear phase develops much in a similar fashion as already shown in the simple beam analysis in Chapter 6. It further demonstrates that when the peak shear response occurs under high rate loading, only a small effective shear span has developed, and this has been an important role in the spontaneous dynamic shear resistance. It is the relative magnitude of the peak shear force to the corresponding dynamic shear resistance that determines whether the beam would be capable of withstanding the high shear phase before transitioning into a global bending response stage. Since the dynamic resistance depends on the dynamic shear span, which in turn depends on the dynamic loading rate, there is a coupled phenomenon between the force input and the resistance output.

The crucial factor in the analysis of the high shear phenomenon is therefore the effective shear span, which determines the dynamic shear resistance but is in itself is a result of the dynamic response process. This section provides some further analysis in attempt to figure out the trend of correlation between the effective dynamic shear span and the loading rate as represented by the pulse duration, for the two analysed boundary conditions.

7.5.1 Effect of loading rate on effective dynamic shear span

Following the proposed method of shear span calculation in Section 7.2.4, the effective shear spans and dynamic shear resistances as obtained from the analysis in Section 7.3∼7.4, together with some extended cases, are plotted with respect to load duration in Fig. 7.29. The load duration is “normalised” by the flexural periods of the RC beams, which is 35 ms for simply-supported and 16

ms for fixed-supported beams. Data points representing direct and diagonal shear, and flexural failure, are labelled by different colours.

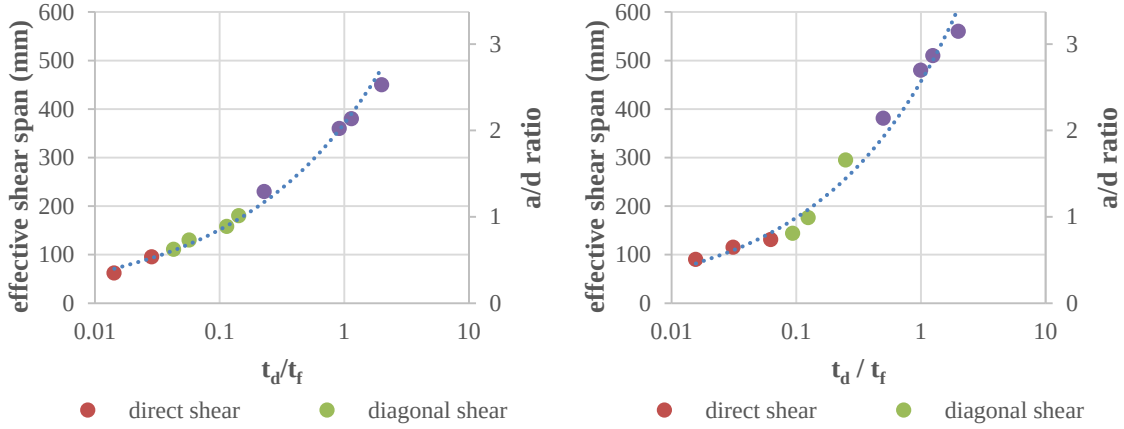

a) Simply-supported b) Fixed-supported

Fig. 7.29 Effective shear span of RC beams under varied load durations

It can be seen from the figure that the general trend of the correlation between effective shear span and the loading rate for the two boundaries are similar. As seen in both boundary conditions, the direct shear failure can only occur when high shear is built to direct shear strength within around 1.0 ms ($<0.03T_f$) for this beam. The measured a/d ratio for direct shear failure is less than $0.6d$ and $0.7d$ in simply-supported and fixed-supported boundary, respectively.

Diagonal shear failure can happen for a limited range of durations. For simply-supported boundary it is around 1~5ms and for fixed-supported boundary is around 1~4 ms, both of which are less than 30% of their respective flexural period T_f. The effective shear span can also vary from $0.8d$ ~$1.5d$.

For t_d higher than 30% of T_f, the beam fails in flexure, and when $t_d = T_f$, a/d equals 2.1 for simply-supported and 2.7 for fixed-supported. The ratio a/d ratio continues to increase with the load duration and gradually approaching the value of 3.5, which is the effective shear span under quasi-static uniformly distributed load. Note that in the flexure mode regime, the developed shear span

in simply-supported cases are generally shorter than that of fixed-supported, this echoes with the observation in Fig. 7.12, in which the shear span is reduced due to expansion of flexural cracking from mid-span towards the ends. A formula has been derived to predict the *a/d* ratio by fitting the parametric results and is as follows:

$$\frac{a_{eff}}{d} = \begin{cases} 2.5673 \cdot \left(\frac{t_d}{T_{f-f}} \right)^{0.4136} & \text{fixed} - \text{supported} \\ 2.0808 \cdot \left(\frac{t_d}{T_{f-s}} \right)^{0.3886} & \text{simply} - \text{supported} \end{cases} \tag{7.3}$$

7.5.2 Effect of loading rate on dynamic increase of shear resistance

The dynamic shear resistance obtained in Section 7.3-7.4, is further plotted against the normalised load duration in Fig. 7.30. The corresponding static shear resistance, as would be developed under the same effective shear span, is plotted

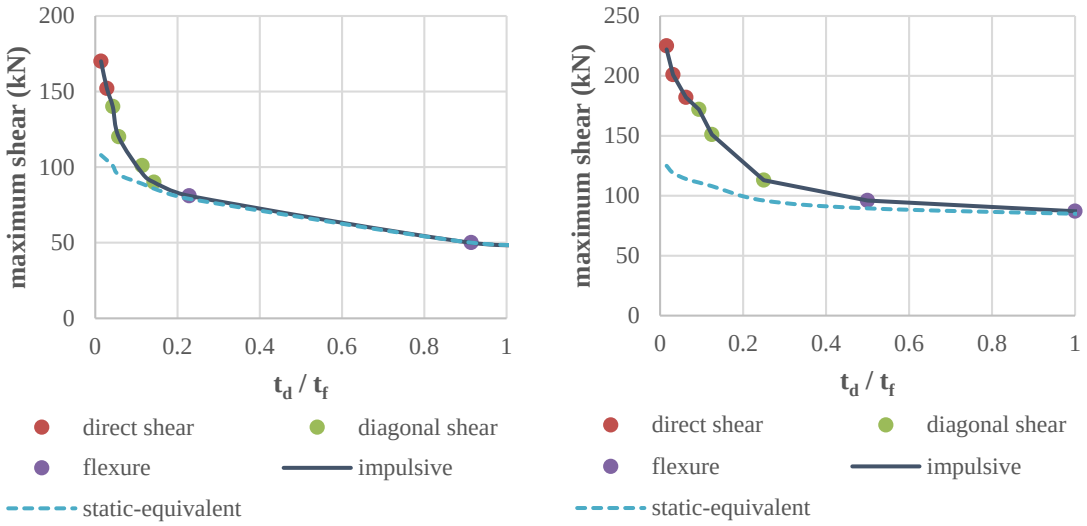

a) Simply-supported b) Fixed-supported

Fig. 7.30 Dynamic shear resistance (maximum shear) of RC beams under varied load durations

in dashed line for comparison purpose. For beams that fail in flexure and the resistance is controlled by the flexural capacity, maximum shear force is plotted.

As can be read from Fig. 7.30, when the overall failure mechanism is governed by flexure, the difference between the maximum dynamic shear force and the static shear resistance under the same shear span, is rather small. The gap between the dynamic and static shear resistance starts to increase when the load duration is reduced and the failure mode switches from flexure to shear. This is believed to be caused by dynamic effect and is seen more significant in the fixed-supported cases. As would be discussed in details in Chapter 8, this is because the flexural period of fixed-supported members is closer to the period of shear-dominated modes.

The dynamic enhancement factor, which is defined as the ratio between the dynamic and static shear resistance, is plotted against the normalised load duration in Fig. 7.31. It reveals that under direct shear mode, an enhancement factor of 1.7~1.8 is found for fixed-supported cases, and 1.4~1.6 is found for simply-supported cases. Under diagonal shear mode, the factor varies from 1.1~1.6 for fixed-supported, and from 1.05~1.4 for simply-supported cases.

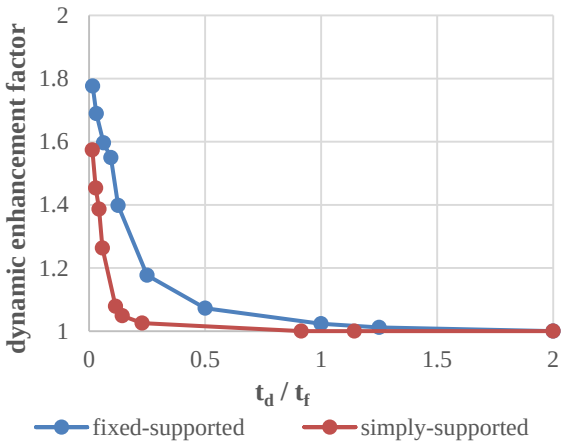

Fig. 7.31 Dynamic enhancement factor under varied load durations

7.6 Definition and implementation of strain rate effect in concrete and reinforcement steel

The previous chapters have already established that while high shear force develops in the early stage of the response, the beam member also exhibits high shear resistance capacity. The increased dynamic shear resistance can be largely attributed to the reduced shear span at the critical shear response, and to some extent the rapid increase rate of the shear force also reduces the progressive failure process at the section level, which adds to the increase of the shear resistance, particularly in the direct shear regime.

The evaluation has so far purposely excluded the material strain rate sensitivity, such that the structural effect as mentioned above can be isolated conveniently. In the following section the possible role of material dynamic strength increase (DIF) due to high strain rate on the dynamic structural shear resistance will be investigated. The degree to which DIF may contribute in the increase of the dynamic shear and dynamic flexural resistance will be discussed.

This investigation is carried out by comparative studies on the dynamic resistance capacities without and with the incorporation of the material rate-sensitivity. The dynamic resistance capacities, particularly direct and diagonal shear resistances, from simulations with the material DIF are extracted and they are compared with their counterparts without the material DIF. To facilitate an examination into the reasons behind the level of the material DIF contribution in the observed dynamic resistance capacities, the strain rates at critical positions during the dynamic response are extracted, from which the actual strain rate attained at the time a particular failure mode occurs can be determined, and this is anticipated to tally with the observed material DIF contribution to the overall structural resistance.

7.6.1 DIF curves

The increase of the bulk strength of materials with the strain rate is generally defined by a dynamic increase factor, or DIF, which is a function of the strain rate. There has been extensive research interest in recent years into explaining the real nature of the DIF for concrete-like materials and it tends to be generally agreed that the increase of the apparent dynamic compressive strength of concrete at the sample scale can largely be attributed to the lateral inertia confinement effect, rather than a basic material property. The discussion on the mechanisms underlying the DIF is beyond the scope of the present investigation. Furthermore from the material point of view the dynamic shear resistance is more related to the tension and shear behaviour of concrete, for which a DIF to be imposed at the material model level is generally accepted. Therefore in the present study the strain rate effect is incorporated in the conventional way through the DIF.

There are many empirical and semi-empirical DIF curves in the literature. A set of these curves adopted in the present study are given below. For reinforcement steel, the DIF curves recommended by Malvar and Crawford (1998) is adopted,

$$DIF_s = \begin{cases} \left(\dfrac{\dot{\varepsilon}}{10^{-4}}\right)^{0.074-0.040\frac{f_y}{414}} & for \quad yielding \quad strength \\ \left(\dfrac{\dot{\varepsilon}}{10^{-4}}\right)^{0.019-0.009\frac{f_y}{414}} & for \quad ultimate \quad strength \end{cases} \tag{7.4}$$

where $\dot{\varepsilon}$ is the strain rate (s^{-1}), and f_y is the static yielding strength of steel. The DIFs for the yielding and ultimate strength are plotted in Fig. 7.32.

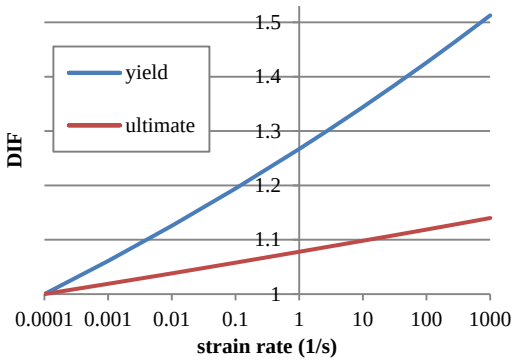

Fig. 7.32 DIF curves for yielding and ultimate strength of reinforcement steel

For concrete, the DIF curves recommended by CEB Mode code (CEB, 1990) are adopted. The DIF for concrete in compression is expressed as:

$$DIF_c = \begin{cases} \left(\dfrac{\dot{\varepsilon}_c}{\dot{\varepsilon}_{c0}}\right)^{0.014} & \dot{\varepsilon}_c \le 30s^{-1} \\ 0.012 \cdot \left(\dfrac{\dot{\varepsilon}_c}{\dot{\varepsilon}_{c0}}\right)^{1/3} & \dot{\varepsilon}_c > 30s^{-1} \end{cases} \tag{7.5a}$$

where $\dot{\varepsilon}_c$ is the compressive strain rate (s^{-1}) and $\dot{\varepsilon}_{c0} = 30\times10^{-6}\,s^{-1}$. The DIF for concrete in tension is expressed as

$$DIF_{ct} = \begin{cases} \left(\dfrac{\dot{\varepsilon}_{ct}}{\dot{\varepsilon}_{ct0}}\right)^{0.018} & \dot{\varepsilon}_{ct} \le 10s^{-1} \\ 0.0062 \cdot \left(\dfrac{\dot{\varepsilon}_{ct}}{\dot{\varepsilon}_{ct0}}\right)^{1/3} & \dot{\varepsilon}_{ct} > 10s^{-1} \end{cases} \tag{7.5b}$$

where $\dot{\varepsilon}_{ct}$ is the tensile strain rate (s^{-1}) and $\dot{\varepsilon}_{ct0} = 1\times10^{-6}\,s^{-1}$. Fig. 7.33 compares the above DIF relations of concrete in dynamic compression and tension, respectively.

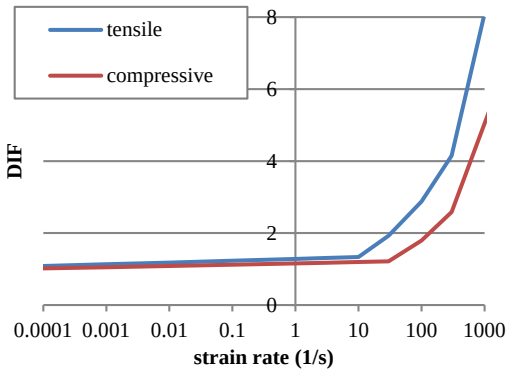

Fig. 7.33 Tensile and compressive DIF curves for concrete

7.6.2 Numerical implementation of material DIF effect in the concrete model

In the concrete model adopted in the present study (KCC model), the rate effects are implemented into both the damage accumulation and strength surface (Crawford et al. 2012), so that DIF simultaneously slows down the damage accumulation and increases the strength, leading to the fracture energy effectively being amplified by the square of DIF. Clearly, this treatment represents an upper bound of the effect of a certain DIF on the enhancement of the material. Thus direct application of the same DIF to both the strength and the ultimate failure strain, as the default treatment in KCC model, would overestimates the fracture energy of concrete under dynamic loading. Existing observations from laboratory tests on the increase of the fracture energy have not led to a generally accepted theory about this, although some test results do suggest a simultaneous increase in the ultimate failure strain as the dynamic strength increases, as presented in Fig. 7.34.

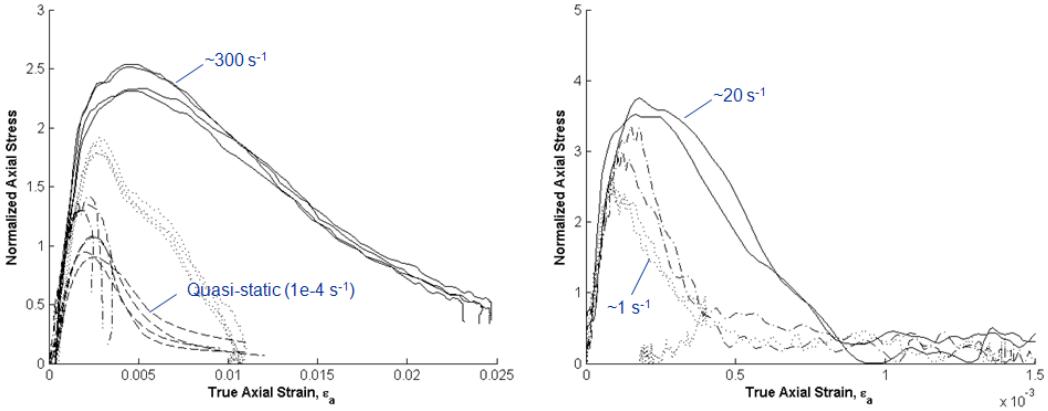

a) Unconfined compression b) Uniaxial tension

Fig. 7.34 Measured stress-strain data reflecting the effect of strain rate (Crawford et al. 2012)

A seemingly more sensible approach is to consider an approximately proportional increase of the fracture energy as strength increases on the DIF, which also implies that the dynamic ultimate strain at total failure remains generally the same as that under static load.

To realise the above rate enhancement within the current material model formulation, the static fracture energy is modified into ½ of its original value, so the dynamic fracture energy with DIF is expected to be in a normal range when the strain rate lies in the range between 10~100 /s, which are typical loading rates for blast-related load scenarios. In a way this simple approach makes the concrete to be more brittle in the quasi-static regime of the response, which should not affect the RC beam behaviour as far as the dynamic resistance capacity is concerned.

7.6.3 Verification of modified DIF effect on dynamic fracture energy

Fig. 7.35 presents the compressive and tensile stress-strain curves using default and modified settings of fracture energy, as obtained from a single element. It

can be seen that under the default treatment in Fig. 7.35a and 7.35b, both the strength and ultimate strain are enlarged, leading to the fracture energy being amplified effectively by the square of DIF. When the strain rate is larger than 10 /s, the compressive failure strain is greater than 0.10, which is not reasonable. After modification, the ultimate strains have reduced into a similar range with the static values in the target strain rate range of 100 /s, as shown in Fig. 7.35c and 7.35d.

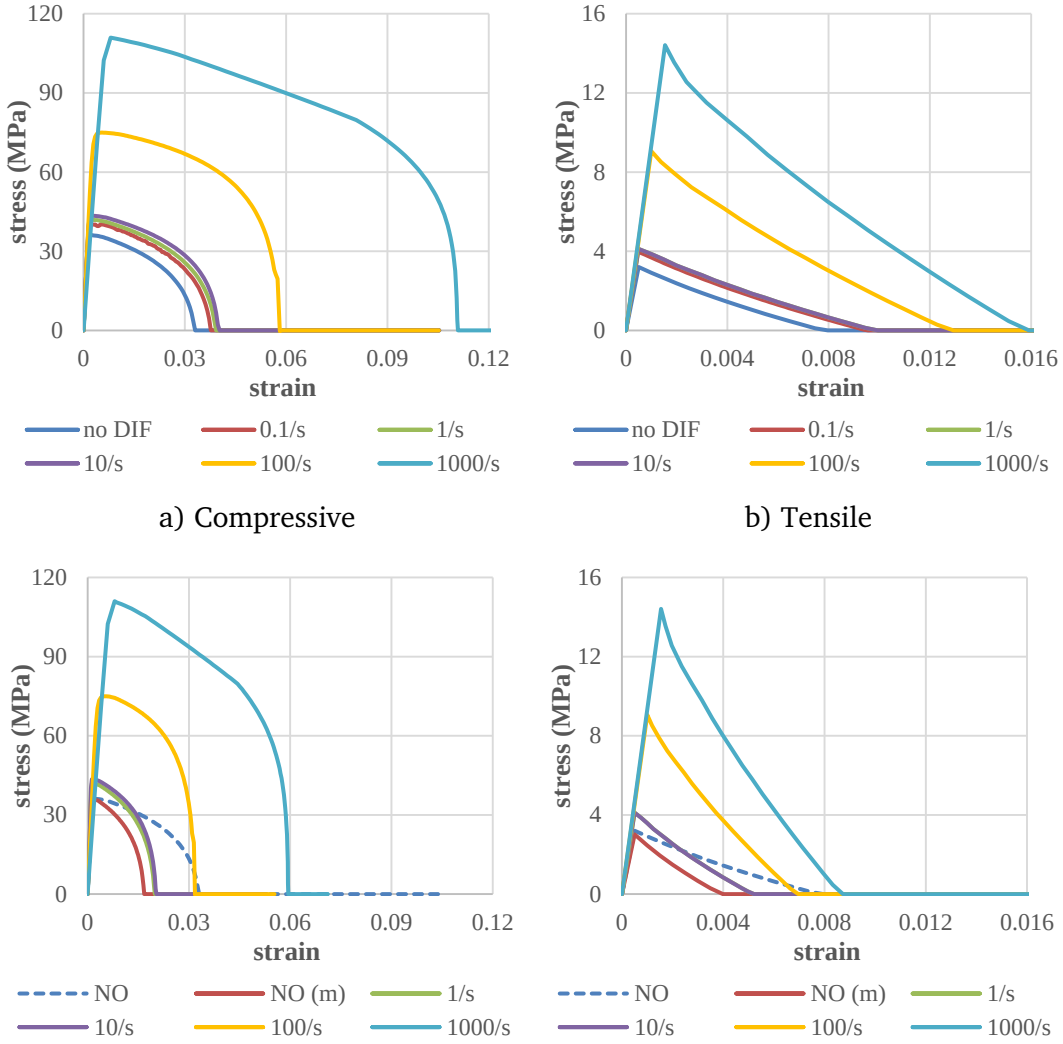

a) Compressive

b) Tensile

c) Compressive (modified)

d) Tensile (modified)

Fig. 7.35 Dynamic stress-strain relation for concrete in KCC model (element size = 7mm; "NO (m)" mean no DIF but with modified fracture energy)

7.7 Influence of material rate effect: simply-supported RC beam

The influence of the material rate effect, i.e. DIF, on the shear resistance of simply-supported RC beam, is identified through a comparative analysis between FE models using rate-sensitive material for concrete and rebar, and simulation using rate-insensitive material as previously done in Section 7.3.

For each loading rate regime (represented by load duration), the increase of dynamic shear resistance due to material rate effect can be identified through direct comparison between FE results using materials with and without DIF. These analysed cases are then re-visited to check the actual strain rate experienced during different loading stages.

7.7.1 Material rate effect on dynamic shear strength in "impulsive" regime

Fig. 7.36 presents the comparison of time histories of the shear force and bending moment between the two sets of simply-supported FE models, under the same blast load duration of 1.0 ms. The model using materials without DIF is fully damaged under an impulse of 7 kPa·s. for the model using material with DIF, the impulse has to increase to 7.3 kPa·s to break the RC beam.

The peak shear force is reached at about the same time between the two models, and it can be seen that the shear resistance has increased from 152 kN to 166 kN, so the amplification factor for shear resistance is around 1.09. The bending moment at mid-span has been increased by 8% as well.

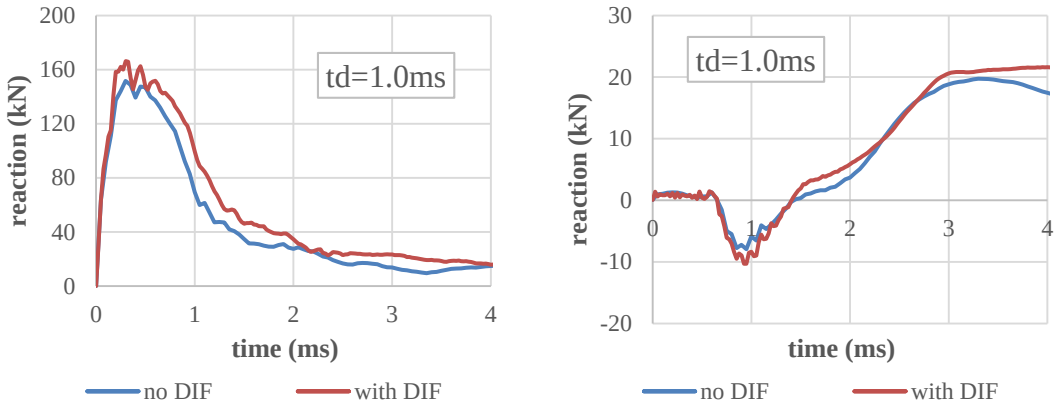

a) Shear force b) Mid-span moment

Fig. 7.36 Response of simply-supported RC beam under load duration t_d=1.0 ms

The damage pattern at failure of the two cases are presented in Fig. 7.37. It reveals that the developed width of resulted shear span in both cases are around 0.35*d*, and more cracking has been developed in the model with DIF. This is because the increased dynamic shear resistance with DIF helps to bridge over larger shear force through the short shear span towards the middle of the beam.

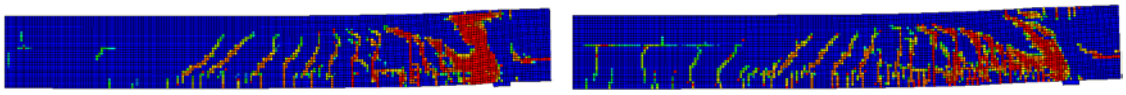

a) No DIF (t=2.0ms) b) With DIF (t=2.0ms)

Fig. 7.37 Final damage patterns of simply-supported RC beam under load duration t_d=1.0 ms

To further understand the observed material strain rate effect on the dynamic shear strength in the previous section, it is necessary to examine into the magnitude of the strain rates that develop at the critical times, particularly at the times immediately before and when the dynamic shear failure occurs.

The strain rate contours from the initial arrival of blast pressure to the formation of finial direct shear crack is shown in Fig. 7.38. It can be seen the crack starts from the edge of the support at t=0.2 ms and propagate almost vertically until fully opening-up at t=1.0 ms. Within the direct shear cracked region, the strain

rate appears to reach up to around 100 /s at some critical positions during t=0.4~0.6 ms, and then decreases to around 50 /s when the crack fully opens at t=1.0 ms.

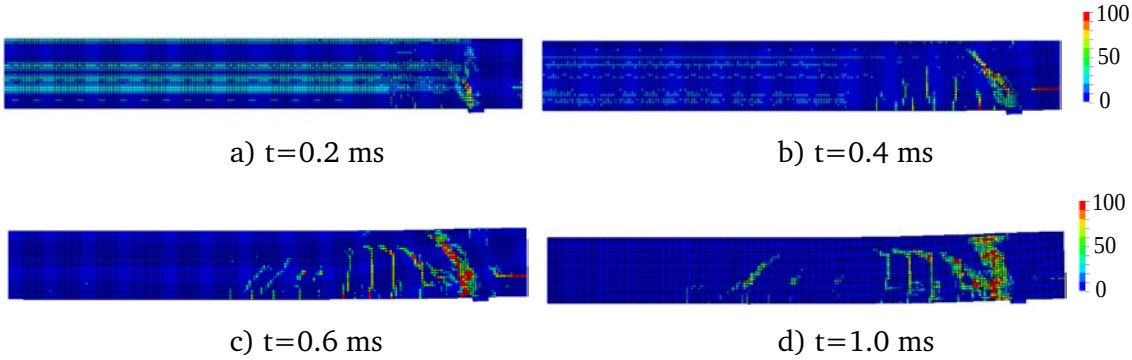

Fig. 7.38 Strain rate contour of simply-supported beam under load duration t_d=1.0 ms

As the strain rate at different locations can be different at a given time, and the structural shear failure occurs over a sizable critical region, it is constructive to also look at the strain rate as an average measure over the critical region of interest, in addition to the distribution of the strain rate. For each cracking pattern, i.e., inclined direct and diagonal shear cracking or crushing in compression region, a 30mm-width of the shear failure zone (approximately 4 elements wide) has been picked up and the average strain rate within this particular region is measured. The time history of average strain rate in the direct shear crack region, as illustrated in Fig. 7.39a, is plotted in Fig. 7.39b. The time at which the peak shear force is reached (t=0.2 ms) is also shown (dashed lines) in the plot for reference purpose.

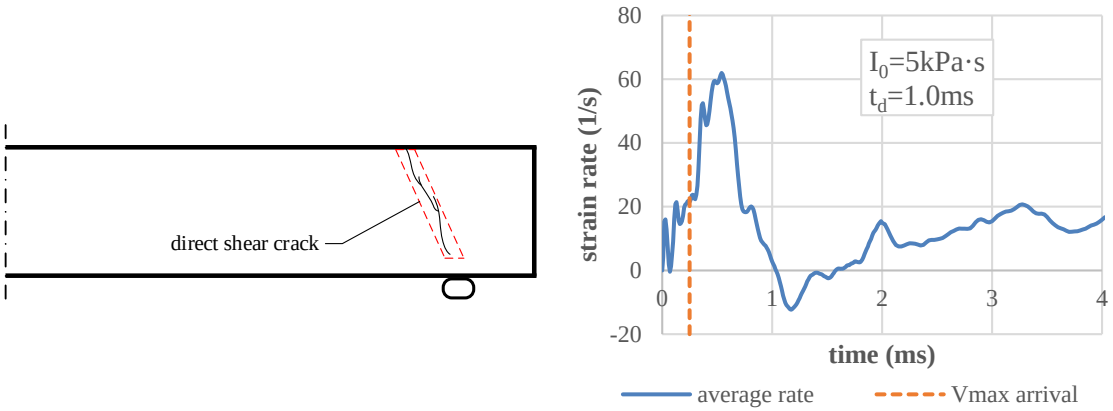

a) Measured region b) Time history

Fig. 7.39 Average strain rate in the shear failure zone load duration t_d=1.0 ms

It can be seen from Fig. 7.39b that, the strain rate at the time instant when the peak shear force is reached is around 20 /s, and the defined strength enhancement brought by this particular strain rate for concrete is around 1.9 in tension and 1.2 in compression. Note that the resulted amplification factor of shear resistance is around 1.09. This suggests that, despite of the development of shear cracking, the shear resistance is mainly controlled by concrete in compression and arch action within the very short span. The high strain rate around 60/s is measured after the arrival of peak shear force, because of the opening up of cracks due to concrete fracture, which should not contribute to the increase of dynamic shear resistance.

7.7.2 Material rate effect on dynamic shear strength in "dynamic" regime

Fig. 7.40 presents the comparison of time histories of the shear force between the two sets of simply-supported FE models, under a same blast load duration of 4.0ms. As discussed in Section 7.3.2, loading rate (represented by load duration) generally leads to a diagonal shear type of failure. A critical impulse level of 11 kPa·s is sufficient to break both models without and with material DIF effect.

The peak shear force appears at a similar time, and has increased from 102 kN to 110 kN, resulting an amplification factor of 1.08. The maximum bending moment at mid-span has increased by 10%. The failure patterns from the two cases are quite similar, as observed from the damage pattern at failure given in Fig. 7.41.

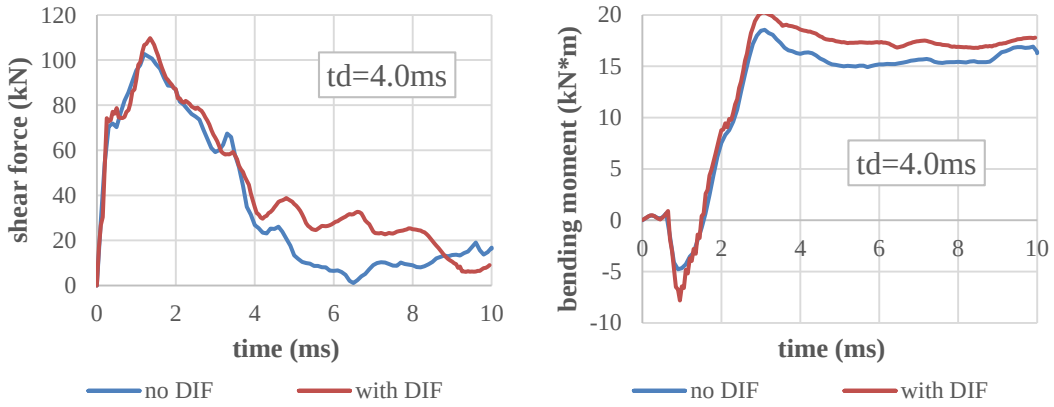

a) Shear force b) Mid-span moment

Fig. 7.40 Response of simply-supported RC beam under load duration t_d=4.0 ms

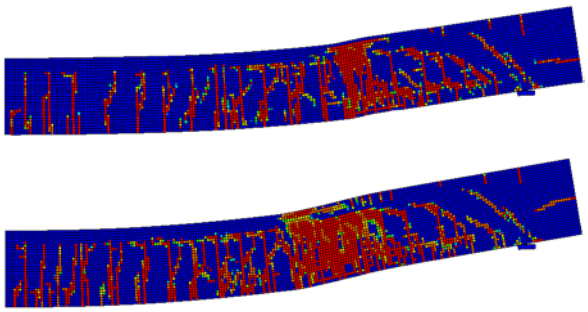

a) No DIF (t=5.0ms) b) With DIF (t=5.0ms)

Fig. 7.41 Final damage patterns of simply-supported RC beam under load duration t_d=4.0 ms

Fig. 7.42 shows the strain rate contours of the simply-supported beam failed in diagonal shear. It can be seen that the tips of critical inclined shear cracks are linked at around t=2.0~3.0 ms, and the strain rate along the crack line has reached 50 /s at some locations.

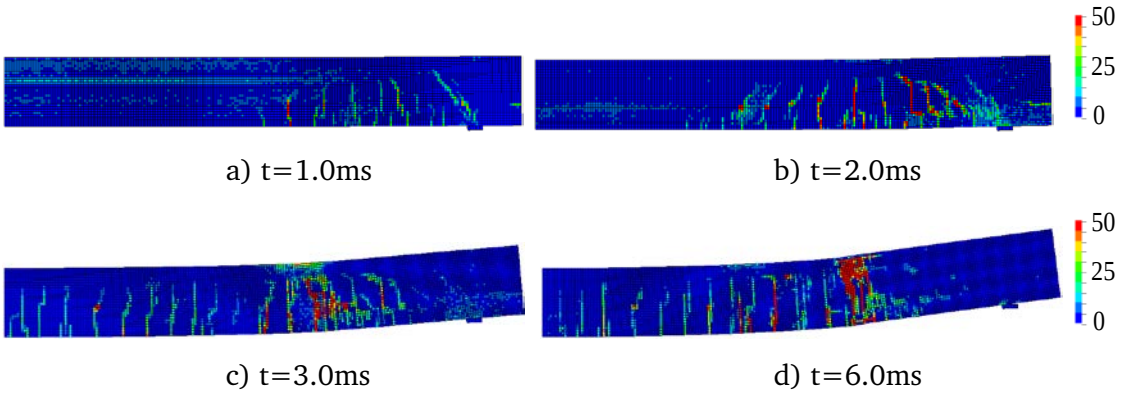

a) t=1.0ms b) t=2.0ms

c) t=3.0ms d) t=6.0ms

Fig. 7.42 Strain rate contour of simply-supported beam under load duration t_d=4.0 ms

Similar to the approach used earlier, a 30 mm width region has been picked up along the diagonal shear crack, and the average strain rate within this region is plotted in Fig. 7.43. It can be seen that the critical strain rate at the arrival time of maximum shear force is less than 20 /s, concrete at this rate could have a DIF factor of 1.6~1.7 in tension, but the measured increase in shear resistance is just 8%, which suggests that the shear resistance is mainly influenced by concrete in compression and arch action.

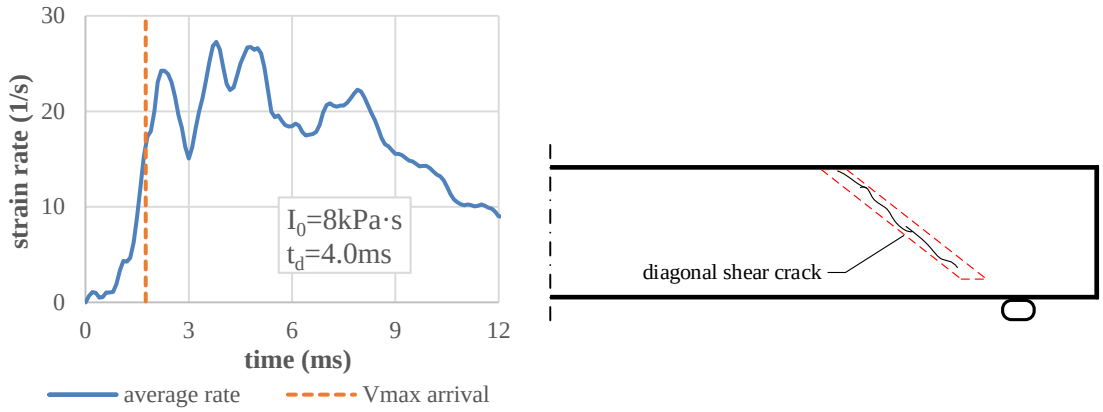

a) Time history b) Measured region

Fig. 7.43 Average strain rate in the shear failure zone load duration t_d=4.0 ms

7.7.3 Material rate effect on dynamic shear strength in "quasi-static" regime

The comparison is then moved to blast load duration in the range of 40 ms, in which the beam is expected to be failed in flexure. The critical impulse levels for both FE models using materials with and without DIF are 12 kPa·s. The time histories of shear force at support and mid-span bending moment are plotted in Fig. 7.44. The peak shear force and bending moment are reached at the same time in both models. The bending moment at mid-span has increased from 17.6 kNm to 20.8 kNm by 18%, resulting the maximum shear force increased from 44 kN to 50 kN by 14%. Besides, a similar flexure-dominated failure mode, in which a plastic hinge formed at mid-span, is seen in both models, as shown in Fig. 7.45.

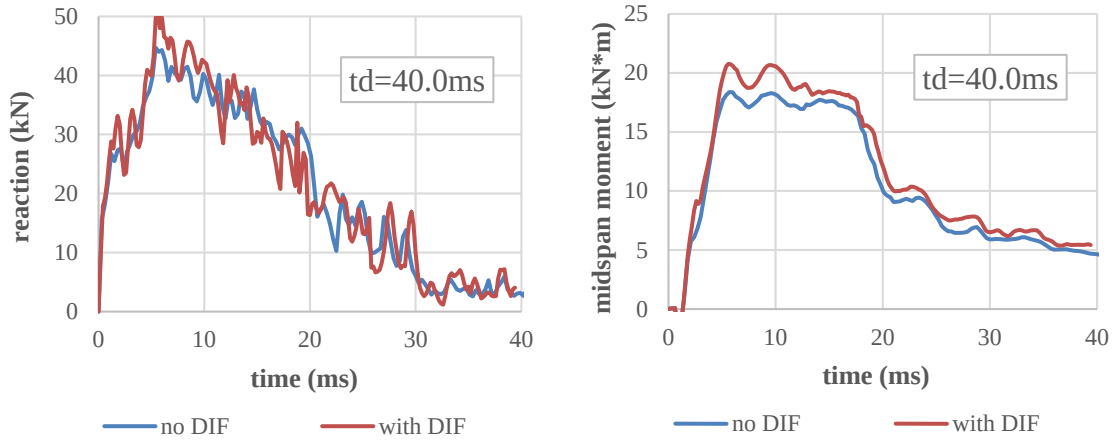

a) Shear force b) Mid-span moment

Fig. 7.44 Response of simply-supported RC beam under load duration t_d=40 ms

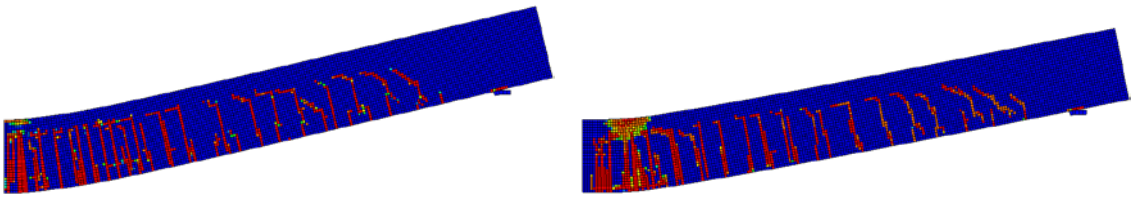

a) No DIF (t=20ms) b) With DIF (t=20ms)

Fig. 7.45 Final damage patterns of simply-supported RC beam under load duration t_d=40 ms

Fig. 7.46 shows the strain rate contour of the RC beam, and the time histories of average strain rate in the compression region and the tension rebar at mid-span, are plotted in Fig. 7.47. It can be seen that, at the time of peak shear force, the strain rate in the compressive region is close to 0, and in the tension rebar it's less than 5/s. In fact, the high strain rate measured in the rebar is due to rapture of tension rebar, and the one measured in concrete is caused by concrete crushing in compression region.

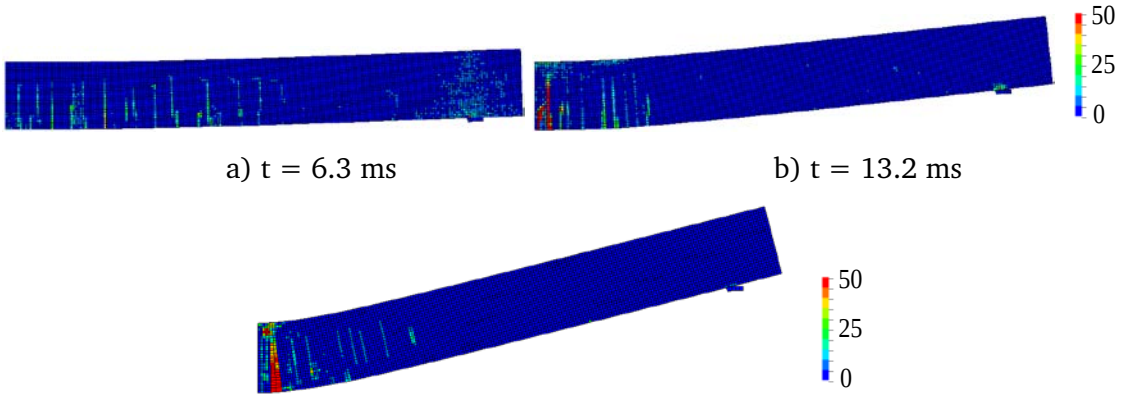

a) t = 6.3 ms b) t = 13.2 ms

c) t = 22.3 ms

Fig. 7.46 Strain rate contour of simply-supported beam under load duration t_d=40 ms

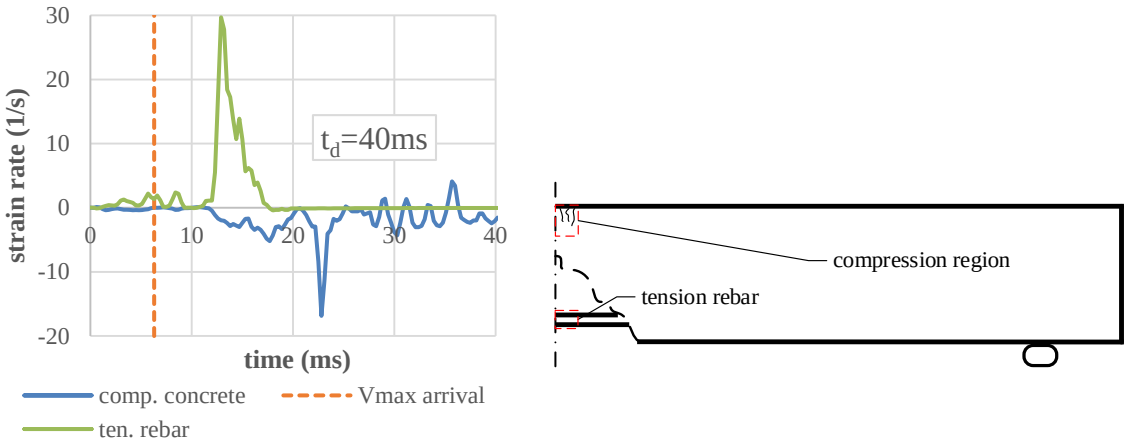

a) Time history b) Measured region

Fig. 7.47 Average strain rate in the shear failure zone load duration t_d=40 ms

7.8 Influence of material rate effect: fixed-supported RC beam

Similar to simply-supported cases, the analysis of fixed-supported RC beam conducted in Section 7.4 is revisited with a comparative simulation using rate-sensitive material models. For representative load durations, the dynamic shear resistance is compared and the actual strain rate experienced during whole loading stages at critical cracking locations are also investigated.

7.8.1 Material rate effect on dynamic shear strength in "impulsive" regime

Fig. 7.48 presents the comparison between of time histories between the two sets of FE models, under a blast load duration of 0.5 ms. The critical impulse levels for both models are 5 kPa·s. It can be seen that the peak shear forces are reached at the same time in both cases. With the DIF effect, the maximum shear force has increased from 206 kN to 235 kN, resulting an amplification factor of 1.14. The maximum negative moment at the fixed support is reached at the same time as the shear force, and has increased from 18.4 kNm to 25.2 kNm by 37% due to DIF effect.

In the meantime, it can be seen that the stress in the top rebar has also increased by 20% due to DIF effect, which helps to explain that the overall growth of shear resistance has largely contributed by the dowel action of the rebar at fixed support.

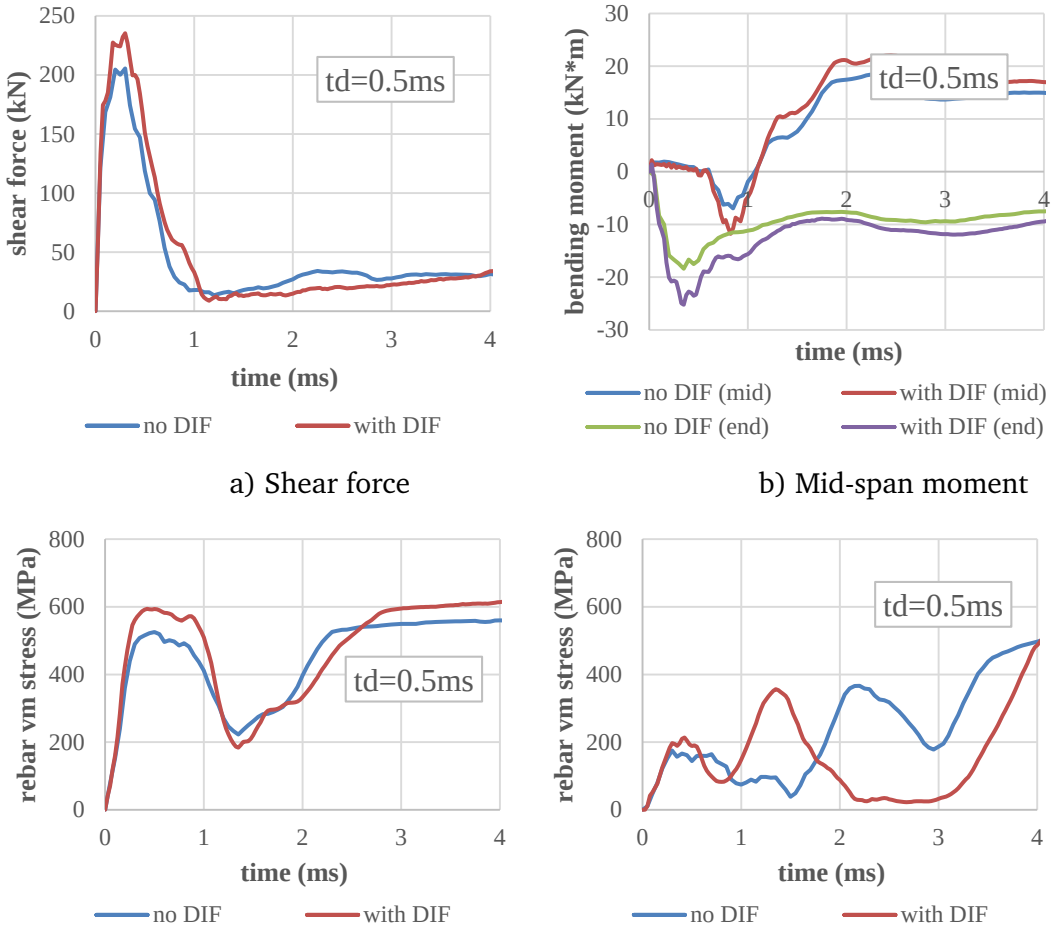

a) Shear force b) Mid-span moment

c) Top rebar near support d) Bottom rebar near support

Fig. 7.48 Response of simply-supported RC beam under load duration t_d=0.5 ms

Fig. 7.49 gives the final failure patterns of the two cases. Both beams have experienced a typical direct shear failure mode, and the width of developed shear span is around 0.8*d*.

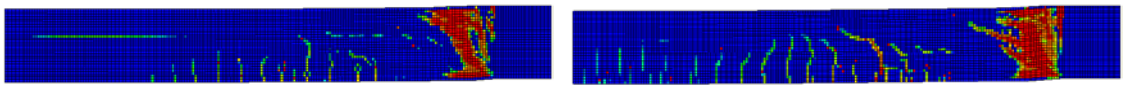

a) No DIF (t=1.0ms) b) With DIF (t=1.0ms)

Fig. 7.49 Final damage patterns of simply-supported RC beam under load duration t_d=0.5 ms

The strain rate distribution for representative time instants during the formation of direct shear crack are plotted in Fig. 7.50. It can be seen that the crack at the upper surface opens at t=0.2 ms, and the inclined crack begins to develop since t=0.4 ms. The strain rate along the inclined crack reaches to around 100/s at t=0.6 ms.

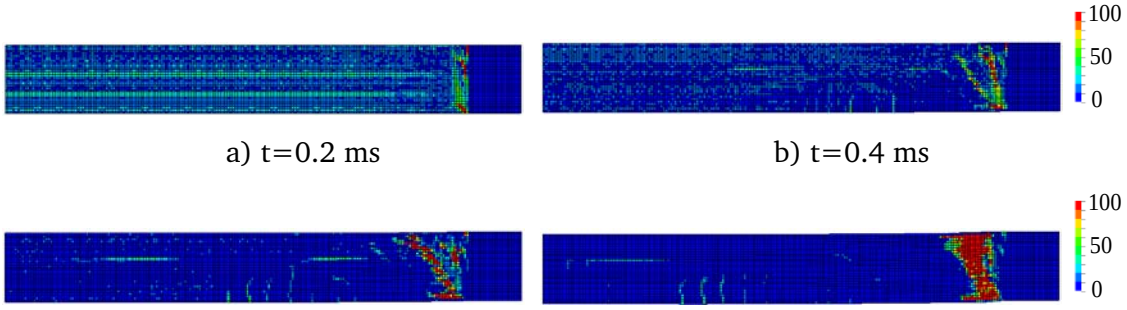

a) t=0.2 ms b) t=0.4 ms

c) t=0.6 ms d) t=1.0 ms

Fig. 7.50 Strain rate contour of simply-supported beam under load duration t_d=0.5 ms

The average strain rate in a 30 mm width region along the direct shear crack, as illustrated in Fig. 7.52a, is extracted and plotted in Fig. 7.51b. The strain rates of top and bottom rebars as plotted in Fig. 7.51c. It can be seen that when maximum shear force is reached at t=0.3 ms, the average strain rate in the concrete is around 15/s, while strain rate in the top and bottom rebars are around 50/s and 25/s, respectively. Similar to previous findings, it reveals that it is the compressive behaviour of concrete and dowel action of rebar that contribute to the increase of overall shear resistance.

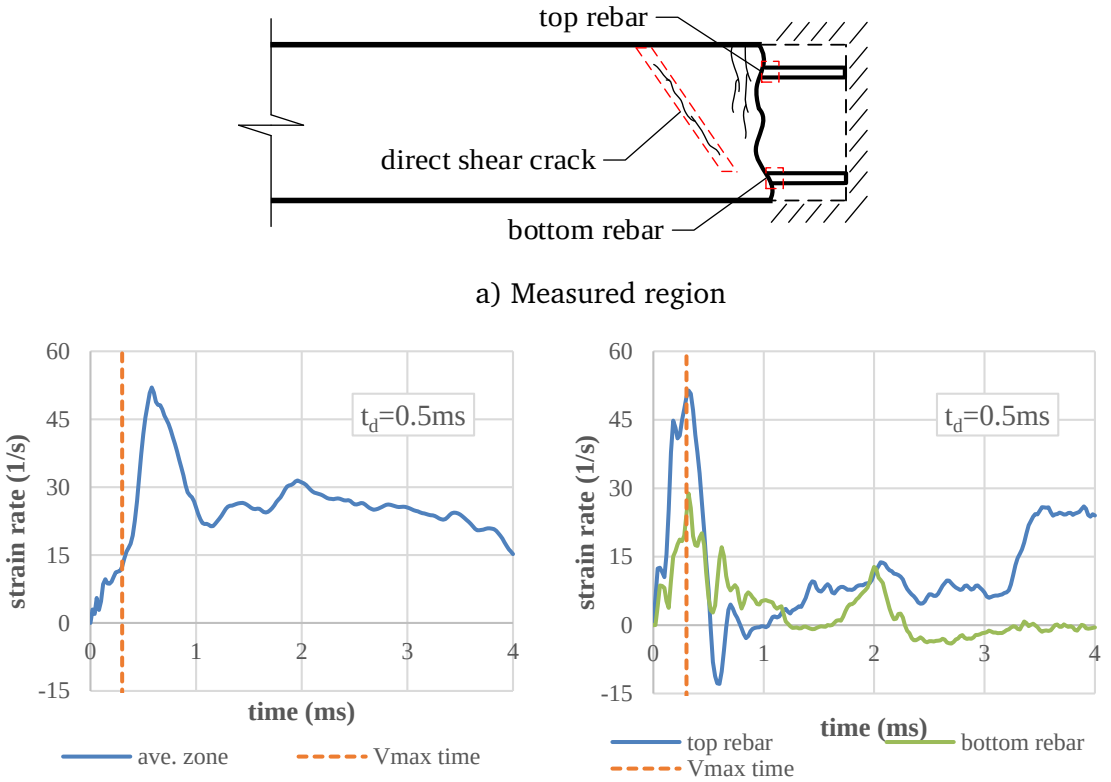

a) Measured region

b) Strain rate in direct cracked region

c) Strain rate in steel rebars

Fig. 7.51 Average strain rate in the shear failure zone load duration t_d=0.5 ms

7.8.2 Material rate effect on dynamic shear strength in "dynamic" regime

The comparative analysis is then moved to the load duration regime of 4.0ms, in which the fixed-supported beam fails in a diagonal shear mode. The time histories of the two sets of FE models under a blast impulse of 6 kPa·s, are plotted in Fig. 7.52. The calculated increase factor by DIF effect for shear force is 1.10.

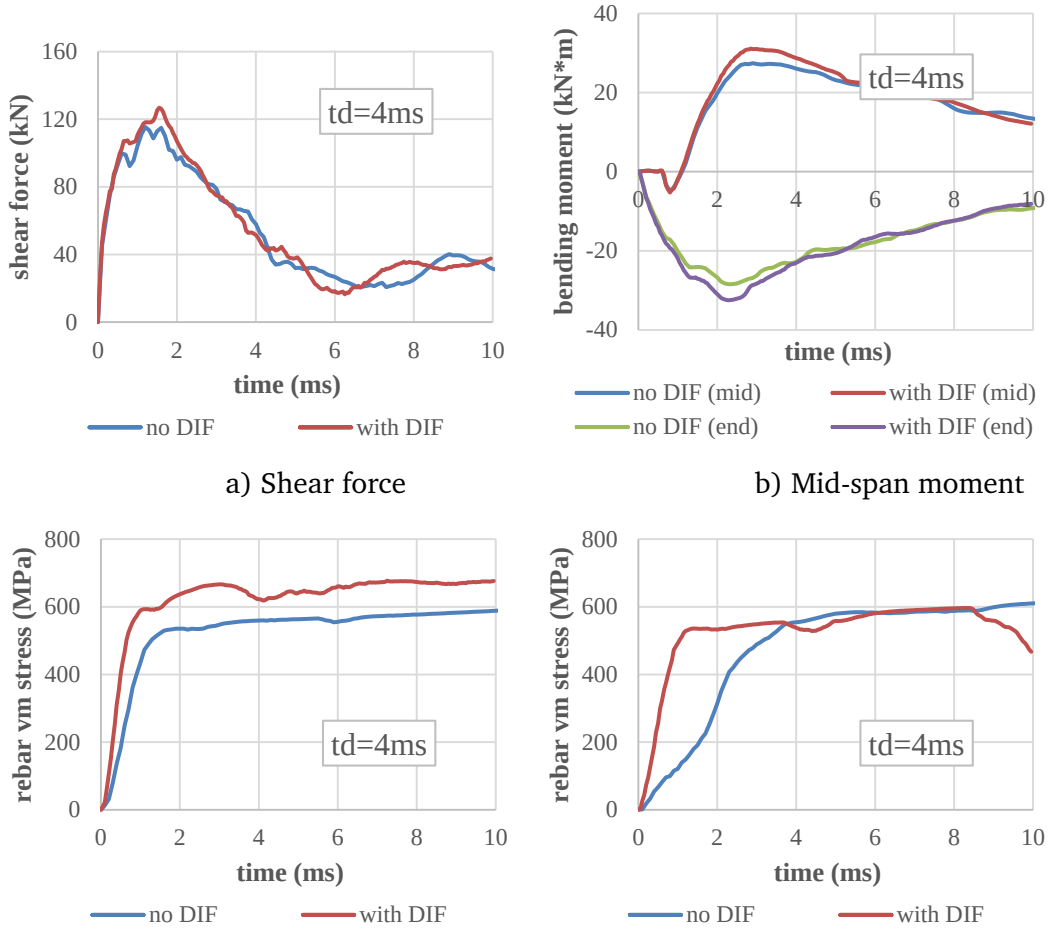

a) Shear force b) Mid-span moment

c) Top rebar near the support d) Bottom rebar near the support

Fig. 7.52 Response of simply-supported RC beam under load duration t_d=4.0 ms

The final damage patterns of the two cases are presented in Fig. 7.53. The two beams fail in a similar fashion, and the widths of the developed diagonal shear span are both close to 1.5*d*.

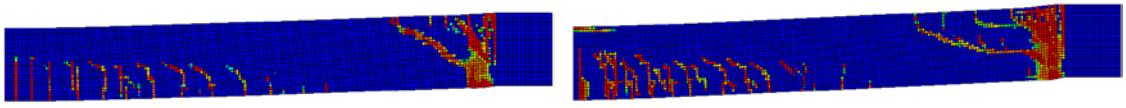

a) No DIF (t=6.0ms) b) With DIF (t=6.0ms)

Fig. 7.53 Final damage patterns of simply-supported RC beam under load duration t_d=4.0 ms

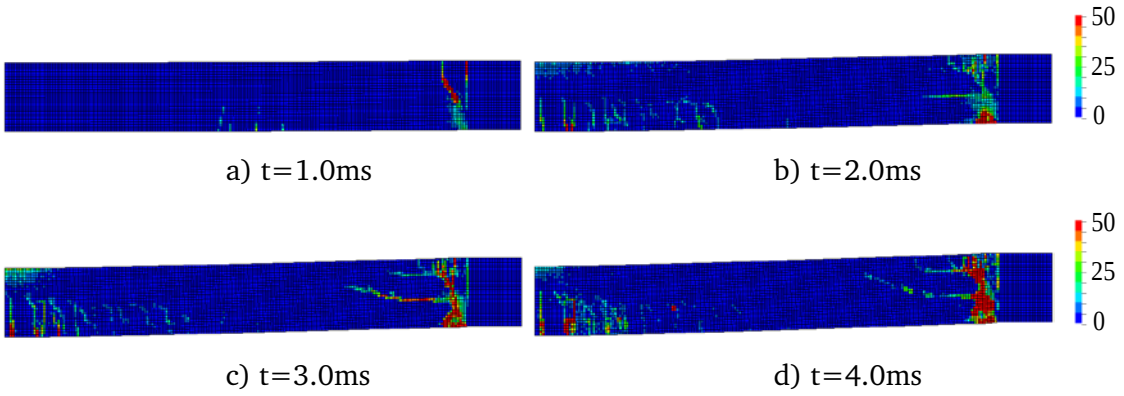

Fig. 7.54 Strain rate contour of simply-supported beam under load duration t_d=4.0 ms

Fig. 7.54 gives the distribution of strain rate at representative time instants. As read from the strain rate contour, the major diagonal crack starts to develop at t=2.0 ms, and the strain rate along the crack direction is close to 50/s. Based on this observation, a 30 mm width region along the diagonal shear crack has been picked up, as illustrated in Fig. 7.55a, and the average strain rate of concrete in compression region and rebars are plotted in Fig. 7.55b and 7.55c.

It can be seen that, at the time when peak shear resistance is reached in the beam, the actual strain rate in the concrete is less than 10/s and in the rebars are around 5∼15/s. This has led to an increase of stress in tension rebar by 15%, which is believed to be one of the major sources of shear resistance increase, while the compression rebar has largely remained the same. The high strain rate at t=1.3 ms in Fig. 7.55c is due to the yielding of top rebars after the flexural cracking on the negative moment side. The high strain rate in concrete as shown in Fig. 7.55b is due to the opening of diagonal crack after reaching the shear resistance, which occurs after reaching the peak shear resistance.

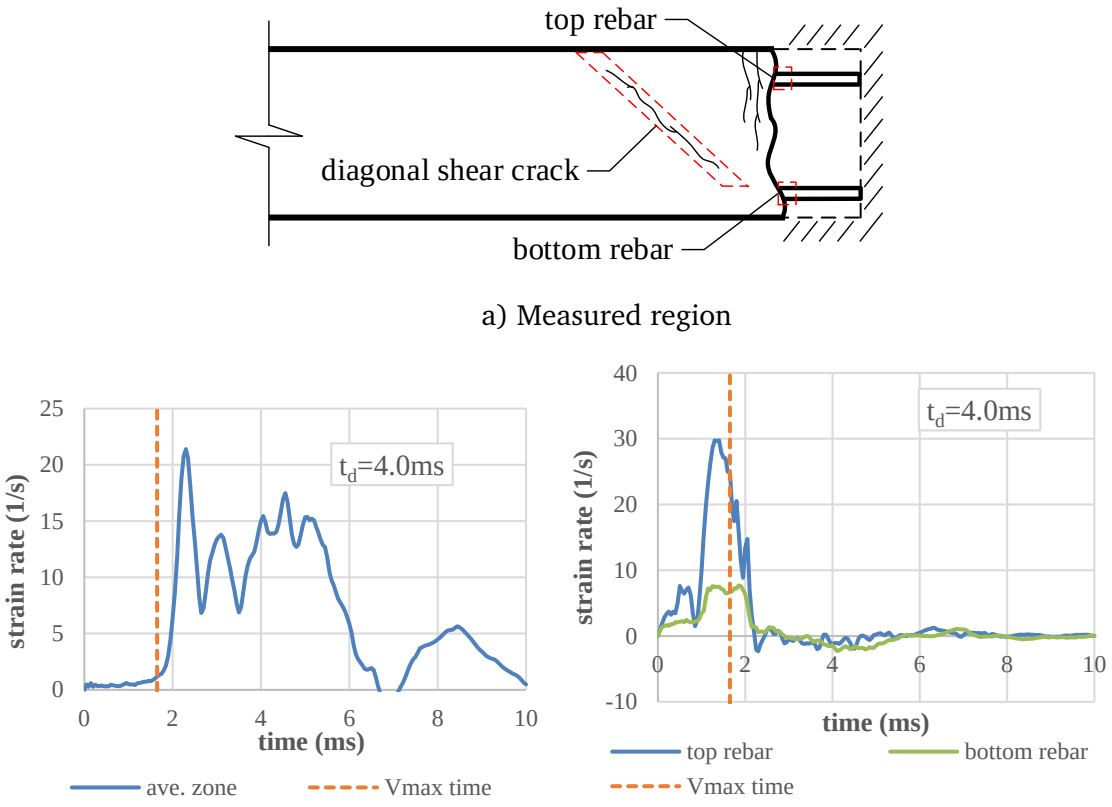

a) Measured region

b) Strain rate in direct cracked region

c) Strain rate in steel rebars

Fig. 7.55 Average strain rate in the shear failure zone under load duration t_d=4.0 ms

7.8.3 Material rate effect on dynamic shear strength in "quasi-static" regime

Fig. 7.56 gives the comparison of the time histories and damage patterns of two FE models subjected to a blast load duration of 16ms, which equals to 2.4 times of the flexural period and thus in the "quasi-static" regime. The fixed-supported RC beam is expected to fail in a flexure-dominated mechanism. The critical impulse level for both models are 11 kPa·s.

It can be seen that bending moment at support is arrives at its peak value at around t=2.5 ms, while the maximum shear force is reached at t=3.2 ms when the bending moment at mid-span reaches to its flexural resistance. With the DIF

effect, the flexural resistance has increased by about 10% at both the mid-span and the support, resulting that the maximum shear force being increased from 104 kN to 110 kN. It is noticed that the stress in tension and compression rebar near the support has increased by 13% and 4%, when the maximum shear force is reached at t=5 ms.

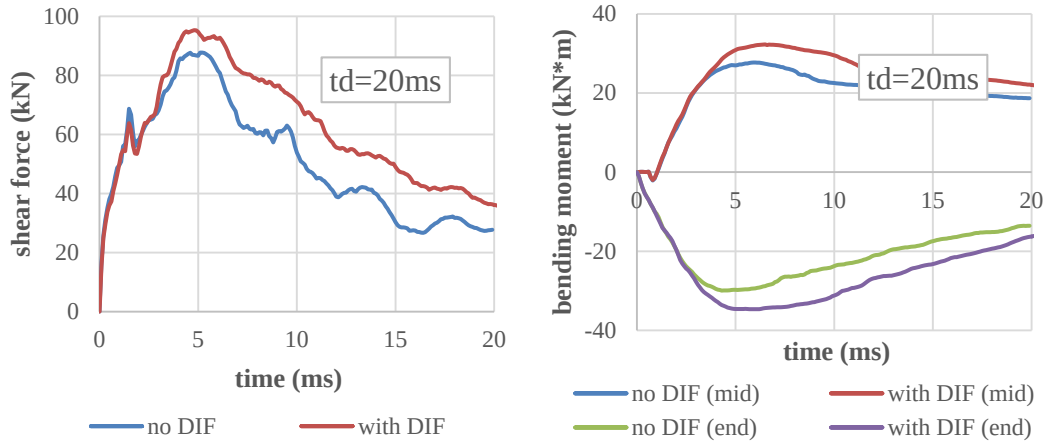

a) Shear force

b) Mid-span moment

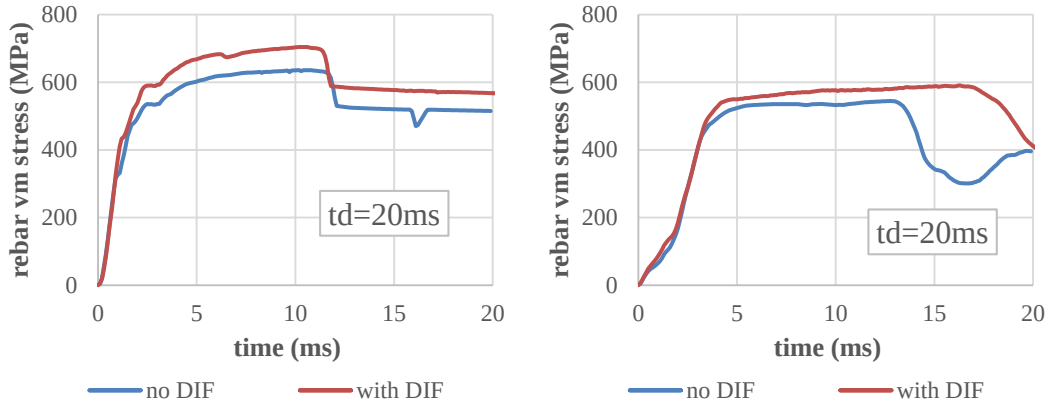

c) Top rebar near support

d) Bottom rebar near support

Fig. 7.56 Response of simply-supported RC beam under load duration t_d=16.0 ms

Fig. 7.58 shows the distribution and time histories of strain rates in concrete and rebar under a load duration of 16ms. It reveals that when flexural plastic hinges form, the strain rate of concrete in the compression region, both in the mid-span and near the support, are around 5/s, while the strain rate in the steel rebar at the tension side is between 5~15/s.

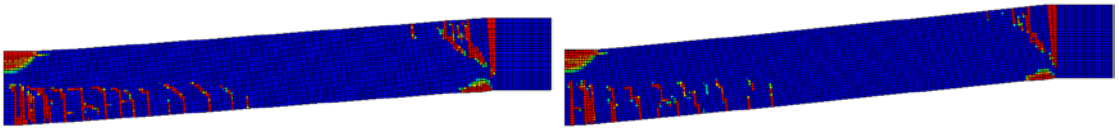

a) No DIF (t=15ms) b) With DIF (t=15ms)

Fig. 7.57 Final damage patterns of simply-supported RC beam under load duration t_d=20 ms

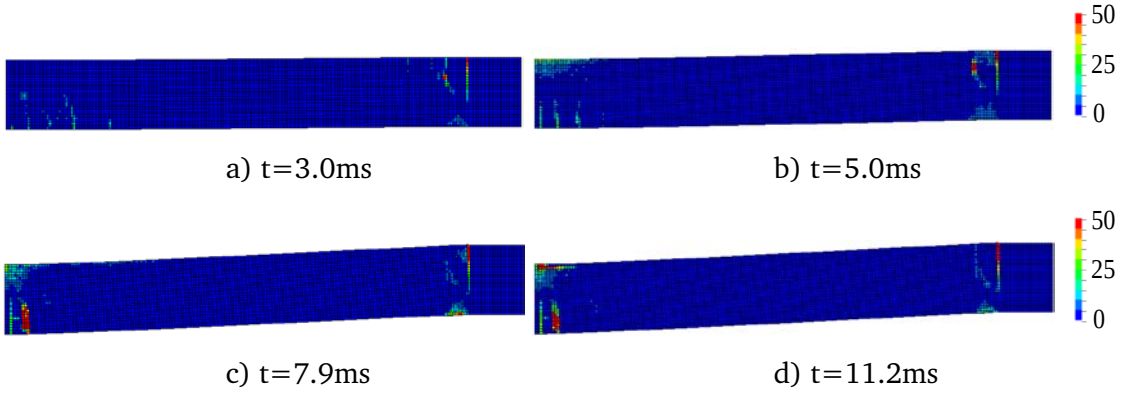

a) t=3.0ms b) t=5.0ms

c) t=7.9ms d) t=11.2ms

Fig. 7.58 Strain rate contour of simply-supported beam under load duration t_d=16.0 ms

Similar to previous cases, the average strain rate in the compressive region of concrete and the rebars at the mid-span and support shown in Fig. 7.59a, is plotted in Fig. 7.59b and 7.59c. It can be seen that, when peak shear resistance is reached in the beam, the actual strain rate in the concrete is less than 5/s and in the rebars are around 20/s. This suggests that the increase in flexural resistance is mainly brought by the growth of strength in the tension rebar due to steel material rate effect.

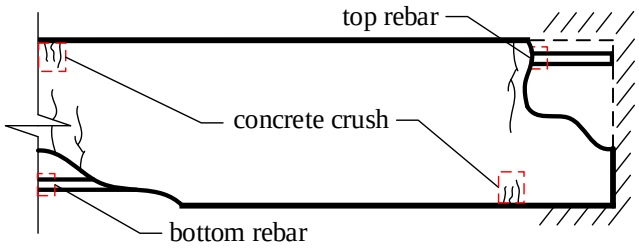

a) Measured region

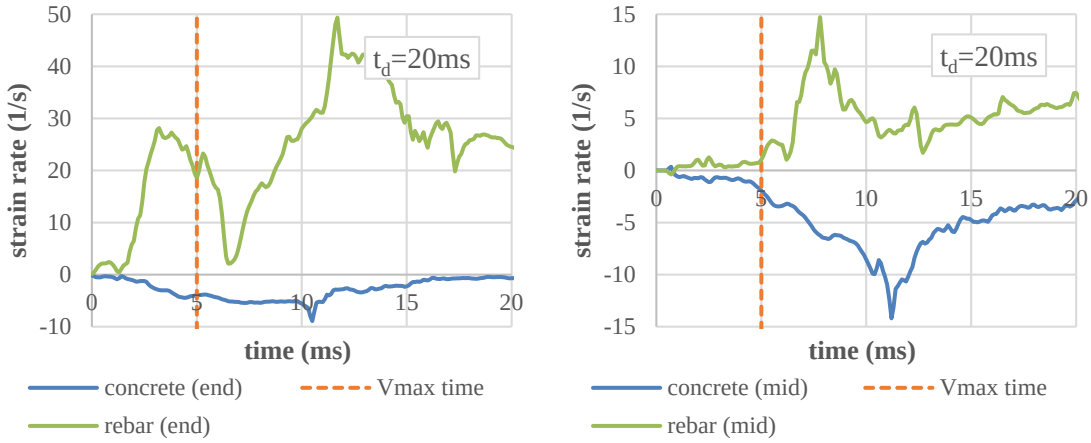

b) Strain rate near support

c) Strain rate at mid-span

Fig. 7.59 Average strain rate in the shear failure zone; load duration t_d=16.0 ms

7.9 Influence of material rate effect on dynamic shear resistance under varied load durations

The above analysis has demonstrated that when material rate effect is considered, the correlation between the failure modes and the loading rate, as previously established through FE analysis using rate-insensitive material, still holds. The strain rate at the time when the maximum shear resistance is reached is in the range of 20/s.

The dynamic shear resistances, using materials with and without DIF effect, are plotted against normalised load duration in Fig. 7.60a and 7.60b. The increase factor, which is the ratio between the two resistances, is plotted in Fig. 7.60c.

Result reveals that the material rate effect is relatively limited, and resulted DIF (structural) factor generally lies in between 1.1~1.2. Simply linear fitting lines are proposed in Eq. 7.6.

$$DIF_s = 1.119 - 0.030 \cdot \frac{t_d}{t_f}$$
$$DIF_f = 1.149 - 0.027 \cdot \frac{t_d}{t_f} \tag{7.6}$$

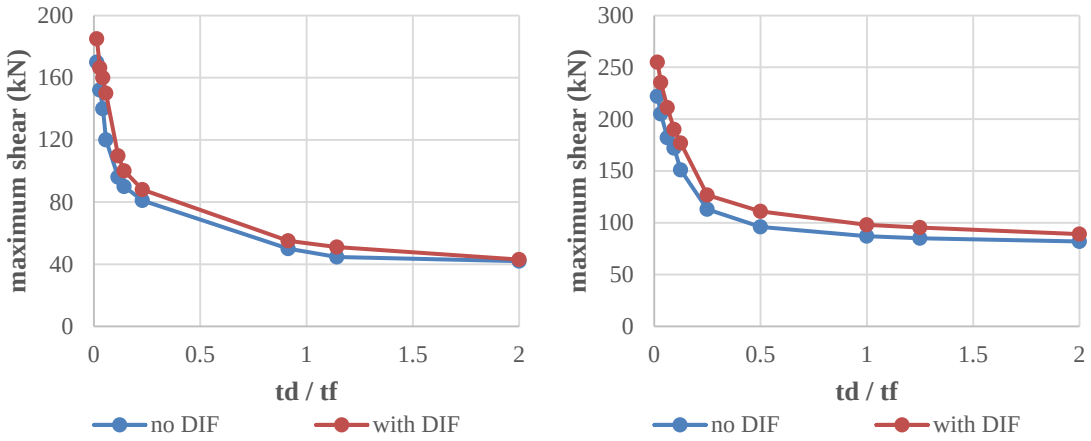

a) Simply-supported

b) Fixed-supported

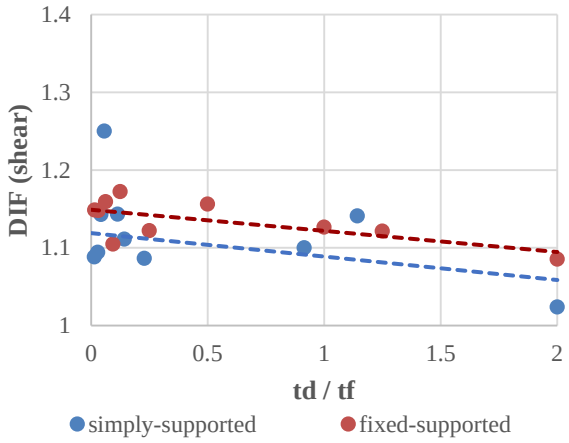

c) Dynamic increase factor for shear resistance due to material DIF

Fig. 7.60 Dynamic shear resistance of RC beams with and without DIF effect

7.10 Concluding remarks

Following from the previous chapter using beam-element based numerical analysis, in this chapter the transient dynamic shear phenomenon in RC member subjected to blast loading is investigated in a realistic reinforced concrete environment. The study demonstrates that, as the blast loading rate increases (or pulse duration decreases), shear failure of RC member can occur during the high shear phase before the response develops into the normal global bending mode.

While the development of high shear is a transient dynamic response, whether or not a shear failure will take place depends also on the dynamic shear resistance. Therefore the determination of the dynamic shear resistance capacities is a key and it has been the main theme of the chapter.

From the RC beam analysis, it can be observed that the dynamic shear resistance does increase remarkably with the increase of the loading rate (decrease of pulse duration). By examining the effective shear span length at the time when the respective dynamic shear failure mode is reached, a general trend of correlation between the effective shear span length and the loading rate has been established.

The trend of decrease of shear span length tally well with the trend of the dynamic shear resistance with the loading rate. Apart from the effect of reduced shear span, some extra dynamic enhancement of the shear strength is observed as compared to similar failure mode in the four-point quasi-static load analysis and this is deemed to be attributable to the fact that there is a lack of time for the development of the mechanism over the failure zone which translates to an enhancement of the corresponding resistance.

As the dynamic shear phenomenon takes place in a short timescale in general, the contribution of material dynamic strength increase (DIF) and additional

enhancement to the dynamic shear resistance is assessed by comparing the results without and with the incorporation of the material rate-sensitivity in the FE model.

Based on the numerical results of the dynamic shear resistance without and with the material DIF, an empirical dynamic increase factor for the shear resistance due to the material DIF, called DIF (shear), is developed. Such a DIF factor for the shear resistance is found to be on order of 1.1～1.2. The critical strain rates that are reached in the direct and diagonal shear modes of failure have been found to be on the order of 15-20 s^{-1}, which explains the relatively small dynamic increase of the shear strength due to the material strain rate effect.

Chapter 8: Analysis of dynamic shear demands using simplified SDOF models and assessment of shear response

8.1 Introduction

In light of the discussion in Chapter 6 and 7, it may be generally stated that RC structures can exhibit three distinctive types of deformation modes, namely direct shear, diagonal shear, and global flexure. When a RC member is subjected to an impulsive load, it will undergo the above three phases of response in a consecutive manner, and whether the member will fail in direct shear or diagonal shear before developing into the global bending mode will depend on the magnitude of the shear response with respect to the corresponding shear resistances. Therefore it is important to be able to a) predict the magnitude of the dynamic shear responses, in addition to the flexural response, and b) evaluate the dynamic shear resistance capacities. Only then can the actual failure modes be correctly predicted.

On the resistance side, Chapter 7 has demonstrated the important factors that will affect the dynamic shear resistance, chiefly the shear span length, and to a lesser extent the material strain rate effect. Some empirical trends have also

been established which allow an estimation of the dynamic shear resistance. On the other hand, as demonstrated in Chapter 6, using a relatively simple beam-clement finite element model, it is also possible to predict the transient high shear phenomenon; however specific quantification will require a more detailed nonlinear finite element model, making the prediction of the high shear response through numerical analysis to be computationally expensive and time consuming. For these reasons, and to enable practical applications, a simplified analytical model for this category of dynamic response is desired.

Single-degree-of-freedom (SDOF) systems have been widely used for predicting the dynamic response of RC member subjected to blast (Li and Meng 2002). Most of them have been catered for the prediction of the flexural response and it has been assumed that the RC member would not fail in shear. Experimental observations of RC slabs under blast loading (Kiger et al. 1980; Slawson 1984), and the numerical studies presented in the last two chapters, indicate that the structure could fail in shear at critical locations at very early time, e.g., within one or two millisecond after the arrival of load, before significant global flexural response developed. Similarly, structures that survive the early high shear forces and fail later in flexure would have developed into a global flexural mode during which the high shear force would have vanished. Therefore, it is reasonable to simplify the high shear phase and the flexural phase as two uncoupled processes. This assumption has already been introduced in early studies by Krauthammer et al. (1986, 1990) and T. Ross (1983), and adopted later by many researchers (Dragos and Wu 2014; Low and Hao 2002; Luckyram et al. 1992; Wang et al. 2013; Xu et al. 2014).

In this chapter, a simplified SDOF based approach is proposed to assess the dynamic shear response under impulsive load. The high shear demand developed in RC members is analysed through three proposed SDOF systems based on the characterisation of the three distinctive deformation modes. Given

an adequate description of the deflected shapes and the natural periods, the participation of the three modes and the possible interaction between the global and the shear modes can be reasonably described, and the characteristic responses, including maximum shear forces, can be computed analytically.

This prediction, in conjunction with the empirical formulas proposed in Chapter 7 to predict the dynamic shear resistance, will enable a quick and reasonable estimation of the dynamic shear responses and whether RC members would fail in shear, direct or diagonal.

8.2 Representative SDOF systems

Three SDOF systems are proposed to represent the three distinctive modes of response of RC members under impulsive loading. The first is the conventional flexural SDOF system, and the other two are shear-based SDOF systems that reflect the shear mode response and shear failure modes. For each time step, the flexural and shear responses are computed and compared to their respective failure criteria. In fact the flexure and shear SDOF systems are loosely coupled, in the sense that the dynamic shear force from the flexural response is regarded as the external load acting on the direct/diagonal shear SDOF system.

The analytical expression for dynamic shear force is firstly introduced by Biggs (1964) and adapted by Krauthammer et al. (1990) into prediction for direct shear response, assuming that the flexural inertia forces have the same distribution as the deflected shape subjected to the static application of the dynamic blast load. The present approach has extended the above assumption into the prediction for diagonal shear mode.

The flexural resistance function is assumed as tri-linear for fixed supported beams and bi-linear for simply-supported beams. Considering that both the

direct and diagonal shear failure occurs in a rather brittle manner, the resistance function for direct and diagonal shear modes is assumed to be elastic-brittle. Thus if the dynamic shear force exceeds the dynamic shear resistance, shear failure is regarded to have occurred. Details of the prediction for dynamic shear resistance are discussed in Section 8.4.

8.2.1 Flexural mode

Classic single degree of freedom models assume a flexural mode of response, and this approach has been widely used to predict the structure behaviour subjected to blast and impact, and has been accepted in protective design guides (TM5-1300 1990; TM5-855-1 1986; UFC 3-340-02 2008; UPD Center 2006). The SDOF system, as shown in Fig. 8.1, usually consists only of a point mass and a weightless spring, whereas damping is usually neglected. For a flexural mode of response under uniformly distributed blast pressure, it is customary to assume a deflection shape that follows the static deflection under a static uniformly distributed load, and the mid-span deflection is employed as the representation of the system response, and so form the equivalent degree of freedom.

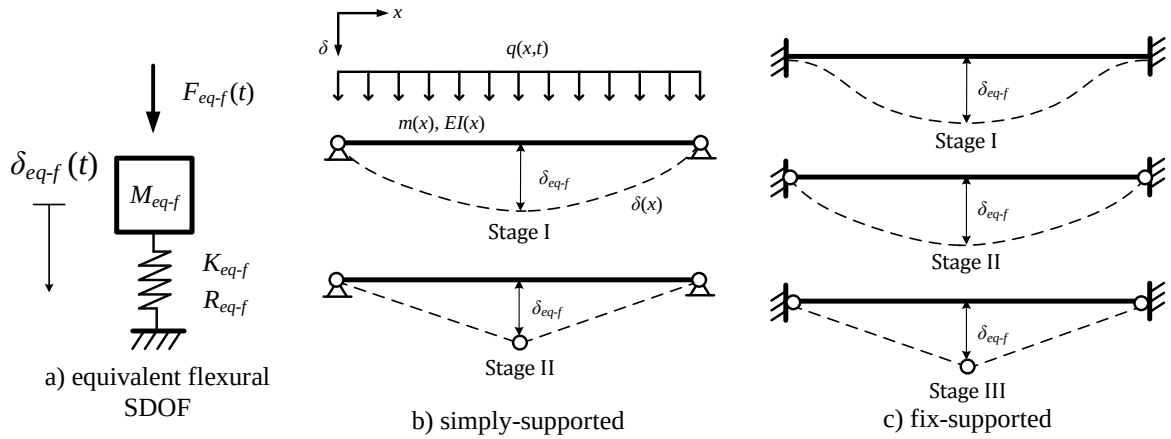

Fig. 8.1 Equivalent SDOF model for flexural mode

The dynamic response of the equivalent SDOF system can be described by the following equation:

$$M_{eq-f} \cdot \ddot{\delta}_{eq-f}(t) + R_{eq-f}\left(\delta_{eq-f}\right) = F_{eq-f}(t) \tag{8.1}$$

where M_{eq-f}, R_{eq-f} and F_{eq-f} are the equivalent mass, resistance and external force for flexural mode.

The equivalent quantities in the SDOF system can be derived with the assumption of a deformed shape. Assuming the deflected shape follows the static shape under a uniformly distributed load,

$$\phi_f(x) = \begin{cases} \dfrac{16}{5L^4}\left(L^3x - 2Lx^3 + x^4\right) & \text{simply} - \text{supported} \\ \dfrac{16}{L^4}\left(L^2x^2 - 2Lx^3 + x^4\right) & \text{fixed} - \text{supported} \end{cases} \tag{8.2}$$

When plastic hinge forms, the above deflected shape is no longer valid. Assuming a plastic hinge at the mid-span position and neglecting the elastic deformation, the deflected shape is in a triangular form:

$$\phi_f(x) = \begin{cases} \dfrac{2x}{L} & 0 \le x < L/2 \\ \dfrac{L-2x}{L} & L/2 \le x < L \end{cases} \tag{8.3}$$

The corresponding equivalent load and mass factors K_{L-f} and K_{M-f} can be found as

$$K_{L-f} = \frac{F_{eq-f}}{F} = \frac{\int_0^L q(x)\phi_f(x)dx}{\int_0^L q(x)dx} = \begin{cases} 0.64 & \text{simply} - \text{supported} \\ 0.53 & \text{fixed} - \text{supported} \end{cases} \tag{8.4a}$$

$$K_{M-f} = \frac{M_{eq-f}}{M} = \frac{\int_0^L m(x)\phi_f^2(x)dx}{\int_0^L m(x)dx} = \begin{cases} 0.50 & \text{simply-supported} \\ 0.41 & \text{fixed-supported} \end{cases} \tag{8.4b}$$

The resistance function of structure under flexural response may be assumed as a bilinear function for simply-supported members, and trilinear function for fixed-supported members, as shown in Fig. 8.2. The yield and maximum flexural strength are controlled by the maximum bending moment capacity of the cross-section at mid-span and supports.

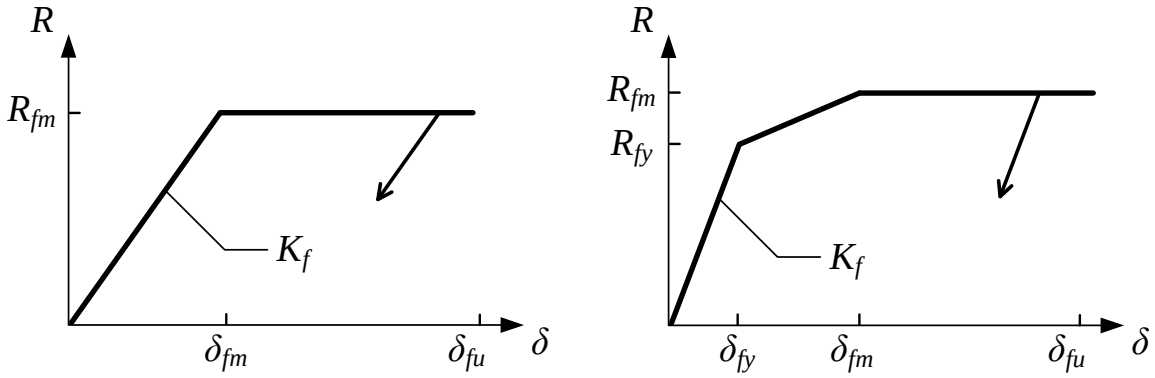

a) Simply-supported b) Fixed-supported

Fig. 8.2 Resistance function for flexural mode

For simply-supported members, the yield flexural resistance R_{fm} and the yield deflection δ_{fm} are expressed as

$$\begin{cases} R_{fm} = \dfrac{8M_P}{L}; \\ \delta_{fm} = \dfrac{5M_P L^2}{48EI}; \end{cases} \tag{8.5}$$

where M_p and EI is the maximum bending moment and flexural rigidity of the cross-section for the structural member. For fixed-supported members, the yield and maximum flexural resistance R_{fy} and R_{fm} and their corresponding deflection δ_{fy} and δ_{fm} can be calculated as:

$$\begin{cases} R_{fy} = \dfrac{12M_P}{L}; \quad \delta_{fy} = \dfrac{3M_P L^2}{96EI} \\ R_{fm} = \dfrac{16M_P}{L}; \quad \delta_{fm} = \dfrac{8M_P L^2}{96EI} \end{cases} \tag{8.6}$$

Before reaching the yielding/maximum resistance, the beam member in its elastic stage and the stiffness for flexural mode is calculated by

$$K_f = \frac{R_f}{\delta_f} = \begin{cases} \dfrac{384EI}{5L^3} & \text{simply} - \text{supported} \\ \dfrac{384EI}{L^3} & \text{fixed} - \text{supported} \end{cases} \tag{8.7}$$

The natural period of the SDOF system, which represents the fundamental flexure mode, can be calculated as:

$$T_f = 2\pi\sqrt{\frac{M_{eq-f}}{K_{eq-f}}} = 2\pi\sqrt{\frac{K_{M-f}M}{K_{L-f}K_f}} = \begin{cases} 2\pi\sqrt{\dfrac{5K_{LM}mL^4}{384EI}} & \text{simply} - \text{supported} \\ 2\pi\sqrt{\dfrac{K_{LM}mL^4}{384EI}} & \text{fixed} - \text{supported} \end{cases} \tag{8.8}$$

where the load-mass factor $K_{LM} = K_M / K_L$.

Consider that for RC members cracking will develop before yielding and this will cause reduction of the stiffness. Ignoring such an effect would significantly underestimate the vibration period. An accurate determination of the cracked flexural stiffness of a RC member is complicated by the fact that the effective moment of inertia along the element changes depending on the severity and distribution of the cracks. A practical way to include the effect of stiffness degradation, as adopted in UFC 3-340-02 (2008), is to use a moment of inertia I_{cr} for cracked concrete cross-sections, which is defined as

$$I_{cr} = \frac{1}{2}Fbd^3 \tag{8.9}$$

where I_{cr} are the moment of inertia of the gross section neglecting reinforcing steel. b, h, and d are the width, overall and effective depth of the cross-section. F is a coefficient determined by relative stiffness $\left(E_s/E_c\right)$ and the reinforcing ratio, as read from the charts given in Fig. 8.3. For instance, the coefficient F for a rectangular C30 concrete section reinforced with 1% tension-only rebar made of British 500C steel, is around 0.045, and if the effective depth $d = 0.9h$, one will find that the moment of inertia for the cracked section is around 39% of the uncracked value.

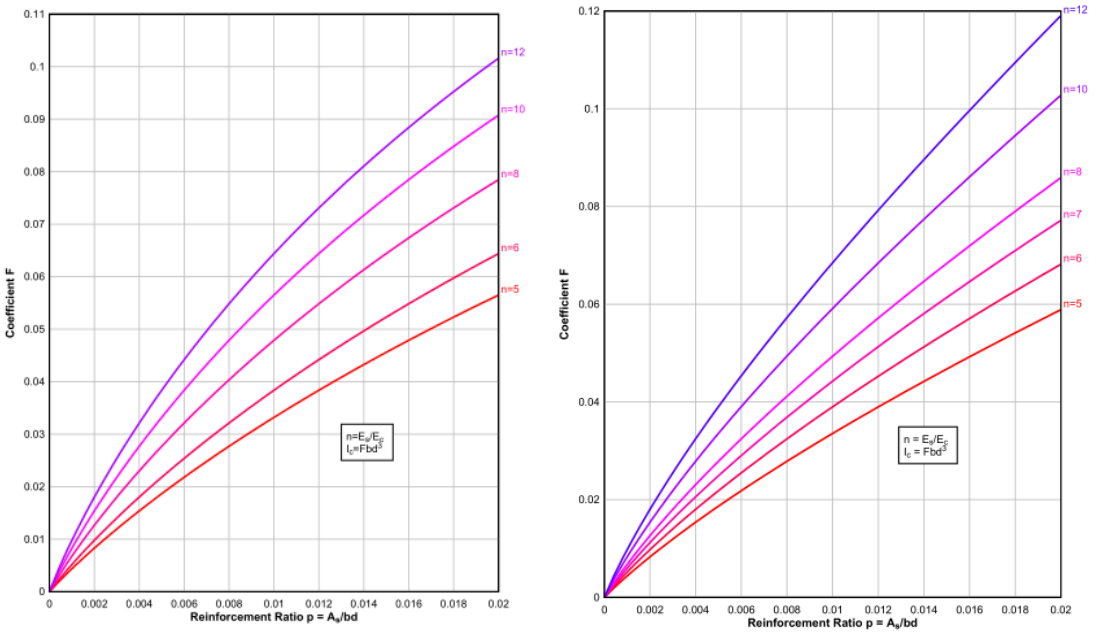

a) Single-reinforced RC section b) Double-reinforced RC section

Fig. 8.3 Coefficient for moment of inertia of cracked sections (UFC 3-340-02, 2008)

8.2.2 Direct shear mode

The shear SDOF model established here is based on the hypothesis that direct shear mode of response occurs at very early stage of the response and it can be reasonably uncoupled from the bending mode, as illustrated in Fig. 8.4a. Thus,

the overall deflection response can be regarded as a superposition of two separated parts; the first one being the flexural deflection in Fig. 8.4b, as obtained from the flexural SDOF system (described earlier), and the second is the direct shear displacement. As stated earlier, direct shear mode is mainly characterised as sliding or large displacement along the interface shear plane or within a very limited span close to the support region. Thus it is reasonable to assume that the deflected shape for direct shear mode can be represented by shear slip displacement $\delta_{eq-s1}(t)$ at supports, in which the rest of structure moves as a rigid body and the shape function is unity ($\phi_{s1}(x)=1$), as shown in Fig. 8.4c.

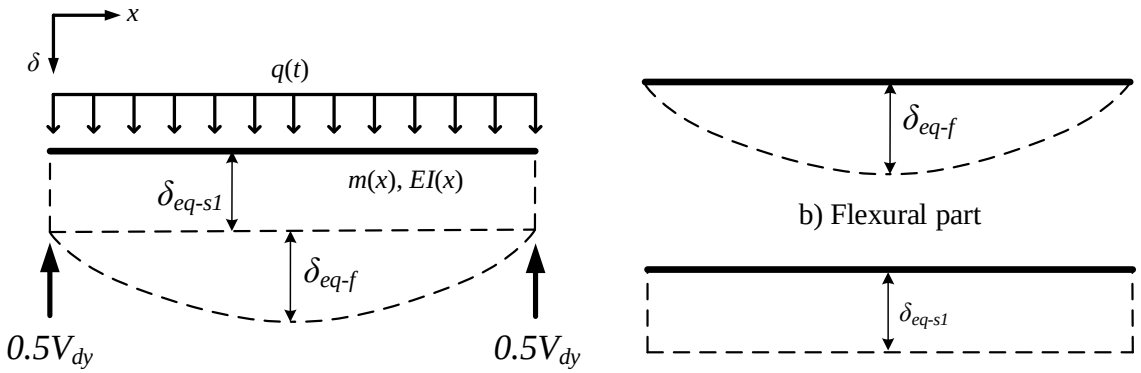

Fig. 8.4 Assumed deflected shape for direct shear mode

For any point along the span, the total deflection $\delta(x,t)$ can be expressed as a combination of its flexural part $\delta_f(x,t)$ and direct shear part $\delta_{s1}(x,t)$.

$$\delta(x,t)=\delta_f(x,t)+\delta_{s1}(x,t) \tag{8.10}$$

Using their shape functions $\phi_f(x)$ and $\phi_{s1}(x)$, the overall deflection can be further expressed as

$$\begin{aligned}\delta(x,t) &= \delta_{eq-f}(t)\cdot\phi_f(x)+\delta_{eq-s1}(t)\cdot\phi_{s1}(x)\\ &= \delta_{eq-f}(t)\cdot\phi_f(x)+\delta_{eq-s1}(t)\end{aligned} \tag{8.11}$$

The two parts of deflection in Eq. 8.17 can be separately described by two SDOF systems, as depicted in Fig. 8.5a. The flexural part $\delta_{eq-f}(t)$ follows Eq. 8.1 for the flexural mode, and the relevant parameters including M_{eq-f}, R_{eq-f} and F_{eq-f} can be determined through the discussion in Section 8.2.1.

For the direct shear part $\delta_{eq-s1}(t)$, the dynamic equilibrium equation of the SDOF system can be written as follows:

$$M_{eq-s1}\cdot\ddot{\delta}_{eq-s1}(t)+R_{eq-s1}(\delta_{eq-s1})=F_{eq-s1}(t) \tag{8.12}$$

where M_{eq-s1}, R_{eq-s1} and F_{eq-s1} are the equivalent mass, resistance and external force for direct shear mode.

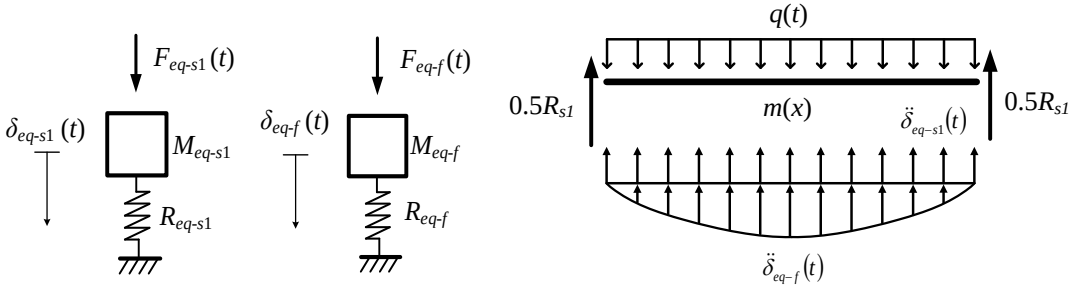

a) SDOF models b) Dynamic equilibrium

Fig. 8.5 Equivalent SDOF system for direct shear mode

For dynamic equilibrium of the beam in the shear mode, the dynamic shear force can be calculated by via considering the dynamic equilibrium of the structural member, as illustrated in Fig. 8.5b, and written as:

$$m\int_0^L\left[\ddot{\delta}_{eq-f}(t)\cdot\phi_f(x)+\ddot{\delta}_{eq-s1}(t)\right]dx+R_{s1}=F(t) \tag{8.13}$$

where the external force $F(t)=\int_0^L q(t)dx=q(t)L$. R_{s1} is the overall reaction force at the supports. Evaluate the integral Eq. 8.13 can be re-written as:

$$K_{L-f}M\ddot{\delta}_{eq-f}(t)+M\ddot{\delta}_{eq-s1}(t)+R_{s1}=q(t)L \tag{8.14}$$

where K_{L-f} is the load factor for flexural mode and the overall mass $M=mL$. Rearrange Eq. 8.14,

$$M\ddot{\delta}_{eq-s1}(t)+R_{s1}=q(t)L-K_{L-f}M\ddot{\delta}_{eq-f}(t) \tag{8.15}$$

One may find that the right hand side of Eq. 8.15 is the equivalent external load F_{eq-s1}, which is the combined effect of blast load and inertial force from flexural SDOF response.

The resistance R_{s1} only depends on the direct shear slip displacement $\delta_{eq-s1}(t)$. Since the direct shear failure is very brittle and experiences little ductility, here the SDOF model for direct shear mode is considered to be linear elastic and the resistance function is also simplified as linear elastic but with a strength cap:

$$R_{s1}=K_{s1}\cdot\delta_{eq-s1}\le R_{s1,u} \tag{8.16}$$

where K_{s1} is the equivalent stiffness for direct shear. For this study, the stiffness and resistance function of direct shear is calculated from a commonly adopted empirical formula proposed by Krauthammer et al. (1986), which is defined via the relation between the shear stress and the slip displacement, as given in Fig. 8.6.

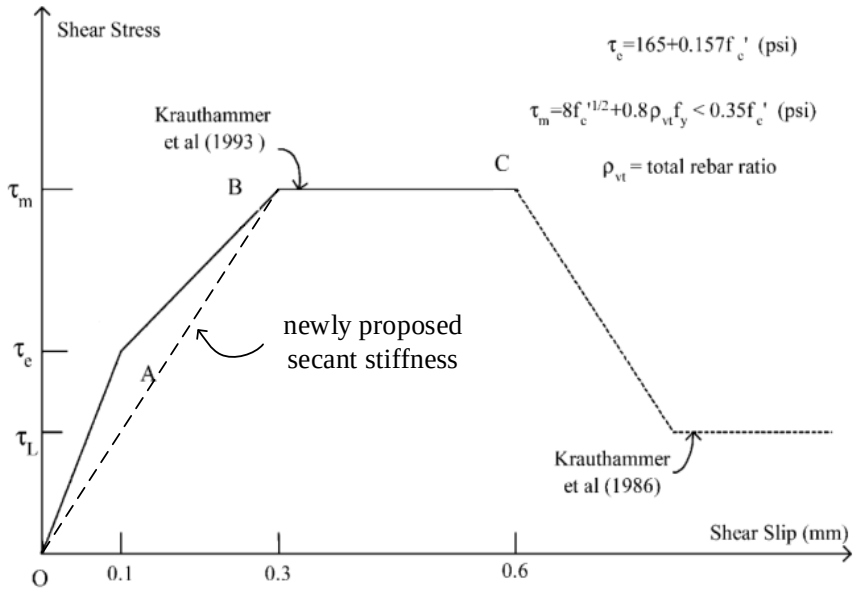

Fig. 8.6 The shear stress-slip model proposed by Krauthammer et al. (1986)

As shown in the portion OAB of Fig. 8.6, the elastic limit and the maximum shear stress, which correspond to a slip displacement of 0.1 mm and 0.3 mm, respectively, are proposed as:

$$\begin{aligned} \tau_e &= 1.14 + 0.157 f_c^{'} \\ \tau_m &= 0.664\sqrt{f_c^{'}} + 0.8\rho_{vt} f_y \end{aligned} \quad \text{(in MPa)} \qquad (8.17)$$

in which τ_e and τ_m are the elastic limit and maximum value of average shear stress over the section, $f_c^{'}$ is the compressive strength of concrete, and f_y is the yielding strength of steel rebar, all in MPa. ρ_{vt} is the ratio of total reinforcement area to the area of the plane that it crosses.

Since direct shear mode will not practically develop without going into at least some level of inelastic response, a more meaningful estimation of the shear stiffness is to introduce a secant stiffness from the OB portion of the shear stress-slip curve shown in Fig. 8.6, for a shear force level into the shear crack range.

Therefore, the resistance and equivalent stiffness for direct shear mode can be written as:

$$R_{s1} = 2\tau_m \mu A \tag{8.18a}$$

$$K_{s1} = \frac{R_{s1}}{s_{0.3}} = \frac{2\tau_m \mu A}{s_{0.3}} \tag{8.18b}$$

where $s_{0.3}$ is an assumed slip of 0.3 mm, A is the cross-section area, and μ is the correction factor, which is used to take into account an assumption of constant shear stress distribution over a cross section. $\mu = 5/6$ for rectangular cross sections, as proposed by Krauthammer et al. (1993). Then it can be derived that the natural period for direct shear mode is

$$T_{s1} = 2\pi \sqrt{\frac{K_{M-s1}}{K_{L-s1}} \frac{M}{K_{s1}}} = 2\pi \sqrt{\frac{mLs_{0.3}}{2\tau_m \mu A}} \tag{8.19}$$

Due to the very nature of the assumed shear deflection as a rigid body motion (flat line), the SDOF system will appear to be the same the direct shear mode of both simply-supported and fixed-supported boundary conditions. Differences could be introduced when the details of the direct shear resistance between the two boundary conditions are examined, but this is not considered in the basic formulation here.

As has been evidenced in the numerical simulation in Chapter 7, a realistic direct shear deformation will occur over a finite width of shear span, rather than the extreme situation of a single direct shear line. Therefore, the shear sliding at the supports may be expressed in a more general way taking into consideration of the average shear strain over a short shear span length a :

$$\delta_{eq-s1} = \gamma_V \cdot a = \gamma_V \cdot \lambda_{ss} \cdot d_{eff} \tag{8.20}$$

where shear sliding δ_{eq-s1} is a cumulative quantity over the shear band, γ_V is the average shear strain, a is the width of the shear band, which can be further be expressed as a span-to-depth ratio λ_{ss} multiplied by the effective depth of the member d_{eff} .

The specific value of λ_{ss} should be determined by experiments for beams made of different materials. For example, Li and Jones (2000) derived 0.866 for a beam with a solid rectangular cross-section using von Mises yielding criterion, and Ma et al. (2007) assumed a factor of 0.8 based on rigid-plastic model. In this study the shear span under direct shear mode is assumed to be half of the effective shear depth, on the basis of the numerical results presented in Chapter 7; thus the factor λ_{ss} is set as 0.5.

8.2.3 Diagonal shear mode

Similarly, the overall response of RC response under diagonal shear mode can be regarded as a combination of two separate SDOF systems presented in Fig. 8.7a, in which the first is the flexural part (described earlier in Section 8.2.1) shown in Fig. 8.7b, and the second defines the diagonal shear part, as shown in Fig. 8.7c.

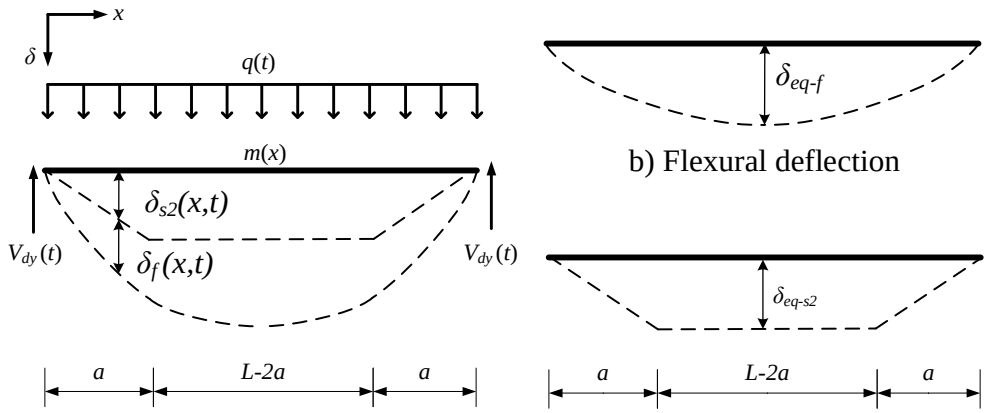

Fig. 8.7 Assumed deflected shape for diagonal shear mode

For the diagonal shear deflection, only pure shear deformation is considered here and it is assumed to be concentrated in a short span near the supports that has a width of *a*, and the rest $(l-2a)$ portion in the middle of span acts as a rigid body. For simplicity, and based on the numerical parametric results in Chapter 7, we can assume that the diagonal shear failure occurs at a shear span equals to 1.5 times of the effective depth. To give an idea, if the slenderness ratio (overall span to full depth) *L/h* is 15, then the diagonal shear span *a* as 1.5d will account for 10% of the overall span length *L*.

To simplify the calculation procedure, the deflected shape for the direct shear part is assumed to be perfect straight lines in both the short shear spans and non-shear region in between. So the shape function for diagonal shear deflection in Fig. 8.7c can be written as

$$\phi_{s2}(x)=\begin{cases}\dfrac{x}{a} & x<a\\ 1 & a\le x<L-a\\ \dfrac{L-x}{a} & L-a\le x<L\end{cases} \tag{8.21}$$

For any point along the span, the overall deflection $\delta(x,t)$ can therefore be expressed as a combination of its flexural part $\delta_f(x,t)$ and diagonal shear part $\delta_{s2}(x,t)$, and further described by its shape function and the equivalent displacements.

$$\begin{aligned}\delta(x,t) &= \delta_f(x,t)+\delta_{s2}(x,t)\\ &= \delta_{eq-f}(t)\cdot\phi_f(x)+\delta_{eq-s2}(t)\cdot\phi_{s2}(x)\end{aligned} \tag{8.22}$$

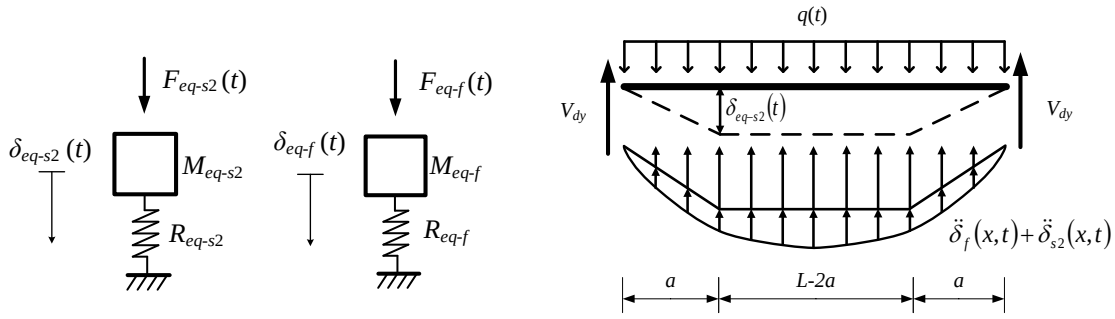

a) SDOF models b) Dynamic equilibrium

Fig. 8.8 Equivalent SDOF system for diagonal shear mode

The two parts in Eq. 8.22 are separately described by a flexural SDOF system and a diagonal shear SDOF system, as depicted in Fig. 8.8a. The flexural part $\delta_{eq-f}(t)$ follows Eq. 8.1 for the flexural mode, while for the diagonal shear part the overall dynamic equilibrium of the structural system can be illustrated in Fig. 8.8b, and can be expressed in a general form as

$$I_{eq-s2}(t)+R_{eq-s2}=F_{eq-s2}(t)-I_{eq-f-s2}(t) \tag{8.23}$$

where $F_{eq-s2}(t)$, $I_{eq-s2}(t)$ and $R_{eq-s2}(\delta_{eq-s2})$ are the equivalent external load, flexural and diagonal shear inertia forces, and resistance functions. $I_{eq-f-s2}(t)$ is the equivalent flexural inertia force acting on the diagonal shear deflection. These parameters can be further expressed as

$$\begin{aligned} F_{eq-s2}(t) &= \int_0^L q(x)\phi_{s2}(x)dx \\ &= \int_a^{L-a} q dx + 2\int_0^a q\frac{x}{a}dx \\ &= q(t)(L-a) \\ &= K_{L-s2}F(t) \end{aligned} \tag{8.24a}$$

$$\begin{aligned} I_{eq-s2}(t) &= \int_0^L m(x)\ddot{\delta}_{s2}(x,t)\phi_{s2}(x)dx \\ &= m\ddot{\delta}_{eq-s2}\int_0^L {\phi_{s2}}^2(x)dx \\ &= K_{M-s2}mL\ddot{\delta}_{eq-s2} \end{aligned} \tag{8.24b}$$

$$\begin{aligned} I_{eq-f-s2}(t) &= \int_0^L m(x)\ddot{\delta}_f(x,t)\phi_{s2}(x)dx \\ &= m\ddot{\delta}_{eq-f}\int_0^L \phi_f(x)\phi_{s2}(x)dx \\ &= K_{L-s2-f}mL\ddot{\delta}_{eq-f} \end{aligned} \tag{8.24c}$$

where load and mass factors for diagonal shear mode are calculated by

$$\begin{aligned} K_{L-s2} &= \frac{1}{L}\int_0^L \phi_{s2}(x)dx \\ &= \frac{1}{L}\int_a^{L-a} dx + \frac{2}{L}\int_0^a \frac{x}{a}dx \\ &= 1-\frac{a}{L} \end{aligned} \tag{8.25a}$$

$$\begin{aligned} K_{M-s2} &= \frac{1}{L}\int_0^L {\phi_{s2}}^2(x)dx \\ &= \frac{1}{L}\int_a^{L-a} dx + \frac{2}{L}\int_0^a \left(\frac{x}{a}\right)^2 dx \\ &= 1-\frac{4a}{3L} \end{aligned} \tag{8.25b}$$

$$\begin{aligned} K_{L-f-s2} &= \frac{1}{L}\int_0^L \phi_f(x)\phi_{s2}(x)dx \\ &= \begin{cases} \dfrac{32}{150L^5}\left(3L^5-5L^3a^2+3La^4-a^5\right) & \text{simply}-\text{supported} \\ \dfrac{32}{60L^5}\left(L^5-5L^3a^2+6La^4-2a^5\right) & \text{fixed}-\text{supported} \end{cases} \end{aligned} \tag{8.25c}$$

If we assume $a=1.5h$ and $L/h=15$, then $a/L=0.1$, $K_{L-s2}=0.90$ and $K_{M-s2}=0.87$. The factor K_{L-s2-f} is 0.63 for simply-supported and 0.53 for fixed-supported. Then the overall equilibrium equation in Eq. 8.23 can be rewritten into

$$K_{M-s2}M\ddot{\delta}_{eq-s2}(t)+K_{L-s2}R_{s2}=K_{L-s2}F(t)-K_{L-f-s2}M\ddot{\delta}_{eq-f}(t) \tag{8.26}$$

The diagonal shear resistance R_{s2} is a function of the diagonal shear displacement $\delta_{eq-s2}(t)$, and since the diagonal shear failure is generally brittle, here the resistance function is simplified as linear elastic and expressed as

$$R_{s2}=K_{s2}\cdot\delta_{eq-s2} \tag{8.27}$$

where K_{s2} is the equivalent stiffness for diagonal shear. Then it can be derived that the natural period for the diagonal shear mode is

$$T_{s2}=2\pi\sqrt{\frac{K_{M-s2}mL}{K_{L-s2}K_{s2}}} \tag{8.28}$$

To determine the value for the stiffness K_{s2}, the shear force diagrams under the blast load, the inertia force and their combined effect are further analysed as illustrated in Fig. 8.9a-8.9c, and the distribution of shear strain is presented in Fig. 8.9d.

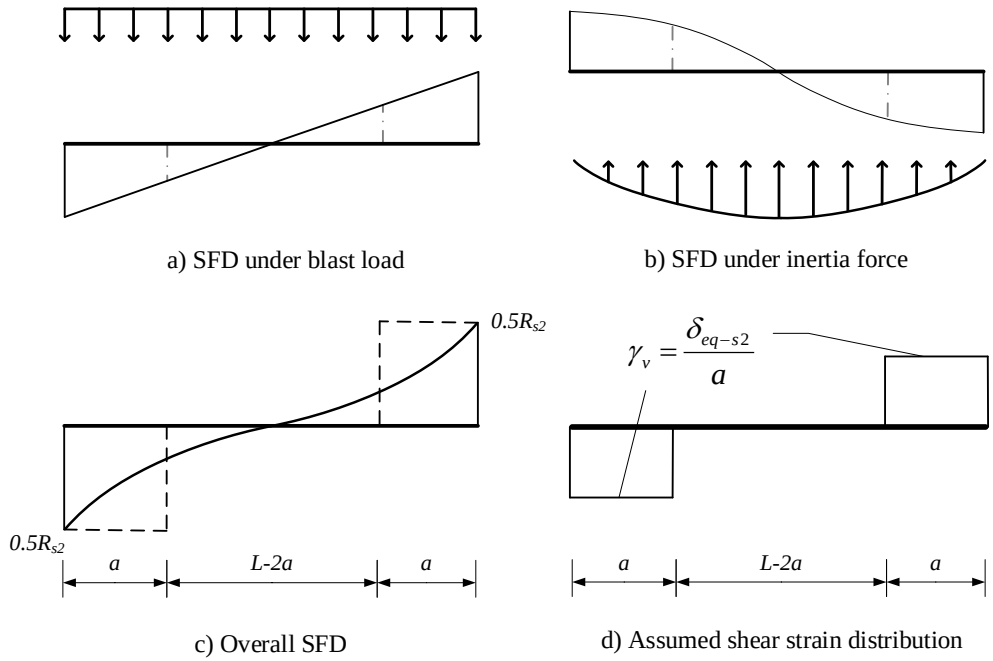

Fig. 8.9 Shear force diagrams and shear deformation under diagonal shear mode

It can be inferred that the maximum shear force always appears at the ends and equals to $0.5R_{s2}$. Meanwhile, since the diagonal shear deformation is assumed to be a straight line, the average shear strain within the shear span is constant and equals to

$$\gamma_v = \frac{\delta_{eq-s2}}{a} \tag{8.29}$$

So if shear force is resisted by the material within the shear span of a, the relation between the maximum shear force, which equals to half of the dynamic shear resistance, and the diagonal shear displacement can be established as

$$\gamma_v = \frac{\delta_{eq-s2}}{a} = \frac{R_{s2}}{2GA} \tag{8.30}$$

where GA is the shear rigidity at the cross-section, and so:

$$R_{s2} = \frac{2GA}{a}\delta_{eq-s2} \tag{8.31}$$

Hence the equivalent stiffness for diagonal shear can be calculated as:

$$K_{s2} = \frac{R_{s2}}{\delta_{eq-s2}} = \frac{2GA}{a} \tag{8.32}$$

Prior to cracking, the shear stiffness over a cross-section can be directly calculated via the elastic method,

$$GA_e = \frac{E_c A_v}{2(1+\nu)} \approx 0.417 E_c b d_v \tag{8.33}$$

where E_c is the concrete Young's modulus and d_v is the effective shear depth. This is deduced by assuming the Poisson's ratio as 0.20.

However after the development of diagonal cracking, Eq. 8.33 is no longer valid. For such short span case, variable angle truss model proposed by Kim and Mander (2007, 1999) as presented in Fig. 8.10, is employed to calculate the fully diagonally cracked shear rigidity.

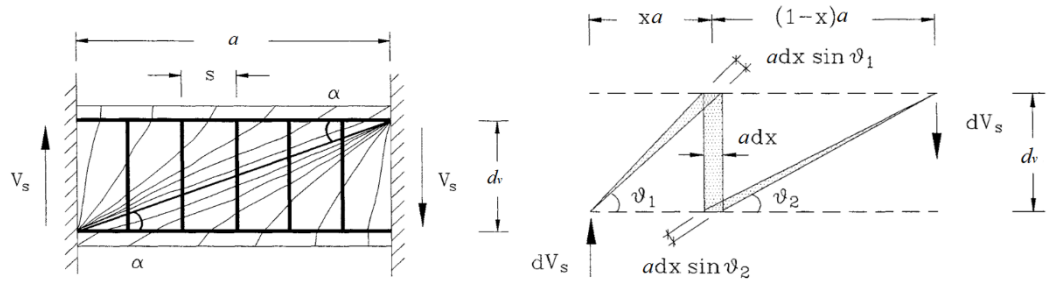

a) Beam model layout b) Differential element

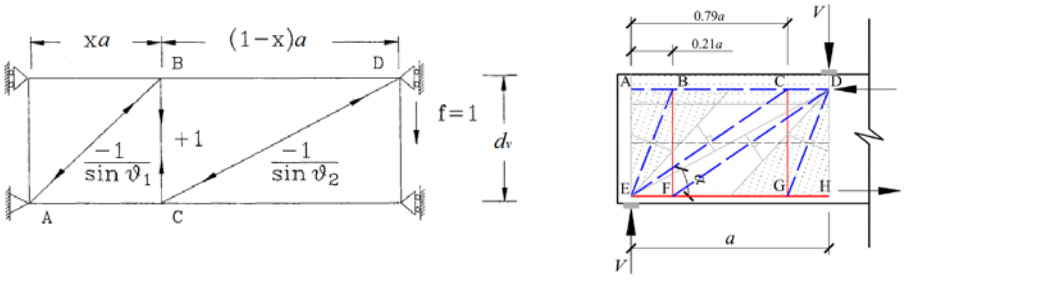

c) Member force under unit shear d) Simplified two-point truss model

Fig. 8.10 Shear stiffness calculation using VATM (After Kim and Mander 2007)

It follows a continuous truss assumption in which the transverse reinforcement is smeared along the shear span, as shown in Fig. 8.10a. Each of the single differential truss element Ldx subjected to the differential shear force dV_s, as shown in Fig. 8.10b, consists of an idealised steel tie with a finite depth and two tapered diagonal concrete struts, where *x* is a non-dimensionalised parameter varying from 0 to 1.

The force diagram of the truss under a unit shear force is given in Fig. 8.10c. The basic rationale is that for each differential element, its shear deformation is caused by the elongation of transverse ties and compression of inclined concrete struts. The total shear deformation then can be obtained by integrating over the entire length of the truss.

However there is no closed-form analytical solution to this, and a simplified two-point numerical approach employed by the same authors is found to provide quite accurate prediction (Kim and Mander 1999). The shear rigidity for such cracked cross-section can be expressed as

$$GA_{cr} = \frac{V}{\gamma} = \frac{n\rho_v E_c b d_v \cot^2\alpha}{1+4n\rho_v\left(1+0.39\cot^2\alpha\right)^2} \tag{8.34}$$

where $\alpha = \arctan\left(\frac{d_v}{a}\right)$, $n = \frac{E_s}{E_c}$, and ρ_v is the transverse reinforcing ratio.

To account for a realistic estimation for shear rigidity, an average value is taken to count for both the elastic and cracked sections, which is defined as

$$GA_a = \frac{1}{2}\left(GA_e + GA_{cr}\right) \tag{8.35}$$

8.3 Validation and modification of the proposed SDOF parameters

To validate the proposed calculation method for equivalent stiffness in the three representative modes, three key parameters proposed in Section 8.2, namely the flexural rigidity EI_{cr} over cracked cross-sections for flexural mode, the shear rigidity GA_a for cracked cross-section in diagonal shear mode, and the direct shear stiffness K_{s1}, are firstly calibrated with quasi-static experiment discussed in Chapter 4 in conjunction with complementary numerical simulations.

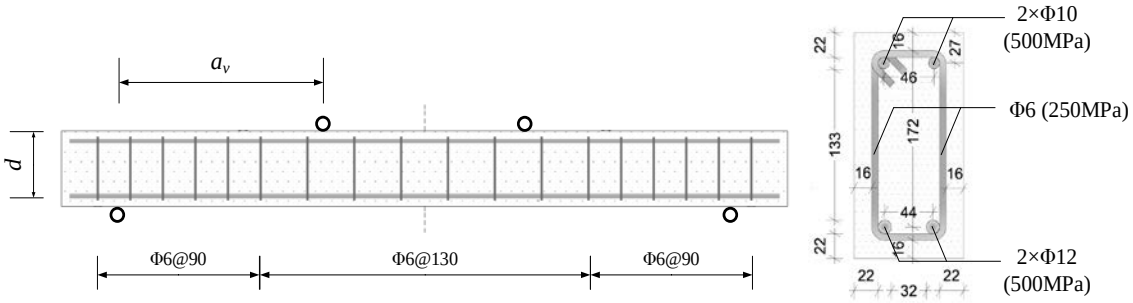

Fig. 8.11 Dimensions and cross-section of the RC beam specimen D18

The tested beam D18, firstly introduced in Section 4.5, has a length of 2m and a cross-section of 200 mm×100 mm. The specimen was tested under four-point load with a normal shear span of a=567 mm that equals to a span to depth ratio of 3.2, and failed in flexure, as shown in Fig. 8.11. It uses C40 concrete and has a reinforcing ratio of 1%. Detailed information of the experiment can be found in Section 4.5.

For an evaluation of the shear stiffness in smaller shear span, additional "numerical" experiments are conducted. The intended shear deformation mode is realised by adjusting the location of the point loads, for example at span to depth ratios of 0.5 and 1.5, to simulate the direct and diagonal shear deform patterns.

For RC specimen loaded with a four-point load setup in Fig. 8.11, the deflection under a normal span to depth ratio, if measured from the loading plate of the applied point load, can be calculated by

$$\Delta = \frac{Pa^2(3L-4a)}{6EI_{cr}} \quad (a/d = 3.2) \tag{8.36}$$

where P is the total applied point load and a is the width of shear span. EI_{cr} is the average flexural rigidities over cracked cross-sections, as defined in Eq. 8.9.

When the span-to-depth ratio is reduced to 1.5, the shear deformation within the span needs to be included, and the overall deflection is then expressed as

$$\Delta = \frac{Pa^2(3L-4a)}{6EI_{cr}} + \frac{Pa}{2GA_a} \quad (a/d = 1.5) \tag{8.37}$$

where GA_a is the average shear rigidities over cracked cross-sections as defined in Eq. 8.35.

When the shear span is reduced to half of the effective depth, the deflection is then predicted by the equivalent stiffness proposed by Krauthammer model discussed in Section 8.2.2.

$$\Delta = \frac{P}{2K_{s1}} \quad (a/d = 0.5) \tag{8.38}$$

where K_{s1} is the equivalent shear stiffness for direct shear, as determined from Eq. 8.18.

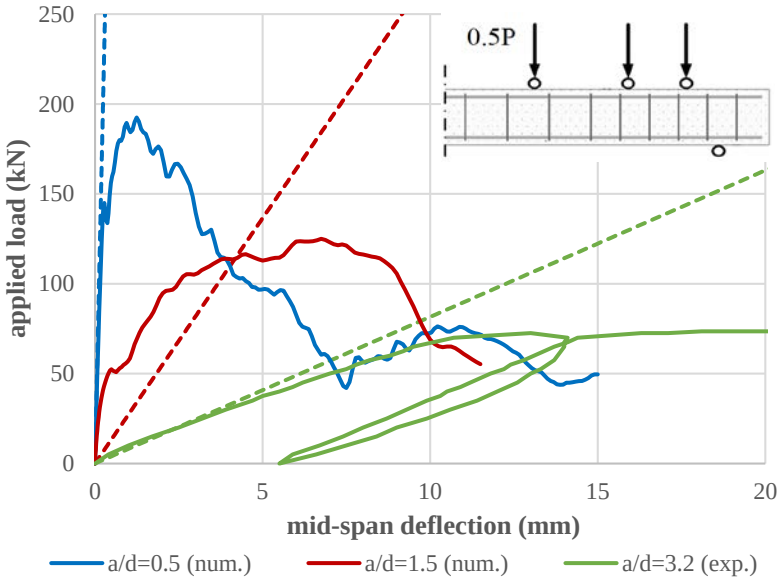

Fig. 8.12 Prediction for flexural and shear stiffness of cracked cross-section

Fig. 8.12 gives the comparisons of stiffnesses for RC beam loaded in a four-point load settings with representative shear spans. Solid lines represent load-displacement curves obtained from four-point laboratory test and extended numerical cases, while the dashed lines presents the equivalent stiffness predicted by the proposed parameters, as given in Eq. 8.36-38.

It can be observed that the predicted flexural and direct-shear stiffnessses agree favourably. The diagonal-shear stiffness looks acceptable in the initial hardening stage but under-estimated when the hardening effect becomes significant and the damaged state is close to the ultimate load and the diagonal cracks are fully-opened.

Based on the validation results, a more comprehensive evaluation of the soundness of the stiffness calculations would be worth considering for future investigations. For the purpose of the present study, the proposed methods of estimating the shear stiffnesses in general may be regarded as reasonable.

8.4 Correlation between SDOF predictions and actual responses concerning transient high shear

The proposed SDOF models are applied to calculate the peak shear force under blast loading, and the results are compared with the numerical results using beam-element model and FE model respectively. The particular focus is on the validity of the SDOF model in capturing the dynamic response and high shear demand. For each flexural and shear deformation mode, the correspondent SDOF model is examined via structural response under blast load with duration in the corresponding regimes, and the maximum dynamic shear force is extracted and compared.

For the convenience of comparing with the FE simulation results, the SDOF models are developed using the same properties as used in the FE models. The RC beam is assumed to have a cross-section of 200 mm×100 mm and length of 3m. The resistance functions for the flexural SDOF models are simplified as bi-linear for simply-supported case and tri-linear for fixed-supported case, while the shear response in the direct and diagonal shear SDOF models are assumed to be elastic with a strength limit.

Table 8.1 Natural period of flexure and shear modes

Type of modes	*Boundary condition*	*Natural period (ms)*
Flexure (T_f)	simple	33.5
Flexure (T_f)	fixed	14.9
Diagonal shear (T_{s2})	both	4.74
Direct shear (T_{s1})	both	2.08

Based on the SDOF properties calculated according to the method described in the previous section, the natural periods of the flexure and shear modes can be calculated and compared. Table 8.1 shows the natural periods of the RC beam with two different boundary conditions.

8.4.1 Shear response dominated by flexural mode

The proposed SDOF models are firstly applied to predict the shear response of simply-supported RC beam under a load duration in the order of the flexural period ($t_d \approx 1.1T_f$). The magnitude of applied impulse was initially set as 4 kPa·s that is not to cause shear failure, but able to develop a flexural hinge at the mid-span and force the response into the global bending stage, as presented in Fig. 8.13. Then the impulse is increased to 12 kPa·s, which is sufficient to cause ultimate flexural failure at the mid-span, as shown in Fig. 8.14.

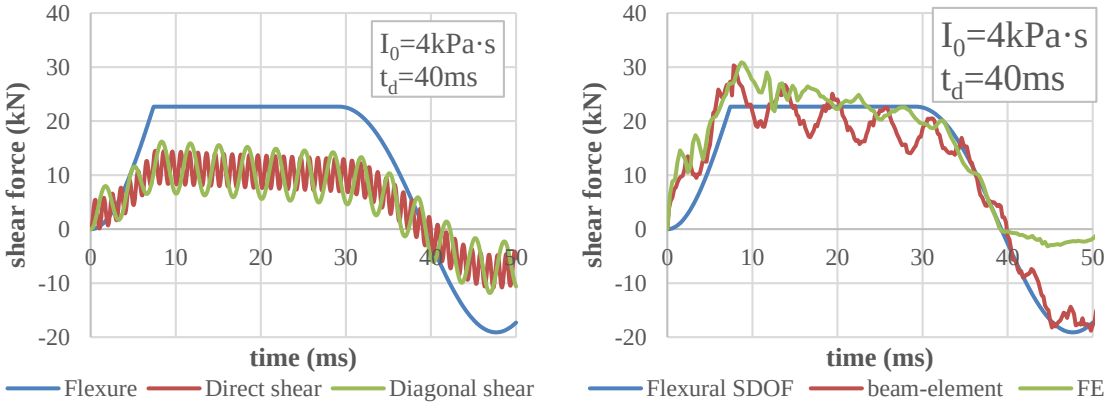

a) Responses in 3 SDOFs b) Validation with other predictions

Fig. 8.13 Validation of SDOF model for simply-supported RC beam dominated by flexural mode (I_0=4 kPa·s; t_d=40 ms)

Fig. 8.13a summarises the shear force responses of the three SDOF models. It can be observed that the three responses have distinctively different frequencies, which mainly depend on the equivalent mass and stiffness. The maximum shear force in the flexural mode is 23 kN, which is effectively limited by the cross-sectional flexural resistance and significantly larger than that in the other two shear modes, indicating the dominance of flexure mode. The response from flexural SDOF system is further compared with results from the beam model and

FE simulation in Fig. 8.13b, which sees a favourable agreement among shear forces predicted by the three approaches.

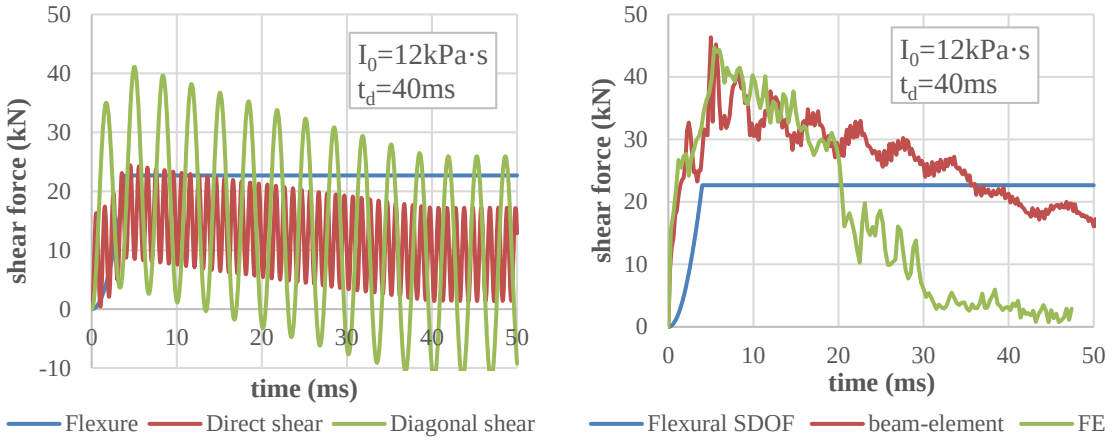

a) Responses in 3 SDOFs b) Validation with other predictions

Fig. 8.14 Validation of SDOF model for simply-supported RC beam dominated by flexural mode (I_0=12 kPa·s; t_d=40 ms)

When the impulse level has increased to 12 kPa·s, as depicted in Fig. 8.14a, the maximum shear force in the diagonal shear mode has largely increased to around 41 kN and has surpassed that in the flexural mode. On the other hand, the actual shear response, as predicted by beam and FE models in Fig. 8.14b, has also increased to around 46 kN.

This is mainly brought by the dynamic effect, and for simply-supported members, the flexural hinge would not merely isolate at the mid-span but inevitably extend over a sizable segment length (plastic hinge), which effectively results in a shorter shear span and higher shear force. The damage pattern, shear force and bending moment diagrams analysed for this load scenario using FE model can be found in Fig. 7.10 and 7.12 in Section 7.3.1.

Besides, note that the equivalent SDOFs do not consider damping and thus significant oscillation occurs; but the purpose is to capture the peak response

following the pulse load and for this reason we shall not be too worried about the oscillation phenomenon.

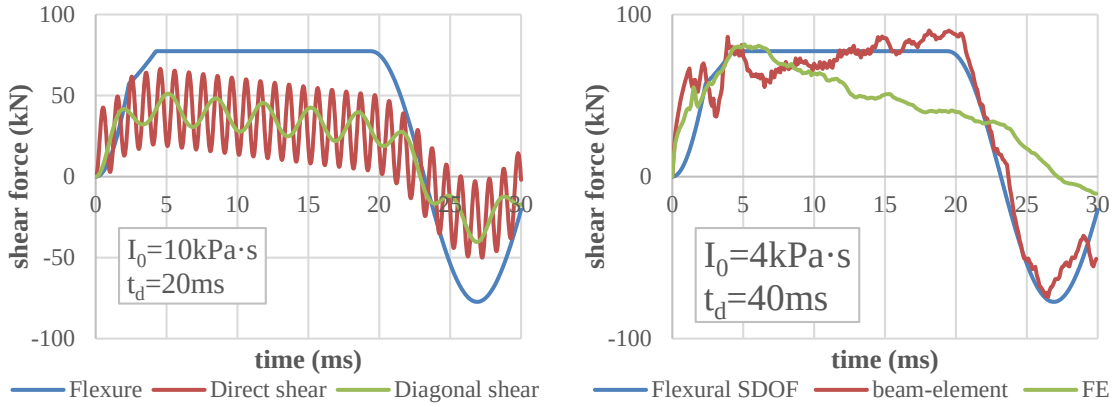

a) Responses in 3 SDOFs b) Validation with other predictions

Fig. 8.15 Validation of SDOF model for fixed-supported RC beam dominated by flexural mode (I_0=10 kPa·s; t_d=20 ms)

For fixed-supported boundary, the SDOF predictions of RC beam under a load duration of 20 ms ($t_d \approx 1.2T_f$) is presented in Fig. 8.16a, and the flexural SDOF prediction is further validated with other analysis approaches in Fig. 8.16b. The applied impulse is 10 kPa·s, which is sufficiently large to cause plastic hinges at both supports and midspan, and to cause ultimate collapse of the beam. It can be seen that the flexural SDOF system gives the largest shear force response, and its peak shear force agrees favourably with the ones predicted by Timoshenko beam model and FE model.

8.4.2 Shear response dominated by direct shear mode

Fig. 8.16 and 8.17 give the validation of direct shear SDOF predictions under a load duration of 2~3% of flexural period T_f. The applied impulse and load durations are set as 7 kPa·s and 1.0 ms for simply-supported, and 5 kPa·s and 0.5 ms for fixed-supported boundary, both of which are sufficient to cause a

direct shear failure at the support, as previously demonstrated in Section 7.3.3 and 7.4.3.

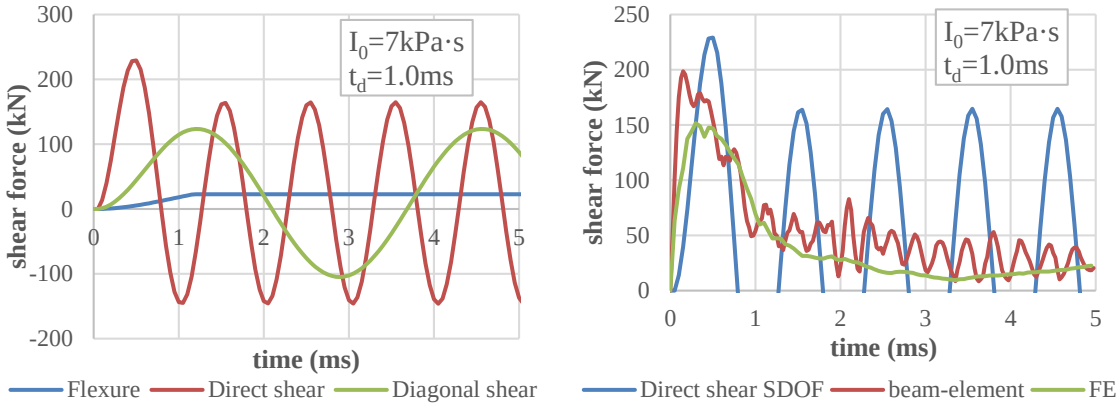

a) Responses in 3 SDOFs b) Validation with other predictions

Fig. 8.16 Validation of SDOF model for simply-supported RC beam dominated by direct shear mode (I_0=7 kPa·s; t_d=1.0 ms)

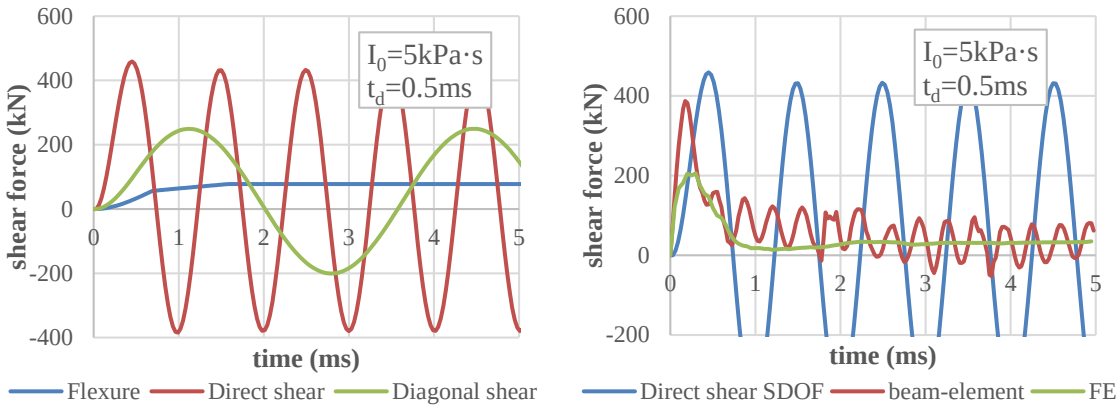

a) Responses in 3 SDOFs b) Validation with other predictions

Fig. 8.17 Validation of SDOF model for fixed-supported RC beam dominated by direct shear mode (I_0=5 kPa·s; t_d=0.5 ms)

As presented in the time histories of SDOF systems in Fig. 8.16a and 8.17a, under such load duration, the shear response in direct shear mode becomes the dominated one and has the maximum shear force. The shear demand for simply-supported and fixed-supported beams is 229 kN and 452 kN, respectively.

It can be seen from Fig. 8.16b and 8.17b that, the maximum shear forces predicted by SDOF models are around 15% higher than the shear forces obtained from the beam models and more than 50% higher than the actual shear resistance, as analysed via the FE model in Chapter 7. This reveals that with a proper description of the direct shear mode, SDOF model, especially without damping, is not meant to predict the overall time history but can capture the shear force demand (maximum shear force) in a reasonably conservative way. Without the shear SDOFs, the shear force demand predicted through the conventional flexural-only SDOF system cannot capture the high shear phenomenon.

8.4.3 Shear response dominated by diagonal shear mode

The proposed SDOF models are further validated in a typical load scenario in the regime of diagonal shear mode. The applied load duration is 4 ms and the impulses are 11 kPa·s and 6 kPa·s for simply- and fixed-supported boundaries, respectively. The shear responses predicted by the 3 SDOF models are presented in Fig. 8.18a and 8.19a, in which the diagonal shear mode develops the largest shear force response.

The SDOF response from diagonal shear mode is further compared with Timoshenko beam and FE models in Fig. 8.18b and 8.19b. Results reveal that the shear demand under diagonal shear mode, as predicted by SDOF models, are around 155 kN in both boundary conditions, which are about 20% higher that the estimation by Timoshenko beam model. The dynamic shear resistance in this case, as analysed via FE simulation, are 98 kN and 113 kN for simply- and fixed-supported RC beams, respectively.

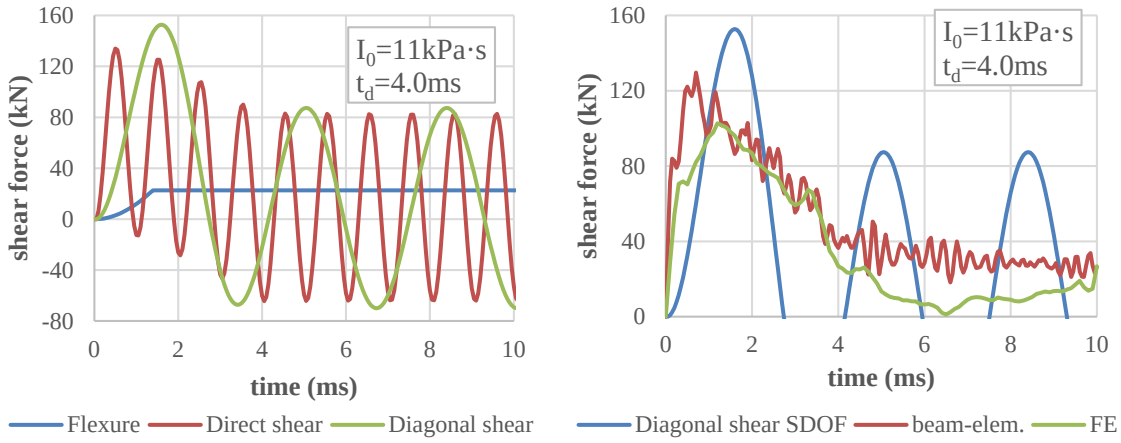

a) Responses in 3 SDOFs b) Validation with other predictions

Fig. 8.18 Validation of SDOF model for simply-supported RC beam dominated by diagonal shear mode (I_0=11 kPa·s; t_d=4.0 ms)

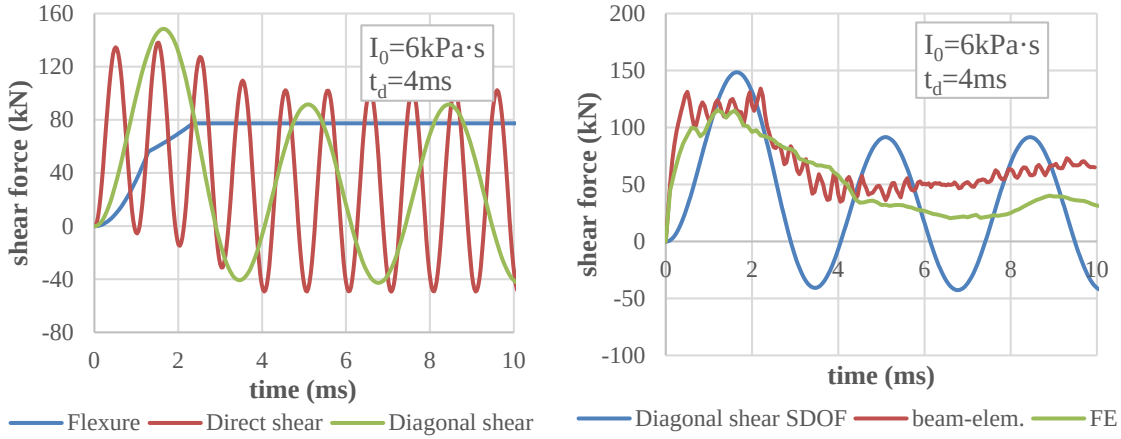

a) Responses in 3 SDOFs b) Validation with other predictions

Fig. 8.19 Validation of SDOF model for fixed-supported RC beam dominated by diagonal shear mode (I_0=6 kPa·s; t_d=4.0 ms)

8.5 Simplified assessment of dynamic shear response

To identify the shear failure under the direct and diagonal shear modes, it is necessary to specify the criteria for dynamic shear resistance. As discussed in Chapter 7, it is clear that the increase of dynamic shear resistance comes from

two effects: a) the reduction of shear span and b) the material rate effect. A general form for the dynamic shear resistance V_{Rd} can be therefore proposed as

$$V_{Rd1} = \alpha_1\left(\frac{t_d}{T_{s1}}\right)\cdot\beta_1\left(\frac{t_d}{T_{s1}}\right)\cdot V_{Rs1}\left(\frac{a_{eff}}{d}\right) \tag{8.39a}$$

$$V_{Rd2} = \alpha_2\left(\frac{t_d}{T_{s2}}\right)\cdot\beta_2\left(\frac{t_d}{T_{s2}}\right)\cdot V_{Rs2}\left(\frac{a_{eff}}{d}\right) \tag{8.39b}$$

where the subscript "1" or "2" represents the direct shear or diagonal shear model. V_{Rs1} and V_{Rs2} are the static shear resistance for direct and diagonal shear mode, under a developed effective shear span a_{eff}.

The factor α_1 and α_2 represent the influence of structural dynamic effect, in which the rapid increase of shear force in the shear span region leaves little time for fracture to develop in a progressive manner as would be the case under static loading, and is therefore a function of the load duration normalised by the period of the correspondent shear mode (T_{s1} or T_{s2}). Factor β represents solely the effect of material DIF effect.

In the following two sections empirical formulas to estimate the static shear resistance for the two shear modes are presented. The factors α_1, α_2, β_1 and β_2, are derived based on numerical results from Chapter 7. The general procedure of the simplified analytical method to assess dynamic shear response is summarised in Section 8.4.4.

8.5.1 Direct shear resistance

Most application in predicting the direct shear resistance function of RC structures is empirical estimation based on experimental observation. The commonly cited formula proposed by Krauthammer et al. (1986), as mentioned

earlier in Section 8.2.2, is established between direct shear resistance and slip displacement, through analysis of experimental data and material behaviour of RC slabs, based on the work of Hawkins (1973, 1982), Mattock (1974) and Walraven and Reinhardt (1981). This resistance function has also been adopted by other researchers in application for SDOF models (Dragos and Wu 2014; Low and Hao 2002; Luckyram et al. 1992; Wang et al. 2013; Xu et al. 2014) and Timoshenko beam based models (Krauthammer et al. 1993; Lu and Gong 2007; T. Ross 1983).

As shown earlier in Fig. 8.6, the shear resistance proposed by Krauthammer et al. (1986, 1990), was developed based on interface transfer in members having well-anchored main reinforcement without axial force and a shear-to-depth ratio less than 0.5. The maximum shear force value is defined via the maximum shear stress over the cross-section, and expressed as

$$\begin{aligned} V_{Rs1} &= \mu \tau_m A \\ &= \mu(0.664\sqrt{f_c^{'}} + 0.8\rho_{vt} f_y)A \end{aligned} \quad \text{(in MPa)} \qquad (8.40)$$

in which τ_m is the maximum value of average shear stress over the section, A is the cross-section area, and μ is the correction factor, which is $\mu = 5/6$ for rectangular cross sections $f_c^{'}$ is the compressive strength of concrete, and f_y is the yielding strength of steel rebar, all in MPa. ρ_{vt} is the ratio of total reinforcement area to the area of the plane that it crosses.

As for the dynamic rate enhancement effect, Krauthammer et al. (1986) proposed a factor of 1.4 to incorporate the influence of both compressive stress and material rate effect on the concrete shear strength, based on calibration with experiments by Ross (1983) and Kiger et al. (1980). This is effectively the combined effect of α_1 and β_1 as proposed in Eq. 8.46. A similar enhancement factor of 2.0 was adopted by Low and Hao (2002) and Wang et al. (2013).

In order to determine the dynamic factor α_1, Fig. 8.20 presents the comparison between the dynamic shear resistance, previously obtained in direct shear cases with rate-insensitive materials in Section 7.5, and the static shear resistance for direct shear mode predicted by Eq. 8.40. The load duration is normalised by the period T_{s1} of direct shear mode.

The ratio between the two shear resistances, by definition equals to the factor α_1. An empirical formula for α_1 is proposed in Eq. 8.41 by linear fitting.

$$\alpha_1 = \begin{cases} 1.31 - 0.50 \cdot \left(\dfrac{t_d}{T_{s1}} \right) & \text{fixed} - \text{supported} \\ 1.45 - 0.57 \cdot \left(\dfrac{t_d}{T_{s1}} \right) & \text{simply} - \text{supported} \end{cases} \tag{8.41}$$

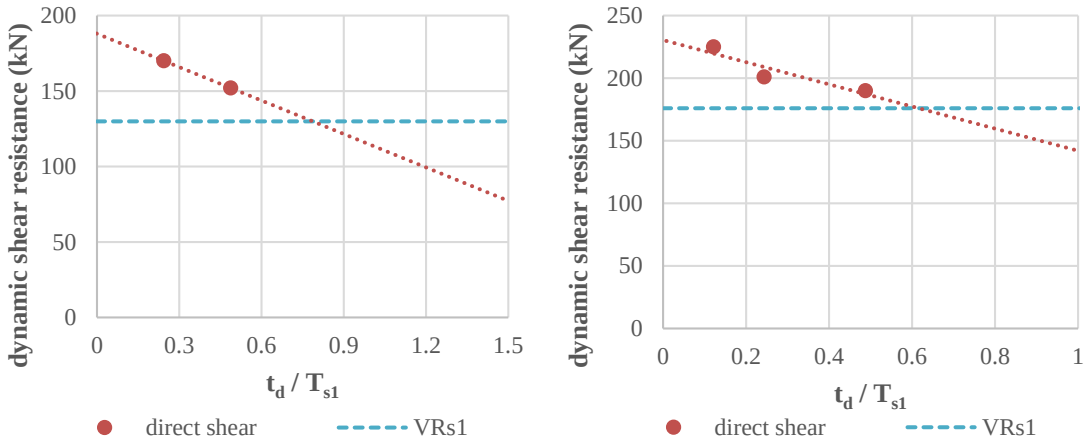

a) Simply-supported b) Fixed-supported

Fig. 8.20 Determination of factor α_1 for dynamic shear resistance

In the meantime, as discussed in Fig. 7.60c in Section 7.9, the DIF factor provided by material rate effect under direct shear mode is around 1.1~1.2. So on the conservative side, the factor β_1 can be defined as

$$\beta_1 = 1.1 \tag{8.42}$$

8.5.2 Diagonal shear resistance

Although the diagonal shear failure mode of RC members under impulsive loading has been identified by many researchers, and most of them adopts Timoshenko beam based models, in which the diagonal shear is often seen modelled by the generalized shear force vs. shear strain resistance function. For instance, Gong and Lu (2007) employed a softened membrane model (SMM) proposed by Hsu and Zhu (2002). Krauthammer (1990) predicted the diagonal shear resistance by compression field theory (Vecchio and Collins, 1986).

For static shear resistance in a reinforced concrete member, Fenwick and Pauley (1968) explained two primary resisting mechanisms in a RC member: a) the "beam action" which sees the shear resistance associated with plane sections remain plane, and b) "arch action" or "strut-and-tie action" which generally associates with diagonal compression struts in the web tied by flexural tension reinforcement. When the RC member transits from a slender member to a deep beam, normal assumptions of plane strain and uniform shear stress distribution are no longer appropriate. It is reported by Collins and Mitchell (1991) and Kani (1979) that the for a/d values less than 2.5, the shear resistance is governed by strut-and-tie action and crushing of compressive struts.

Most codes of practice use sectional methods for design of conventional slender RC beams under bending and shear. For example, traditional truss model assumes the compression struts are parallel to the diagonal cracking and no stress is transferred across the cracks. This is generally based on the 45-degree truss model (ACI 318 2008; Choi and Park 2007; Choi et al. 2007; GB50010 2010) and modified variable-angle truss models (CEB-FIP 1990; EN 1992-1-1 2004; Ramirez and Breen 1991). Other application in this regard includes and modified compression field theory (MCFT) by (Vecchio and Collins 1986), the disturbed stress field model by (Vecchio 2000), the rotating-angle softened truss models proposed by (Hsu 1993), and the softened membrane model (Hsu and

Zhu 2002). For the design of deep RC beam, the strut-and-tie model (Kani, 1979; Alan H Mattock, 1974; Schlaich et al., 1987) is also adopted by the latest design codes (ACI 318, 2008; CEB, 2010).

In the present study, an unified shear strength model for RC beams proposed by Choi and Park (2007) and Choi et al. (2007), which is applicable to both slender beams and deep beams with and without shear reinforcement, is adopted to predict the static shear resistance under diagonal shear mode. The adopted model assumes that the shear failure of a concrete beam is closely associated with the failure mechanism of the compression zone, regardless of *a/d* ratio, as demonstrated in Fig. 8.21.

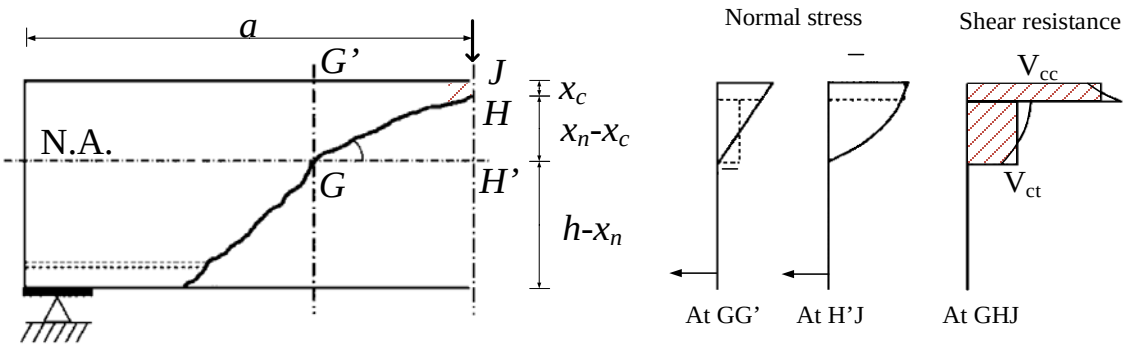

a) Cross-section b) Stress state

Fig. 8.21 Resultant forces in the investigated compressive region (after Choi and Park 2007)

In the case of a slender beam ($a/d > 2.3$) under diagonal tension failure, the compression zone is subjected to a shear failure mechanism controlled by tension. In case of a deep beam with $a/d < 2.3$, the shear strength is determined by a combined shear-compressive stress state. Rankine's failure criteria of concrete is then used to describe the failure state of the compression zone, either in a slender or deep beam.

The shear resistance of a RC beam is the sum of the shear contribution from the shear reinforcement and the concrete.

$$V_{Rs2} = V_c + V_s \tag{8.43}$$

The shear resistance provided by shear reinforcements can be calculated by

$$V_s = \rho_{vh} f_{vy} b \cdot (d - 2x_c) \tag{8.44}$$

where ρ_{vh} and f_{vy} are the shear reinforcing ratio and yielding strength of shear rebar. The shear resistance of concrete can be further expressed by the combination of contribution from the tensile cracking and compression crushing.

$$V_c = V_{ct} + V_{cc} = 0.52\sqrt{f_c^{'}} \cdot b \cdot (x_n - x_c) + 0.45 f_c^{'} \cdot b \cdot x_c \tag{8.45}$$

in which $f_c^{'}$ equal the tensile and compressive strength of concrete. x_c is the height of the neutral axis. Other geometric parameters, including the height of neutral axis x_n, the depth of the failure surface of compression crushing x_c, are determined by:

$$x_n = \frac{3\varepsilon_0 E_s(\rho_{vh} + \rho)}{4 f_c^{'}} d \cdot \left(\sqrt{1 + \frac{4 f_c^{'}(\rho_{vh} + 2\rho)}{3\varepsilon_0 E_s(\rho_{vh} + 1\rho)^2}} - 1 \right) \tag{8.46}$$

$$x_c = \left(1 - 0.43\frac{a}{d}\right) \cdot x_n \geq 0 \tag{8.47}$$

where ρ is the longitudinal reinforcing ratio, ε_0 is the compressive strain of concrete corresponding to $f_c^{'}$, which equals 0.002. E_s is the Young's modulus of steel rebar.

In Fig. 8.22, the static shear resistance predicted by Eq. 8.43-8.47, is compared with the results from FE analysis in Section 7.2. It can be seen that the formula generally gives favourable prediction for simply-supported beams that fail in

diagonal shear in the range of $1< a/d <3$. While for fixed-supported beams, an increase factor of 1.3 is manually considered.

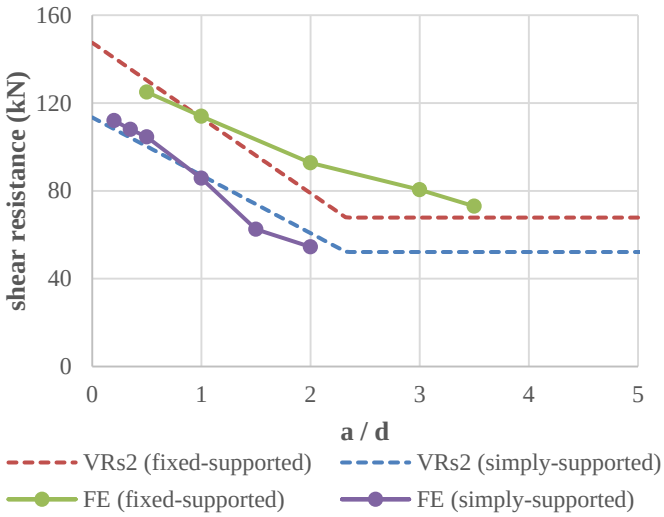

Fig. 8.22 Static shear resistance V_{Rs2} for diagonal shear mode under varied a/d ratios

Combining Eq. 8.44-8.47, the two parts of the static diagonal shear resistance for shear, can be expressed as a function of a/d ratio, as:

$$V_{Rs2-c} = \begin{cases} \left[0.45 f_c^{'} + \left(0.224\sqrt{f_c^{'}} - 0.194 f_c^{'}\right)\cdot\frac{a}{d}\right]\cdot b x_n & \frac{a}{d} \le 2.3 \\ 0.52\sqrt{f_c^{'}}\cdot b x_n & \frac{a}{d} > 2.3 \end{cases} \tag{8.48a}$$

$$V_{Rs2-s} = \begin{cases} \rho_{vh} f_{vy} b\cdot\left(d - 2x_n + 0.86 x_n\cdot\frac{a}{d}\right) & \frac{a}{d} \le 2.3 \\ \rho_{vh} f_{vy} b d & \frac{a}{d} > 2.3 \end{cases} \tag{8.48b}$$

where the a/d ratio is a function of the loading rate, and can be further expressed by the load duration normalised by the period of diagonal shear mode, as re-written from Eq. 7.3,

$$\frac{a}{d}=\begin{cases}1.560\cdot\left(\dfrac{t_d}{T_{s2}}\right)^{0.4136} & \text{fixed}-\text{supported}\\ 0.957\cdot\left(\dfrac{t_d}{T_{s2}}\right)^{0.3886} & \text{simply}-\text{supported}\end{cases} \tag{8.49}$$

To determine the increase factor α_2 for structural dynamic effect, Fig. 7.31 is reproduced in Fig. 8.23 and the load duration is normalised by the period of diagonal shear mode T_{s2}. A formula was derived to predict the increase factor α_2 by fitting the parametric study results and is as follows:

$$\alpha_2=\begin{cases}1.174\cdot\left(\dfrac{t_d}{T_{s2}}\right)^{-0.218} & \text{fixed}-\text{supported}\\ 1.085\cdot\left(\dfrac{t_d}{T_{s2}}\right)^{-0.187} & \text{simply}-\text{supported}\end{cases} \tag{8.50}$$

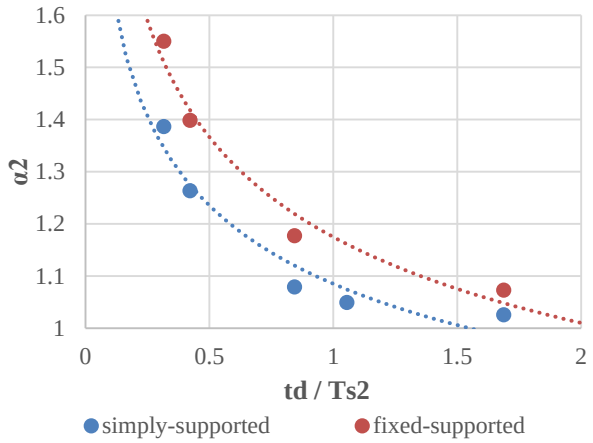

Fig. 8.23 Dynamic increase factor α_2 for structural dynamic effect under varied load durations

In the meantime, the DIF factor β_2 due to material rate effect, as previously defined in Eq. 7.6, is updated with the load duration normalised by period of diagonal shear mode.

$$\beta_2 = \begin{cases} 1.119 - 0.0041 \cdot \dfrac{t_d}{t_{s2}} & \text{simply-supported} \\ 1.149 - 0.0081 \cdot \dfrac{t_d}{t_{s2}} & \text{fixed-supported} \end{cases} \tag{8.51}$$

Based on the above derivation of parameters to include both structural and material rate effect, the envelope of the two the simplified formula for dynamic shear resistances V_{Rd1} and V_{Rd2}, has been compared with the FE simulation results using rate-sensitive materials in Section 7.10. The load duration is normalised by their respective period. It can be seen that the proposed simplified method generally gives a conservative result.

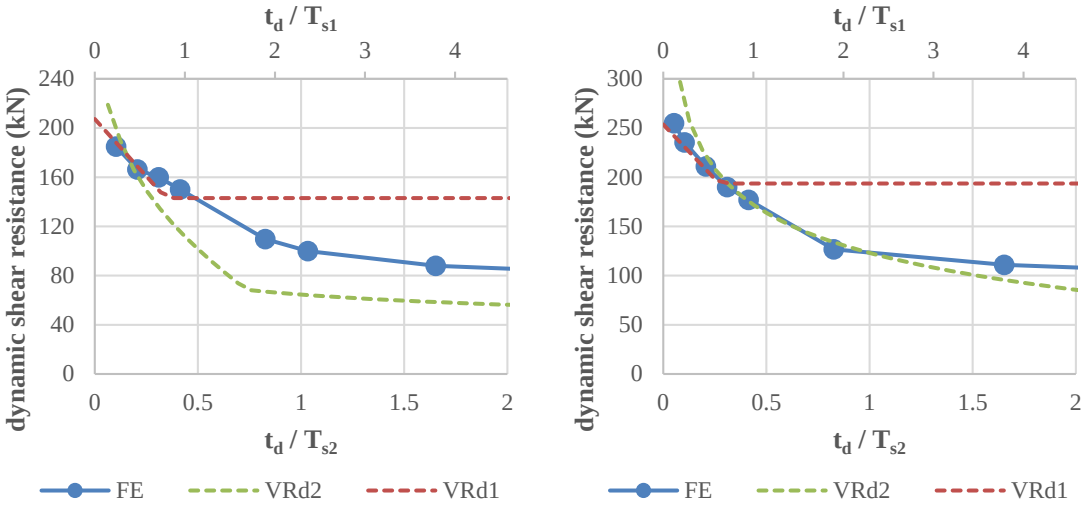

a) Simply-supported b) Fixed-supported

Fig. 8.24 Comparison of dynamic shear resistance prediction

8.5.3 General procedure of simplified assessment for dynamic shear response

Based on above discussion, a simplified assessment method for dynamic shear response of RC structures under blast loading is proposed. The following procedure explains the SDOF systems implemented in this study for obtaining

the response of the RC member and the empirical formula to predict the dynamic shear resistance. The main steps are summarized as follows:

1. Assume the shape functions for direct shear, diagonal shear and flexure mode, namely $\phi_{s1}(x)$, $\phi_{s2}(x)$ and $\phi_f(x)$;
2. Calculate the equivalent load L_{eq}, mass M_{eq}, and the stiffness K_{eq} for each mode, and derive the correspondent natural periods T_{s1}, T_{s2} and T_f ;
3. Establish the three SDOF systems, calculate the shear response based on the load duration t_d and overpressure p_m of the blast load, and obtain the maximum shear forces under the two shear modes, $V_{\max-s1}(t_d, p_m)$ and $V_{\max-s1}(t_d, p_m)$;
4. Based on the characteristic loading rate (load duration t_d), calculate the static shear resistance V_{Rs1}, amplification factor α_1 and β_1 under direct shear mode, and determine the dynamic shear resistance V_{Rd1};
5. Compare the dynamic shear demand $V_{\max-s1}(t_d, p_m)$ and shear resistance under direct shear mode $V_{Rd-s1}(t_d, p_m)$. If $V_{\max-s1}(t_d, p_m) > V_{Rd-s1}(t_d, p_m)$, the beam will fail under direct shear, otherwise continues to the 6th step;
6. Based on the characteristic loading rate (load duration t_d), determine the width of the achieved effective shear $a_{eff}(t_d)$ for diagonal shear mode, calculate the static shear resistance $V_{Rs2}(a_{eff})$, amplification factor α_2 and β_2 under diagonal shear mode, and determine the dynamic shear resistance V_{Rd2};
7. Compare the dynamic shear demand $V_{\max-s2}(t_d, p_m)$ and shear resistance under direct shear mode $V_{Rd-s2}(t_d, p_m)$. If $V_{\max-s2}(t_d, p_m) > V_{Rd-s2}(t_d, p_m)$, the beam will fail under diagonal shear, otherwise continues to the conventional flexure-based SDOF method.

8.6 Concluding remarks

This chapter brought together the observation made in previous two chapters and proposed a simplified analytical approach to assess the dynamic shear response for RC structures under blast loading. It consists of SDOF-based models to predict the high shear demand, and empirical formulas to assess the dynamic shear resistance.

Due to the fact that the three basic deformation modes are sequential in time and have distinctive deflected shape, critical failure positions and fundamental periods, it is reasonable to uncouple the responses from such three deformation modes. Simplified SDOF models have been developed that can describe the major failure mechanisms of direct shear, diagonal shear and flexure failure. Thus, the proposed model can be used to predict the RC shear demand in both the initial transient high shear stage, and the later global bending stage.

To estimate the dynamic shear resistance under direct shear mode, an empirical formula has been proposed extending from a commonly adopted direct shear model to take into account the dynamic rate effect. An empirical formula is also proposed to estimate the dynamic shear resistance under diagonal shear based on the results from Chapter 7 taking into account the effective shear span and dynamic shear resistance with the loading rate. Further dynamic enhancement due to structural and material rate effects are also considered.

The proposed model and analysis approach have been verified by comparisons with the finite element results. The comparisons demonstrate that the proposed SDOFs and the dynamic shear resistance formulas can predict the dynamic shear strength of RC beams with reasonable accurately and generally on the safe side.

Chapter 9: General conclusions and recommendation for further works

The principle objectives of this research have been to develop a holistic FE modelling framework for reinforced concrete structures subjected to impulsive loading, with the capability of representing different regimes of responses throughout the entire process. On this basis, specific FE analyses have subsequently been conducted to investigate into the dynamic shear response of RC members from the initial transient high shear stage to the global bending state, with a particular focus on the contribution of structural dynamic effect brought the effective dynamic shear span as a function of the relative loading rate as well as the contributions of material strain date effect (DIF).

9.1 Summary of main conclusions

9.1.1 Development of a holistic FE framework for modelling RC structures under impulsive loading

Starting with a preliminary benchmark analysis of RC slabs under blast loading in the global deformation phase, the validity of commonly applied FE setup and typical material models for blast related analysis are examined. This is followed

by a detailed discussion of the demands on the concrete material model in terms of preserving a realistic representation of the tension/shear behaviour and the significance of such features in simulating realistically the structural response to blast loading extending to the global flexural response regime. Deficiencies of a widely used concrete material model, namely the KCC model, in this respect are investigated and a modification scheme to the relevant aspects of the material model is proposed. Further study has been carried out to demonstrate the overall performance of KCC model in terms of predicting both shear and flexure failure under monotonic static loading. More specifically, the following conclusions have been drawn:

1. The root cause of the abnormal performance and premature failure in the FE model of the RC member into the global response phase is due to the rapid descending rate in the later softening phase and an abrupt change to a stress-less state. While this feature may not pose a significant problem in high pressure applications, it becomes problematic in low pressure situations, especially in a RC structure in which the premature failure of bond interaction between concrete and reinforcement would accelerate unrealistically the failure process towards a premature collapse.

2. Modelling rebar with a 1D beam-like element will not fundamentally alter the stress condition in the concrete in the rebar-concrete interface region, however it can cause magnified issue when the scheme is employed in a high fidelity analysis with a refined mesh size, and it also tends to render the behaviour of concrete material adjacent to the rebar to be more sensitively influenced by the mesh size. Further analysis leads to the observation that the transverse reinforcements in RC components would in effect help alleviate the demand on a realistic rebar-concrete interaction, and hence could mask the potential problem with an

inadequate behaviour of a material model when it comes to a reinforced concrete response simulation.

3. The rectification of the problem with too quick a descending rate into a zero-stress state of KCC model has been focused on an appropriate modification to a more gradual development of the damage accumulation in the late stage of the softening phase. The proposed modification includes a modified damage accumulation law, as well as an adjustment of the plastic strain accumulation factor in the KCC model.

4. Further examination on a benchmark model, i.e. the CSC model, discovered that this model is inclined towards the opposite direction of KCC model in a tension or shear dominated response subjected to low pressure regime, in that it tends to be excessively ductile in tension with the presence of a limited amount of confining pressure. The cause of this abnormal phenomenon is deemed to originate from the use of a reduction of damage in a confined stress condition. This problem justifies the choice of enhancing the KCC model in the development of a holistic FE platform for RC structures under general impulsive load.

5. Following the proposed modification to KCC model, the overall FE modelling framework is further verified with tests from an experimental programme conducted at UoE on RB beams under monotonic loading, and it demonstrated that the failure mechanisms of diagonal shear flexure and the shear resistance can be reasonably predicted using the modified model.

9.1.2 Development of a transitional layer model to estimate the bond interaction between concrete and rebar

An equivalent transitional layer model is proposed to simulate the bond interaction between rebar and concrete, to cater for the needs of modelling such interaction in a realistic manner while the rebar is modelled with one-dimensional line (beam) elements in a RC member response analysis. The following conclusions have been drawn:

1. The equivalent stress state in the translational layer is derived through a simplified theoretical model taking into account the effect of the pressure that can develop around the rebar space. On this basis, the yield surfaces are established by modifying the basic failure surfaces employed in the standard KCC model.
2. The generalised strains and internal variables include characteristic length parameters related to the rebar properties.
3. The proposed transitional layer model is validated against results from RC pull-out experiments, and comparisons of the FE modelling results using the proposed transitional layer model with the experimental data show good agreement across different experimental conditions.

9.1.3 Transition of response modes, transient high shear phenomenon and dynamic shear resistance of RC structures under impulsive loading

The rigorously calibrated FE modelling framework for reinforced concrete is applied to carry out a comprehensive investigation into the high shear phenomena in the blast response of RC components, as represented by typical RC beams.

A simplified beam model is utilised first to look into and demonstrate the key phenomena associated with the development of high shear forces, especially when the blast pulse duration gets very short. The process of the beam response moving through the high shear stages to global bending is examined and the dominated deformation modes are characterised. Then the study moved on to investigating the transient dynamic shear phenomenon in a more realistic reinforced concrete response environment. In particular, the dynamic shear failure mechanisms and the dynamic shear resistance is analysed from the perspective of both the dynamic structural effect, namely the shear failure zone (shear span), and the material strain rate effect. The following conclusions have been drawn from these studies:

1. The numerical analysis reveals that, as the blast loading rate increases, the response of an RC beam will undergo an increasingly more significant high shear phase before the response develops into a global bending mode.
2. If the shear strength is reached while high shear force develops, shear failure could occur, and, the developed shear span is much shorter than in a quasi-static shear scenario. The quicker high shear force and shear failure develops, the shorter the shear span, and ultimately the shear failure enters into a direct shear scenario with very short shear span.
3. If the shear strength is not reached in the transient shear phase, the high shear effect will quickly diminish as the response develops into a global bending mode. The shear force distribution correspondingly resumes a typical distribution as one can expect under a statically uniform distributed load. The maximum shear force in the global bending stage is dictated by the yield bending strength of the member.
4. While the development of high shear is a transient dynamic response, whether or not a shear failure will occur depends also on the dynamic

shear resistance. It is observed from the RC member analysis that, the dynamic shear resistance increases remarkably with the increase of the loading rate, which is largely due to the reduction of the effective shear span length at the reaching of the respective dynamic shear failure mode. A general trend of correlation between the effective shear span length and the loading rate has been established.

5. Analysis reveals that the trend of decrease of shear span length echoes well the trend of the dynamic shear resistance with the loading rate. Apart from the effect of reduced shear span, some extra dynamic enhancement of the shear strength is observed and is deemed to be attributable to the fact that there is a lack of time for the development of the mechanism over the failure zone which translates to an enhancement of the corresponding resistance.

6. The contribution of material dynamic strength increase (DIF) is assessed by comparing the results without and with the incorporation of the material rate-sensitivity in the FE model. An empirical dynamic increase factor for the shear resistance due to the material DIF, called DIF (shear), is developed. Such a DIF factor for the shear resistance is found to be on order of 1.1～1.2.

7. Based on the numerical results, the critical strain rates that are reached in the direct and diagonal shear modes of failure have been found to be on the order of 15～20 s^{-1}, which explains the relatively small dynamic increase of the shear strength due to the material strain rate effect.

9.1.4 Proposal of a SDOF based simplified assessment for dynamic shear response of RC structures under blast loading

In light of the preceding discussion that the development of the high shear response is originated from the shear mode, ranging from direct shear to diagonal shear, and independent from the global bending mode, a simplified method using multiple single-degree-of-freedom (SDOF) systems is proposed to take into account the shear modes and assess dynamic shear response. More specifically, the following conclusions have been drawn:

1. Three deformation modes, namely direct shear, diagonal shear and flexure, have been characterised. Due to the fact that they are sequential in time and have distinctive basic deformation modes, critical failure positions and fundamental periods, it is reasonable to assume that responses from these modes can be un-coupled and analysed by separate SDOF systems.

2. Simplified SDOF models have been developed that can describe the major failure mechanisms of direct shear, diagonal shear and flexure failure. For each shear mode, the deflected shape is assumed, equivalent load and mass are calculated, and practical estimation of the equivalent stiffnesses are derived. Thus, the proposed model can be used to predict the RC shear demand in both the initial transient high shear stage, and the later global bending stage.

3. To estimate the dynamic shear resistance under direct shear mode, an empirical formula has been proposed from a commonly adopted direct shear model to take into account the dynamic rate effect. An empirical formula is also proposed to estimate the dynamic shear resistance under diagonal shear based on analysis results taking into account the effective shear span and dynamic shear resistance with the loading rate. Further

dynamic enhancement due to structural and material rate effects are also considered.

4. The proposed SDOF models, the determination of their model properties, as well as the implementation procedure have been verified by comparisons with numerical results. Comparisons demonstrate that, the proposed SDOFs can predict the dynamic shear strength of RC members with reasonable accuracy, and the results, in conjunction with the prediction of the dynamic shear resistance, are generally on the safe side.

9.2 Recommendations for future works

The research work conducted in this study covers comprehensively the dynamic response, transient high shear phenomena, the dynamic shear strength, and the adequate FE modelling approaches. The study represents a good advancement concerning the dynamic shear resistance of reinforced concrete structures under blast loading, resulting in a good extension of existing knowledge in this subject area and the understanding of the fundamental failure mechanisms. However, the effects of some of the contributory factors have not been investigated sufficiently thoroughly within the present scope of work. Further research is recommended in the following few closely related topics:

1. Continued improvement of the FE modelling framework can focus on more rigorous ways of modelling the bond interaction between concrete and rebar, and to incorporate more explicit representation of the fracture process of concrete, to cater to aggregate interlock and dowel action for shear dominated failure in reinforced concrete environment.
2. With the availability of the realistic FE modelling framework, comprehensive numerical studies can be carried out to more

systematically evaluate the structural behaviour of reinforced concrete structures under more general impulsive loading scenario.

3. The study should also be extended into the more general situation of reinforced concrete structures and especially the evaluation of residual capacity after blast. To reasonably capture the post-damage concrete behaviour, it is therefore necessary to incorporate more appropriate representation of the anisotropic properties of the concrete, including the crack closure effect.

Reference

Abdel-Kader, M. and Fouda, A., 2014. “Effect of Reinforcement on the Response of Concrete Panels to Impact of Hard Projectiles.” *International Journal of Impact Engineering* 63: 1–17.

Abu-odeh, A., 2008. “Modeling and Simulation of Bogie Impacts on Concrete Bridge Rails Using LS-DYNA.” *10th International LS-DYNA Users Conference* (1): 9–20.

ACI 318, 2008. 2007 American Concrete Institute, Farmington Hills, MI *Building Code Requirements for Structural Concrete and Commentary*.

ACI 440.3R-04, 2004. *Guide Test Methods for Fiber-Reinforced Polymers (FRPs) for Reinforcing Or Strengthening Concrete Structures*. ACI Committee 440.

ACI 445R-99, 2000. Reported by Joint ACI-ASCE Committee 445 *Recent Approaches to Shear Design of Structural Concrete*.

ACI Committee 408, 1992. “State-of-the-Art Report on Bond under Cyclic Loads.” In American Concrete Institute.

Adhikary, S. Das, Li, B., and Fujikake, K., 2012. “Dynamic Behavior of Reinforced Concrete Beams under Varying Rates of Concentrated Loading.” *International Journal of Impact Engineering* 47: 24–38.

Ågårdh, L. and Laine, L., 1999. “3D FE-Simulation of High-Velocity Fragment Perforation of Reinforced Concrete Slabs.” *International Journal of Impact Engineering* 22(9): 911–22.

Algaard, W., Lyle, J., and Izatt, C., 2005. “Perforation of Composite Floors.” In *5th European LS-DYNA User Conference*, Birmingham, UK, 3C – 56.

ANSYS, 2009. 15317 *AUTODYN ® User Manual Version 12.0*. Canonsburg.

ARUP, 2009. *Verification of the Karagozian and Case Material-Model for LS-DYNA 971 R3 Report*.

Bao, X. and Li, B., 2010. “Residual Strength of Blast Damaged Reinforced Concrete Columns.” *International Journal of Impact Engineering* 37(3): 295–308.

Bažant, Z.P., 1978. “Endochronic Inelasticity and Incremental Plasticity.”

Bažant, Z.P. and Oh, B.H., 1983. “Crack Band Theory for Fracture of Concrete.” *Matériaux et Constructions* 16: 155–77.

Belytschko, T., Schwer, L., and Klein, M.J., 1977. “Large Displacement, Transient Analysis of Space Frames.” *International Journal for Numerical Methods in Engineering* 11(1): 65–84.

Bhatti, A.Q., Kishi, N., Konno, H., and Mikami, H., 2012. “Elasto-Plastic Dynamic Response Analysis of Prototype RC Girder under Falling-Weight Impact Loading Considering Mesh Size Effect.” *Structure and Infrastructure Engineering* 8(9): 817–27.

Biggs, J.M., 1964. *Introduction to Structural Dynamics*.

Bonora, N., Gentile, D., Pirondi, A., and Newaz, G., 2005. “Ductile Damage Evolution under Triaxial State of Stress: Theory and Experiments.” *International Journal of Plasticity* 21(5): 981–1007.

Booker, P.M., Cargile, J.D., Kistler, B.L., and La Saponara, V., 2009. “Investigation on the Response of Segmented Concrete Targets to Projectile

Impacts.” *International Journal of Impact Engineering* 36(7): 926–39.

Borrvall, T. and Riedel, W., 2011. “The RHT Concrete Model in LS-DYNA.” In *Preceedings of the 8 Th European LS-DYNA …*,.

British Standards Institution, 2004. *Eurocode 2: Design of Concrete Structures: Part 1-1: General Rules and Rules for Buildings*. British Standards Institution.

Broadhouse, B.J., 1995. “SPD/D(95)363. AEA Technology. Winfrith Concrete Model in LS-DYNA3D.” : 17.

Broadhouse, B.J. and Neilson, A.J., 1987. “Modelling Reinforced Concrete Structures in DYNA3D.” *AEE Winfrith* AEEW-M 246.

Burton, D.E., Lettis Jr, L.A., Bryan, J.B., and Frary, N.R., 1982. “Physics and Numerics of the TENSOR Code.” *Lawrence Livermore National Laboratory, Internal Document UCID-19428,(July 1982)*.

Casanova, a., Jason, L., and Davenne, L., 2012. “Bond Slip Model for the Simulation of Reinforced Concrete Structures.” *Engineering Structures* 39: 66–78.

CEB-FEP, 2010. 1 *CEB-FIP Model Code 2010*. Lausanne, Switzerland: Thomas Thelford.

CEB-FIP, 1990. Bulletin d’Information *CEB-FIP Model Code 1990*. FIB-Féd. Int. du Béton.

Choi, K.-K. and Park, H.-G., 2007. “Unified Shear Strength Model for Reinforced Concrete Beams - Part II: Verification and Simplified Method.” *ACI Structural Journal* 104(2): 153–61.

Choi, K.-K., Park, H.-G., and Wight, J.K., 2007. “Unified Shear Strength Model for Reinforced Concrete Beams—Part I: Development.” *ACI Structural*

Journal 104(2): 142–52.

Collins, M.P. and Mitchell, D., 1991. 9 *Prestressed Concrete Structures*. Prentice Hall Englewood Cliffs, NJ.

Cox, J. V and Herrmann, L.R., 1998. “Development of a Plasticity Bond Model for Steel Reinforcement.” *Mechanics of Cohesive-frictional Materials* 3(2): 155–80.

Crawford, J.E. et al., 2012. *Use and Validation of the Release III K&C Concrete Material Model in LS-DYNA*. Glendale, CA: Karagozian & Case.

Dassault Systèmes, 2007. “Abaqus Analysis User’s Manual.” *Simulia Corp. Providence, RI, USA*.

Dragos, J. and Wu, C., 2014. “Interaction between Direct Shear and Flexural Responses for Blast Loaded One-Way Reinforced Concrete Slabs Using a Finite Element Model.” *Engineering Structures* 72: 193–202.

El-Dakhakhni, W.W., Mekky, W.F., and Changiz Rezaei, S.H., 2009. “Validity of SDOF Models for Analyzing Two-Way Reinforced Concrete Panels under Blast Loading.” *Journal of Performance of Constructed Facilities* 24(August): 311–26.

Eligehausen, R., Popov, E.P., and Bertero, V. V., 1982a. “Local Bond Stress-Slip Relationships of Deformed Bars under Generalized Excitations.” In *Proceedings of the 7th European Conference on Earthquake Engineering. Vol. 4.*, Athens, Greece, 69–80.

Eligehausen, R., Popov, E.P., and Bertero, V. V., 1982b. *Report No. UCB/EERC-83/23: Local Bond Stress-Slip Relationships of Deformed Bars under Generalized Excitations*. Earthquake Engineering Research Center, University of California.

EN 1992-1-1, 2004. *Eurocode 2: Design of Concrete Structures: Part 1-1: General Rules and Rules for Buildings*. British Standards Institution.

Faria, R., Oliver, J., and Cervera, M., 1998. “A Strain-Based Plastic Viscous-Damage Model for Massive Concrete Structures.” *International Journal of Solids and Structures* 35(14): 1533–58.

Farnam, Y., Mohammadi, S., and Shekarchi, M., 2010. “Experimental and Numerical Investigations of Low Velocity Impact Behavior of High-Performance Fiber-Reinforced Cement Based Composite.” *International Journal of Impact Engineering* 37(2): 220–29.

Fenwick, R.C. and Pauley, T., 1968. “Mechanism of Shear Resistance of Concrete Beams.” *Journal of the Structural Division* 94(10): 2325–50.

Fujikake, K., Li, B., and Soeun, S., 2009. “Impact Response of Reinforced Concrete Beam and Its Analytical Evaluation.” *Journal of structural engineering* (August 2009): 938–50.

GB50010, 2010. *Code for Design of Concrete Structures*. Beijing, China: Ministry of Housing and Urban-Rual Developement, People’s Republic of China.

Gibson, P., 1994. *Blast Overpressure and Survivability Calculations for Various Sizes of Explosive Charges*. DTIC Document.

Gong, S. and Lu, Y., 2007. “Combined Continua and Lumped Parameter Modeling for Nonlinear Response of Structural Frames to Impulsive Ground Shock.” *Journal of Engineering Mechanics* 133(11): 1229–40.

Govindjee, S., Kay, G.J., and Simo, J.C., 1995. “Anisotropic Modelling and Numerical Simulation of Brittle Damage in Concrete.” *International Journal for Numerical Methods in Engineering* 38: 3611–33.

Grassl, P. and Jirásek, M., 2006. “Damage-Plastic Model for Concrete Failure.”

International Journal of Solids and Structures 43(22-23): 7166–96.

Grassl, P., Lundgren, K., and Gylltoft, K., 2002. “Concrete in Compression: A Plasticity Theory with a Novel Hardening Law.” *International Journal of Solids and Structures* 39(20): 5205–23.

Grassl, P., Nyström, U., Rempling, R., and Gylltoft, K., 2011. “A Damage-Plasticity Model for the Dynamic Failure of Concrete.” In *8th International Conference on Structural Dynamics*,.

Han, D.J. and Chen, W.-F., 1985. “A Nonuniform Hardening Plasticity Model for Concrete Materials.” *Mechanics of materials* 4(3): 283–302.

Hansson, H. and Skoglund, P., 2002. Swedish Defense Research Agency *Simulation of Concrete Penetration in 2D and 3D with the RHT Material Model*.

Hawkins, N.M., 1973. “The Strength of Stud Shear Connectors.” *Institution of Engineers (Australia) Civ Eng Trans* (1).

Hawkins, N.M., 1982. Letter Report to US Navy *Direct Shear Resistance*.

Holqmuist, T.J. and Johnson, G.R., 1993. “A Computational Constitutive Model for Concrete Subjected to Large Strains, High Strain Rate, and High Pressures.” In *14th International Symposium on Ballistics*, , 591–600.

Hsu, T.T.C., 1992. 5 *Unified Theory of Reinforced Concrete*. CRC press.

Hsu, T.T.C. and Zhu, R.R.H., 2002. “Softened Membrane Model for Reinforced Concrete Elements in Shear.” *ACI Structural Journal* 99(4): 460–69.

Ingraffea, A.R., Gerstk, W.H., Gergely, P., and Saouma, V., 1984. “Fracture Mechanics of Bond in Reinforced Concrete.” *Journal of Structural Engineering* 110(4): 871–90.

Janney, J.R., Hognestad, E., and McHenry, D., 1956. “Ultimate Flexural Strength of Prestressed and Conventionally Reinforced Conrete Beams.” *Journal of the American Concrete Institute Proceedings* 52(January): 601.

Jiang, H. and Chorzepa, M.G., 2014. “Aircraft Impact Analysis of Nuclear Safety-Related Concrete Structures: A Review.” *Engineering Failure Analysis* 46: 118–33.

Jiang, H., Wang, X., and He, S., 2012. “Numerical Simulation of Impact Tests on Reinforced Concrete Beams.” *Materials & Design* 39: 111–20.

Kani, G., 1979. *Kani on Shear in Reinforced Concrete*. Deptartment of Civil Engineering, University of Toronto.

Kiger, S.A., Getchell, J. V, Slawson, T.R., and Hyde, D.W., 1980. “Vulnerability of Shallow-Buried Flat-Roof Structures.” *US Army Engineer Waterways Experiment Station, Technical Report SL-80-7, 6 parts*.

Kim, J. and Mander, J., 1999. “Truss Modeling of Reinforced Concrete Shear-Flexure Behavior.” *Technical Report MCEER-99-0005*.

Kim, J.H. and Mander, J.B., 2007. “Influence of Transverse Reinforcement on Elastic Shear Stiffness of Cracked Concrete Elements.” *Engineering Structures* 29(8): 1798–1807.

Kishi, N. and Bhatti, A.Q., 2010. “An Equivalent Fracture Energy Concept for Nonlinear Dynamic Response Analysis of Prototype RC Girders Subjected to Falling-Weight Impact Loading.” *International Journal of Impact Engineering* 37(1): 103–13.

Kishi, N., Khasraghy, S., and Konno, H., 2011. “Numerical Simulation of Reinforced Concrete Beams under Consecutive Impact Loading.” *ACI Structural Journal* (108).

Koiter, W.T., 1953. “Stress-Strain Relations, Uniqueness and Variational Theorems for Elastic-Plastic Materials with a Singular Yield Surface.” *Quart. Appl. Math* 11(3): 350–54.

Krajcinovic, D., 1983. “Constitutive Equations for Damaging Materials.” *Journal of applied Mechanics* 50(2): 355–60.

Krajcinovic, D., 1985. “Continuous Damage Mechanics Revisited: Basic Concepts and Definitions.” *Journal of Applied Mechanics* 52(4): 829–34.

Krauthammer, T., 1984. “Shallow Buried RC Box Type Structures.” *Journal of Structural Engineering* 110(3): 637–51.

Krauthammer, T., Assadi-Lamouki, A., and Shanaa, H.M., 1993a. “Analysis of Impulsively Loaded Reinforced Concrete Structural elements—I. Theory.” *Computers & Structures* 48(5): 851–60.

Krauthammer, T., Assadi-Lamouki, A., and Shanaa, H.M., 1993b. “Analysis of Impulsively Loaded Reinforced Concrete Structural elements—II. Implementation.” *Computers & Structures* 48(5): 861–71.

Krauthammer, T., Bazeos, N., and Holmquist, T.J., 1986. “Modified SDOF Analysis of RC Box Type Structures.” *Journal of Structural Engineering* 112(4): 726–44.

Krauthammer, T., Shahriar, S., and Shanaa, H.M., 1990. “Response of Reinforced Concrete Elements to Severe Impulsive Loads.” *Journal of Structural Engineering* 116(4): 1061–79.

Kyei, C., 2014. “Effects of Blast Loading on Seismically Detailed Reinforced Concrete Columns.” Carleton University.

Lee, J., 1996. “Theory and Implementation of Plastic-Damage Model for Concrete Structures under Cyclic and Dynamic Loading.” University of

California, Berkeley.

Lee, J. and Fenves, G.L., 1998. “Plastic-Damage Model for Cyclic Loading of Concrete Structures.” *Journal of Engineering Mechanics* 124(8): 892–900.

Li, B., Nair, A., and Kai, Q., 2012. “Residual Axial Capacity of Reinforced Concrete Columns with Simulated Blast Damage.” *Journal of Performance of Constructed Facilities* (June): 287–99.

Li, J. and Hao, H., 2014. “Numerical Study of Concrete Spall Damage to Blast Loads.” *International Journal of Impact Engineering* 68: 41–55.

Li, Q.. and Jones, N., 2000. “Formation of a Shear Localization in Structural Elements under Transverse Dynamic Loads.” *International Journal of Solids and Structures* 37(45): 6683–6704.

Li, Q.M. and Jones, N., 1995. “Blast Loading of Fully Clamped Beams with Transverse Shear Effects*.” *Journal of Structural Mechanics* 23(1): 59–86.

Li, Q.M. and Meng, H., 2002. “Pulse Loading Shape Effects on Pressure–impulse Diagram of an Elastic–plastic, Single-Degree-of-Freedom Structural Model.” *International journal of mechanical sciences* 44: 1985–98.

Liu, Y., Ma, A., and Huang, F., 2009. “Numerical Simulations of Oblique-Angle Penetration by Deformable Projectiles into Concrete Targets.” *International Journal of Impact Engineering* 36(3): 438–46.

Low, H. and Hao, H., 2002. “Reliability Analysis of Direct Shear and Flexural Failure Modes of RC Slabs under Explosive Loading.” *Engineering Structures* 24(2): 189–98.

Lowes, L.N., Moehle, J.P., and Govindjee, S., 2004. “Concrete-Steel Bond Model for Use in Finite Element Modeling of Reinforced Concrete S Tructures.” *ACI Structural Journal* 4(101): 501–11.

LSTC, 2006. *LS-DYNA Theory Manual*. LIVERMORE SOFTWARE TECHNOLOGY CORPORATION.

LSTC, 2012. II *LS-DYNA Keyword User's Manual*. Livermore, California.

Lu, G., Li, X., and Wang, K., 2012. "A Numerical Study on the Damage of Projectile Impact on Concrete Targets." *Computers and Concrete* 9(1): 21–33.

Lu, Y., 2013. "Structural Response To High Impulsive Loads: Dynamic Effects and Analysis Approaches." *Journal of Earthquake and Tsunami* 07(03): 1350017.

Lu, Y. and Gong, S., 2007. "An Analytical Model for Dynamic Response of Beam-Column Frames to Impulsive Ground Excitations." *International Journal of Solids and Structures* 44(3-4): 779–98.

Lubarda, V.A., Krajcinovic, D., and Mastilovic, S., 1994. "Damage Model for Brittle Elastic Solids with Unequal Tensile and Compressive Strengths." *Engineering Fracture Mechanics* 49(5): 681–97.

Lubliner, J., Oliver, J., Oller, S., and Onate, E., 1989. "A Plastic-Damage Model for Concrete." *International Journal of solids and structures* 25(3): 299–326.

Luccioni, B.M., Lopez, D.E., and Danesi, R.F., 2005. "Bond-Slip in Reinforced Concrete Elements." *Journal of Structural Engineering* 131(11): 1690–98.

Luckyram, J., Stewart, B.M., and Zintilis, G.M., 1992. "Blast Loaded R . C . Slabs : A Binary Response Model for Shear and Flexure Interaction." In *Structures Under Shock and Impact II*, Portsmouth, UK, 177–88.

Ma, G.W., Shi, H.J., and Shu, D.W., 2007. "P-I Diagram Method for Combined Failure Modes of Rigid-Plastic Beams." *International Journal of Impact Engineering* 34(6): 1081–94.

Magallanes, J.M., 2008. “Importance of Concrete Material Characterization and Modelling to Predicting the Response of Structures to Shock and Impact Loading.” In *10th International Conference on Structures Under Shock and Impact*, WIT Transactions on The Built Environment, Southampton, UK: WIT Press, 241–50.

Magallanes, J.M., Wu, Y., Malvar, L.J., and Crawford, J.E., 2010. “Recent Improvements to Release III of the K&C Concrete Model.” In *Eleventh International LSDYNA Users Conference*, , 37–48.

Magnusson, J., Ansell, A., and Hansson, H., 2010. “Air-Blast-Loaded, High-Strength Concrete Beams. Part II: Numerical Non-Linear Analysis.” *Magazine of Concrete Research* 62(4): 235–42.

Malvar, L.J., 1991. *Bond of Reinforcemen Under Controlled Confinement.* DTIC Document.

Malvar, L.J. and Crawford, J.E., 1997. “A Plasticity Concrete Material Model for DYNA3D.” *International Journal of Impact Engineering* 19(97): 847–73.

Malvar, L.J., Crawford, J.E., and Morrill, K.B., 2000. *K&C Concrete Material Model Release III--Automated Generation of Material Model Input*. Karagozian & Case.

Mattock, A.H., 1974. “Effect of Aggregate Type on Single Direction Shear Transfer Strength in Monolithic Concrete.” *Report SM74-2, Department of Civil Engineering, University of Washington, Seattle, Washington*.

Mattock, A.H., 1974. “Shear Transfer in Concrete Having Reinforcement at an Angle to the Shear Plane.” *ACI Special Publication* 42: 17–42.

Mazars, J. and Pijaudier-Cabot, G., 1989. “Continuum Damage Theory - Application to Concrete.” *Journal of Engineering Mechanics* 115(2): 345–65.

Murray, Y.D., 2007. *Users Manual for LS-DYNA Concrete Material Model 159*. McLean, VA: Federal Highway Administration.

Murray, Y.D., Abu-Odeh, A.Y., and Bligh, R.P., 2007. *Evaluation of LS-DYNA Concrete Material Model 159*.

Mutalib, A. a. and Hao, H., 2011. "Development of P-I Diagrams for FRP Strengthened RC Columns." *International Journal of Impact Engineering* 38(5): 290–304.

Oliver, J., 1989. "A Consistent Characteristic Length for Smeared Cracking Models." *International Journal for Numerical Methods in Engineering* 28(2): 461–74.

Ortiz, M., 1985. "A Constitutive Theory for the Inelastic Behavior of Concrete." *Mechanics of materials* 4: 67–93.

Ortiz, M. and Popov, E.P., 1982. "A Physical Model for the Inelasticity of Concrete." In *Proceedings of the Royal Society of London A: Mathematical, Physical and Engineering Sciences*, The Royal Society, 101–25.

Ozbolt, J. and Eligehausen, R., 1992. "Numerical Simulation of Cycling Bond-Slip Behaviour." In *Proceedings of International Conference on Bond in Concrete CEB*, , 33.

Pirondi, a. et al., 2006. "Simulation of Failure under Cyclic Plastic Loading by Damage Models." *International Journal of Plasticity* 22(11): 2146–70.

Polanco-Loria, M., Hopperstad, O.S., Børvik, T., and Berstad, T., 2008a. "Numerical Predictions of Ballistic Limits for Concrete Slabs Using a Modified Version of the HJC Concrete Model." *International Journal of Impact Engineering* 35(5): 290–303.

Polanco-Loria, M., Hopperstad, O.S., Børvik, T., and Berstad, T., 2008b.

"Numerical Predictions of Ballistic Limits for Concrete Slabs Using a Modified Version of the HJC Concrete Model." *International Journal of Impact Engineering* 35(5): 290–303.

Ramirez, J.A. and Breen, J.E., 1991. "Evaluation of a Modified Truss-Model Approach for Beams in Shear." *ACI Structural Journal* 5(88): 562–72.

Ranjan, R., Banerjee, S., Singh, R.K., and Banerji, P., 2014. "Local Impact Effects on Concrete Target due to Missile: An Empirical and Numerical Approach." *Annals of Nuclear Energy* 68: 262–75.

Razaqpur, A.G., Tolba, A., and Contestabile, E., 2007. "Blast Loading Response of Reinforced Concrete Panels Reinforced with Externally Bonded GFRP Laminates." *Composites Part B: Engineering* 38(5-6): 535–46.

Reinhardt, H.W., Blaauwendraad, J., and Vos, E., 1984. "Prediction of Bond between Steel and Concrete by Numerical Analysis." *Matériaux et Construction* 17(4): 311–20.

Riedel, W., 2009. "10 Years RHT: A Review of Concrete Modelling and Hydrocode Applications." In *Predictive Modeling of Dynamic Processes*, ed. Stefan Hiermaier. Boston, MA: Springer US, 143–65.

Riedel, W., Mayrhofer, C., Thoma, K., and Stolz, A., 2010. "Engineering and Numerical Tools for Explosion Protection of Reinforced Concrete." *International Journal of Protective Structures* 1(1): 85–102.

Riedel, W., Thoma, K., Hiermaier, S., and Schmolinske, E., 1999. "Penetration of Reinforced Concrete by BETA-B-500 Numerical Analysis Using a New Macroscopic Concrete Model for Hydrocodes." In *Proceedings of the 9th International Symposium on the Effects of Munitions with Structures*,.

Rodríguez, J., Martínez, F., and Martí, J., 2013. "Concrete Constitutive Model ,

Calibration and Applications.” In *2013 SIMULIA Community Conference*, , 1–15.

Ben Romdhane, M.R. and Ulm, F.-J., 2002. “Computational Mechanics of the Steel-Concrete Interface.” *International Journal for Numerical and Analytical Methods in Geomechanics* 26(2): 99–120.

Ross, T., 1983. “Direct Shear Failure in Reinforced Concrete Beams under Impulsive Loading.”

Ross, T.J., 1983. *Direct Shear Failure in Reinforced Concrete Beams under Impulsive Loading*. DTIC Document.

Ross, T.J. and Krawinkler, H., 1985. “Impulsive Direct Shear Failure in RC Slabs.” *Journal of Structural Engineering* 111(8): 1661–77.

Rots, J.G., 1988. “Computational Modeling of Concrete Fracture.”

Sadrnejad, S.A. and Amiri, S.A.G., 2010. “A Simple Unconventional Plasticity Model within the Multilaminate Framework.” *Int. Journal of Civil Engineering* 8(2): 143–58.

Salari, M.R. and Spacone, E., 2001. “Finite Element Formulations of One-Dimensional Elements with Bond-Slip.” *Engineering Structures* 23(7): 815–26.

Schlaich, J., Shafer, K., Jennewein, M., and KOTSOVOS, M.D., 1987. “Toward a Consistent Design of Structural Concrete.” *PCI journal* (32).

Schreyer, H.L., 1983. “A Third-Invariant Plasticity Theory for Frictional Materials.” *Journal of structural mechanics* 11(2): 177–96.

Schwer, L., 2010. “An Introduction to the Winfrith Concrete Model.” *Schwer Engineering & Consulting Services* (April): 1–28.

Schwer, L., 2011. “The Winfrith Concrete Model: Beauty or Beast? Insights into the Winfrith Concrete Model.” In *8th European LS-DYNA Users Conference*,.

Schwer, L.E. and Malvar, L.J., 2005. “Simplified Concrete Modeling with *MAT_CONCRET_DAMAGE_REL3.” In *LS-DYNA Anwenderforum*, Bamberg, 49–60.

Shi, Y., Hao, H., and Li, Z.-X., 2008. “Numerical Derivation of Pressure–impulse Diagrams for Prediction of RC Column Damage to Blast Loads.” *International Journal of Impact Engineering* 35(11): 1213–27.

Shi, Y., Li, Z., and Hao, H., 2009. “Bond Slip Modelling and Its Effect on Numerical Analysis of Blast-Induced Responses of RC Columns.” *Structural Engineering and Mechanics* 32(2): 1225–4568.

Simo, J.C. and Ju, J.W., 1987a. “Strain-and Stress-Based Continuum Damage models—I. Formulation.” *International Journal of Solids and Structures* 23(7): 821–40.

Simo, J.C. and Ju, J.W., 1987b. “Strain-and Stress-Based Continuum Damage models—II. Computational Aspects.” *International journal of solids and structures* 23(7): 841–69.

Simo, J.C. and Ju, J.W., 1989. “On Continuum Damage-Elastoplasticity at Finite Strains.” *Computational Mechanics* 5: 375–400.

Slawson, T., 1984. *Dynamic Shear Failure of Shallow-Buried Flat-Roofed Reinforced Concrete Structures Subjected to Blast Loading*.

Swaddiwudhipong, S., Islamb, M.J., and Liu, Z.S., 2010. “High Velocity Penetration/Perforation Using Coupled Smooth Particle Hydrodynamics-Finite Element Method.” *International Journal of Protective Structures* 1(4): 489–506.

Tabatabaei, Z.S. et al., 2013. “Experimental and Numerical Analyses of Long Carbon Fiber Reinforced Concrete Panels Exposed to Blast Loading.” *International Journal of Impact Engineering* 57: 70–80.

Tai, Y.S., 2009. “Flat Ended Projectile Penetrating Ultra-High Strength Concrete Plate Target.” *Theoretical and Applied Fracture Mechanics* 51(2): 117–28.

Tai, Y.S., Chu, T.L., Hu, H.T., and Wu, J.Y., 2011. “Dynamic Response of a Reinforced Concrete Slab Subjected to Air Blast Load.” *Theoretical and Applied Fracture Mechanics* 56(3): 140–47.

Teng, T.-L. et al., 2008. “Development and Validation of Numerical Model of Steel Fiber Reinforced Concrete for High-Velocity Impact.” *Computational Materials Science* 42(1): 90–99.

Thiagarajan, G., 2013. “2012 Blast Blind Prediction Results - Overview of Methods Used and Observations.” In *ACI Fall 2013 Convention: Blast Blind Predict of Response of Concrete Slabs Subjected to Blast Loading*, Phoenix, Arizona, US.

Thiagarajan, G., Kadambi, A. V., Robert, S., and Johnson, C.F., 2014. “Experimental and Finite Element Analysis of Doubly Reinforced Concrete Slabs Subjected to Blast Loads.” *International Journal of Impact Engineering* 75: 162–73.

Thiagarajan, G., Vasudevan, A.K., and Robert, S., 2011. “Numerical Modeling of Concrete Slabs Reinforced with High Strength Low Alloy Vanadium Steel Bars Subjected to Blast Loads.” *ACI Special Publication* 281.

Thilakarathna, H.M.I., Thambiratnam, D.P., Dhanasekar, M., and Perera, N., 2010. “Numerical Simulation of Axially Loaded Concrete Columns under Transverse Impact and Vulnerability Assessment.” *International Journal of Impact Engineering* 37(11): 1100–1112.

Timoshenko, S., 1976. *Strength of Materials*. New York.

Timoshenko, S., Woinowsky-Krieger, S., and Woinowsky-Krieger, S., 1959. 2 *Theory of Plates and Shells*. McGraw-hill New York.

TM5-1300, 1990. “Structures to Resist the Effect of Accidental Explosions.” *TM5-1300*.

TM5-855-1, 1986. *Fundamentals of Protective Design for Conventional Weapons*. Headquarters, Department of the Army.

Trivedi, N. and Singh, R.K., 2013. “Prediction of Impact Induced Failure Modes in Reinforced Concrete Slabs through Nonlinear Transient Dynamic Finite Element Simulation.” *Annals of Nuclear Energy* 56: 109–21.

Tu, Z. and Lu, Y., 2009. “Evaluation of Typical Concrete Material Models Used in Hydrocodes for High Dynamic Response Simulations.” *International Journal of Impact Engineering* 36(1): 132–46.

Tu, Z. and Lu, Y., 2010. “Modifications of RHT Material Model for Improved Numerical Simulation of Dynamic Response of Concrete.” *International Journal of Impact Engineering* 37(10): 1072–82.

UFC 3-340-02, 2008. *Structures to Resist the Effects of Accidental Explosions*.

University of Missouri-Kansas City, 2013. *Blast Blind Simulation Contest*. http://sce.umkc.edu/blast-prediction-contest/.

UPD Center, 2006. “User’s Guide for the Single-Degree-of-Freedom Blast Effects Design Spreadsheets (SBEDS).” *Rep. PDC-TR*: 2–6.

Vecchio, F.J., 2000. “Disturbed Stress Field Model for Reinforced Concrete: Formulation.” *Journal of Structural Engineering* 126(9): 1070–77.

Vecchio, F.J. and Collins, M.P., 1986. “The Modified Compression-Field Theory

for Reinforced Concrete Elements Subjected to Shear." *ACI J.* 83(2): 219–31.

Voyiadjis, G.Z. and Abu-Lebdeh, T.M., 1994. "Plasticity Model for Concrete Using the Bounding Surface Concept." *International Journal of Plasticity* 10(1): 1–21.

Walraven, J.C. and Reinhardt, H.W., 1981. "Theory and Experiments on the Mechanical Behavior of Cracks in Plain and Reinforced Concrete Subjected to Shear Loading." *Heron* 26(1A).

Wang, F. et al., 2008. "Reinforced Concrete Slab Subjected to Close-in Explosion." *LS-DYNA Anewnderforum. Bamgerg*: 21–28.

Wang, W. et al., 2013. "Pressure-Impulse Diagram with Multiple Failure Modes of One-Way Reinforced Concrete Slab under Blast Loading Using SDOF Method." *Journal of Central South University* 20(2): 510–19.

Wesevich, J.W. et al., 2011. "Comparative Study of Concrete Constitutive Models for Predicting Blast Response." *ACI Special Publication* 281: 1–18.

Williams, G. et al., 2008. 98 WIT Transactions on the Built Environment *Blast-Resistant Highway Bridges: Design and Detailing Guidelines*.

Williams, G.D., 2009. "Analysis and Response Mechanisms of Blast-Loaded Reinforced Concrete Columns." The University of Texas at Austin.

Williams, G.D. and Williamson, E., 2011. "Response of Reinforced Concrete Bridge Columns Subjected to Blast Loads." *Journal of Structural Engineering* 137(9): 903–13.

Williams, W.F., Buth, C.E., and Menges, W.L., 2007. *Repair/Retrofit Anchorage Designs for Bridge Rails*. College Station, Texas.

Wu, K.-C., Li, B., and Tsai, K.-C., 2011a. “Residual Axial Compression Capacity of Localized Blast-Damaged RC Columns.” *International Journal of Impact Engineering* 38(1): 29–40.

Wu, K.-C., Li, B., and Tsai, K.-C., 2011b. “The Effects of Explosive Mass Ratio on Residual Compressive Capacity of Contact Blast Damaged Composite Columns.” *Journal of Constructional Steel Research* 67(4): 602–12.

Wu, Y., Crawford, J.E., Lan, S., and Magallanes, J.M., 2014. “Validation Studies for Concrete Constitutive Models with Blast Test Data.” *13th International LS-DYNA Users Conference*: 1–12.

Wu, Y., Crawford, J.E., and Magallanes, J.M., 2012. “Performance of LS-DYNA® Concrete Constitutive Models.” In *12th International LS-DYNA Users Conference*, Dearborn, Michigan, US, 1–14.

Xu, J. and Lu, Y., 2013. “A Comparative Study of Modelling RC Slab Response to Blast Loading with Two Typical Concrete Material Models.” *International Journal of Protective Structures* 4(3): 415–32.

Xu, J., Wu, C., and Li, Z.-X., 2014. “Analysis of Direct Shear Failure Mode for RC Slabs under External Explosive Loading.” *International Journal of Impact Engineering* 69: 136–48.

Xu, K. and Lu, Y., 2006. “Numerical Simulation Study of Spallation in Reinforced Concrete Plates Subjected to Blast Loading.” *Computers & Structures* 84(5-6): 431–38.

Yonten, K., Manzari, M.T., Marzougui, D., and Eskandarian, A., 2005. “An Assessment of Constitutive Models of Concrete in the Crashworthiness Simulation of Roadside Safety Structures.” *International Journal of Crashworthiness* 10(1): 5–19.

Yun, S.-H. and Park, T., 2013. “Multi-Physics Blast Analysis of Reinforced High Strength Concrete.” *KSCE Journal of Civil Engineering* 17(4): 777–88.

Zhou, X., Kuznetsov, V., Hao, H., and Waschl, J., 2008. “Numerical Prediction of Concrete Slab Response to Blast Loading.” *International Journal of Impact Engineering* 35: 1186–1200.